



HAL
open science

Impact of the spatial and temporal variability of the Mistral on dense water formation in the Mediterranean Sea

Douglas Keller

► **To cite this version:**

Douglas Keller. Impact of the spatial and temporal variability of the Mistral on dense water formation in the Mediterranean Sea. Ocean, Atmosphere. Institut Polytechnique de Paris, 2022. English. NNT : 2022IPPAX113 . tel-04107921

HAL Id: tel-04107921

<https://theses.hal.science/tel-04107921>

Submitted on 26 May 2023

HAL is a multi-disciplinary open access archive for the deposit and dissemination of scientific research documents, whether they are published or not. The documents may come from teaching and research institutions in France or abroad, or from public or private research centers.

L'archive ouverte pluridisciplinaire **HAL**, est destinée au dépôt et à la diffusion de documents scientifiques de niveau recherche, publiés ou non, émanant des établissements d'enseignement et de recherche français ou étrangers, des laboratoires publics ou privés.



INSTITUT
POLYTECHNIQUE
DE PARIS

NNT : 2022IPPAX113

Thèse de doctorat



Impact de la variabilité spatio-temporelle du Mistral sur la formation d'eaux denses en Méditerranée

Thèse de doctorat de l'Institut Polytechnique de Paris
préparée à l'École Polytechnique

École doctorale n°626 École doctorale de l'Institut Polytechnique de Paris (EDIPP)
Spécialité de doctorat : Mécaniques des fluides et des solides, acoustique

Thèse présentée et soutenue à Palaiseau, le 21 octobre 2022, par

DOUGLAS KELLER JR.

Composition du Jury :

Riwal PLOUGONVEN Professeur chargé de cours, Laboratoire de météorologie dynamique, École polytechnique (UMR8539)	Président
Bodo AHRENS Professeur, Institut für Atmosphäre und Umwelt, Goethe Universität Frankfurt am Main	Rapporteur
Marine HERRMANN Directrice de recherche, Laboratoire d'études en géophysique et océanographie spatiales, Institut de recherche pour le développement (UMR5566)	Rapporteur
Sophie BASTIN Chargée de recherche, Laboratoire atmosphères observations spatiales, Centre national de la recherche scientifique (UMR8190)	Examinatrice
Cindy LEBEAUPIN BROSSIER Chargée de recherche, Centre national de recherche météorologiques, Centre national de la recherche scientifique (UMR3589)	Examinatrice
Philippe DROBINSKI Directeur de recherche, Laboratoire de météorologie dynamique, École polytechnique (UMR8539)	Directeur de thèse
Romain PENNEL Ingénieur de recherche, Laboratoire de météorologie dynamique, École polytechnique (UMR8539)	Co-directeur de thèse

Remerciements

This thesis was a challenging but extremely rewarding part of my life. Many hours at the lab and at home were spent honing my craft, which may or not be reflected in this thesis. This thesis has been through the COVID pandemic of 2020, so have mercy.

I would like to first give my thanks to my friends and family, of whom I have been away from in France now for the better part of three years. I'm thankful for their patience and support as I traversed an ocean to achieve the next level of academic study (if you're wondering, I'm from Alaska). Mom and Dad, I'm sorry I moved so far away, but I promise to keep in touch with you and visit as much as I can.

I would next like to give my thanks to my advisors, Philippe Drobinski and Romain Pennel. Both have been patient with me and offered me important guidance as I made my way through the journey of being a doctoral student. I've come to regard them both as friends in addition to valuable mentors. I look forward to continuing to cultivate my friendship and collaboration with them.

My final thanks goes to Javier Fochesatto, currently a professor the University of Alaska Fairbanks, to whom I express my deepest gratitude to for mentoring me during my bachelor and master degrees, hinting at but never pushing me to doctoral studies. He always had time to spare to discuss science and politics despite his busy schedule and started me on my journey to where I am now.

To those reading this thesis who are on their own journey to completing their doctoral degree, have patience and stay committed. But don't be afraid to take a minute and step away. A motto that has served me well in life is "moderation". Don't forget to keep a balance between work and free time. Yourself and others in your life will appreciate it.

Résumé

La convection profonde dans le golfe du Lion conduit à la formation d'une eau dense qui entraîne une partie de la circulation thermohaline en mer Méditerranée. Le mélange vertical résultant de ce processus distribue l'oxygène et les nutriments dans toute la colonne d'eau, entraînant de grandes proliférations de phytoplancton. Par conséquent, la convection profonde et la formation d'eau dense qui en résulte dans le golfe du Lion est un processus important pour la circulation générale et les processus biologiques de la mer Méditerranée. L'objectif de la thèse est d'identifier les principaux attributs du Mistral et les forçages atmosphériques saisonniers qui contrôlent le préconditionnement de la convection profonde et la formation d'eau dense dans le Golfe du Lion.

Pour cela, nous avons utilisé des données de modèles atmosphériques (WRF/ORCHIDEE et RCM6) et un modèle océanique (NEMO) qui nous ont permis de simuler en détail la circulation océanique dans le Golfe du Lion. Deux séries de simulations NEMO ont été utilisées, une série témoin et une série saisonnière. La série saisonnière a été forcée avec un forçage atmosphérique filtré, qui a supprimé l'effet du Mistral. Les deux séries ont ensuite été comparées pour déterminer l'effet du Mistral et des changements atmosphériques saisonniers sur la réponse de l'océan. Trois études dans cette thèse ont utilisé cette technique : une étude de cas de l'année 2012 à 2013, une étude de climatologie des années 1993 à 2013, et une étude de scénario des années 2015 à 2100.

La première étude a révélé l'importance de la composante saisonnière du forçage atmosphérique sur le préconditionnement de la stabilité verticale de l'océan, démontrant qu'elle représentait plus de la moitié de la déstratification conduisant à la convection profonde. L'étude a également déterminé que l'attribut le plus important du Mistral pour la déstratification est sa force, plutôt que sa durée ou sa fréquence.

La deuxième étude a déterminé que l'existence de la composante basse fréquence du Mistral, qui apparaît en hiver, contrôle quelles années présentent une convection profonde et quelles années ne le font pas. Les années avec des vitesses de vent plus élevées dans le forçage saisonnier, causées par la composante basse fréquence du Mistral, comportaient une convection profonde, contrairement aux autres.

La troisième étude a déterminé que le forçage atmosphérique dans la région reste à peu près constant jusqu'à la fin du scénario, l'advection apportant des eaux plus stratifiées dans la région à partir de 2060. Le résultat est une colonne verticale fortement stratifiée en raison de l'advection, conduisant à l'extinction de la convection profonde dans la région après l'année 2060.

Une quatrième étude, légèrement distincte des autres études, utilise les données du modèle de la deuxième étude et examine une méthode potentielle pour atténuer l'utilisation des combustibles

fossiles en Méditerranée et capturer le carbone de l'océan : une île productrice de méthanol. Les résultats de cette étude suggèrent que le meilleur endroit pour placer une telle île se trouve dans les mers d'Alboran, Levantine et Crétoise, en raison de la disponibilité de l'énergie solaire (Alboran et Levantine) et éolienne (Crétoise). Un tel dispositif pourrait permettre aux communautés insulaires et éloignées de devenir plus indépendantes énergétiquement.

La conclusion générale de cette thèse est que le mistral et le forçage atmosphérique saisonnier entraînent une convection profonde et une déstratification océanique dans le golfe du Lion. La composante saisonnière contribue davantage, mais ni le Mistral ni la composante saisonnière ne sont en mesure de surmonter la stratification par advection prédite dans le futur. Cela conduit à l'effondrement de la convection profonde dans la région, soulignant l'importance de l'atténuation du changement climatique et la nécessité d'appareils comme l'îlot de production de méthanol.

Abstract

Deep convection in the Gulf of Lion leads to the formation of dense water that drives part of the thermohaline circulation in the Mediterranean Sea. The vertical mixing from this process distributes oxygen and nutrients throughout the water column, leading to large phytoplankton blooms. Therefore, deep convection and the resulting formation of dense water in the Gulf of Lion is an important process for the general circulation and biological processes of the Mediterranean Sea. The aim of the thesis is to identify key attributes of the Mistral and seasonal atmospheric forcing that control the preconditioning of deep convection and formation of dense water in the Gulf of Lion.

For this purpose, we used atmospheric model data (WRF/ORCHIDEE and RCM6) and an ocean model (NEMO) that allowed us to simulate in detail the ocean circulation in the Gulf of Lion. Two series of NEMO simulations were used, one control series and one seasonal series. The seasonal series was forced with filtered atmospheric forcing, that removed the effect of the Mistral. The two series were then compared to determine the effect of the Mistral and seasonal atmospheric change on the ocean response. Three studies in this thesis used this technique: a case study of the year 2012 to 2013, a climatology study of the years 1993 to 2013, and a scenario study of the years 2015 to 2100.

The first study revealed the importance of the seasonal component of the atmospheric forcing on preconditioning the ocean vertical stability, demonstrating it accounted for more than half of the destratification leading to deep convection. The study also determined that the most important attribute of the Mistral for destratification is its strength, rather than its duration or frequency.

The second study determined that the existence of the low frequency component of the Mistral, which appears in the winter, controls which years feature deep convection and which years do not. Years with higher wind speeds in the seasonal forcing, caused by the low frequency component of the Mistral, featured deep convection, while the others did not.

The third study determined that the atmospheric forcing in the region remains roughly constant until the end of the scenario, with advection bringing in more stratified waters to the region starting after 2060. The result is a strongly stratified vertical column due to the advection, leading to the extinction of deep convection in the region after the year of 2060.

A fourth study, slightly separate from the other studies, utilizes the model data from the second study and looks at a potential method to mitigate fossil fuel use in the Mediterranean and capture carbon from the ocean: a methanol producing island. Results from this study suggest the best place to place such an island are in the Alboran, Levantine, and Cretan Seas, due to solar (Alboran and Levantine) and wind power (Cretan) availability. Such a device could allow island and remote

communities to become more energy independent.

The overall conclusion for this thesis is both the Mistral and seasonal atmospheric forcing drive deep convection and ocean destratification in the Gulf of Lion. The seasonal component contributes more, but neither the Mistral nor seasonal component are able to overcome the advected stratification predicted in the future. This leads to the collapse of deep convection in region, highlighting the importance of climate change mitigation and the need for devices like the methanol producing island.

Prologue

This work is part of a collaboration between the Laboratoire de Météorologie Dynamique (LMD) of the Institut Pierre-Simon Laplace (IPSL) and the Department of Planetary Sciences at the Weizmann Institute of Science (WIS). Two teams, each with a doctoral student and advisors, form this collaboration. The LMD team contains the following personnel: Douglas Keller (doctoral student), Romain Pennel (co-advisor), and Philippe Drobinski (advisor). The WIS team contains the following personnel: Yonatan Givon (doctoral student) and Shira Raveh-Rubin (advisor). The collaboration itself is part of a larger collaboration between the Centre national de recherche scientifique (CNRS) and WIS.

The focus of the LMD team was the title of this work: to investigate the effect the Mistral wind has on dense water formation in the Gulf of Lion. In other words, this group focused on the ocean aspect of the Mistral air-sea interface exchange. The WIS team focused on the atmospheric aspects of the Mistral wind, determining and laying out the synoptic conditions that drive it. While this work focuses on the ocean response, many aspects and discoveries from the WIS team will be discussed as well due to the nature of this study.

Contents

1	Introduction	1
1.1	Mediterranean Sea and its Thermohaline Circulation	1
1.1.1	Mediterranean Sea Thermohaline Circulation	2
1.2	Mistral	3
1.2.1	Mistral Generation and Rossby Wave Breaking	5
1.3	Deep Convection	7
1.3.1	Phases of Deep Convection	10
1.4	Review of Current Literature	11
1.4.1	Idealized Investigations	11
1.4.2	Observations	12
1.4.3	Realistic Investigations	13
1.4.4	Biological Effects of Deep Convection	14
1.5	Thesis Outline	14
1.6	Research Questions	14
1.7	Thesis Structure	15
1.8	Climate Change Mitigation	17
2	Methodology	18
2.1	Ocean Modelling	19
2.2	Atmospheric Forcing	20
2.2.1	Filtering	21
2.3	Mistral Detection	23
2.4	Stratification Index	23
2.5	Simple Model	24
2.5.1	Solution for Seasonal SI	26
2.5.2	Solution with Mistral Forcing Function	28
3	Impact of the Mistral on Deep Water Formation	36
3.1	Introduction	37
3.2	Mistral Events	38
3.3	Model Validation	40
3.4	Stratification Index and Mixed Layer Depth	43

3.5	Process Analysis	46
3.5.1	Seasonal Solution and Forcing	46
3.5.2	Anomaly Solution and Forcing	48
3.5.3	Mistral Strength and Destratification	51
3.5.4	Dominating Mistral Attribute	51
3.5.5	Simple Model Results	56
3.6	Comparison with Additional Years	57
3.6.1	Stratification Index	57
3.6.2	Seasonal Forcing	59
3.6.3	Anomaly Forcing	60
3.7	Discussion	61
4	Variability of Seasonal Atmospheric Drivers affecting Deep Convection	64
4.1	Introduction	65
4.2	Model Validation	67
4.3	Results and Discussion	70
4.3.1	Seasonal Contribution	70
4.3.2	Prior Questions	77
4.4	Conclusions	80
5	Impact of Climate Change on Water Masses in the Gulf of Lion	82
5.1	Evolution of Seasonal Stratification and Forcing	83
5.1.1	Changes in Atmospheric Forcing	83
5.1.2	Advected Stratification	89
5.2	Conclusions	96
6	Climate Change Attenuation and Mitigation in the Mediterranean	97
6.1	Introduction	98
6.2	Methodology	99
6.2.1	Power generation	101
6.2.2	Environmental risk	103
6.2.3	Methanol production - pyseafuel	103
6.3	Power Generation	109
6.3.1	Solar	109
6.3.2	Wind	110
6.4	Environmental Hazards	111
6.5	Methanol Production	112
6.6	Integrated Production	115
6.7	Optimal Locations	118
6.8	Remote and Island Communities	121
6.9	Discussion	121

List of Figures

1.1	The Mediterranean Sea and its various internal seas and subbasins. The blue contour lines show the 500 meter depth contours of the sea.	1
1.2	Schematic of the thermohaline circulation of the Mediterranean Sea (Taupier-Letage 2021).	3
1.3	A Mistral and Tramontane event on the 10th of October, 2012. Subplot (a) shows the wind speed magnitude and vectors with the sea level pressure contours. (b) shows the same event as seen through satellite imagery from NASA's MODIS satellite [109, 108]. The Genoa low (cyclone) can be clearly seen in both subplots, with the Mistral responding as a geostrophic flow, wrapping around the isobars after being funneled through the Rhône Valley.	4
1.4	Time series data at 42°N 5°E of the Mistral event shown in Fig. 1.3. The duration of the event is marked with green shading. The specific humidity, temperature, wind speed and wind direction are shown, from top down in the that order. Blue shading denotes a northerly flow ($\pm 45^\circ$ about 90°). Notice the sharp decrease in temperature and humidity at the onset of the event, along with the rise in wind speed and shift towards a northerly flow.	5
1.5	A Mistral event case study showing its generation due to Rossby wave breaking. The event lasts from April 8th to April 12th, 2005 and shows an elongation of a PV filament that eventually breaks off and rolls up into a cyclone over the Ligurian Sea. Taken from Fig. 11 of Givon et al. 2021[50]. The first column shows the PV of the general clusters the event was taken from in Givon et al. 2021 for the given date, while the second and third columns show the PV and surface heat fluxes of the event, respectively.	7
1.6	Deep convection (a.k.a. open ocean convection) and shelf convection in the Gulf of Lion. Taken from Fig. 1 from [116].	8
1.7	The deep convection zone in the Gulf of Lion, with the favored cyclonic ocean circulation forming the Gulf of Lion gyre. The blue shading shows the bathymetry at 200 meter levels.	9
1.8	Average temperature and salinity for each layer (modified Atlantic water (MAW), Levantine intermediate water (LIW), western Mediterranean deep water (WMDW)) from Jan. 1st, 2005 to Jan. 1st, 2012 from the Coriolis Argo dataset (https://www.coriolis.eu.org).	9

1.9	The three phases of deep convection: (1) preconditioning, (2) deep convection, (3) lateral exchange and redistribution. The third phase is separated into two graphics as the newly formed dense water (WMDW) is redistributed through the destruction of the convection patch with baroclinically driven eddies (3a) and density flows (3b), the former rapidly restratifying the water column. The contours represent the isopycnals.	11
2.1	The domains of both the WRF domain from the RegIPSL coupled WRF/ORCHIDEE simulation within the Med-CORDEX framework, (a), and the NEMOMED12 configuration domain, (b). The region of interest, the NW Med., is outlined by the box. The location used to study the temporal development of deep convection in the GOL is at 42° N 5° E, and the other location, used in conjunction with the aforementioned point to determine Mistral events, is Montélimar, FR, at 44.56° N 4.75° E.	20
2.2	The domain of CNRM-RCSM6 (http://www.umr-cnrm.fr/spip.php?article1098&lang=en ; last accessed: Sept. 13th, 2022).	20
2.3	An illustration of the filtering (averaging) process described by Eq. 2.3. Here the variables q , T , u , and v are shown for both the unfiltered (control; black) and filtered (seasonal; blue) datasets at the nearest grid point to 42° N 5° E. Note how the peaks of the time series are removed and the general wind direction is conserved. The filtered forcing for Chap. 4 and 5 are similar.	22
2.4	The Mistral forcing as a pulse function used to solve Eq. 2.24. k corresponds to the event and δF_k corresponds to the forcing strength of the Mistral event. Δt_k corresponds to the duration of the Mistral event, and $\Delta \tau_k$ to the period between events, with t_k denoting the start of event k .	28
3.1	SST comparison between the NEMO control run and the Azur, (a), and Lion, (b), buoy SST datasets. Where the data is available, the model results match the buoy data fairly well.	40
3.2	Locations of the CTD and Argo profiles. The red circles represent the CTD locations and the blue triangles represent the Argo float profile locations. The deep convection area is marked by the box with a dashed perimeter and 42° N 5° E is marked by an "X".	41
3.3	Comparison of CTD and NEMO control simulation density profiles. The CTD profiles were averaged by combining multiple vertical profiles collected at the date and location into one profile. The standard deviation of this averaging, $\sigma_{\rho_{CTD}}$, is marked in red and is present for all plots, yet may be difficult to see for March 7th and May 9th.	42
3.4	Same as Fig. 3.3 but for potential temperature.	43

3.5	The stratification index across the GOL (the area marked as NW Med. in Fig. 2.1 (b)) at different timestamps. Row (a) displays the values of SI for the control simulation and row (b) displays the values of SI for the seasonal simulation. The box denoted by DC indicates the area of deep convection in the GOL that was not seen in the seasonal simulation.	44
3.6	The stratification index of the nearest NEMO grid point to 42° N 5° E and MLD over the year of both simulations. Plot (a) shows the stratification index for the control run, $SI_S + \delta SI$, and the seasonal run, SI_S . Plot (b) shows the difference between the control and seasonal stratification index, δSI . Plot (c) shows the MLD for both simulations. Mistral events are shown in all three plots: colored green for events during the preconditioning and deep convection phase and red for events outside the preconditioning phase. Mistral events with dotted hatching (the blue colored intervening time between events) are used as ideal destratification (restratification) events to compute the simple model restoration coefficients. The specific timestamps t_A through t_D correspond to the timestamps of the plots in Fig. 3.5: Aug. 30th, 2012, Dec. 11th 2012, Feb. 13th, 2013, June 1st, 2013, respectively. Two definitions of MLD are plotted in (c): one calculated by a vertical change in density less than 0.01 kg/m^3 , denoted by $\Delta\rho$, and one calculated by a vertical diffusivity less than $5 \times 10^{-4} \text{ m}^2/\text{s}$, denoted by K_z . The MLD denoted by the vertical diffusivity criteria follows the turbocline depth and is taken to represent the mixed layer depth more accurately, as it matches the deep convection timing in the stratification index.	45
3.7	The smoothed (with Eq. 2.3) seasonal surface heat fluxes over the point 42° N 5° E for the seasonal simulation. (a) contains the seasonal stratification index, SI_S , and its derivative, $\frac{\partial SI_S}{\partial t}$, comparing it to the seasonal net heat flux, Q_{net} (the subscript S is dropped for convenience). (b) shows the net heat flux separated into its components: Q_E , Q_H , Q_{SW} , and Q_{LW} for latent heat, sensible heat, shortwave downward, and longwave downward fluxes, respectively (neglecting contributions from precipitation and snowfall). The different line colors correspond to the similarly colored axes.	47
3.8	The Mistral forcing as a pulse function used to solve Eq. 2.24. k corresponds to the event and δF_k corresponds to the forcing strength of the Mistral event. Δt_k corresponds to the duration of the Mistral event, and $\Delta \tau_k$ to the period between events, with t_k denoting the start of event k	49

3.9	The normalized theoretical solutions (Eq. 2.68 and 2.74) for during, (a), and after, (b), a destratification event fitted to the ideal Mistral events from Table 3.1 and δSI values from the NEMO results in Fig. 3.6. A value of 0.235 day^{-1} for α_d and a value of 0.021 day^{-1} for α_a was found. Plot (c) shows the δSI response using the determined restoration coefficients, given an ideal Mistral event with the average values of 5.69 days for the duration and 10.88 days for the period. The average strength of a Mistral, $\delta F = 4.01 \times 10^{-8} \text{ s}^{-2} \text{ days}^{-1}$, was taken from values found in Table 3.5.	50
3.10	Equation (3.4) plotted with one variable varying in each plot with the other variables held constant at the mean value. (a) varies the strength of the Mistral, δF , (b) varies the duration, Δt , and (c) varies the period between events, $\Delta \tau$. (d) varies the restoration coefficient during the destratification phase, α_d and (e) varies the restoration coefficient for the restratification phase. (f) varies the number of events.	53
3.11	Same as Fig. 3.10, however, SI_S is added to the results from Eq. 3.4.	54
3.12	The combined effect of Eq. 3.3 for multiple Mistrals with the Mistral data from Table 3.1 and 3.5. (a) shows the calculated $\delta SI + SI_S$ response, while (b) is the calculated simple model δSI versus the NEMO δSI simulation results. Effects from Mistrals after deep convection are included with the dashed blue line and show that Mistrals after deep convection can retard the proceeding restratification during the restratification phase.	56
3.13	The stratification index for the 1994 winter for both the control and seasonal runs are in subplot (a), spatially averaged over the area of 42 to 42.5° N and 4.25 to 5° E . The simplified model anomaly solution added to the seasonal SI is denoted by the dashed line. Subplot (b) shows the NEMO determined δSI and the δSI calculated from the anomaly solution of the simple model.	58
3.14	Same as Fig. 3.13 for the 2005 winter.	59
3.15	The smoothed seasonal sea surface fluxes spatially averaged over the 42 to 42.5° N and 4.25 to 5° E area, with the green dashed line denoting the estimated derivative w.r.t. time of the seasonal SI from the NEMO results, multiplied by $10^9 \text{ m}^4/\text{Js}^2$. A negative value means heat is leaving the ocean.	60
4.1	Vertical distribution of bias (model minus observation) and RMSE from the comparison of our control set model results and combined Argo/CTD observations. (a) and (b) show the mean and standard deviation of the bias for potential temperature and salinity, respectively. The mean is the solid red line, with the shading representing the area encompassed by ± 1 standard deviation. (c) and (d) show the RMSE for potential temperature and salinity, respectively.	68

4.2	Spatial distribution of the bias from the comparison of our control set model results and combined Argo/CTD observations. (a) and (b) show the bias in the potential temperature for the layers above and below 500 m, respectively. (c) and (d) show the same for salinity. The black box from 42 to 42.5 °N and from 4.25 to 5 °E bounds the spatial averaging performed in Sec. 4.3.	69
4.3	Mixed layer depth of the averaged area in Fig. 4.2 for the 20 years, calculated by the point in the column with a vertical diffusivity less than $5 \times 10^{-4} \text{ m}^2/\text{s}$. The red circle labels the first point at which the MLD is deeper than 250m and the red triangle marks the first main maximum depth for the deep-convection years. Mistral events are shown with the colored green shading.	71
4.4	The stratification index of the area averaged in Fig. 4.2 for the 20 years, with the control run, $SI_S + \delta SI$, in black and the seasonal run, SI_S , in blue. The difference between the control and seasonal stratification index, δSI , is shown with a dashed red line with a separate scale. Mistral events are shown with the colored green shading.	72
4.5	The stratification index for the winter of 1994 to demonstrate how the contributions from the different timescales are calculated.	73
4.6	The seasonal maximum stratification and minimum control stratification is shown in subplot (a). The seasonal and Mistral contributions are shown in (b) and (c) (normalized in (c)). (d) shows just the normalized Mistral contribution to destratification.	74
4.7	Distributions of the different flux components making the stratification change in SI_S , determined using Eq. 2.39 per component, i , are shown in subplot (a). DC and NDC stand for deep-convection and non-deep-convection, respectively. Subplots (b), (c), and (d) show the ensemble averaged (discarding Feb. 29th from leap years) driving components of the flux bulk formulae in Eq. 2.1, Δq , $\Delta\theta$, and $ \vec{u}_z $. Note: in this plot $SI_{Est,i} = SI_{S,Q,i}$	76
4.8	Distributions of the destratification incurred by Mistral events during DC years. $\Delta\delta SI$ is calculated using Eq. 2.64 per event k	79
5.1	The change in stratification in the Gulf of Lion over the 2015 to 2100 period. The minimum of the control stratification index, SI_{min} , and maximum seasonal stratification index, $SI_{S,max}$ are shown in subplot (a). (b) shows the stratification contributions due to the seasonal change, $SI_{S,Cont}$, and seasonal change plus the Mistral, δSI_{Cont} . See Fig. 4.5 and Sec. 4.3.1 in Chap. 4 for the definition of stratification contributions and Fig. 4.6 for the results of the 1993 to 2013 period. (c) shows the trends (in dashed lines; one set for 2015 to 2060 and one set for 2060 to 2100) of the different components in Eq. 2.38: SI_S , the total, $SI_{\Phi,S}$, the advective component, and $SI_{Q,S}$, the component due to the net heat flux. $t_0 = t_{SI_{S,max}}$ and $t_1 = t_{SI_{min}}$. (d) shows the trends of the different components of $SI_{Q,S}$, after separating $Q_{net,S}$ into its individual parts (Eq. 2.1). Trends found in (d) are quantified in Tab. 5.1.	84

5.2	Evolution of the driving variables in the bulk formulae for NEMO (Eq. 2.1). (a) shows the difference in atmospheric and sea surface temperature, $\Delta\theta = \theta_z - SST$. (b) shows the difference in atmospheric and sea surface humidity (assumed to be saturated), $\Delta q = q_z - q_0$. (c) shows the wind speed, $ \vec{u}_z \approx \Delta\vec{u} $. (d) shows the atmospheric longwave downwelling, $Q_{LW,A}$, and the oceanic downwelling component, $Q_{LW,O}$. (e) shows the atmospheric shortwave downwelling, Q_{SW} . The oceanic component is not shown as it is just the reflected atmospheric shortwave downwelling and has a effectively constant albedo. (f) shows the annual precipitation (rain and snowfall). The dashed lines are the linear regression trend lines.	88
5.3	Evolution of the vertical column properties in the simulation results. Only the upper 800 meters of the 2344 meter deep column is shown, as these are the most active water masses. The results have been averaged with a moving average with a window size of a year to more easily display the decadal trends, particularly in the upper 150 meters, as is evident by the cycling in Fig. 5.4. (a) shows the plot of the integrand of Eq. 2.5 and (b) shows it change from 2015. (c), (d), and (e) show the potential density, potential temperature, and salinity respectively.	91
5.4	Evolution of the vertical column properties averaged (with exception for (a)) over the ranges of 0 to 150 meters, 150 to 600 meters, and 600 meters to the bottom. (a) was instead integrated over these ranges. (a) shows the stratification index, (b) shows the potential density, (c) shows the potential temperature, and (d) shows the salinity.	92
5.5	Contributions to stratification from potential temperature, $N^2 z_T$, (a), and salinity, $N^2 z_S$, (b), with the overall stratification shown in (d). (c) shows the contributions separated and integrated over the ranges given in Fig. 5.4. Note: (a), (b), and (c) show the difference in the contributions from their initial value during the year of 2015. Like Fig. 5.3, the values have been averaged with a moving window of a year in length to more easily the decadal trends.	95
6.1	Global atmospheric CO ₂ (Ed Dlugokencky and Pieter Tans, NOAA/GML; https://gml.noaa.gov/ccgg/trends/ ; last accessed June 13th, 2022).	98
6.2	Earth system modelling provides shortwave downward radiation, 10 meter wind speed and direction, sea surface temperature, and sea surface salinity. The shortwave downward radiation and 10 meter wind speed are used to determine the power availability in the region. The 10 meter wind speed is used to determine maximum wave height. The sea surface temperature and salinity are used to determine the methanol production.	100
6.3	Domains of the WRF/ORCHIDEE simulation, (a), and NEMO simulations (b). Both were run within the RegIPSL regional model.	101
6.4	Power curve for the SWT-3.6-120 turbine. Provided by the windpowerlib python library [56].	102

6.5 Layout of a methanol island simulated by **pyseafuel**. Two arms are fed seawater, one through the degasser to extract CO₂ and one through the desalinator and electrolyzer to produce H₂. The CO₂ and H₂ is then combined in the reactor to produce CH₃OH, methanol. Waste brine and O₂ are produced as part of the process. 104

6.6 The ocean carbon buffer system. The equilibriums and dominant species were calculated using Eq. 6.4 through 6.7. Dissolved inorganic carbon (DIC) is the sum of the three species. 105

6.7 The fitted quadratic curves for the energy consumption per mole of extracted CO₂ depending on pH, (a), and for pH versus the ratio of outflow CO₂ over inflow seawater, (b). The fitted equation for (a) is $58.29x^2 - 524.44x + 1423.21 = 0$ where $x = pH$, and for (b) is $-1195.47x^2 + 311.11x + 3.90 - pH = 0$ where $x =$ the CO₂ outflow / seawater inflow ratio. 105

6.8 A single tube for a plug flow reactor. a_{tubes} is the single tube area. P and T are the reactor operating pressure and temperature. x is the coordinate along the length of the tube, which has a length of L_{tubes} . ρ_{cat} is the density of the catalyst packed into the reactor tube. $\dot{N}(x)$ is the molar flow rate along the length of the tube, with subscripts *in* for the inflow and *out* for outflow. 107

6.9 The conversion factor, ξ , or the percentage of moles of CO₂ transformed into CH₃OH. It was calculated using the equilibrium equations presented in Terreni et al. 2020, with varying state conditions (P and T) and molar ratios of H₂ and CO₂. The state dependence curve was calculated with a H₂/CO₂ molar ratio of 3, which is the stoichiometric ratio. 108

6.10 Seasonally averaged effective irradiance calculated from with the **pvlib** python package and WRF/ORCHIDEE shortwave radiation data. 109

6.11 Same as Fig. 6.10 but for the calculated solar panel power generation. 110

6.12 Seasonally averaged wind speeds and directions of the WRF/ORCHIDEE 10 meter wind data. During the winter months, the Bora [67], Mistral and Tramontane [36, 31], Tramontana [164], and Cierzo [100] winds can be seen. During the summer months, the summer Mistral [34], Levanter [164], and Etesian [165] winds can be seen. 110

6.13 Seasonally averaged calculated power generation using a SWT-3.6-120 industrial turbine with height corrected wind speed data (with Eq. 6.2) from the WRF/ORCHIDEE 10 meter wind speed data. 111

6.14 Calculated maximum wave heights using the 10 meter wind speeds from the WRF/ORCHIDEE model outputs and Eq. 6.3. 112

6.15 Seasonally averaged sea surface temperature from the NEMO simulation set. 114

6.16 Seasonally averaged sea surface salinity from the NEMO simulation set. 114

6.17 Methanol production powered by the solar panel power shown in Fig. 6.11. Note the values are in milliliters per day per area. 115

6.18	Same as Fig. 6.17 but the production is powered with the turbine power from Fig. 6.12.	115
6.19	Ensemble time series for the point locations in Table 6.2. Solar panel and SWT-3.6-120 wind power generation are presented, as well as the corresponding methanol production from the two power resources. The solar panel power generation and methanol production time series are window averaged to make the temporal trends more visible, as production drops to zero every night.	116
6.20	The integrated methanol production over the course of the ensemble averaged year for a simulated island running on solar power, wind power, and the difference between the two production simulations.	118
6.21	Optimal locations for solar or wind powered methanol producing islands. Subplot (a) shows the poor (none shown), marginal, and good locations according to the maximum significant wave heights (poor: above 1.5 m, marginal: between 1 and 1.5 m, good: below 1 m). (b) shows the combined above maximum significant wave height and solar-powered methanol production optimal locations (poor: below 400 mL m ⁻² integrated methanol production over a year, marginal: between 400 and 470 mL m ⁻² , good: above 470 mL m ⁻²). (c) is the same as (b) but for wind powered islands (poor: below 140 mL m ⁻² , marginal: between 140 and 350 mL m ⁻² , good: above 350 mL m ⁻²).	120

List of Tables

3.1	The start date of, duration of, Δt_k , and period between each event, $\Delta \tau_k$, for each Mistral event, k , for the entire NEMO simulation period of Aug. 1st, 2012 to July 31st, 2013. Superscripts d and a denote events used as ideal cases for calculating α_d and α_a , respectively. The average values for Mistral events from 2012-08-30 to 2013-02-16 are: $\overline{\Delta t} = 5.69 \text{ days}$ and $\overline{\Delta \tau} = 10.88 \text{ days}$. The standard deviations for the same time frame are: $\sigma_{\Delta t} = 4.22 \text{ days}$ and $\sigma_{\Delta \tau} = 4.59 \text{ days}$	39
3.2	The start date of, duration of, Δt_k (<i>days</i>), and period between each event, $\Delta \tau_k$ (<i>days</i>), for each Mistral event, k , and event strength, δF_k ($s^{-2} \text{days}^{-1}$), for the preconditioning phase of the NEMO simulation period of Jun. 1st, 1993 to May 31st, 1994. Preconditioning phase for this year is considered from 1993-08-28 to 1994-04-03 (210 total days).	39
3.3	Same as Tab. 3.2, however the NEMO simulation period is from Jun. 1st, 2004 to May 31st, 2005. Preconditioning phase for this year is considered from 2004-09-15 to 2005-04-08 (170 total days).	40
3.4	RMSE and bias between the averaged observed CTD density and potential temperature profiles and the nearest NEMO control grid point profiles, for the respective variables. The average RMSE and bias for the density profiles was 0.025 kg/m^3 and -0.009 kg/m^3 , respectively. The average RMSE and bias for potential temperature was $0.094 \text{ }^\circ\text{C}$ and $0.032 \text{ }^\circ\text{C}$, respectively.	43
3.5	The Mistral strengths, δF_k , for each of the preconditioning phase events, using α_d and α_a from Sec. 2.5.2.3, and the rest of the preconditioning period Mistral characteristics from Table 3.1, plugged into Eq. 2.76. $\overline{\delta F_k} = 4.01 \times 10^{-8} \text{ s}^{-2} \text{day}^{-1}$ and $\sigma_{\delta F_k} = 1.196 \times 10^{-8} \text{ s}^{-2} \text{day}^{-1}$	50
4.1	Number of and start and end dates for the Argo and CTD profiles from the Coriolis database for the July 1st, 1993, to June 30th, 2013. The number of profiles used for the spatial distribution of bias in the layers above and below 500 <i>m</i> in depth are shown in their respective columns.	67
4.2	Statistics for the normalized $SI_{S,Cont}$ and δSI_{Cont} contributions from Fig. 4.6 (c) and (d).	75

4.3	Estimated changes in destratification due to changing one variable at a time (between Δq , $\Delta\theta$, and $ \vec{u}_z $) to DC versus NDC ensemble averaged values, utilizing Eq. 4.3. Note, the saturation humidity is based on sea surface temperature, which means keeping the temperature at NDC ensemble averaged values is technically non-physical, as the saturation humidity would change with a different air temperature.	77
5.1	Trends of the atmospheric variables and surface heat fluxes. Δ is the change from the beginning value, x_{beg} , to the final value, x_{end} , of the linear regression trend line from 2015 to 2100. $\% \Delta$ is the relative change of the is difference, equal to $(x_{end} - x_{beg})/ x_{beg} $. The p-value is the 95% confidence null hypothesis that no trend exists (values over 0.05 fail to reject the null hypothesis and have been emboldened). Δ for e is 4.43 mb.	86
5.2	Coefficients for Eq. 5.8, available in the NEMO ocean model [55].	93
5.3	Trends of the components of the stratification index integrand, $N^2 z_{S,T}$ (see Eq. 2.11 and 5.9). Δ is the change from the beginning value, x_{beg} , to the final value, x_{end} , of the linear regression trend line from 2015 to 2100. $\% \Delta$ is the relative change of the is difference, equal to $(x_{end} - x_{beg})/ x_{beg} $. All linear regressions rejected the null hypothesis of zero trend (p-value equal to 0.0).	96
6.1	These are parameters and their values that are used to numerically simulate a methanol island with pyseafuel , separated by subprocess (Fig. 6.5). The electrolyzer parameters are common values in industry [134, 106]. T and P for the reactor are within the range of previously tested temperatures and pressures for the methanol production from carbon dioxide hydrogenation [136]. Note: around 2 V minimum is typically required to generate the necessary current densities for electrolysis to occur [52].	113
6.2	Point locations examined in more detail due to their favorable solar and wind power generation.	116

Chapter 1

Introduction

1.1 Mediterranean Sea and its Thermohaline Circulation

The Mediterranean (Med.) Sea is a partially enclosed sea, connected to the Atlantic Ocean through the Strait of Gibraltar (see Fig. 1.1). It is an evaporative basin, losing more water to evaporation than what it receives through precipitation. The flow through the Strait of Gibraltar from the Atlantic Ocean accounts for the difference and keeps the basin filled. The main basin consists of two primary basins, a western and eastern basin, themselves connected by the Strait of Sicily. Additionally, the Mediterranean is separated into a number of different seas, with the major ones labeled in Fig. 1.1 (the Adriatic Sea, Aegean Sea, Ionian Sea, Levantine Sea, and Tyrrhenian Sea). The shape and location of the Med. Sea and its composition of different seas and subbasins lead to very interesting thermohaline circulation patterns, which are to be explored in the next section (Sec. 1.1.1).

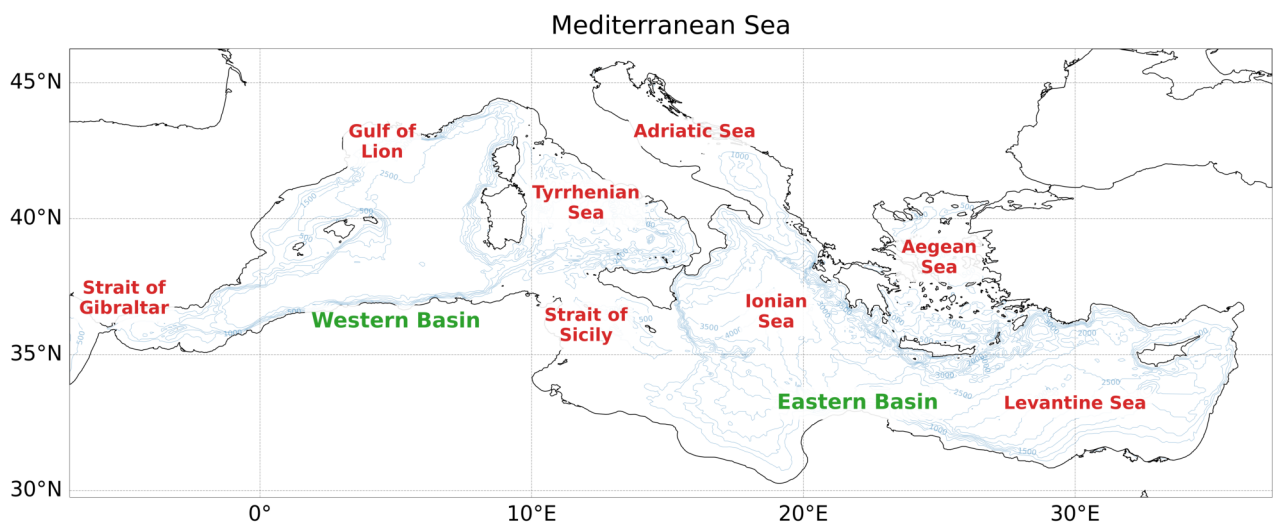


Figure 1.1: The Mediterranean Sea and its various internal seas and subbasins. The blue contour lines show the 500 meter depth contours of the sea.

1.1.1 Mediterranean Sea Thermohaline Circulation

The general circulation of the Med. Sea is forced through its evaporative behavior, requiring an input flow from the Atlantic to maintain its depth [118]. Fig. 1.2 shows the general cyclonic pattern of water circulation around the Med. Sea. First, relatively fresh Atlantic Water (AW) enters through the Strait of Gibraltar at the surface. It then flows along the northern coast of Africa before reaching the Levantine Sea, in the east. There, it becomes denser and more saline due to evaporation, forming the Modified Atlantic Waters (MAW), remaining at the surface, the Levantine Intermediate Water (LIW), dropping to intermediate depths, and Levantine Deep Water (LDW), which makes its way to the deepest depths. Some MAW enters the Aegean Sea, more precisely in the Cretan Sea, where it also experiences enhanced evaporation, forming Cretan Intermediate Water (CIW) and Cretan Deep Water (CDW). The MAW, LIW, and CIW continue north along the Balkan coast, reaching the Adriatic Sea, while the LDW and CDW remain in the Levantine basin. In the Adriatic, strong winds known as the Bora winds cause large evaporative cooling in the winter, forming Adriatic Deep Water (ADW) from the MAW and intermediate waters. The LDW, CDW, and ADW combined form the Eastern Mediterranean Deep Waters (EMDW).

The remaining MAW, LIW and CIW continue along the southern coast of Europe, with the LIW and CIW forming the Eastern Intermediate Water (EIW). However, the EIW is typically referred to LIW in literature, as LIW makes up the bulk of EIW, and therefore will be referred to as such during this thesis. The LIW passes through the Strait of Sicily (westward) underneath incoming AW (eastward). The LIW then follows the northern coast of Sicily and the west coast of mainland Italy, cyclonically flowing around the Tyrrhenian Sea. Instead of flowing through the Corsican Channel, between the island of Corsica and mainland Italy, directly into the Ligurian Sea, the LIW flows around the island of Sardinia, following the coastline north to the Ligurian Sea. These waters then reach the Gulf of Lion (GOL), where large evaporative cooling events due to the Mistral winds form the Western Mediterranean Deep Water (WMDW). These waters, along with the EIW and EMDW eventually spill out through the Strait of Gibraltar, below the incoming AW.

More precisely, deep convection in the GOL forms the WMDW, and it is the major process in the western Med. Sea that does so. As mentioned in the prior paragraph, the Mistral winds drive the large evaporation that occurs in the GOL, and drives the deep convection process. The Mistral, its forcing of the GOL, and the deep convection process form the heart of this thesis, and will be described in the following sections (the Mistral in Sec. 1.2 and deep convection in Sec. 1.3).

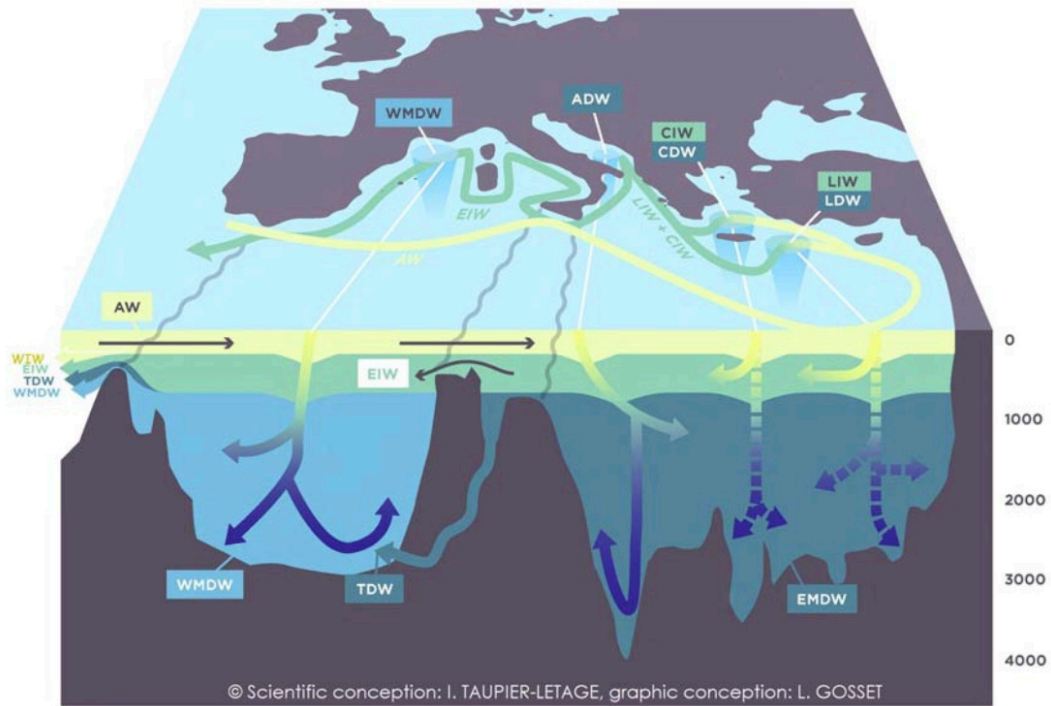


Figure 1.2: Schematic of the thermohaline circulation of the Mediterranean Sea (Taupier-Letage 2021).

1.2 Mistral

The Mistral is a northerly flow through the Rhône Valley, and brings the relatively cold and dry European continental air out over the Gulf of Lion leading to large sea surface fluxes. It typically occurs more often in winter than in summer [50]. The Rhône Valley separates the Alps from the Massif Central and funnels the flow, accelerating it, sometimes in excess of 20 m/s , which intensifies the aforementioned surface fluxes. An example event is shown in Fig. 1.3 that occurred on October 10th, 2012, with winds exceeding 22 m/s . Fig. 1.3 a) shows the wind magnitude of the event through coloration. The large, red (high wind speed) region primarily over the GOL is the main structure of the Mistral wind.

The Mistral has a sister wind called the Tramontane, which flows through the Aude Valley and typically occurs at the same time. The Aude Valley separates the Pyrenees and the Massif Central, channeling the flow similarly to the Rhône Valley, with the same consequences. The Tramontane can be slightly seen in Fig. 1.3 in addition to the Mistral, however it doesn't form the bulk of the flowing airmass. As the Mistral and Tramontane occur at roughly the same time, driven by the same synoptic scale phenomena, both will be referred to simply as just the Mistral for the remainder of this thesis.

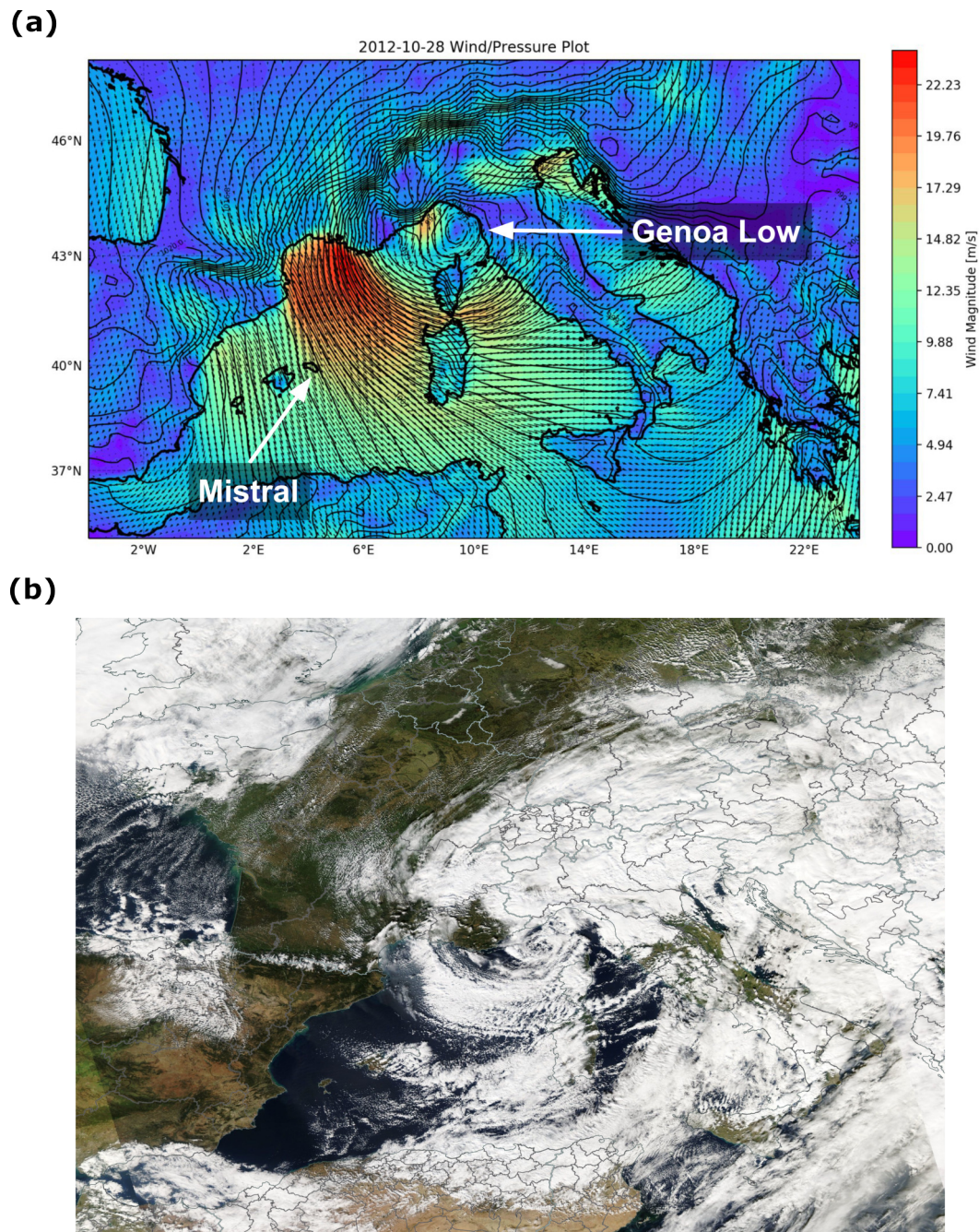


Figure 1.3: A Mistral and Tramontane event on the 10th of October, 2012. Subplot (a) shows the wind speed magnitude and vectors with the sea level pressure contours. (b) shows the same event as seen through satellite imagery from NASA's MODIS satellite [109, 108]. The Genoa low (cyclone) can be clearly seen in both subplots, with the Mistral responding as a geostrophic flow, wrapping around the isobars after being funneled through the Rhône Valley.

As mentioned before, the surface fluxes over the GOL are radically altered by the Mistral winds. The most affected fluxes are the latent heat and sensible heat flux, with the former being the larger of the two. The time series data of the Mistral event presented in Fig. 1.3 is shown in Fig. 1.4. The green shading marks the event. With the rise the wind speed at the beginning of the event, notice the sharp drop in the temperature and humidity, denoting the clear change in airmass above the GOL. The increased wind speed and sharp decrease in temperature and humidity lead to the sudden intensification of the GOL cooling surface fluxes.

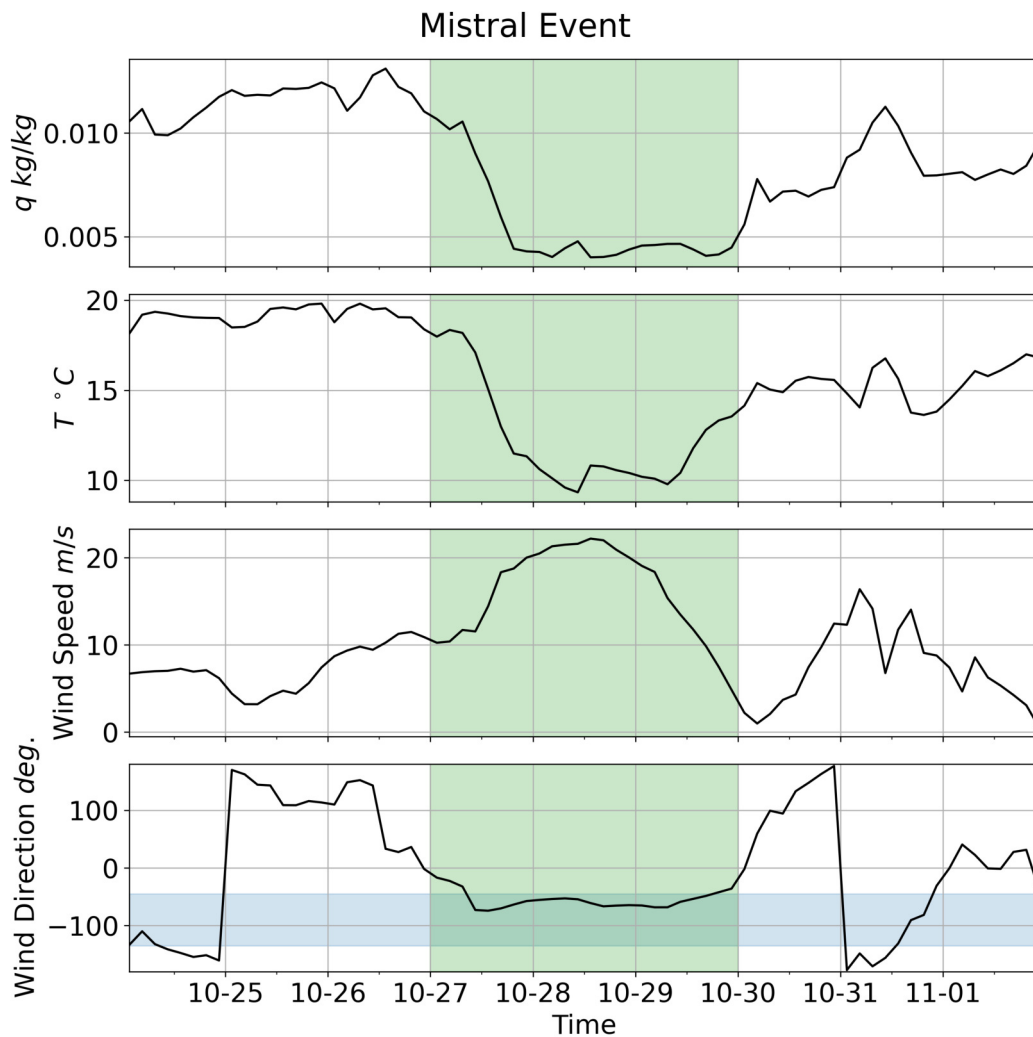


Figure 1.4: Time series data at 42°N 5°E of the Mistral event shown in Fig. 1.3. The duration of the event is marked with green shading. The specific humidity, temperature, wind speed and wind direction are shown, from top down in the that order. Blue shading denotes a northerly flow ($\pm 45^{\circ}$ about 90°). Notice the sharp decrease in temperature and humidity at the onset of the event, along with the rise in wind speed and shift towards a northerly flow.

1.2.1 Mistral Generation and Rossby Wave Breaking

The main driver of the funneled flow leading to the Mistral is a low pressure system in the Genoa region (the Ligurian Sea). This can be clearly seen in Fig. 1.3 a) by the isobar contours, forming a low sea level pressure closed contour over the Ligurian Sea. This low pressure system is typically an extratropical cyclone, which can be seen more clearly in Fig. 1.3 b), with the classic midlatitude cyclone spiraling cloud structure. The Mistral wind follows the isobars as a geostrophic flow around the cyclone out over the western Med. basin.

The driver of these Genoa cyclones is lee cyclogenesis, forced primarily by Rossby waves stretching and breaking over the Alps [50, 16, 43, 2]. This leads to isolated patches of high potential vorticity (PV) over the Ligurian Sea. In finer detail, a baroclinic wave trough travels towards the Alps which block the lower level flow. This causes the upper level trough to stall over the 2500 meter

terrain, forming a surface pressure dipole, with high pressure northwest of the Alps and low pressure southeast of them. This leads to a lee cyclone and the Mistral forming a geostrophic flow as it is pushed through the Rhône Valley by the high pressure system over mainland Europe. Unsurprisingly, these cyclones happen more often in winter than in summer [44], leading to the already mentioned higher abundance of Mistral events in the winter.

A demonstrable case is shown in Fig. 1.5, occurring from April 8th to April 12th in 2005. A baroclinic wave (shown by the high PV in the second column of Fig. 1.5), travels towards Europe and hangs up on the Alpine ridge. The high PV airmass then stretches and elongates as the polar airmass continues its rotation, before finally breaking on April 11th. All the while, the Mistral flows at the surface level, generating large surface fluxes, which can be seen in the third column of Fig. 1.5. These surface fluxes break down the ocean vertical stratification leading to deep convection, which is presented in the next section.

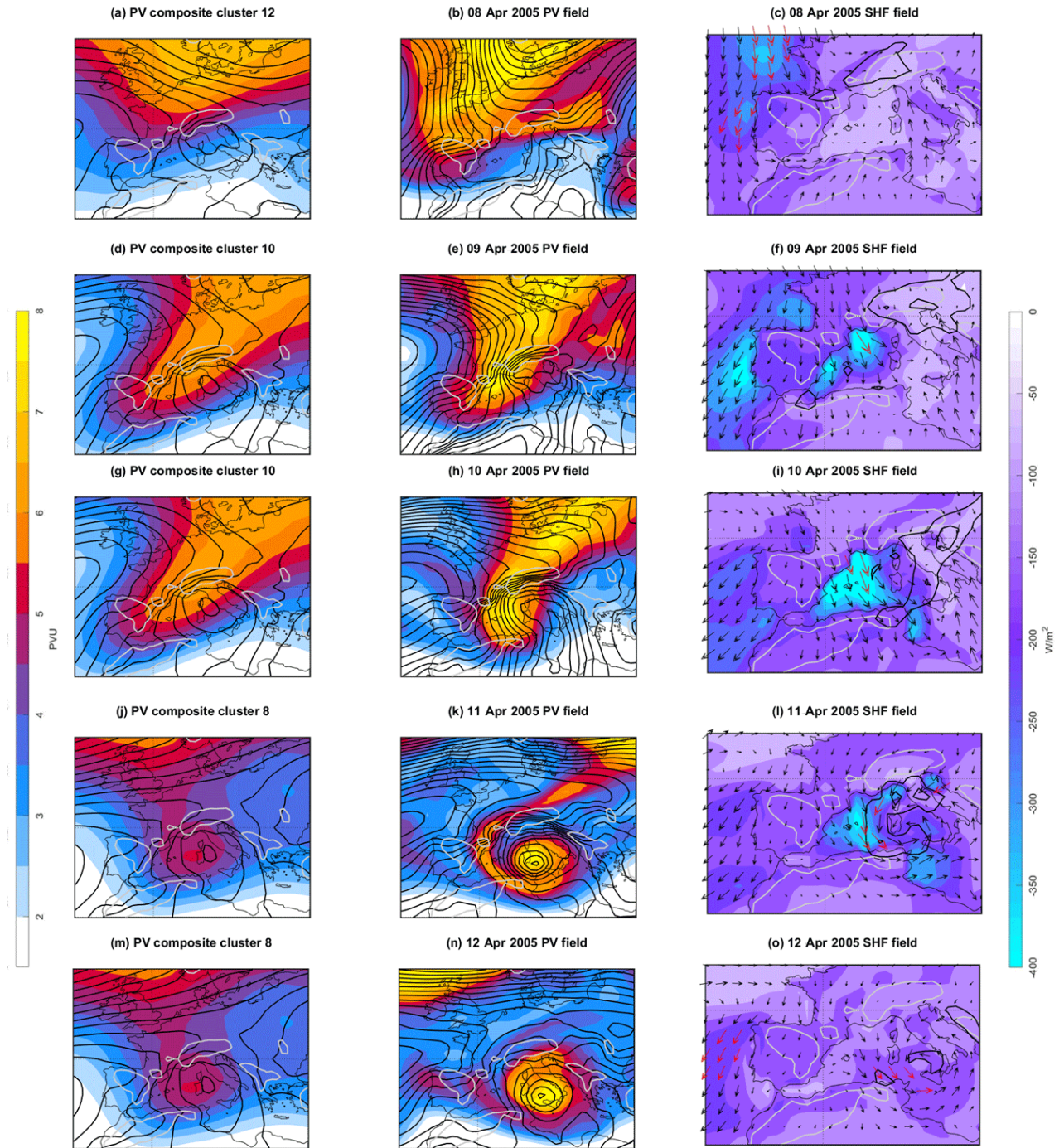


Figure 1.5: A Mistral event case study showing its generation due to Rossby wave breaking. The event lasts from April 8th to April 12th, 2005 and shows an elongation of a PV filament that eventually breaks off and rolls up into a cyclone over the Ligurian Sea. Taken from Fig. 11 of Givon et al. 2021[50]. The first column shows the PV of the general clusters the event was taken from in Givon et al. 2021 for the given date, while the second and third columns show the PV and surface heat fluxes of the event, respectively.

1.3 Deep Convection

Deep convection, also known as open-ocean convection, is an important ocean circulation process that typically occurs in the high latitude regions [97]. A few sites are known to reliably produce deep

convection: the Gulf of Lion in the Mediterranean [104], the Labrador Sea off the coast of Canada and Greenland [53], and the Weddell Sea off the coast of Antarctica [99, 73, 20, 46]. Localized events are triggered by the reduction of the stable density gradient through sea surface layer buoyancy loss (see Fig. 1.6). The areas mentioned before feature stationary cyclonic circulation, which lifts the isopycnals towards the surface, exposing denser waters to the surface cooling, making them more prone to the complete erosion of the vertical density gradient, a.k.a. stratification.

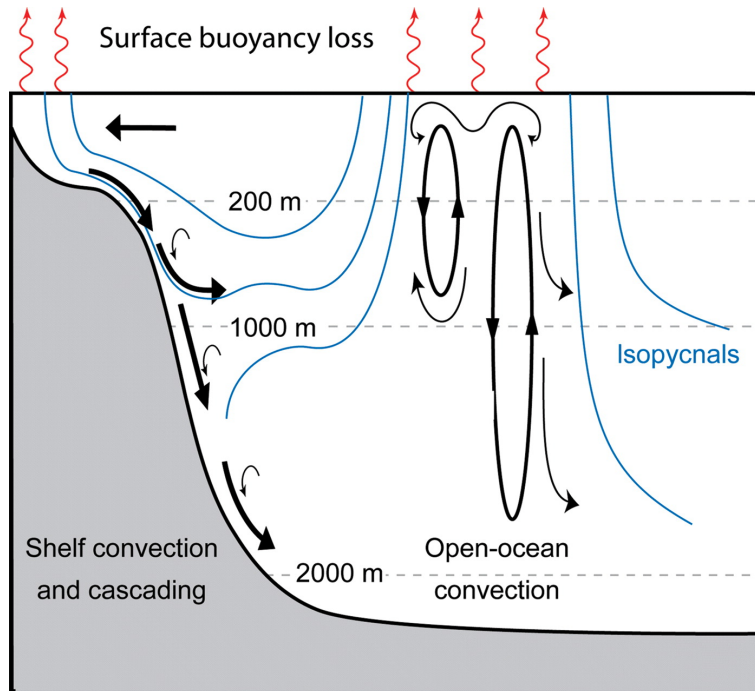


Figure 1.6: Deep convection (a.k.a. open ocean convection) and shelf convection in the Gulf of Lion. Taken from Fig. 1 from [116].

The Gulf of Lion features the favored cyclonic circulation due to the Northern Current flowing from east to west along the coast and the local bathymetry [92]. This is shown in Fig. 1.7. The cyclonic circulation also helps to corral the surface waters to maintain interaction with the cooling fluxes. Eventually, this surface cooling causes the confined water to become denser and cause vertical mixing. However, for this vertical mixing to become deep convection, it has to reach two deeper layers of water masses in the gulf, the intermediate and deep layers. These layers are shown in Fig. 1.8 with their average temperatures and salinities and were mentioned in Sec. 1.1.1. The modified Atlantic water (MAW) forms the surface layer, while the Levantine intermediate water (LIW) forms the intermediate layer. The deepest layer is composed of the preexisting western Mediterranean deep water (WMDW).

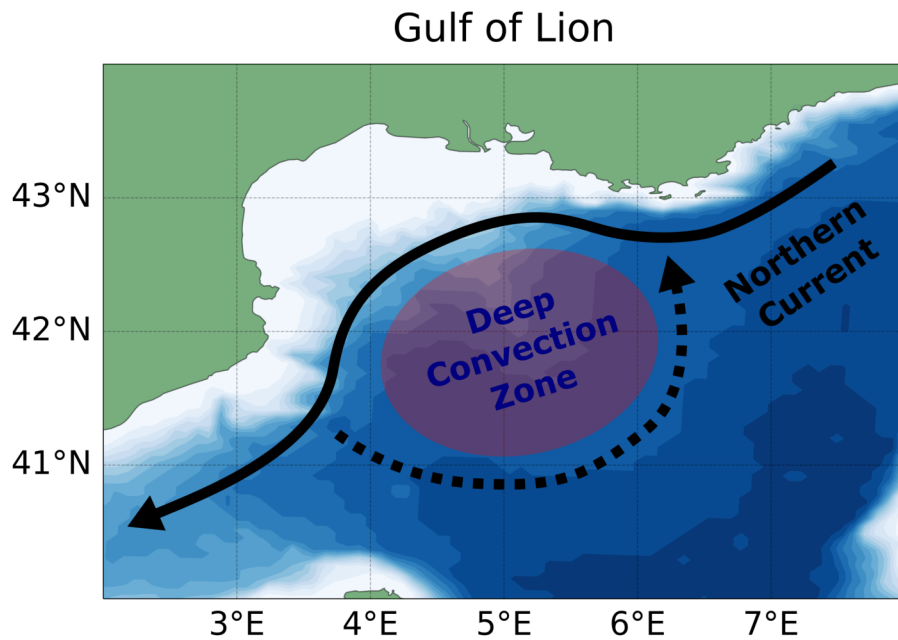


Figure 1.7: The deep convection zone in the Gulf of Lion, with the favored cyclonic ocean circulation forming the Gulf of Lion gyre. The blue shading shows the bathymetry at 200 meter levels.

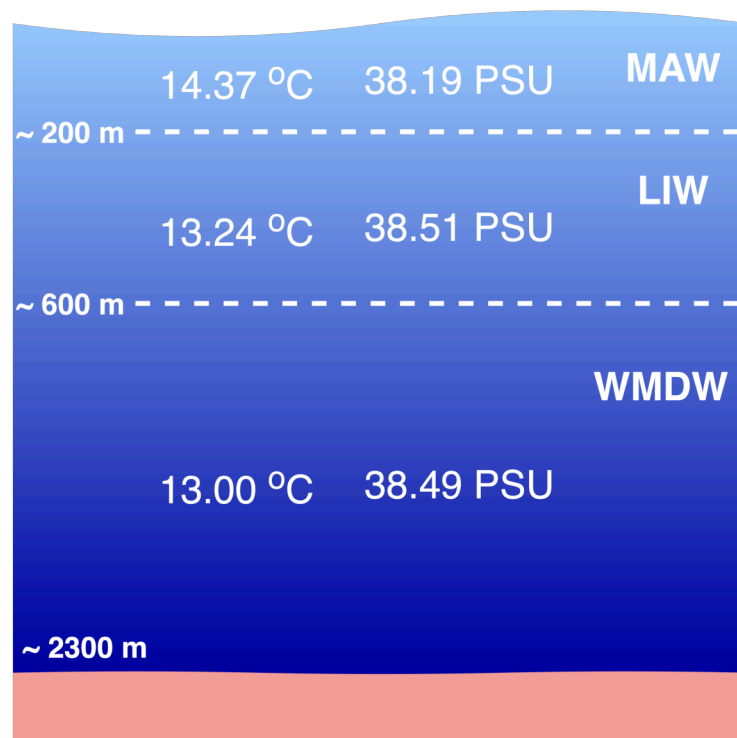


Figure 1.8: Average temperature and salinity for each layer (modified Atlantic water (MAW), Levantine intermediate water (LIW), western Mediterranean deep water (WMDW)) from Jan. 1st, 2005 to Jan. 1st, 2012 from the Coriolis Argo dataset (<https://www.coriolis.eu.org>).

The MAW is the freshest layer, with less salinity than the other layers below at 38.19 *PSU*. The LIW is the saltiest layer, even more saline the deepest layer, at 38.51 *PSU*. This high salinity feature distinguishes the LIW, which at times can be warmer than the MAW aloft but remains denser due

to its higher salinity. As mentioned before, the process of deep convection, shown in Fig. 1.6, forms the WMDW, which features the coldest temperatures. For deep convection to occur, not only must the MAW layer must become dense enough to freely mix with the LIW layer, but once the two mix, the mixed water mass must become as dense as the WMDW to break past the roughly 600 meters depth mark. Once this occurs, the newly formed WMDW features cooler temperatures due to the surface cooling and the salinity levels of the diluted LIW layer that existed pre-deep convection.

After the WMDW is formed, this dense water spreads out along the northwestern basin, among the deeper layers of the Med. Sea [104], with some transported along the northern boundary current towards the Balearic Sea [130], and some transported to the south within eddies [12, 150] into the southern Algerian Basin and towards the Strait of Gibraltar [17], completing the thermohaline circulation pattern of the sea.

1.3.1 Phases of Deep Convection

Deep convection consists of three phases: the preconditioning phase, deep convecting phase, and restratification phase [97, 53]. The last is also known as the lateral exchange phase. These phases are visualized in Fig. 1.9. The preconditioning phase includes both the natural cyclonic circulation of the ocean in the gulf and the Mistral winds. Over the fall and winter months, the Mistral winds and seasonal atmospheric change gradual erode the vertical density gradient of the gulf. Meanwhile, the induced baroclinic instability tries to reestablish a barotropic setting. Eventually, the integrated cooling from the atmospheric forcing is enough to induce the second phase: deep convection. Convective plumes are formed that enhance the mixing of the cooled waters and rim current forms around the convective patch. As spring approaches the surface cooling wanes, the surface buoyancy is no longer strong enough to maintain convection. The baroclinic instability and rim current break apart the convective patch into eddies that then laterally transport the newly formed dense waters and the vertical density gradient forms again.

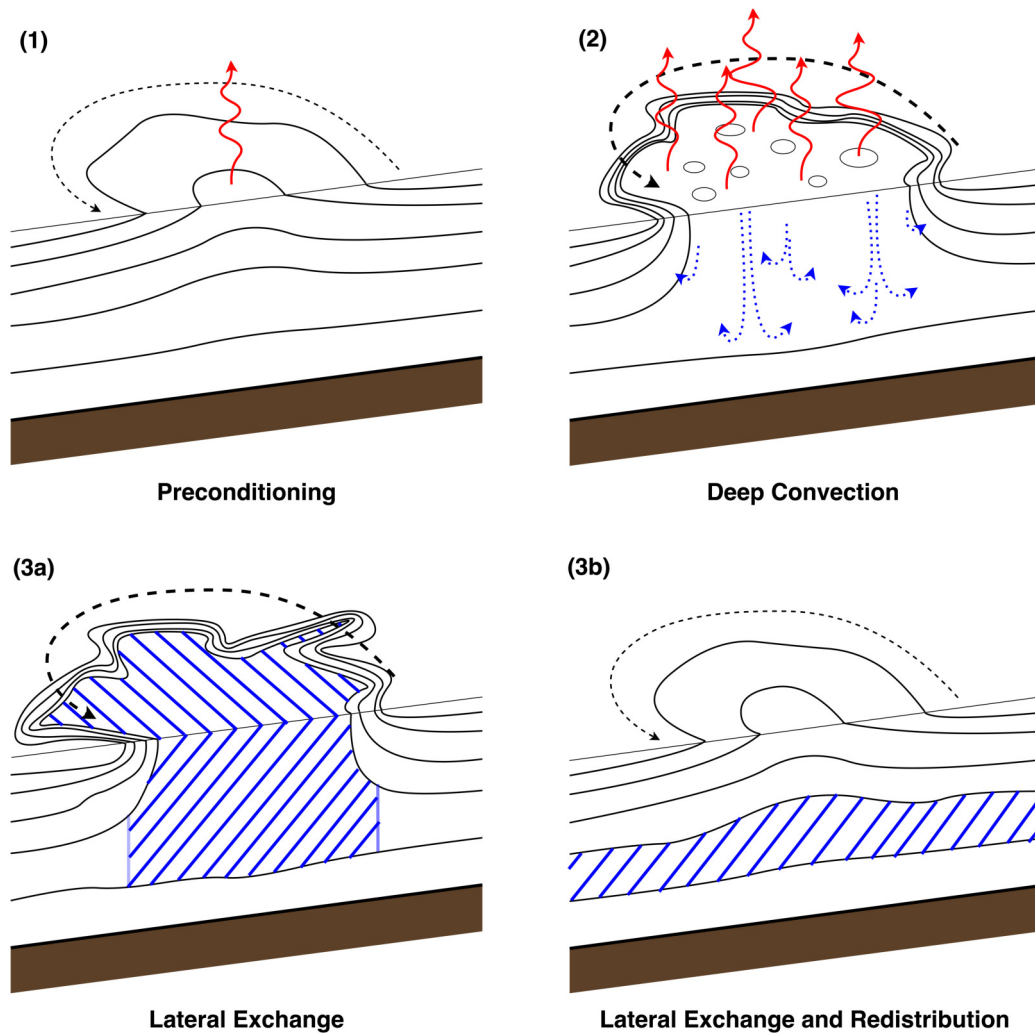


Figure 1.9: The three phases of deep convection: (1) preconditioning, (2) deep convection, (3) lateral exchange and redistribution. The third phase is separated into two graphics as the newly formed dense water (WMDW) is redistributed through the destruction of the convection patch with baroclinically driven eddies (3a) and density flows (3b), the former rapidly restratifying the water column. The contours represent the isopycnals.

1.4 Review of Current Literature

Numerous researchers have studied deep convection, the water masses, and the effect on marine biology in the western Mediterranean basin. They are organized by subsection below.

1.4.1 Idealized Investigations

Many groups have looked at idealized models and lab experiments of deep convection [90, 91, 64, 21, 129, 123, 92, 84, 155, 65, 147, 86, 24, 110, 139]. Madec et al. 1991 [90] performed a 3D simulation of deep convection with varying atmospheric forcing, finding that the frequency of

forcing has an effect on the process. This was supported by the numerical experiment of Levy et al. in 2000 [86]. Madec et al. 1991 [91] and Visbeck et al. 1996 [155] illustrated meanders around 40 km in diameter form along the edges of the convective patch along with a rim current, the process Gascard 1978 [47] proposed as the main cause of breakup. This was confirmed by Coates et al. in 1995 [21] and Jones and Marshall in 1997 [65]. Jones and Marshall 1993 [64] ran a simulation and noted the inverted structure of the baroclinic eddies formed at the onset of convection breakup. Send and Marshall 1995 [129] noted the vertical mixing was better represented through a chimney model than a convection plume model, suggesting rather that the plumes act more as mixing agents rather than increasing the mixed layer depth. Sander et al. 1995 [123] performed a simulation experiment with a nonhydrostatic model, noting the difficulty of convection parameterizations to properly account for vertical mass transport. Madec et al. 1996 [92] determined the importance of the bathymetry of the GOL to maintain the favored cyclonic rotation for deep convection. Legg et al. 1996 [84] demonstrated the ability of a heton model to describe the process. Straneo and Kawase 1999 [147], Cui et al. 2001 [24], and Noh et al. 2003 [110] noted the importance of cyclonic rotation in preconditioning the ocean for deep convection. Sohail et al. 2020 highlighted a need for convection parameterizations to be linked to the horizontal baroclinic instability.

1.4.2 Observations

Multiple observations have captured the deep convection process in the gulf [104, 11, 38, 125, 127, 45, 126, 138, 27, 35, 14, 39, 62, 95, 130, 151, 13]. Two particularly important campaigns to thesis being the **DEep Water formation EXperiment** (DEWEX) [151] and the **Hydrological cycle in the Mediterranean EXperiment** (HyMeX) [35, 39]. Both experiments collected significant hydrological data for the 2012-2013 deep convection event in the gulf. This data is taken advantage of in Sec. 3.

The first observations of deep convection in the gulf were captured by the MEDOC group in 1969 [104]. Schott et al. 1996 [125] were able to observe the convective plumes in the convection patch and confirm their purpose as mixing agents. Margirier et al. 2017 [95] characterized them further, noting that they're colder, saltier and therefore denser attributes when compared to surrounding water. Durrieu de Madron et al. 2013 [27] observed the intense formation of dense water from the Gulf of Lion shelf that rested below the recently formed dense water from deep convection. Houpert et al. 2016 [62] determined the seasonal and annual variability of deep mixing of deep convection from 2007 to 2013, and were able to observe the three separate phases of deep convection.

A particularly close eye has been given towards the 2005 deep convection event, that altered the main mass of deep waters in the western basin [127, 45, 126, 138]. This shift in the typical temperature and salinity of the WMDW was caused by the Eastern Mediterranean Transient (EMT) [119], where changes in atmospheric fluxes [120] are believed to have shifted the primary deep water formation sight in the eastern basin from the Adriatic to the Aegean. This has lead to a sudden shift in the LIW, causing it to become saltier and warmer, resulting in knock-on effects for when

it reaches the western basin. Consequently, there has been increased interest in characterizing the overall trends of the LIW, which have becoming warmer and saltier even after the EMT [93, 41, 96]. This pattern has been seen in the deeper waters of the western basin as well [11].

1.4.3 Realistic Investigations

Perhaps the most investigation on deep convection in the GOL has been performed with realistic simulations with an ocean model, sometimes coupled with an atmospheric model. Lascaratos 1993 [78] used air-sea fluxes to estimate the dense water formation rates across the different locations in the Med. basin: the Gulf of Lions, Levantine Basin, Adriatic Sea, and Aegean Sea. They found the GOL to be the main source of WMDW in the western basin. Wu et al. 1996 [163] modelled the production and spreading of LIW, focusing on its impact on the western basin. Castellari et al. 2000 [18] and Artale et al. 2002 [6] found that higher frequency atmospheric forcing was necessary to accurately reproduce dense water formations rates. Herrmann et al. 2008 [59] and Waldman et al. 2017 [158] ran two ocean simulations, one eddy permitting and the other eddy resolving. Both find that the eddy resolving simulation better represent the mesoscale features of deep convection. Herrmann et al. 2008 [60] determined the spatial resolution of atmospheric forcing, if too low, failed to recreate deep convection in the gulf. Lebeaupin Brossier et al. 2009 [79] investigated the ocean mixed layer response to two Mistral events with a high resolution model and differing sea surface temperature information. Grignon et al. 2010 [51] determined that even a normal winter would have lead to deep convection in 2005. Herrmann et al. 2010 [58] modelled the 2005 convection event and found that while the EMT did not fundamentally change the deep convection process, it led to observed changes found in the newly formed deep water [127, 126]. Lebeaupin Brossier et al. 2011 [80] and Lebeaupin Brossier et al. 2012 [81] performed a series of eddy permitting simulations with differing atmospheric forcing (differing in frequency and spatial resolution). They found increased spatial resolution improves wind channelling (supported by Béranger et al. 2010 [9]) and hence surface fluxes in the gulf, as well as increased temporal resolution (3 hourly) captures the diurnal cycle. Beuvier et al. 2012 [12] simulated 20 years from 1998 to 2008 with an eddy permitting model investigating the spreading of the WMDW. The dense waters were found to favor transport by eddies to the coast of Sardinia. Small et al. 2012 [137] performed a coupled ocean-atmosphere model simulation and determined surface fluxes were greatly impacted by the coupling, while the surrounding synoptic atmosphere was relatively unchanged. L'Hévéder et al. 2013 [87] found that the cyclonic gyre area and stratification of the gyre in December could reasonably predict deep convection for that year. Lebeaupin Brossier et al. 2014 [15] performed an eddy resolving ocean simulation in the fall of 2012, capturing the ocean response of the three Mistral events. They found the ocean surface waters destratified briefly during the event before restratifying after the winds stopped. Estournel et al. 2016 [40] demonstrated in a high resolution model that advection actively attempts to stratify the convective patch. Léger et al. 2016 [83] determined the high sensitivity of deep convection in the gulf to the ocean model's initial conditions. Accurate conditions

are required for accurate deep convection. Somot et al. 2016 [142] ran a hindcast simulation from 1980 to 2013 to capture the variability of deep convection. Waldman et al. 2016 [160] determined ensemble modelling is necessary to capture the intrinsic variability of deep convection in the gulf. Waldman et al. 2016 [160] used a high resolution model and the MOOSE observation network (<https://www.moose-network.fr>) to estimate the dense water formation of the 2012-2013 deep convection event. Damien et al. 2017 [25] used high resolution modelling (1 km) to study submesoscale coherent vortices formed from the breakup of deep convection in the gulf. Giordani et al. 2017 [49] used an eddy resolving model to investigate the PV structure of the convective patch. Lebeaupin Brossier et al. 2017 [82] ran a coupled (to an atmospheric model) and uncoupled eddy resolving ocean simulation. Waldman et al. 2018 [159] found with a eddy resolving hindcast of the gulf that deep convection is mostly a forced phenomenon, with some inherent intrinsic variability (random about 18% of the time). Waldman et al. 2018 [157] determined with modelling and observations that most of the dense water sinking occurs at the rim of the convective patch, leading to the vertical overturning. Seyfried et al. 2019 [133] found the North Balearic front forming the southern limit of the convective patch retreats south when exposed to the strong northerly flow. Bosse et al. 2021 [13] found wind can induce instability at the southern edge of the convection patch with observations and 1 km spatial resolution model.

1.4.4 Biological Effects of Deep Convection

The vertical mixing due to deep convection changes the distribution of nutrients in the convection patch [132, 72]. It mixes oxygen rich waters down, ventilating the deepest layers [22], and mixes sediment and nutrient rich waters up, greatly increasing the nepheloid layer [28, 146]. The vertical mixing also enriches the benthic (bottom-most) layer with fresh resources [116]. However, during the intense vertical mixing, phytoplankton activity is low due to limited available light, as they too are mixed downward away from the surface [85, 7, 153, 95, 71]. Once the column restratifies, the abundance of nutrients leads to a large spring bloom, as the phytoplankton now have access to light and nutrients within the now-collapsed convection region [103]. The heterogeneity of available nutrients between the convection patch and outside it lead to changes in the distribution of phytoplankton [63, 102]. Interestingly, the vertical mixing has a negative impact on zooplankton by limiting predator/prey interactions through dilution [7], but still leads to a growth in population with the spring phytoplankton bloom [30].

1.5 Thesis Outline

1.6 Research Questions

Despite the large assortment of studies listed in the last section (Sec. 1.4), only two investigate the time series shape of the atmospheric forcing: Madec et al. 1991 [90] and Lévy et al. 2000 [86]. Both show that pulse like forcing results in a cyclical destratification/restratification like response in the ocean. However, where this thesis steps further is to *separate* the effect of the pulse like behavior of the Mistral, which acts in the high frequency domain, and the low frequency forcing of the seasonal atmospheric change. This leads us to the thesis's first main question to answer:

1. How does the cooling of the Mistral compare to the seasonal change in the atmosphere in terms of forcing deep convection?

The two prior mentioned studies only performed their experiment over the course of one deep convection event. There are multiple studies that look at deep convection over multiple years [157, 142, 87], but do not differentiate the atmospheric forcing between the seasonal and Mistral timescales. Naturally, this leads us to the thesis's second main question:

2. How does the seasonal and Mistral forcing and its effects on deep convection evolve over multiple years?

Deep convection is expected to disappear by the end of the century [140, 1, 114, 144, 113]. One study in particular investigated as to why this occurs: Parras-Berrocal et al. 2022 [113]. They found that the atmospheric forcing changes very little with climate change and that the changes in the surface and intermediate layers account for the disappearance of deep convection. The freshening of surface waters and the warming and saltening of the intermediate layers agrees with the other studies [144, 114]. This is perplexing however, as one might expect the atmospheric forcing to change with the warming climate. This brings us to the thesis's third and final main question:

3. How does climate change impact the air-sea interaction in the Gulf of Lion?

1.7 Thesis Structure

To answer the above questions and to study the interaction of the Mistral and atmospheric cooling with the GOL, this thesis is separated into three main studies:

1. a case study on the 2012 to 2013 winter, which featured a well observed deep convection event in the GOL (Chap. 3)

2. a climatology study from 1993 to 2013, which featured seven deep convection years (Chap. 4)
3. a scenario study from 2015 to 2100, investigating the changes in stratification and atmospheric forcing in the gulf with climate change (Chap. 5)

In the first study, we look at how Mistral and seasonal atmospheric forcing interplay with the vertical stability of the GOL and dig into the details with a derived simple model. We investigated the Mistral's role in deep convection in the GOL (as the Mistral and Tramontane winds are sister winds, we will refer to them jointly as "Mistral" winds). Its role was determined by running two NEMO ocean simulations of the Med. Sea from Aug. 1st, 2012 to July 31st, 2013, forming a case study of the encapsulated winter. One simulation was forced by unmodified atmospheric forcing data, while the other was forced by a filtered atmospheric dataset with the signal of the Mistral removed from the forcing. Thus, the ocean response due to the Mistral events could be separated and examined, revealing the effects of seasonal atmospheric change alone. A multitude of observational data was collected during this year in the framework of the HyMeX [40, 35], which provided a solid base of observations to validate the ocean model results.

As mentioned before, there are three distinct sections of the deep convection cycle: the preconditioning phase in the fall, the large overturning phase in the winter and early spring (when deep convection occurs), and the restratification/spreading phase during the proceeding summer [104, 53]. The focus of this study is on the preconditioning and overturning phase where the Mistral is stronger and more frequent [50] and therefore plays a larger role in the deep convection cycle.

Two additional years were also studied with the same methodology as the 2012 to 2013 winter: the 1993 to 1994 and 2004 to 2005 winter. The 1993 to 1994 winter does not have a deep convection event, and allows us to compare a deep convecting year versus a non-deep convecting year. The 2004 to 2005 winter is a well studied deep convecting winter and offers some additional literature to draw analysis upon, as well as an additional deep convecting year to compare and contrast with, using the same methodology as the 2012 to 2013 winter.

The second study builds on the results of the first study. The seasonal atmospheric change, regarding its impact on the preconditioning phase, was determined and discovered to be a more significant source of destratification than the Mistral, providing roughly 2/3 of the destratification for the 2012 to 2013 winter. The second investigation looks into the variability of the contribution to destratification for each component, the seasonal and the Mistral, over multiple years to see if this importance remains true over multiple years. 20 years of the Med. Sea, from July 1st, 1993 to June 30th, 2013, were simulated using the NEMO ocean model. NEMO was driven by two sets of WRF/ORCHIDEE atmospheric data: a control set and a filtered (seasonal) set. This resulted in two sets of the simulated ocean data: one set including the effects of the Mistral and the seasonal effects, and the other set just including the seasonal effects, allowing us to separate the effects due to the Mistral (just like in the first study).

For the third study, we applied the same approach as in the first two studies, running two sets of ocean simulations: a control and seasonal set. However, this was performed for a scenario forecast

(SSP5-8.5) over the course of 85 years, from 2015 to 2100, to investigate the effect of climate change on the Mistral and seasonal forcing. In this study, atmospheric forcing and oceanic data were the outputs of a fully coupled regional model, CNRM-RCSM6. The changes in the GOL vertical stability were investigated in terms of atmospheric influences and oceanic influences.

1.8 Climate Change Mitigation

A fourth study was actually performed for this thesis that is slightly different from the rest. With the effects of climate change investigated in the third study and demonstrated to have a large impact in the Mediterranean [23], this study looks into mitigating climate change in the Mediterranean region. Model data is taken from the second study and used to investigate a potential climate mitigation technology: methanol production from seawater. A realistic device is simulated using a purpose built python library to determine the most optimal locations to place said device for methanol production in the Mediterranean. As this study is significantly different from the rest, it is left as more self-contained chapter, and is more properly introduced within the chapter (Chap. 6).

The methodology of the four studies overlap and are organized in one methodology section, Sec. 2, with some of the methodology for the fourth study retained in its section, as it doesn't relate to the other sections. The results and discussion for each study is presented in their respective sections, with a general conclusion presented at the end in Chap. 7.

Chapter 2

Methodology

Contents

2.1 Ocean Modelling	19
2.2 Atmospheric Forcing	20
2.2.1 Filtering	21
2.3 Mistral Detection	23
2.4 Stratification Index	23
2.5 Simple Model	24
2.5.1 Solution for Seasonal <i>SI</i>	26
2.5.2 Solution with Mistral Forcing Function	28

The majority of this thesis relies on ocean modelling forced by modified and unmodified atmospheric forcing datasets. In essence, two series of ocean simulations were performed, a control run, forced by unaltered atmospheric forcing data and seasonal run, forced by filtered atmospheric forcing data. The filtering ideally removes the Mistral from the forcing dataset, which means the two series of ocean simulations can be compared to determine the effect of the Mistral on the ocean response. For Chap. 3, two single year runs for the year of 2012 to 2013, one control and one seasonal, were performed. For Chap. 4, 40 single year runs for the years between 1993 and 2013 were performed, resulting in 20 control simulations and 20 seasonal simulations. For Chap. 5, 170 single year runs were performed, this time from the years 2015 to 2100, again resulting in 85 control simulations and 85 seasonal simulations. Chap. 6 used the control set of simulations from Chap. 4. The model, data, and filtering used are presented in this chapter (Sec. 2.1 and 2.2), as well as the development of a simple model to explain our results (Sec. 2.5). Additional methods are explained as needed.

2.1 Ocean Modelling

The **Nucleus for European Modelling of the Ocean (NEMO)** ocean model (<https://www.nemo-ocean.eu/>; last accessed: Sept. 21st, 2022) was used to simulate the Mediterranean Sea, in bulk configuration, for this thesis. In bulk configuration, the following parameterized equations are used to determine the surface fluxes:

$$\begin{aligned}
 Q_E &= \rho_{a,0} \Lambda C_E (\Delta q) |\Delta \vec{u}| \\
 Q_H &= \rho_{a,0} c_p C_H (\Delta \theta) |\Delta \vec{u}| \\
 Q_{LW} &= Q_{LW,A} - \epsilon \sigma SST_K^4 \\
 \tau &= \rho_{a,0} C_D \Delta \vec{u} |\Delta \vec{u}|
 \end{aligned} \tag{2.1}$$

Where Q_E , Q_H , Q_{LW} , and τ are the latent heat, sensible heat, longwave radiation fluxes and the surface shear stress, respectively. z is the height above the sea surface where the atmospheric variables are provided at, with the naught values ($_0$) at the sea surface. \vec{u} is the horizontal wind vector, with $\Delta \vec{u} = \vec{u}_z - \vec{u}_0$ as the difference between the wind velocity and sea surface current. $\Delta q = q_z - q_0$ and $\Delta \theta = \theta_z - SST$; q and θ are the specific humidity and potential temperature of air, respectively. Λ and c_p are the latent heat of evaporation and the specific heat of water, respectively. ρ_a is the density of air. SST_K as the sea surface absolute temperature. ϵ is the sea surface emissivity, σ is the Stefan-Boltzmann constant, and $Q_{LW,A}$ is the atmospheric longwave radiation. The coefficients C_E , C_H , and C_D are the parameterized coefficients of latent heat, sensible heat, and drag, respectively, and are defined in [77] and [76].

Q_{net} , the net downward heat flux, is the summation of the components in the following equation ([77] and [40]; ignoring snowfall):

$$Q_{net} = Q_{SW} + Q_{LW} + Q_H + Q_E \tag{2.2}$$

Where Q_{SW} is downward shortwave radiation.

The NEMO model was also run in the NEMOMED12 configuration, using NEMO v3.6. NEMOMED12 is described, with boundary conditions, in [157, 57, 12, 80]; a brief description follows: the domain covers the Mediterranean Sea and a portion of the Atlantic Ocean (Fig. 2.1 (b)). The latter buffer zone is used to represent the exchanges between the two bodies of water at the Strait of Gibraltar, and its sea surface height (SSH) fields are restored towards the ORAS4 global ocean reanalysis [8]. The 3-D temperature and salinity fields of the buffer zone are restored towards an ocean objective analysis for Chap. 3 [40], towards the MEDRYS reanalysis [57] for Chap. 4 and 6, and towards a CNRM-RCSM6 SSP5-8.5 scenario run (described in further detail in the Sec. 2.2) for Chap. 5. The Black Sea, runoff of 33 major rivers, and coastal runoff are represented by climatological data from [88]. The initial conditions for each one year run were pulled from the ocean objective analysis of Estournel 2016 [40], the MEDRYS reanalysis [57], and the CNRM-RCSM6 SSP5-8.5 scenario run, for Chap. 3, 4 and 6, and 5, respectively.

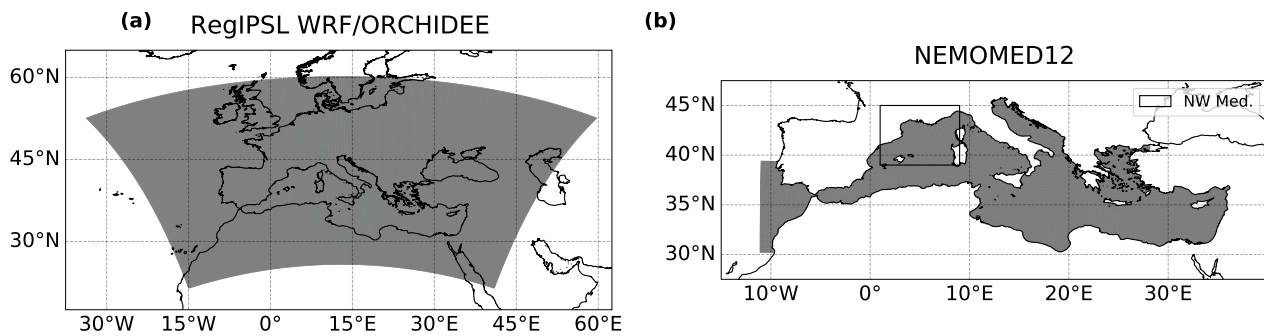


Figure 2.1: The domains of both the WRF domain from the RegIPSL coupled WRF/ORCHIDEE simulation within the Med-CORDEX framework, (a), and the NEMOMED12 configuration domain, (b). The region of interest, the NW Med., is outlined by the box. The location used to study the temporal development of deep convection in the GOL is at 42° N 5° E, and the other location, used in conjunction with the aforementioned point to determine Mistral events, is Montélimar, FR, at 44.56° N 4.75° E.

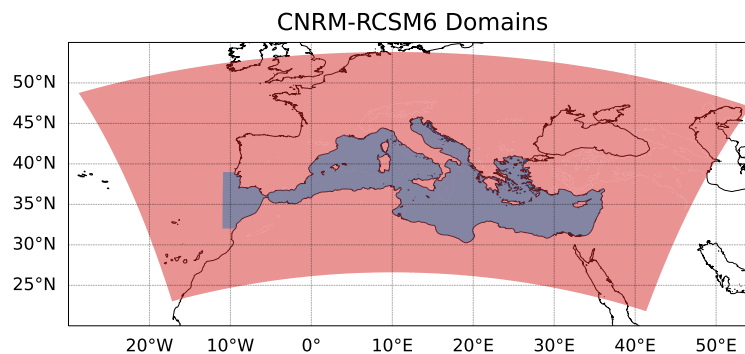


Figure 2.2: The domain of CNRM-RCSM6 (<http://www.umr-cnrm.fr/spip.php?article1098&lang=en>; last accessed: Sept. 13th, 2022).

2.2 Atmospheric Forcing

The atmospheric forcing used in the Chap. 3 and 4 were the outputs of RegIPSL, the regional climate model of IPSL [54], which used the coupling of the Weather Research and Forecasting Model (WRF) [135] and the ORCHIDEE Land Surface Model [75]. The run was a hind-cast simulation (ERA Interim downscaling), performed at 20 km resolution, spanning the period of 1979 to 2016, within the Med-CORDEX framework [121]. The domain is shown in Fig. 2.1 (a). For Chap. 5, the atmospheric data is from the Centre National de Recherches Météorologiques's (CNRM's) fully coupled regional climate system model (RCSM), CNRM-RCSM6 [131] (their results are currently unpublished). The domain is shown in Fig. 2.2. CNRM-RCSM6 itself was forced by CNRM's earth system model (ESM), CNRM-ESM2-1 [128], which was run according to the CMIP6 SSP5-8.5 scenario [111]. This scenario assumes a socio-economic world with increasing energy consumption and utilizing fossil fuels, resulting in a globally averaged radiation forcing increase of 8.5 W m^{-2} by the year 2100. From the available atmospheric variables, the u and v wind components, specific

humidity, potential temperature, shortwave and longwave downward radiation, precipitation, and snowfall were all used to force the NEMO ocean simulations.

2.2.1 Filtering

For the control simulation, the forcing were used as is. For the seasonal simulation, the u and v wind components, specific humidity, and potential temperature were filtered over the entire domains shown in Fig. 2.1 (a) and 2.2. These variables were chosen as they are the primary variables that affect the surface flux calculations in the bulk formulae (Eq. 2.1). The variables relating to radiation and precipitation fluxes were left unchanged. The filtering removes the short term, anomaly scale forcing from the forcing dataset (the phenomena with under a month timescale), effectively removing the Mistral's influence on the ocean response. This creates two separate forcing datasets, one with the anomaly scale forcing included, one with just the seasonal scale forcing (hence the designation of control and seasonal).

The filtering process was performed with a moving window average:

$$\chi_i = \frac{1}{2N + 1} \sum_{j=i-N}^{i+N} x_j \quad (2.3)$$

Where χ_i is the averaged (filtered) value at index i of a time series of variable x with length n , where $i = 0 \rightarrow n$. The window size is equal to $2N + 1$, which, in this case, is equal to 31 days. The ends have a reduced window size for averaging, and thus show edge effects. The edge effects did not affect the forcing used for the NEMO simulations, as they were before and after the ocean simulation dates, as two, full year atmospheric forcing data were used for the simulations.

The moving window average was applied to each time point per day over a 31 day window (i.e. for 3 hourly data, the time series is split into 8 separate series, one for each timestamp per day - 00:00, 03:00, 06:00, etc. - then averaged with a moving window before being recombined). This was done to retain the average intra-day variability yet smooth the intra-monthly patterns, as the diurnal cycle has been shown to retard destratification by temporarily reforming a stratified layer at the sea surface during slight daytime warming. This diurnal restratification has to be overcome first before additional destratification of the water column can continue during the next day [81, 80] and is shorter than the typical Mistral event length of about 5.69 days (for the year of 2012 to 2013; Tab. 3.1).

An important note must be made about the filtering process. The Mistral primarily acts in the higher frequency range but at a lower frequency than the diurnal cycle, as mentioned above. However, it also features signal strength in the lower frequencies on the seasonal scale. This is due to the fact the Mistral becomes stronger, longer, and more frequent during the preconditioning phase than during the rest of the annual cycle [50]. The moving window averaging we have applied to filter the Mistral out of the atmospheric forcing primarily removes the higher frequency portion of the Mistral's presence. But it also removes part of the lower frequency portion as well, that other filters,

such as the Butterworth filter, struggle with, without removing more of the seasonal signal than intended that isn't influenced by the Mistral. This reveals a very interesting point about the structure of the Mistral and the use of "seasonal" and "anomaly" timescales. Since the Mistral primarily acts in the higher frequencies, the "anomaly" timescale will refer to both the higher and lower frequency portions of the Mistral that were filtered out, but will be treated mainly as referring to the higher frequency portion in discussion. The "seasonal" timescale will then refer to the remaining lower frequency signal and average diurnal cycle post filtering.

The result of the filtering for the atmospheric forcing from 2012 to 2013 is shown in Fig. 2.3. Temperature and specific humidity were filtered as is, while the wind speed, was component (u and v) filtered, preserving the general wind direction (Fig. 2.3 wind direction polar plot). Due to the slow movement of intermediate and dense water, which is on the order of about a year scale for newly formed WMDW to move into the southern Algerian Basin [12] and on the order of decades for total circulation [107], we assume the processes outside the NW Med. subdomain in Fig. 2.1 (b), that are affected by the filtering have a negligible impact on the GOL processes on the preconditioning phase timescale.

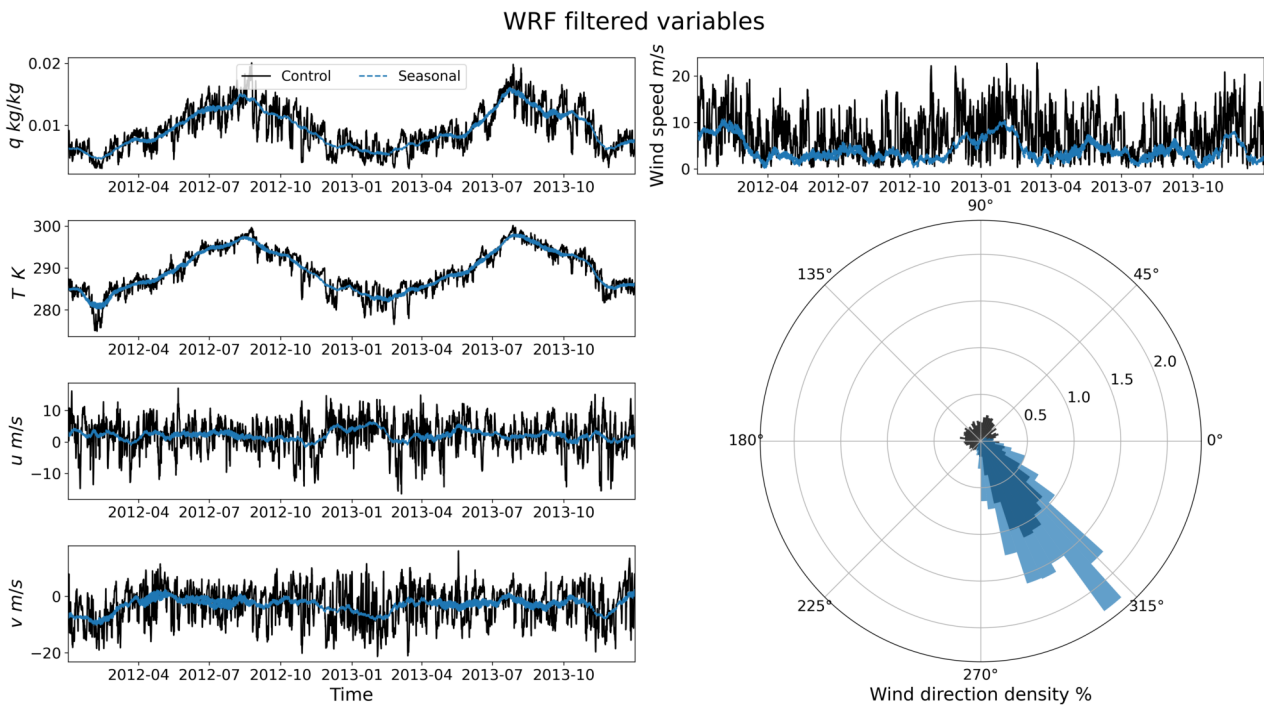


Figure 2.3: An illustration of the filtering (averaging) process described by Eq. 2.3. Here the variables q , T , u , and v are shown for both the unfiltered (control; black) and filtered (seasonal; blue) datasets at the nearest grid point to 42° N 5° E. Note how the peaks of the time series are removed and the general wind direction is conserved. The filtered forcing for Chap. 4 and 5 are similar.

2.3 Mistral Detection

Mistral events will be used for developing the simple model and for their role in driving buoyancy loss at the ocean surface for the first and second study. Events were determined from the RegIPSL atmospheric dataset, in combination with the ERA Interim Reanalysis dataset [29]. Two main criteria were used to define a Mistral event:

1. Northerly flow with a stream-wise flow direction $\pm 45^\circ$ about the south cardinal direction, above 2 m/s at two locations simultaneously: at Mont elimar, France (45.5569° N , 4.7495° E) and in the GOL (42.6662° N , 4.4372° E).
2. The presence of a Genoa Low, defined as a closed sea level pressure contour around a minimum in the field, using 0.5 hPa intervals, anywhere in the box defined by the latitudes 38 and 44° N and longitudes 4 and 14° E (a slightly different domain than that of [50]).

The events during the preconditioning periods in Chap. 3 were then manually checked and edited to remove single day gaps to better represent the data according to a visual inspection of the atmospheric forcing data. For k Mistral events, each event's duration, Δt_k , and period from the beginning of the event to the next event, $\Delta \tau_k$, was determined. The results for the 2012 to 2013 year can be found in Tab. 3.1 (for further analysis into the selection of these criteria, see [50]).

2.4 Stratification Index

A useful metric to quantify the vertical stratification of a column of water is the stratification index, SI ([83, 142, 141]; sometimes called the "convection resistance"). It's derived from the non-penetrative growth of the Mixed Layer Depth (MLD; i.e. without entrainment; [152]), which has been shown to be an accurate approximation for open ocean convection [97]:

$$\frac{\partial z}{\partial t} = \frac{B(t)}{N^2(z)z} \quad (2.4)$$

Where N^2 is the Brunt-V ais al a frequency, z is the vertical coordinate along the water column, $\frac{\partial z}{\partial t}$ is the growth of the mixed layer depth, and B is the potential buoyancy loss the water column can endure before removing stratification (in units of m^2/s^3). Separating by variables and integrating results in the equation for SI :

$$SI = \int_0^D N^2 z dz \quad (2.5)$$

Where D is the depth of water column. If N^2 is assumed to be constant throughout the water column, the integral simplifies to:

$$SI = \frac{D^2}{2} N^2 \quad (2.6)$$

SI provides a 0 dimensional index to track stratification and can be easily related to the buoyancy loss experienced by the water column due to the atmosphere. Because of this, in this thesis SI will be used as the diagnostic to track the atmosphere's impact on the stratification of the GOL waters.

2.5 Simple Model

A simple model relating SI to the atmospheric forcing was developed to better understand how the atmosphere drives the ocean vertical stability. The purpose of this simple model is to separate the seasonal scale atmospheric forcing from the anomaly scale forcing analytically. We start the derivation with the energy equation for incompressible flow [162], as the ocean is very well represented by this:

$$\rho c_p \frac{DT}{Dt} = \frac{Dq}{Dt} \quad (2.7)$$

Where ρ is density, c_p is the specific heat of the fluid with constant pressure, T is temperature, t is time, and q is energy per volume from heat. $\frac{D}{Dt}$ is the material derivative. In this model we're assuming the heat transfer term is equal to the heat removed by the atmosphere and neglect other forms of heat transfer (such as through the ocean floor):

$$\frac{Dq}{Dt} = -q_a \quad (2.8)$$

Where q_a is the volumetric heat forcing from the atmosphere. This leaves us with the following equation:

$$\frac{DT}{Dt} = -\frac{q_a}{\rho c_p} \quad (2.9)$$

The Brunt-Väisälä frequency is defined as:

$$N^2 = \frac{\partial b}{\partial z} = -\frac{g}{\rho_0} \frac{\partial \rho}{\partial z} \quad (2.10)$$

Assuming a fluid whose density varies negatively proportionally to the temperature, $\rho = -\beta T$, which is an acceptable approximation as the density only varies a few tenths of a kg/m^3 and temperature only varies about 10 degrees Celsius, we can describe N^2 in terms of temperature:

$$N^2 = \frac{\partial b}{\partial z} = \frac{g}{T_0} \frac{\partial T}{\partial z} \quad (2.11)$$

Introducing buoyancy as $b = \frac{g}{T_0} T$, we can now rearrange Eq. 2.9 into terms of buoyancy:

$$\frac{g}{T_0} \left[\frac{DT}{Dt} = -\frac{q_a}{\rho c_p} \right] \Rightarrow \frac{Db}{Dt} = -\frac{q_a g}{\rho c_p T_0} \quad (2.12)$$

If we then differentiate by $\frac{\partial}{\partial z}$, we can reorganize the equation in terms of the Brunt-Väisälä

frequency, N^2 :

$$\frac{\partial}{\partial z} \left(\frac{Db}{Dt} = -\frac{\mathbf{q}_{\mathbf{a}}g}{\rho c_p T_0} \right) \Rightarrow \frac{DN^2}{Dt} = -\frac{\partial}{\partial z} \left(\frac{\mathbf{q}_{\mathbf{a}}g}{\rho c_p T_0} \right) \quad (2.13)$$

By renaming the atmospheric forcing term on the right-hand side of Eq. 2.13 to $F(t)$, we can make this equation easier to follow:

$$F(t) = \frac{\partial}{\partial z} \left(\frac{\mathbf{q}_{\mathbf{a}}g}{\rho c_p T_0} \right) \quad (2.14)$$

This brings us to:

$$\frac{DN^2}{Dt} = -F(t) \quad (2.15)$$

This equation allows us to describe the response of the ocean's Brunt-Väisälä frequency to atmospheric heating. To separate the seasonal and Mistral effects, the main assumption we make is that the ocean column is a linear system and responds to the large and short/anomaly timescale atmospheric forcing independently:

$$N^2 = N_S^2 + \delta N^2 \quad (2.16)$$

$$F(t) = \delta F(t) + F_S(t) \quad (2.17)$$

Which describes the response of N^2 on the anomaly timescale, δN^2 :

$$\frac{D\delta N^2}{Dt} = -\delta F(t) \quad (2.18)$$

And the response of N^2 on the seasonal timescale, N_S^2 :

$$\frac{DN_S^2}{Dt} = -F_S(t) \quad (2.19)$$

For the seasonal response, we further make the assumption that N_S^2 negligibly depends on the x , y , and z coordinate directions:

$$\frac{dN_S^2}{dt} = -F_S(t) \quad (2.20)$$

If we want to connect the overall Brunt-Väisälä frequency, N^2 , to the seasonal one, N_S^2 , we can formulate a restoring term, R , in terms of T , or in terms of N^2 following the steps mentioned above:

$$R = \frac{\partial}{\partial z} \left(\frac{g}{T_0} \alpha \rho c_p (T - T_S) \right) \Rightarrow \alpha (N^2 - N_S^2) \quad (2.21)$$

Or, with $\delta N^2 = N^2 - N_S^2$:

$$R = \alpha \delta N^2 \quad (2.22)$$

Where α is the restoring term coefficient. Separating the material derivative into its time and advective components for Eq. 2.18:

$$\frac{\partial \delta N^2}{\partial t} + \vec{V} \cdot \nabla (\delta N^2) = -\delta F(t) \quad (2.23)$$

We will replace the advective component, $\vec{V} \cdot \nabla (\delta N^2)$, with R , which essentially swallows the advective operation into the restoring coefficient, α . This results in the partial differential equation for the anomaly timescale:

$$\frac{\partial \delta N^2}{\partial t} + \alpha \delta N^2 = -\delta F(t) \quad (2.24)$$

2.5.1 Solution for Seasonal SI

To solve the response of N^2 for the seasonal timescale, given by Eq. 2.20, we will assume N_S^2 is vertically homogeneous, giving us the stratification index response through the use of Eq. 2.6:

$$\frac{dSI_S}{dt} = -\frac{D^2}{2} F_S(t) \quad (2.25)$$

We can then separate back out $F_S(t)$ into its components:

$$F_S(t) = \frac{g}{\rho c_p T_0} \frac{\partial \mathbf{q}_{a,S}}{\partial z} \quad (2.26)$$

Dividing $\mathbf{q}_{a,S}$ by D gives us the atmospheric cooling in terms of a surface flux, $-Q_{net,S}$. If we plug this relationship back into Eq. 2.25, we get:

$$\frac{dSI_S}{dt} = \frac{D}{2} \frac{g}{\rho c_p T_0} \frac{\partial Q_{net,S}}{\partial z} \quad (2.27)$$

Integrating this equation by z gives us:

$$\int_0^D \frac{dSI_S}{dt} dz = \frac{D}{2} \frac{g}{\rho c_p T_0} \int_0^D \frac{\partial Q_{net,S}}{\partial z} dz \quad (2.28)$$

$$\frac{dSI_S}{dt} D = \frac{D}{2} \frac{g}{\rho c_p T_0} Q_{net,S} \quad (2.29)$$

$$\frac{dSI_S}{dt} = \frac{g}{2\rho c_p T_0} Q_{net,S} \quad (2.30)$$

And, therefore, we have SI_S expressed in terms of $Q_{net,S}$. This allows to dig deeper into the roles of the different components of $Q_{net,S}$ that drive the changes in stratification.

If we take a step back and do not assume that N_S^2 negligibly depends on x and y , then we can

include the horizontal advection in Eq. 2.20:

$$\frac{\partial N_S^2}{\partial t} + \vec{V}_H \cdot \nabla(N_S^2) = -F_S(t) \quad (2.31)$$

Where \vec{V}_H is the horizontal component of advection. This gives us the following in terms of SI_S :

$$\frac{\partial SI_S}{\partial t} + \vec{V}_H \cdot \nabla(SI_S) = \frac{D}{2} \frac{g}{\rho c_p T_0} \frac{\partial Q_{net,S}}{\partial z} \quad (2.32)$$

We will represent the advection component with ϕ_S to simplify further calculations:

$$\frac{\partial SI_S}{\partial t} + \phi_S = \frac{D}{2} \frac{g}{\rho c_p T_0} \frac{\partial Q_{net,S}}{\partial z} \quad (2.33)$$

Vertically integrating Eq. 2.33 gives us:

$$\int_0^D \frac{\partial SI_S}{\partial t} + \phi_S dz = \frac{D}{2} \frac{g}{\rho c_p T_0} \int_0^D \frac{\partial Q_{net,S}}{\partial z} dz \quad (2.34)$$

$$\left(\frac{\partial SI_S}{\partial t} + \phi_S \right) D = \frac{D}{2} \frac{g}{\rho c_p T_0} Q_{net,S} \quad (2.35)$$

$$\frac{\partial SI_S}{\partial t} + \phi_S = \frac{g}{2\rho c_p T_0} Q_{net,S} \quad (2.36)$$

Integrating the above result with respect to (w.r.t.) time gives us:

$$\int_{t_0}^{t_1} \frac{\partial SI_S}{\partial t} + \phi_S dt = \frac{g}{2\rho c_p T_0} \int_{t_0}^{t_1} Q_{net,S} dt \quad (2.37)$$

Or solved:

$$|_{t_0}^{t_1} SI_S + SI_{S,\Phi} = \frac{g}{2\rho c_p T_0} \int_{t_0}^{t_1} Q_{net,S} dt = SI_{S,Q} \quad (2.38)$$

Where $SI_{S,\Phi} = \int_{t_0}^{t_1} \phi_S dt$. This form allows us to investigate the advective component of stratification. We can further split apart the net heat flux component of Eq. 2.38 into integrals for each of the individual heat flux terms, i , from Eq. 2.2:

$$SI_{S,Q,i} = \frac{g}{2\rho c_p T_0} \int_{t_0}^{t_1} Q_{i,S} dt \quad (2.39)$$

To simplify Eq. 2.39 even further, we can plug in some values for the fraction in front of the integral: c_p taken as $4184 \text{ Jkg}^{-1}\text{K}^{-1}$, g taken as 9.81 ms^{-2} , ρ taken as 1000 kgm^{-3} , and T_0 taken as 290 K ; the average seasonal sea surface temperature over the GOL. Utilizing these values, $\frac{g}{2\rho c_p T_0} \approx 10^{-9} \text{ m}^4 \text{ Js}^{-2}$, a simplification which will be used in Chap. 3, 4, and 5.

2.5.2 Solution with Mistral Forcing Function

Focusing on just the anomaly timescale, we will assume the Mistral is the primary source of forcing. To model the atmospheric cooling of the Mistral, we will model the forcing function, $\delta F(t)$, as a series of k pulse functions, of magnitude δF_k , over a duration of Δt_k , and with a period of $\Delta \tau_k$, visualized in Fig. 3.8 (conveniently agreeing with the attributes we get from Sec. 2.3).

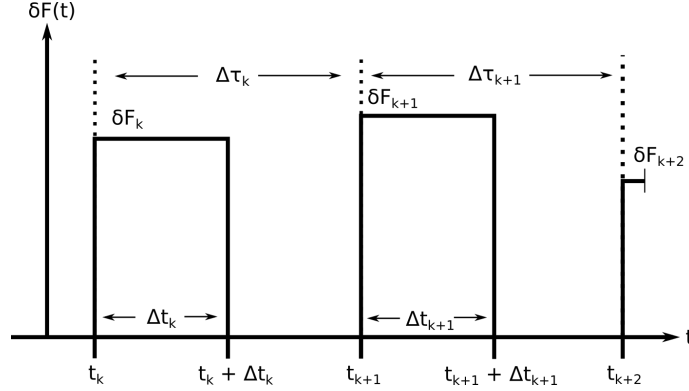


Figure 2.4: The Mistral forcing as a pulse function used to solve Eq. 2.24. k corresponds to the event and δF_k corresponds to the forcing strength of the Mistral event. Δt_k corresponds to the duration of the Mistral event, and $\Delta \tau_k$ to the period between events, with t_k denoting the start of event k .

To solve the Brunt-Väisälä frequency response with the Mistral pulse forcing function, we solve Eq. 2.24 in a piecewise manner, with a solution for each section of the pulse function. We will also make the assumption that for each portion of the Mistral event, during and after, the advective components, hence α , remain constant with respect to time. This leads to α_d and α_a representing the advective components during and after an event, respectively. During a Mistral event, $[t_k, t_k + \Delta t_k)$, we get:

$$\frac{\partial \delta N^2}{\partial t} + \alpha_d (\delta N^2) = -\delta F(t) \quad (2.40)$$

$$\delta N_k^2(t) = -\frac{\delta F_k}{\alpha_d} + c_0 e^{-\alpha_d t} \quad (2.41)$$

$$\delta N_k^2(t_k) = -\frac{\delta F_k}{\alpha_d} + c_0 e^{-\alpha_d t_k} = \delta N_{k-1}^2(t_k) \quad (2.42)$$

$$c_0 = \left[\delta N_{k-1}^2(t_k) + \frac{\delta F_k}{\alpha_d} \right] e^{\alpha_d t_k} \quad (2.43)$$

With the result:

$$\delta N_k^2(t) = \left[\delta N_{k-1}^2(t_k) + \frac{\delta F_k}{\alpha_d} (1 - e^{\alpha_d(t-t_k)}) \right] e^{-\alpha_d(t-t_k)} \quad (2.44)$$

After the event, $[t_k + \Delta t_k, t_{k+1})$:

$$\frac{\partial \delta N^2}{\partial t} + \alpha_a (\delta N^2) = 0 \quad (2.45)$$

$$\delta N_k^2(t) = c_1 e^{-\alpha_a t} \quad (2.46)$$

$$\begin{aligned} \delta N_k^2(t_k + \Delta t_k) &= c_1 e^{-\alpha_a(t_k + \Delta t_k)} \\ &= \left[\delta N_{k-1}^2(t_k) + \frac{\delta F_k}{\alpha_d} (1 - e^{\alpha_d \Delta t_k}) \right] e^{-\alpha_d \Delta t_k} \end{aligned} \quad (2.47)$$

$$c_1 = \left[\delta N_{k-1}^2(t_k) + \frac{\delta F_k}{\alpha_d} (1 - e^{\alpha_d \Delta t_k}) \right] e^{(\alpha_a - \alpha_d) \Delta t_k - \alpha_a t_k} \quad (2.48)$$

With the result:

$$\delta N_k^2(t) = \left[\delta N_{k-1}^2(t_k) + \frac{\delta F_k}{\alpha_d} (1 - e^{\alpha_d \Delta t_k}) \right] e^{(\alpha_a - \alpha_d) \Delta t_k - \alpha_a(t - t_k)} \quad (2.49)$$

Or, to have the results more succinctly put:

$$\delta N_k^2(t) = \begin{cases} \left[\delta N_{k-1}^2(t_k) + \frac{\delta F_k}{\alpha_d} (1 - e^{\alpha_d(t - t_k)}) \right] e^{-\alpha_d(t - t_k)} & [t_k, t_k + \Delta t_k) \\ \left[\delta N_{k-1}^2(t_k) + \frac{\delta F_k}{\alpha_d} (1 - e^{\alpha_d \Delta t_k}) \right] e^{(\alpha_a - \alpha_d) \Delta t_k - \alpha_a(t - t_k)} & [t_k + \Delta t_k, t_k + \Delta \tau_k) \end{cases} \quad (2.50)$$

Therefore, we have the equation that relates a pulsing Mistral event with the Brunt-Väisälä frequency.

2.5.2.1 Periodic Pulse Function $\delta F(t)$

$\delta N_{k-1}^2(t_k)$ is a recursive initial condition, as its initial condition is the event before it, and so on:

$$\delta N_{k-1}^2(t_k) = \left[\delta N_{k-2}^2(t_{k-1}) + \frac{\delta F_{k-1}}{\alpha_d} (1 - e^{\alpha_d \Delta t_{k-1}}) \right] e^{(\alpha_a - \alpha_d) \Delta t_{k-1} - \alpha_a \Delta \tau_{k-1}} \quad (2.51)$$

$$\delta N_{k-2}^2(t_{k-1}) = \left[\delta N_{k-3}^2(t_{k-2}) + \frac{\delta F_{k-2}}{\alpha_d} (1 - e^{\alpha_d \Delta t_{k-2}}) \right] e^{(\alpha_a - \alpha_d) \Delta t_{k-2} - \alpha_a \Delta \tau_{k-2}} \quad (2.52)$$

Therefore, $\delta N_{k-1}^2(t_k)$ can be simplified in expression by combining the initial conditions:

$$\begin{aligned} \delta N_{k-1}^2(t_k) &= \delta N_{k-m}^2(t_{k-(m-1)}) e^{(\alpha_a - \alpha_d) \sum_{i=1}^{m-1} \Delta t_{k-i}} e^{-\alpha_a \sum_{i=1}^{m-1} \Delta \tau_{k-i}} \\ &\quad + \sum_{j=1}^{m-1} \frac{\delta F_{k-j}}{\alpha_d} (1 - e^{\alpha_d \Delta t_{k-j}}) e^{(\alpha_a - \alpha_d) \sum_{i=1}^j \Delta t_{k-i}} e^{-\alpha_a \sum_{i=1}^j \Delta \tau_{k-i}} \end{aligned} \quad (2.53)$$

If $m = k$ and $\delta N_0^2 = 0$:

$$\delta N_{k-1}^2(t_k) = \sum_{j=1}^{k-1} \frac{\delta F_{kj}}{\alpha_d} (1 - e^{\alpha_d \Delta t_{k-j}}) e^{(\alpha_a - \alpha_d) \sum_{i=1}^j \Delta t_{k-i}} e^{-\alpha_a \sum_{i=1}^j \Delta \tau_{k-i}} \quad (2.54)$$

Assuming $\delta F_k = \delta F$, $\Delta t_k = \Delta t$, and $\Delta \tau_k = \Delta \tau$ for all k , or a periodic pulse function, then δN_{k-1}^2 can be expressed as:

$$\delta N_{k-1}^2(t_k) = \frac{\delta F}{\alpha_d} (1 - e^{\alpha_d \Delta t}) \sum_{j=1}^{k-1} e^{[(\alpha_a - \alpha_d) \Delta t - \alpha_a \Delta \tau]j} \quad (2.55)$$

Taking the sum of a finite geometric series:

$$\begin{aligned} \sum_{n=0}^{m-1} r^n &= \left(\frac{1 - r^m}{1 - r} \right) \\ \sum_{n=0}^{m-1} r^n &= \sum_{n=1}^{m-1} r^n + 1 \\ \sum_{n=1}^{m-1} r^n &= \sum_{n=0}^{m-1} r^n - 1 \end{aligned} \quad (2.56)$$

Where $r \neq 1$. If $r = e^{(\alpha_a - \alpha_d) \Delta t - \alpha_a \Delta \tau}$:

$$\sum_{j=1}^{k-1} e^{[(\alpha_a - \alpha_d) \Delta t - \alpha_a \Delta \tau]j} = \left(\frac{1 - e^{[(\alpha_a - \alpha_d) \Delta t - \alpha_a \Delta \tau]k}}{1 - e^{[(\alpha_a - \alpha_d) \Delta t - \alpha_a \Delta \tau]}} - 1 \right) \quad (2.57)$$

We then we get:

$$\delta N_{k-1}^2(t_k) = \frac{\delta F}{\alpha_d} (1 - e^{\alpha_d \Delta t}) \left(\frac{1 - e^{[(\alpha_a - \alpha_d) \Delta t - \alpha_a \Delta \tau]k}}{1 - e^{[(\alpha_a - \alpha_d) \Delta t - \alpha_a \Delta \tau]}} - 1 \right) \quad (2.58)$$

Where $(\alpha_a - \alpha_d) \Delta t - \alpha_a \Delta \tau \neq 0$. Plugging Eq. 2.58 into Eq. 2.44 and (2.49) results in the equation for the response of the Brunt-Väisälä frequency forced by a periodic pulse function:

$$\delta N^2(t) = \begin{cases} \frac{\delta F}{\alpha_d} \left[(1 - e^{\alpha_d \Delta t}) \left(\frac{1 - e^{[(\alpha_a - \alpha_d) \Delta t - \alpha_a \Delta \tau]k}}{1 - e^{[(\alpha_a - \alpha_d) \Delta t - \alpha_a \Delta \tau]}} - 1 \right) \right. \\ \quad \left. + (1 - e^{\alpha_d(t-t_k)}) \right] e^{-\alpha_d(t-t_k)} & [t_k, t_k + \Delta t) \\ \frac{\delta F}{\alpha_d} \left[(1 - e^{\alpha_d \Delta t}) \left(\frac{1 - e^{[(\alpha_a - \alpha_d) \Delta t - \alpha_a \Delta \tau]k}}{1 - e^{[(\alpha_a - \alpha_d) \Delta t - \alpha_a \Delta \tau]}} - 1 \right) \right. \\ \quad \left. + (1 - e^{\alpha_d \Delta t}) \right] e^{(\alpha_a - \alpha_d) \Delta t - \alpha_a(t-t_k)} & [t_k + \Delta t, t_k + \Delta \tau) \end{cases} \quad (2.59)$$

2.5.2.2 δN^2 to δSI

For the anomaly response, Eq. 2.50 and 2.59, assuming a vertically homogeneous δN^2 leads to the stratification index through Eq. 2.6, giving us δSI expressed as:

$$\delta SI_k(t) = \begin{cases} \left[\delta SI_{k-1}(t_k) + \frac{D^2}{2} \frac{\delta F_k}{\alpha_d} (1 - e^{\alpha_d(t-t_k)}) \right] e^{-\alpha_d(t-t_k)} & [t_k, t_k + \Delta t_k) \\ \left[\delta SI_{k-1}(t_k) + \frac{D^2}{2} \frac{\delta F_k}{\alpha_d} (1 - e^{\alpha_d \Delta t_k}) \right] e^{(\alpha_a - \alpha_d) \Delta t_k - \alpha_a(t-t_k)} & [t_k + \Delta t_k, t_k + \Delta \tau_k) \end{cases} \quad (2.60)$$

And:

$$\delta SI_k(t) = \begin{cases} \frac{D^2}{2} \frac{\delta F}{\alpha_d} \left[(1 - e^{\alpha_d \Delta t}) \left(\frac{1 - e^{[(\alpha_a - \alpha_d) \Delta t - \alpha_a \Delta \tau] k}}{1 - e^{[(\alpha_a - \alpha_d) \Delta t - \alpha_a \Delta \tau]}} - 1 \right) \right. \\ \quad \left. + (1 - e^{\alpha_d(t-t_k)}) \right] e^{-\alpha_d(t-t_k)} & [t_k, t_k + \Delta t) \\ \frac{D^2}{2} \frac{\delta F}{\alpha_d} \left[(1 - e^{\alpha_d \Delta t}) \left(\frac{1 - e^{[(\alpha_a - \alpha_d) \Delta t - \alpha_a \Delta \tau] k}}{1 - e^{[(\alpha_a - \alpha_d) \Delta t - \alpha_a \Delta \tau]}} - 1 \right) \right. \\ \quad \left. + (1 - e^{\alpha_d \Delta t}) \right] e^{(\alpha_a - \alpha_d) \Delta t - \alpha_a(t-t_k)} & [t_k + \Delta t, t_k + \Delta \tau) \end{cases} \quad (2.61)$$

For the period pulse function case.

2.5.2.3 Restoring coefficients, α_d and α_a

The restoration coefficients, α_d and α_a , can be solved for the separate phases of a Mistral event in Eq. 2.60 by normalizing the equations during their respective phases. These normalized equations are then fitted to selected, ideal Mistral destratification and restratification cases to retrieve the values of the restoration coefficients.

2.5.2.3.1 Restoration coefficient α_d , during a Mistral

To solve for α_d , we normalize Eq. 2.60 for during a Mistral event, $[t_k, t_k + \Delta t_k)$, with δSI given as:

$$\delta SI_k(t) = \left[\delta SI_{k-1}(t_k) + \frac{D^2}{2} \frac{\delta F_k}{\alpha_d} (1 - e^{\alpha_d(t-t_k)}) \right] e^{-\alpha_d(t-t_k)} \quad (2.62)$$

We first reference the time, t , to the starting time of event k as $t' = t - t_k$, giving us:

$$\delta SI_k(t') = \left[\delta SI_{k-1}(t_k) + \frac{D^2}{2} \frac{\delta F_k}{\alpha} (1 - e^{\alpha t'}) \right] e^{-\alpha t'} \quad (2.63)$$

Next, we normalize δSI_k to the value of zero at $t' = 0$, resulting in $\delta SI_{k,NI}$:

$$\begin{aligned}
\delta SI_{k,NI}(t') &= \delta SI_k(t') - \delta SI_k(t' = 0) \\
&= \left[\delta SI_{k-1}(t_k) + \frac{D^2}{2} \frac{\delta F_k}{\alpha_d} (1 - e^{\alpha_d t'}) \right] e^{-\alpha_d t'} - \delta SI_{k-1}(t_k) \\
&= \left[\delta SI_{k-1}(t_k) + \frac{D^2}{2} \frac{\delta F_k}{\alpha_d} \right] (e^{-\alpha_d t'} - 1)
\end{aligned} \tag{2.64}$$

Then the height or magnitude of destratification for each event is normalized to 1, resulting in $\delta SI_{k,NH}$:

$$\delta SI_{k,NH}(t') = \frac{\delta SI_{k,NI}(t')}{\text{extremum}(\delta SI_{k,NI}(t'))} \tag{2.65}$$

The extremum value for $\delta SI_{k,NI}(t')$ is when $t' = \Delta t_k$, or at the end of the Mistral event. This simplifies $\delta SI_{k,NH}$ to:

$$\delta SI_{k,NH}(t') = \frac{\left[\delta SI_{k-1}(t_k) + \frac{D^2}{2} \frac{\delta F_k}{\alpha_d} \right] (e^{-\alpha_d t'} - 1)}{\left[\delta SI_{k-1}(t_k) + \frac{D^2}{2} \frac{\delta F_k}{\alpha_d} \right] (e^{-\alpha_d \Delta t_k} - 1)} = \frac{(e^{-\alpha_d t'} - 1)}{(e^{-\alpha_d \Delta t_k} - 1)} \tag{2.66}$$

Then, to normalize the length of the event duration from 0 to 1, we divide t' by the event length, Δt_k , which results in t'' :

$$t'' = \frac{t'}{\Delta t_k} \Rightarrow t' = t'' \Delta t_k \tag{2.67}$$

Plugging t'' into $\delta SI_{k,NH}(t')$ returns $\delta SI_{k,NT}$:

$$\delta SI_{k,NT}(t'') = \frac{e^{-\alpha_d t'' \Delta t_k} - 1}{e^{-\alpha_d \Delta t_k} - 1} \tag{2.68}$$

This final equation, $\delta SI_{k,NT}$, can be used with a fitting function to solve for α_d , if Δt_k is supplied.

2.5.2.3.2 Restoration coefficient α_a , after a Mistral

To solve for α_a , we normalize Eq. 2.60 for after a Mistral event, $[t_k + \Delta t_k, t_k + \Delta \tau_k)$, with δSI given as:

$$\delta SI_k(t) = \left[\delta SI_{k-1}(t_k) + \frac{D^2}{2} \frac{\delta F_k}{\alpha_d} (1 - e^{\alpha_d \Delta t_k}) \right] e^{(\alpha_a - \alpha_d) \Delta t_k - \alpha_a (t - t_k)} \tag{2.69}$$

Referencing the time, t , to the end of the event, $t''' = t - (t_k + \Delta t_k)$ and plugging t''' into Eq. 2.69, we get:

$$\delta SI_k(t''') = \left[\delta SI_{k-1}(t_k) + \frac{D^2}{2} \frac{\delta F_k}{\alpha_d} (1 - e^{\alpha_d \Delta t_k}) \right] e^{-\alpha_d \Delta t_k} e^{-\alpha_a t'''} \tag{2.70}$$

Normalizing the vertical intercept of $\delta SI_k(t''')$ results in $\delta SI_{k,NI}$:

$$\begin{aligned}
\delta SI_{k,NI} &= \delta SI_k(t''') - \delta SI_k(t''' = 0) \\
&= \left[\delta SI_{k-1}(t_k) + \frac{D^2}{2} \frac{\delta F_k}{\alpha_d} (1 - e^{\alpha_d \Delta t_k}) \right] e^{-\alpha_d \Delta t_k} e^{-\alpha_a t'''} \\
&\quad - \left[\delta SI_{k-1}(t_k) + \frac{D^2}{2} \frac{\delta F_k}{\alpha_d} (1 - e^{\alpha_d \Delta t_k}) \right] e^{-\alpha_d \Delta t_k} \\
&= \left[\delta SI_{k-1}(t_k) + \frac{D^2}{2} \frac{\delta F_k}{\alpha_d} (1 - e^{\alpha_d \Delta t_k}) \right] e^{-\alpha_d \Delta t_k} (e^{-\alpha_a t'''} - 1)
\end{aligned} \tag{2.71}$$

Each post event restratification is normalized to the height of 1 by dividing $\delta SI_{k,NI}$ by $(\delta SI_k(t''' = \Delta \tau_k - \Delta t_k) - \delta SI_k(t''' = 0))$:

$$\begin{aligned}
\delta SI_{k,NH} &= \frac{\delta SI_{k,NI}}{\delta SI_k(t''' = \Delta \tau_k - \Delta t_k) - \delta SI_k(t''' = 0)} \\
&= \frac{\left[\delta SI_{k-1}(t_k) + \frac{D^2}{2} \frac{\delta F_k}{\alpha_d} (1 - e^{\alpha_d \Delta t_k}) \right] e^{-\alpha_d \Delta t_k} (e^{-\alpha_a t'''} - 1)}{\left[\delta SI_{k-1}(t_k) + \frac{D^2}{2} \frac{\delta F_k}{\alpha_d} (1 - e^{\alpha_d \Delta t_k}) \right] e^{-\alpha_d \Delta t_k} (e^{-\alpha_a (\Delta \tau_k - \Delta t_k)} - 1)} \\
&= \frac{e^{-\alpha_a t'''} - 1}{e^{-\alpha_a (\Delta \tau_k - \Delta t_k)} - 1}
\end{aligned} \tag{2.72}$$

Which gives us $\delta SI_{k,NH}$.

To normalize the length of time of post event restratification, we will divide t''' by the post event time length, $\Delta \tau_k - \Delta t_k$, resulting in t'''' :

$$t'''' = \frac{t'''}{\Delta \tau_k - \Delta t_k} \Rightarrow t''' = t'''' (\Delta \tau_k - \Delta t_k) \tag{2.73}$$

Which leads to $\delta SI_{k,NT}$:

$$\delta SI_{k,NT} = \frac{e^{-\alpha_a t'''' (\Delta \tau_k - \Delta t_k)} - 1}{e^{-\alpha_a (\Delta \tau_k - \Delta t_k)} - 1} \tag{2.74}$$

This leaves us with an equation of α_a , which can be fitted against NEMO model data, if Δt_k and $\Delta \tau_k$ are provided.

2.5.2.4 Determining δF_k

With the restoring coefficients determined in the prior section, Sec. 2.5.2.3, and the duration and period of each event, the strength of each Mistral event, δF_k , can be determined. If we take Eq. 2.62 and note the value of δSI_{k-1} to be the same as $\delta SI_k(t_k)$ at the beginning of an event, we can simplify the equation in the following steps:

$$\begin{aligned}
\delta SI_k(t_k) &= \delta SI_{k-1} \\
\delta SI_k(t_k + \Delta t_k) &= \delta SI_{k-1} e^{-\alpha_d \Delta t_k} + \frac{D^2}{2} \frac{\delta F_k}{\alpha_d} (e^{-\alpha_d \Delta t_k} - 1)
\end{aligned} \tag{2.75}$$

And then solve for δF_k :

$$\delta F_k = \frac{2 (\delta SI_k(t_k + \Delta t_k) - \delta SI_k(t_k) e^{-\alpha_d \Delta t_k}) \alpha_d}{(e^{-\alpha_d \Delta t_k} - 1) D^2} \quad (2.76)$$

2.5.2.5 Time Derivative of δN^2 and δSI

Taking the derivative with respect to time of Eq. 2.50 and 2.60 results in:

$$\frac{\partial \delta N_k^2(t)}{\partial t} = \begin{cases} -\alpha_d \left[\delta N_{k-1}^2(t_k) + \frac{\delta F_k}{\alpha_d} \right] e^{-\alpha_d(t-t_k)} & [t_k, t_k + \Delta t_k) \\ -\alpha_a \left[\delta N_{k-1}^2(t_k) + \frac{\delta F_k}{\alpha_d} (1 - e^{\alpha_d \Delta t_k}) \right] e^{(\alpha_a - \alpha_d) \Delta t_k - \alpha_a(t-t_k)} & [t_k + \Delta t_k, t_k + \Delta \tau_k) \end{cases} \quad (2.77)$$

And:

$$\frac{\partial \delta SI_k(t)}{\partial t} = \begin{cases} -\alpha_d \left[\delta SI_{k-1}(t_k) + \frac{D^2 \delta F_k}{2 \alpha_d} \right] e^{-\alpha_d(t-t_k)} & [t_k, t_k + \Delta t_k) \\ -\alpha_a \left[\delta SI_{k-1}(t_k) + \frac{D^2 \delta F_k}{2 \alpha_d} (1 - e^{\alpha_d \Delta t_k}) \right] e^{(\alpha_a - \alpha_d) \Delta t_k - \alpha_a(t-t_k)} & [t_k + \Delta t_k, t_k + \Delta \tau_k) \end{cases} \quad (2.78)$$

The derivative w.r.t time will be discussed further in Chap. 3.

2.5.2.6 Asymptotic Destratification

The following sections under Sec. 2.5.2.6 differentiate Eq. 2.61 at $t = t_k + \Delta t_k$, or at the end of a Mistral event, where the destratification is the largest, by k , and then by the other components, δF , Δt , and $\Delta \tau$, once $k \rightarrow \infty$. This allows us to perform a sensitivity analysis in Sec. 3.5 in Chap. 3.

2.5.2.6.1 $\frac{\partial \delta SI_k}{\partial k}$

Differentiating by k , allows us to see what happens to δSI_k as k approaches infinity, so see if $k \rightarrow \infty$ is the direction we want to go before performing the sensitivity analysis. Equation 2.61, at $t = t_k + \Delta t$ results in:

$$\delta SI_k(t_k + \Delta t) = \frac{D^2 \delta F}{2 \alpha_d} (e^{-\alpha_d \Delta t} - 1) \left(\frac{1 - e^{[(\alpha_a - \alpha_d) \Delta t - \alpha_a \Delta \tau] k}}{1 - e^{(\alpha_a - \alpha_d) \Delta t - \alpha_a \Delta \tau}} \right) \quad (2.79)$$

The derivative of Eq. 2.79 w.r.t. k is:

$$\frac{\partial \delta SI_k}{\partial k} = \frac{D^2 \delta F}{2 \alpha_d} \frac{(e^{-\alpha_d \Delta t} - 1)}{(1 - e^{(\alpha_a - \alpha_d) \Delta t - \alpha_a \Delta \tau})} \left(-e^{[(\alpha_a - \alpha_d) \Delta t - \alpha_a \Delta \tau] k} \right) [(\alpha_a - \alpha_d) \Delta t - \alpha_a \Delta \tau] \quad (2.80)$$

As $k \rightarrow \infty$, with $\alpha_d > \alpha_a$, Eq. 2.79 goes to:

$$\delta SI_{\infty} = \frac{D^2 \delta F}{2 \alpha_d} (e^{-\alpha_d \Delta t} - 1) \left(\frac{1}{1 - e^{(\alpha_a - \alpha_d) \Delta t - \alpha_a \Delta \tau}} \right) \quad (2.81)$$

2.5.2.6.2 $\frac{\partial \delta SI_{\infty}}{\partial \delta F}$

The derivative of Eq. 2.81 w.r.t. δF is:

$$\frac{\partial \delta SI_{\infty}}{\partial \delta F} = \frac{D^2}{2} \frac{1}{\alpha_d} (e^{-\alpha_d \Delta t} - 1) \left(\frac{1}{1 - e^{(\alpha_a - \alpha_d) \Delta t - \alpha_a \Delta \tau}} \right) \quad (2.82)$$

2.5.2.6.3 $\frac{\partial \delta SI_{\infty}}{\partial \Delta t}$

The derivative of Eq. 2.81 w.r.t. Δt is:

$$\begin{aligned} \frac{\partial \delta SI_{\infty}}{\partial \Delta t} = \frac{D^2 \delta F}{2 \alpha_d} \frac{1}{(1 - e^{(\alpha_a - \alpha_d) \Delta t - \alpha_a \Delta \tau})} & \left[-\alpha_d e^{-\alpha_d \Delta t} \right. \\ & \left. + (e^{-\alpha_d \Delta t} - 1) \left(\frac{(\alpha_a - \alpha_d) e^{(\alpha_a - \alpha_d) \Delta t - \alpha_a \Delta \tau}}{1 - e^{(\alpha_a - \alpha_d) \Delta t - \alpha_a \Delta \tau}} \right) \right] \end{aligned} \quad (2.83)$$

2.5.2.6.4 $\frac{\partial \delta SI_{\infty}}{\partial \Delta \tau}$

The derivative of Eq. 2.81 w.r.t. $\Delta \tau$ is:

$$\frac{\partial \delta SI_{\infty}}{\partial \Delta \tau} = \frac{D^2 \delta F}{2 \alpha_d} (e^{-\alpha_d \Delta t} - 1) \frac{(-\alpha_a e^{(\alpha_a - \alpha_d) \Delta t - \alpha_a \Delta \tau})}{(1 - e^{(\alpha_a - \alpha_d) \Delta t - \alpha_a \Delta \tau})^2} \quad (2.84)$$

Chapter 3

Impact of the Mistral on Deep Water Formation

Contents

3.1	Introduction	37
3.2	Mistral Events	38
3.3	Model Validation	40
3.4	Stratification Index and Mixed Layer Depth	43
3.5	Process Analysis	46
3.5.1	Seasonal Solution and Forcing	46
3.5.2	Anomaly Solution and Forcing	48
3.5.3	Mistral Strength and Destratification	51
3.5.4	Dominating Mistral Attribute	51
3.5.5	Simple Model Results	56
3.6	Comparison with Additional Years	57
3.6.1	Stratification Index	57
3.6.2	Seasonal Forcing	59
3.6.3	Anomaly Forcing	60
3.7	Discussion	61

This first study is organized as a case study focused on the year of Aug. 1st, 2012 to July 31st, 2013 (referred to as the 2013 winter). The purpose of this case study was to determine the impact the Mistral had on the ocean response in the Gulf of Lion, particularly during the preconditioning phase. Two single year ocean simulations were run, one control run and one seasonal run, with the difference between the two elucidating the effect of the Mistral on the ocean. Two additional

winters, the winters of 1994 and 2005, were investigated to confirm the results of the case study winter. The results are presented in five main parts:

1. the Mistral events during the years studied (Sec. 3.2)
2. model validation against available observational data (Sec. 3.3)
3. the model results for stratification and deep convection during the 2013 winter (Sec. 3.4)
4. the analysis of the processes leading to destratification and deep convection using the simple model from Sec. 2.5 (Sec. 3.5)
5. repeating the process analysis for the additional two winters (Sec. 3.6)

Finally, the chapter is closed with some discussion (Sec. 3.7).¹

3.1 Introduction

Deep convection, also known as open-ocean convection, is an important ocean circulation process that typically occurs in the high latitude regions [97]. Localized events are triggered by the reduction of the stable density gradient through sea surface layer buoyancy loss. One such area of deep convection is the Gulf of Lion (GOL) in the Mediterranean Sea. The deep convection events that occur in this region aid the general thermohaline circulation of the Mediterranean Sea by forming the Western Mediterranean Dense Water (WDMW) [118]. After its formation, this dense water spreads out along the northwestern basin, among the deeper layers of the Med. Sea [104], with some transported along the northern boundary current towards the Balearic Sea [130], and some transported to the south within eddies [12, 150] into the southern Algerian Basin and towards the Strait of Gibraltar [17], completing the cyclonic circulation pattern of the sea. The water column mixing that occurs during a deep convection event also brings oxygenated water down from the oxygen-rich sea surface layer and injects sea-bottom nutrients upwards towards the surface [22, 132], resulting in increased phytoplankton blooms in the following season [132].

Significant deep convection events occur every few years in the GOL [142, 62, 97, 105], driven by the Mistral and Tramontane winds. These sister, northerly flows bring cool, continental air through the Rhône Valley (Mistral) and the Aude Valley (Tramontane) leading to large heat transfer events with the warmer ocean surface [31, 43]. These cooling and evaporation events destabilize the water column in the GOL, and are widely accepted to be the primary source of buoyancy loss leading to deep convection [82, 62, 87, 81, 58, 79, 110, 97, 105, 92, 125, 91, 90, 47].

Here, we investigated the Mistral's role in deep convection in the GOL (as the Mistral and Tramontane winds are sister winds, we will refer to them jointly as "Mistral" winds). Its role was determined by running two NEMO ocean simulations of the Med. Sea from Aug. 1st, 2012 to

¹This chapter is adapted from a published article in the journal of Ocean Science: Keller et al. (2022) "Untangling the mistral and seasonal atmospheric forcing driving deep convection in the Gulf of Lion: 2012-2013" [70].

July 31st, 2013, forming a case study of the encapsulated winter. One simulation was forced by unmodified atmospheric forcing data, while the other was forced by a filtered atmospheric dataset with the signal of the Mistral removed from the forcing. Thus, the ocean response due to the Mistral events could be separated and examined, revealing the effects of seasonal atmospheric change alone. A multitude of observational data was collected during this year in the framework of the HYdrological cycle in the Mediterranean EXperiment (HyMeX) [40, 35], which provided a solid base of observations to validate the ocean model results.

In particular, our findings quantify:

- the separated and combined effect of the Mistral and seasonal atmospheric cycle on deep convection,
- the dominant attribute of the Mistral causing buoyancy loss,
- the source of the buoyancy loss due to the seasonal atmospheric cycle.

Two additional years were also studied with the same methodology as the 2012-2013 winter: the 1993-1994 and 2004-2005 winter. The 1993-1994 winter does not have a deep convection event, and allows us to compare a deep convecting year versus a non-deep convecting year. The 2004-2005 winter is a well studied deep convecting winter and offers some additional literature to draw analysis upon, as well as an additional deep convecting year to compare and contrast with, using the same methodology as the 2012-2013 winter.

There are three distinct sections of the deep convection cycle: the preconditioning phase in the fall, the main, large overturning phase in the winter and early spring (when deep convection occurs), and the restratification/spreading phase during the proceeding summer [104, 53]. The focus of study is on the preconditioning and overturning phase where the Mistral is stronger and more frequent [50] and therefore plays a larger role in the deep convection cycle.

3.2 Mistral Events

Using the Mistral detection method in Sec. 2.3, in conjunction with a visual check and adjustment according to the daily wind and pressure plots, the determined Mistral events for this case study are provided in Tab. 3.1 for 2012 to 2013. The Mistral events for an additional two years of 1993 to 1994 and 2004 to 2005 are found in Tab. 3.2 and 3.3, respectively. These Mistral events are used in the process analysis sections, Sec. 3.5 and Sec. 3.6, with the simple model formulated for the impact of the Mistral (Sec. 2.5.2).

Start Date	Δt_k days	$\Delta \tau_k$ days	Start Date	Δt_k days	$\Delta \tau_k$ days
2012-08-03	1	3	2012-12-26	5	7
2012-08-06	1	2	2013-01-02	17	21
2012-08-08	1	5	2013-01-23	6	10
2012-08-13	1	12	2013-02-02 ^d	15	18
2012-08-25	2	5	2013-02-20	7	10
2012-08-30 ^{d,a}	8	13	2013-03-02	1	11
2012-09-12 ^{d,a}	4	7	2013-03-13	3	7
2012-09-19 ^{d,a}	2	9	2013-03-20	1	6
2012-09-28 ^{d,a}	5	14	2013-03-26	1	5
2012-10-12 ^{d,a}	4	15	2013-03-31	1	6
2012-10-27 ^d	5	15	2013-04-06	2	13
2012-11-11 ^{d,a}	3	8	2013-04-19	4	8
2012-11-19	2	8	2013-04-27	1	25
2012-11-27 ^d	6	11	2013-05-22	2	10
2012-12-08 ^d	4	9	2013-06-01	2	23
2012-12-17 ^d	3	4	2013-06-24	1	4
2012-12-21	2	5	2013-06-28	1	41

Table 3.1: The start date of, duration of, Δt_k , and period between each event, $\Delta \tau_k$, for each Mistral event, k , for the entire NEMO simulation period of Aug. 1st, 2012 to July 31st, 2013. Superscripts d and a denote events used as ideal cases for calculating α_d and α_a , respectively. The average values for Mistral events from 2012-08-30 to 2013-02-16 are: $\overline{\Delta t} = 5.69$ days and $\overline{\Delta \tau} = 10.88$ days. The standard deviations for the same time frame are: $\sigma_{\Delta t} = 4.22$ days and $\sigma_{\Delta \tau} = 4.59$ days.

Date	Δt_k	$\Delta \tau_k$	δF_k	Date	Δt_k	$\Delta \tau_k$	δF_k
1993-08-28	4	7	9.23e-09	1993-12-05	1	21	2.57e-08
1993-09-04	2	21	8.39e-09	1993-12-26	3	13	2.52e-08
1993-09-25	4	25	1.94e-08	1994-01-08	1	3	2.17e-08
1993-10-20	6	16	2.92e-08	1994-01-11	2	6	2.07e-08
1993-11-05	1	3	2.96e-08	1994-01-17	15	19	2.91e-08
1993-11-08	2	4	2.54e-08	1994-02-05	7	14	3.62e-08
1993-11-12	5	9	2.42e-08	1994-02-19	1	15	4.19e-08
1993-11-21	2	5	2.42e-08	1994-03-06	3	7	3.88e-08
1993-11-26	7	9	2.57e-08	1994-03-13	6	7	3.74e-08
1993-12-05	1	21	2.57e-08	1994-03-20	3	6	3.72e-08

Table 3.2: The start date of, duration of, Δt_k (days), and period between each event, $\Delta \tau_k$ (days), for each Mistral event, k , and event strength, δF_k ($s^{-2}days^{-1}$), for the preconditioning phase of the NEMO simulation period of Jun. 1st, 1993 to May 31st, 1994. Preconditioning phase for this year is considered from 1993-08-28 to 1994-04-03 (210 total days).

Date	Δt_k	$\Delta \tau_k$	δF_k	Date	Δt_k	$\Delta \tau_k$	δF_k
2004-09-15	2	4	-2.61e-10	2004-11-23	2	4	1.93e-08
2004-09-19	10	37	6.93e-09	2004-11-27	1	7	1.88e-08
2004-10-26	1	6	7.86e-09	2004-12-04	7	14	2.30e-08
2004-11-01	2	4	6.13e-09	2004-12-18	17	31	2.30e-08
2004-11-05	16	18	2.06e-08	2005-01-18	17	24	4.10e-08
2004-11-23	2	4	1.93e-08	2005-02-11	18	21	4.43e-08

Table 3.3: Same as Tab. 3.2, however the NEMO simulation period is from Jun. 1st, 2004 to May 31st, 2005. Preconditioning phase for this year is considered from 2004-09-15 to 2005-04-08 (170 total days).

3.3 Model Validation

To validate the model results, data from the HyMeX (<https://www.hymex.org/>) database was compared to the NEMO control simulation. Sea surface temperature (SST) data from Météo France's Azur and Lion buoy were compared with the control simulation SST of the nearest grid point in NEMOMED12. Figure 3.1 shows the comparison. The Azur buoy data was missing SST measurements from Jan. 19th, 2013 to July 10th, 2013, but where the data is available, NEMO corresponds well to the observations. The same is true for the Lion buoy data, which had measurements for the entire time covered by the simulations. This comes as no surprise, as the NEMOMED12 simulations' SST is restored to the observational dataset of [40]. However, this also means that the calculated surface sensible heat fluxes should be fairly accurate, as both the sensible heat flux and latent heat flux calculations depend on the SST (Eq. 2.1).

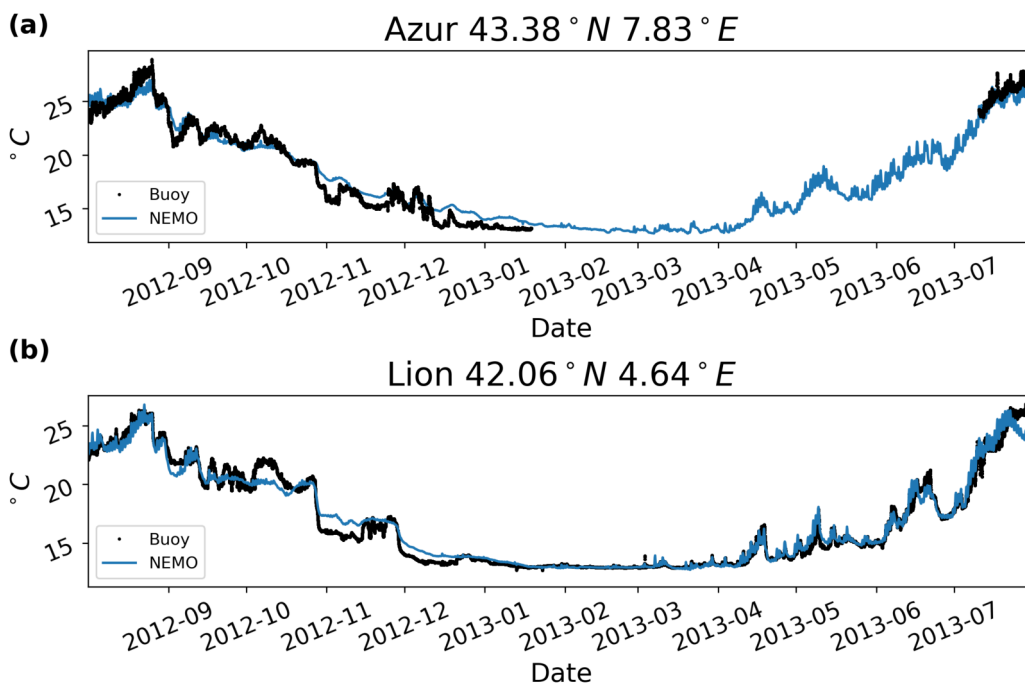


Figure 3.1: SST comparison between the NEMO control run and the Azur , (a), and Lion, (b), buoy SST datasets. Where the data is available, the model results match the buoy data fairly well.

Additionally, the control simulation density and potential temperature profiles were compared to Conductivity-Temperature-Depth (CTD) measurements also procured from the HyMeX database. The CTD measurements were collected during the HyMeX Special Observation Period 2 [148, 39, 35] mission. The CTD profiles collected at approximately the same time and location were averaged together to adjust for small variances and gaps in the data. The averaged profiles and their standard deviations are visualized in Fig. 3.3 and Fig. 3.4. The locations of the CTD profiles are shown in Fig. 3.2.

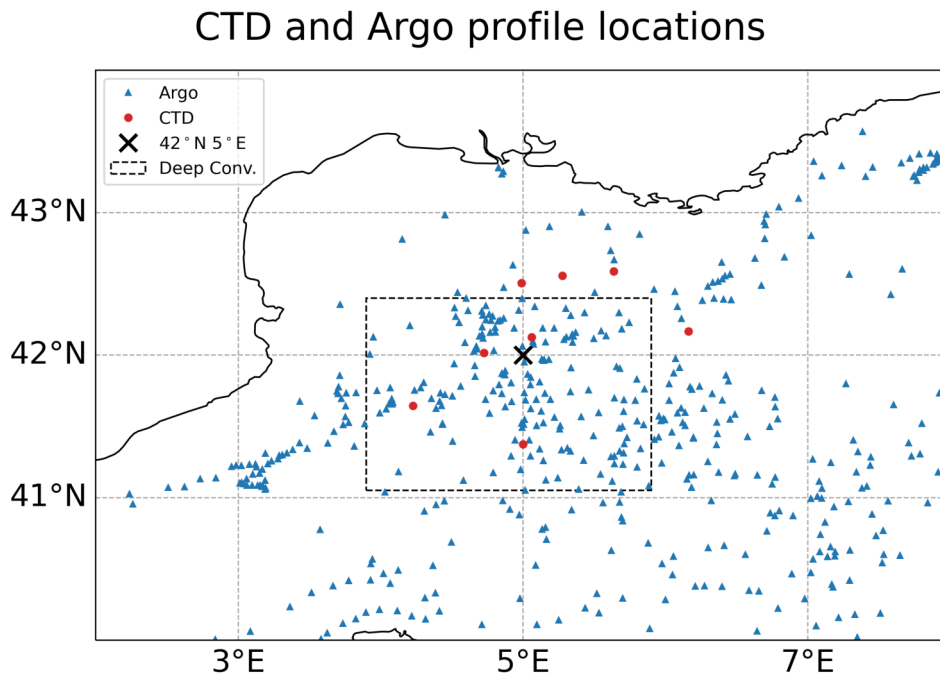


Figure 3.2: Locations of the CTD and Argo profiles. The red circles represent the CTD locations and the blue triangles represent the Argo float profile locations. The deep convection area is marked by the box with a dashed perimeter and 42° N 5° E is marked by an "X".

Like with the SST comparisons, the profiles from the nearest grid point in the control simulation domain were used for the CTD comparisons. The Root Mean Square Error (RMSE) and bias (calculated as the difference between the model values and the observation values) for each of the averaged CTD profiles and corresponding control simulation profiles was calculated and is presented in Table 3.4. Overall, the control simulation and CTD profiles are decently well correlated but not perfect, with low RMSE and bias for both density and potential temperature. The density profiles have an average RMSE less than the average RMSE for the potential temperature profiles: 0.025 kg/m^3 and $0.094 \text{ }^\circ\text{C}$, respectively.

Argo float profiles from the HyMeX database were also compared to the control simulation, again with profiles from the nearest grid point being used. 3118 potential temperature profiles within the box bounded by the 40 to 44° N latitudes and the 2 to 8° longitudes, to represent the GOL area, were considered (see Fig. 3.2). The average RMSE between the Argo profiles and control simulation profiles was $0.43 \text{ }^\circ\text{C}$, with an average bias of $0.23 \text{ }^\circ\text{C}$. These values are larger than the values of the comparison with the CTD profiles. However, considering the sheer volume of profiles and, during

stratified conditions the temperature can range a few degrees from the surface to the lower layers, these results aren't unexpected.

Temperature differences on the order of $10^{-2} \text{ }^\circ\text{C}$ are potentially all that is required to sustain an ocean convective cycle [97] and density differences for the same order of magnitude, 10^{-2} kg/m^3 , are used to separate newly formed dense water during deep convection [62, 142, 12]. This means our model results should be studied with a critical eye, as they may not be fully representative of the true ocean response, given the bias and RMSE values from comparing the simulation to CTD and Argo profiles. Additionally, meanders around 40 km in wavelength form due to baroclinic instability along edge of the convection patch [47]. This could mean the deviations from observations are due to out-of-phase meanders around the convective patch region in the model relative to actuality. Regardless, we believe the simulations are accurate enough to provide interesting results for the transient and regional scale response of the GOL, which covers the main interest of our study.

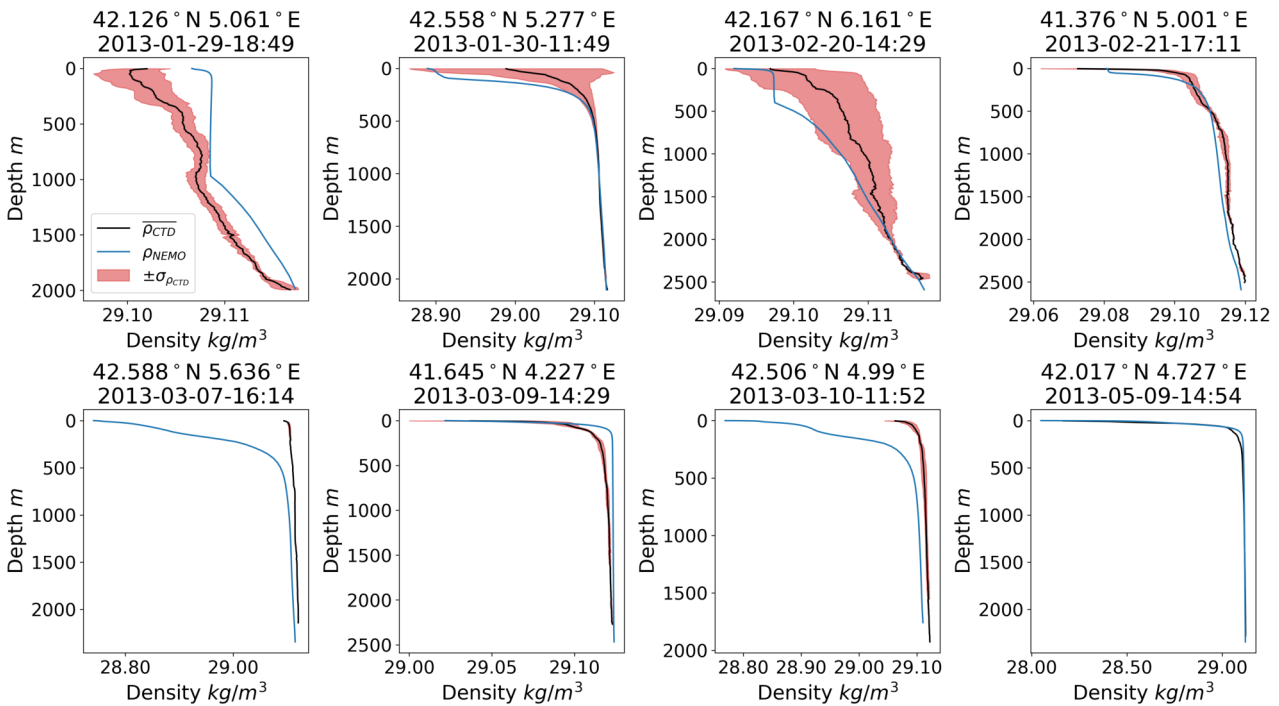


Figure 3.3: Comparison of CTD and NEMO control simulation density profiles. The CTD profiles were averaged by combining multiple vertical profiles collected at the date and location into one profile. The standard deviation of this averaging, $\sigma_{\rho_{CTD}}$, is marked in red and is present for all plots, yet may be difficult to see for March 7th and May 9th.

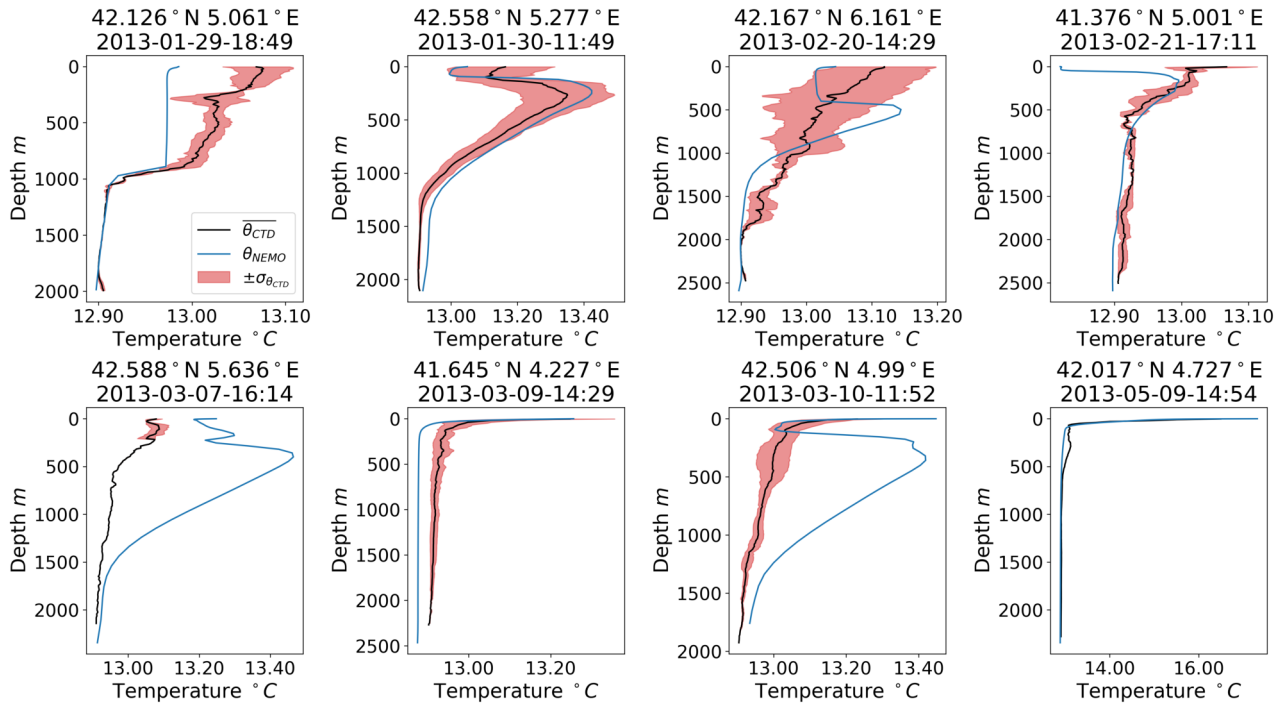


Figure 3.4: Same as Fig. 3.3 but for potential temperature.

Date	Lat. deg	Lon. deg	RMSE $_{\rho}$ kg/m ³	RMSE $_{\theta}$ °C	Bias $_{\rho}$ kg/m ³	Bias $_{\theta}$ °C
2013-01-29-18:49	42.126	5.061	0.004	0.041	0.0032	-0.0265
2013-01-30-11:49	42.558	5.277	0.030	0.055	-0.0093	0.0348
2013-02-20-14:29	42.167	6.161	0.004	0.050	-0.0026	-0.0059
2013-02-21-17:11	41.376	5.001	0.003	0.033	-0.0019	-0.0120
2013-03-07-16:14	42.588	5.636	0.077	0.233	-0.0377	0.1751
2013-03-09-14:29	41.645	4.227	0.005	0.043	0.0036	-0.0414
2013-03-10-11:52	42.506	4.990	0.058	0.224	-0.0320	0.1719
2013-05-09-14:54	42.017	4.727	0.018	0.077	0.0046	-0.0367

Table 3.4: RMSE and bias between the averaged observed CTD density and potential temperature profiles and the nearest NEMO control grid point profiles, for the respective variables. The average RMSE and bias for the density profiles was 0.025 kg/m³ and -0.009 kg/m³, respectively. The average RMSE and bias for potential temperature was 0.094 °C and 0.032 °C, respectively.

3.4 Stratification Index and Mixed Layer Depth

Figure 3.5 shows the SI calculated over the GOL for both simulations: row (a) for the control and row (b) for the seasonal. An important distinction between the two results is deep convection is present in the control simulation but not the seasonal. This is more clearly seen in Fig. 3.6 (c) (closest NEMOMED12 grid point to 42° N, 5° E), as the control simulation MLD reaches the sea floor on Feb. 13, 2013, while the seasonal MLD remains close to the sea surface. This confirms that atmospheric forcing with timescales less than a month, e.g. the Mistral winds, provide a significant amount of buoyancy loss, as without them deep convection fails to occur. There is, however, still

significant loss of stratification at the location of the GOL gyre in the seasonal simulation, which is visible in row (b) of Fig. 3.5 on the date of Feb. 13th, 2013. This spot of destratification is present, but less so, in the preceding and proceeding plots of the same row.

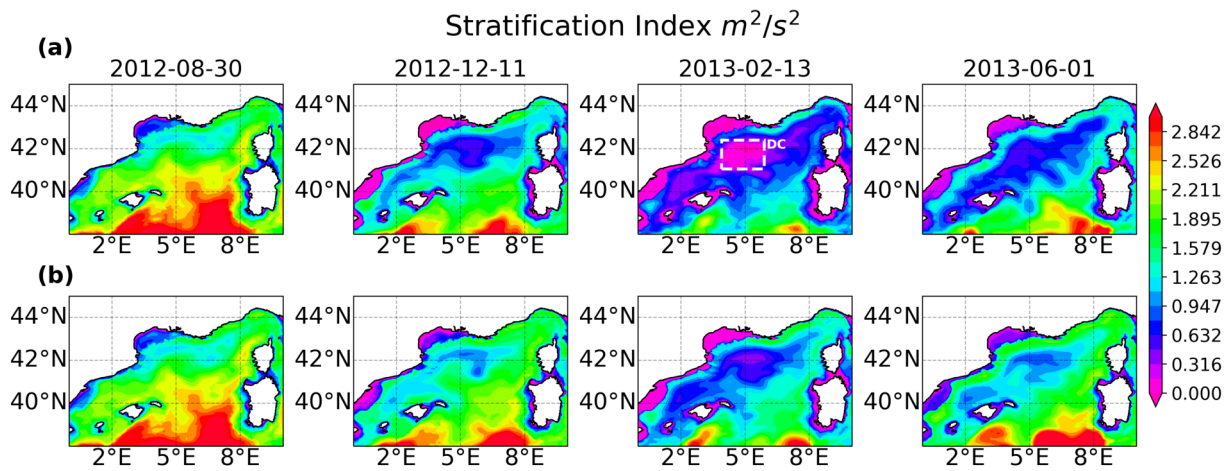


Figure 3.5: The stratification index across the GOL (the area marked as NW Med. in Fig. 2.1 (b)) at different timestamps. Row (a) displays the values of SI for the control simulation and row (b) displays the values of SI for the seasonal simulation. The box denoted by DC indicates the area of deep convection in the GOL that was not seen in the seasonal simulation.

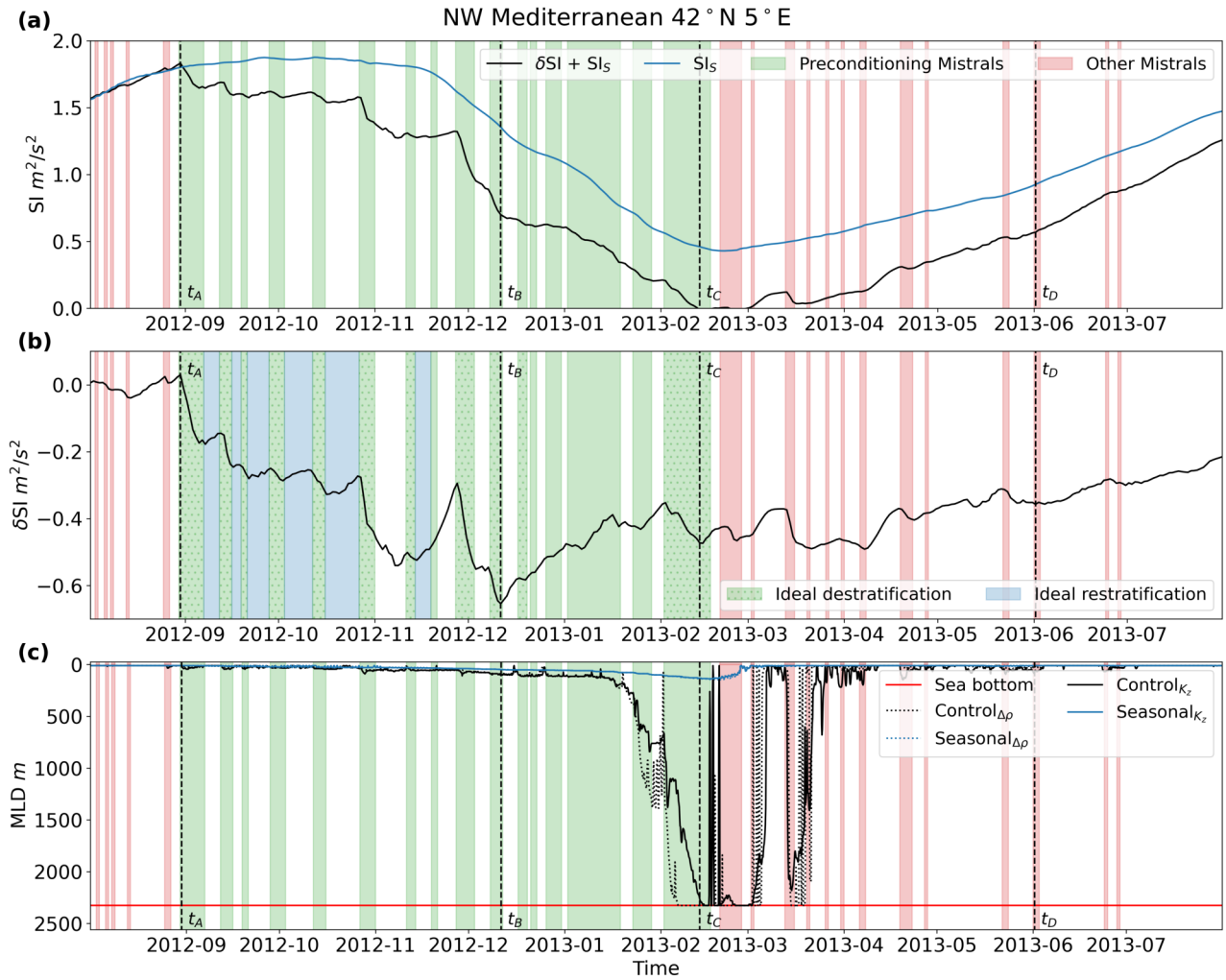


Figure 3.6: The stratification index of the nearest NEMO grid point to 42° N 5° E and MLD over the year of both simulations. Plot (a) shows the stratification index for the control run, $SI_S + \delta SI$, and the seasonal run, SI_S . Plot (b) shows the difference between the control and seasonal stratification index, δSI . Plot (c) shows the MLD for both simulations. Mistral events are shown in all three plots: colored green for events during the preconditioning and deep convection phase and red for events outside the preconditioning phase. Mistral events with dotted hatching (the blue colored intervening time between events) are used as ideal destratification (restratification) events to compute the simple model restoration coefficients. The specific timestamps t_A through t_D correspond to the timestamps of the plots in Fig. 3.5: Aug. 30th, 2012, Dec. 11th 2012, Feb. 13th, 2013, June 1st, 2013, respectively. Two definitions of MLD are plotted in (c): one calculated by a vertical change in density less than $0.01 \text{ kg}/\text{m}^3$, denoted by $\Delta\rho$, and one calculated by a vertical diffusivity less than $5 \times 10^{-4} \text{ m}^2/\text{s}$, denoted by K_z . The MLD denoted by the vertical diffusivity criteria follows the turbocline depth and is taken to represent the mixed layer depth more accurately, as it matches the deep convection timing in the stratification index.

To investigate the time series ocean response in more detail, a spatially averaged time series of the SI for both simulations was analyzed at the grid point nearest to 42° N, 5° E. These coordinates were selected as it is the point with the most destratification in Fig. 3.5, and is the typical center of deep convection in the GOL [97, 104]. The spatial averaging involved horizontally averaging the immediately adjacent grid points, such that 9 grid points in total were averaged, centered around 42° N, 5° E. The stratification index from the control simulation is given as the sum of $\delta SI + SI_S$, while the stratification index of the seasonal simulation is given as SI_S . The difference between the

two, δSI , should contain the change in stratification due to shorter timescale atmospheric events, such as the Mistral, because of the filtering performed in Sec. 2.2.1. $\delta SI + SI_S$, SI_S , and δSI are all shown in Fig. 3.6.

Both the control and seasonal runs start off with an SI value of $1.57 \text{ m}^2/\text{s}^2$ (beginning of Fig. 3.6 (a)), then diverge at the first major Mistral event starting on August 30th, 2012. After diverging, the two runs remain diverged until the end of the simulation run time, ending with a difference of about $-0.22 \text{ m}^2/\text{s}^2$, which is seen in δSI (shown in Fig. 3.6 (b)). As commented earlier, the most striking difference between the control and seasonal run is the occurrence of deep convection in the control run, occurring when $\delta SI + SI_S$ is equal to 0 (signified also when the MLD reaches the sea floor), and the lack of deep convection in the seasonal run, as SI_S only reaches a minimum of $0.43 \text{ m}^2/\text{s}^2$. Additionally, if only the anomaly timescale atmospheric forcing is considered, hence δSI is the only stratification change from the initial $1.57 \text{ m}^2/\text{s}^2$, the roughly $-0.6 \text{ m}^2/\text{s}^2$ of maximum destratification that the anomaly timescale provides is not enough to overcome the initial stratification. This means that both the intra-monthly and the inter-monthly variability of the buoyancy loss, reflected in $\delta SI + SI_S$, are required for deep convection to occur.

Another significant result is the timing of the deep convection. Deep convection initially occurs on Feb. 13th, 2013, which is before SI_S reaches its minimum on Feb. 21th, 2013, but after δSI reaches its minimum on Dec. 11th, 2012. After δSI reaches its minimum, it stays around $-0.43 \text{ m}^2/\text{s}^2$ until May 2013, where it starts to increase. This means that while the induced destratification from the anomaly scale forcing would have been able to overcome $0.6 \text{ m}^2/\text{s}^2$ of stratification to form deep convection in Dec., the seasonal stratification was only low enough in Feb. for both δSI and SI_S to have a combined destratification strong enough for the water column to mix. In other words, the seasonal atmospheric forcing destratified the already preconditioned water column into deep convection along with a simultaneous Mistral event. This means buoyancy loss due to the anomaly forcing may not necessarily be the only trigger for deep convection, at least for this year. This can be seen more clearly in the MLD, as the MLD grows over two Mistral events preceding it reaching the seafloor.

3.5 Process Analysis

To pick apart how the atmospheric forcing influences the stratification in the Gulf of Lion, the simple model in Sec. 2.5 was developed to separate out the individual components of interest for both the seasonal and anomaly time scales.

3.5.1 Seasonal Solution and Forcing

The solution for the seasonal timescale is relatively straight forward. As shown before, Eq. 2.25 relates the seasonal stratification, SI_S , to the seasonal atmospheric forcing, $F_S(t)$. We have the

following definition of $F_S(t)$ from Eq. 2.26:

$$F_S(t) = \frac{\partial}{\partial z} \left(\frac{\mathbf{q}_{a,S} g}{\rho c_p T_0} \right) = \frac{g}{\rho c_p T_0} \frac{\partial \mathbf{q}_{a,S}}{\partial z} \quad (3.1)$$

Where c_p is the specific heat capacity of water, taken as $4184 \text{ Jkg}^{-1}\text{K}^{-1}$, g is gravity, ρ is the density of water, taken as 1000 kgm^{-3} , and T_0 is the reference temperature, taken as the average seasonal sea surface temperature of 292.4 K . This means SI_S can be related to the seasonal volumetric atmospheric heat transfer, $\mathbf{q}_{a,S}$. Setting $\mathbf{q}_{a,S} = -Q_{net,S}/D$, where $Q_{net,S}$ is the seasonal net downward heat flux at the ocean surface from Eq. 2.2, we can calculate $\frac{dSI_S}{dt}$ from $Q_{net,S}$. If we integrate both sides of Eq. 2.25 by z , after plugging in Eq. 3.1 and the relationship for $Q_{net,S}$, as SI_S is constant with respect to (w.r.t.) z , Eq. 2.25 becomes:

$$\frac{dSI_S}{dt} = \frac{g}{2\rho c_p T_0} Q_{net,S} \quad (3.2)$$

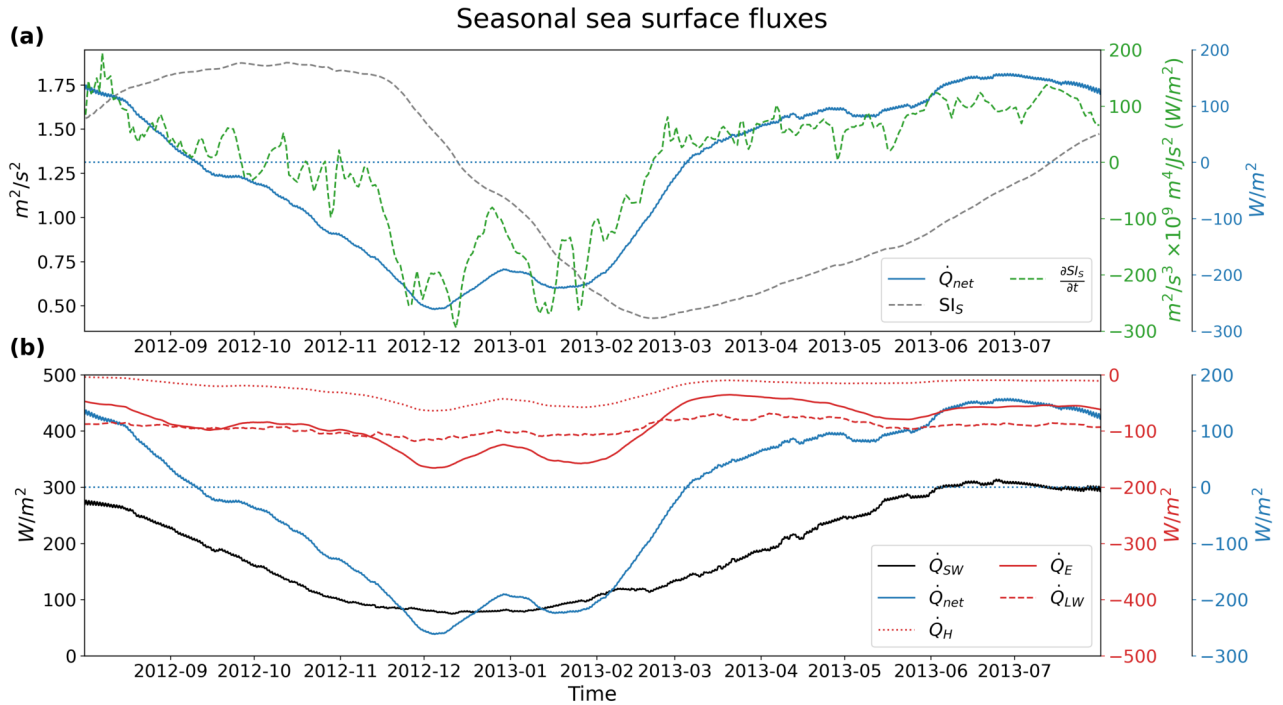


Figure 3.7: The smoothed (with Eq. 2.3) seasonal surface heat fluxes over the point $42^\circ \text{ N } 5^\circ \text{ E}$ for the seasonal simulation. (a) contains the seasonal stratification index, SI_S , and its derivative, $\frac{\partial SI_S}{\partial t}$, comparing it to the seasonal net heat flux, Q_{net} (the subscript S is dropped for convenience). (b) shows the net heat flux separated into its components: Q_E , Q_H , Q_{SW} , and Q_{LW} for latent heat, sensible heat, shortwave downward, and longwave downward fluxes, respectively (neglecting contributions from precipitation and snowfall). The different line colors correspond to the similarly colored axes.

$\frac{g}{2\rho c_p T_0} \approx 10^{-9} \text{ m}^4/\text{Js}^2$, which means the derivative of SI_S w.r.t. time, t , multiplied by 10^9 is on the same order of magnitude as Q_{net} (with the subscript S now dropped for convenience, as the rest of the subsection discusses seasonal heat fluxes), which is what we see in Fig. 3.7 (a) for the 2013 winter, with $\frac{dSI_S}{dt} \times 10^9$ following the curve of Q_{net} . This relationship means when Q_{net} crosses zero

with a negative derivative, SI_S experiences a maximum and vice versa for a minimum. Additionally, the longer Q_{net} remains negative, the more seasonal destratification is incurred by the ocean. The seasonal variation of Q_{net} is primarily driven by the solar radiation, Q_{SW} , which is evident in Fig. 3.7 (b). Consequently, the maximum and minimum values for SI_S occur around Sept. 21st and March 21st, the fall and spring equinoxes. The asymmetry in Q_{net} is mostly caused by the slightly seasonally varying latent heat flux, Q_E , followed by the sensible heat flux, Q_H , both of which also decrease the net heat flux by roughly 100 W/m^2 to 200 W/m^2 , depending on the time of the year. Q_{LW} remains roughly constant during the year, decreasing Q_{net} by roughly -100 W/m^2 . These results are corroborated by the results of multiple model reanalysis for the region as well [143].

Equation 3.2 and Fig. 3.7 convey that the seasonal stratification is primarily driven by shortwave downward radiation. The other terms, the longwave, latent heat, and sensible heat, shift the net heat flux negative enough for the ocean to have a destratification/restratification cycle. If the net heat flux was always positive, stratification would continue until the limit of the simple model applicability. This is an important finding, as, if future years feature less latent and sensible heat exchange due to warming or more humid winters, there will be less seasonal destratification, requiring more destratification from the anomaly timescale to cause deep convection. Consecutive years of decreasing latent and sensible heat fluxes could form a water column that is too stratified to allow deep convection to occur.

3.5.2 Anomaly Solution and Forcing

To solve for the anomaly timescale, described by Eq. 2.24, we assume $\delta F(t)$ can be represented by a pulse function shown in Fig. 3.8. This pulse function assumes the primary forcing at the anomaly timescale is represented by the Mistral events. Each Mistral event, k , has a duration, Δt_k , and a period between the start of the current and following event, $\Delta \tau_k$. δF_k is the strength of the forcing for each event. Inserting this into Eq. 2.24 allows us to solve it in a piecewise manner. Like what we did for the seasonal timescale, we assume the water column has a homogeneous Brunt-Väisälä frequency, allowing us to make use of Eq. 2.6. The restoring coefficient then only represents the horizontal advection, as the vertical component becomes zero with our assumption of a homogeneous N^2 . The last assumption is the restoring coefficient remains constant for each section of the forcing function:

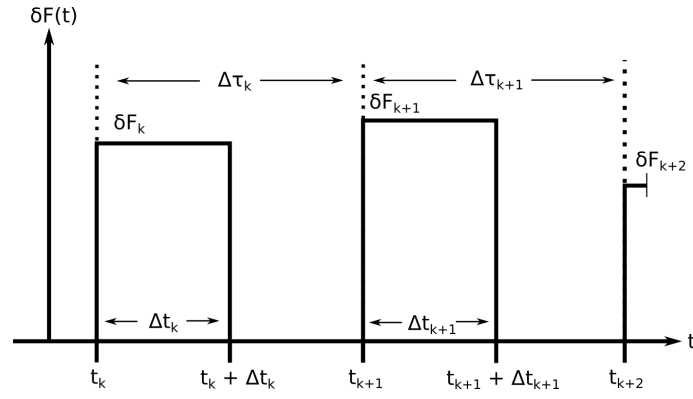


Figure 3.8: The Mistral forcing as a pulse function used to solve Eq. 2.24. k corresponds to the event and δF_k corresponds to the forcing strength of the Mistral event. Δt_k corresponds to the duration of the Mistral event, and $\Delta \tau_k$ to the period between events, with t_k denoting the start of event k .

$$\delta SI_k(t) = \begin{cases} \left[\delta SI_{k-1}(t_k) + \frac{\delta F_k}{\alpha_d} (1 - e^{\alpha_d(t-t_k)}) \right] e^{-\alpha_d(t-t_k)} & [t_k, t_k + \Delta t_k) \\ \left[\delta SI_{k-1}(t_k) + \frac{\delta F_k}{\alpha_d} (1 - e^{\alpha_d \Delta t_k}) \right] e^{(\alpha_a - \alpha_d)\Delta t_k - \alpha_a(t-t_k)} & [t_k + \Delta t_k, t_k + \Delta \tau_k) \end{cases} \quad (3.3)$$

Where α_d and α_a are the restoring coefficients during ($[t_k, t_k + \Delta t_k)$) and after ($[t_k + \Delta t_k, t_k + \Delta \tau_k)$) a Mistral event, respectively.

Further, assuming $\delta F_k = \delta F$, $\Delta t_k = \Delta t$, and $\Delta \tau_k = \Delta \tau$ for all k , which results in a periodic pulse function with constant amplitude and period, we can simplify Eq. 3.3 using the sum of a finite geometric series. At the beginning of the preconditioning period, destratification hasn't yet begun, therefore the initial δSI is zero, resulting in the following equation set:

$$\delta SI_k(t) = \begin{cases} \frac{D^2}{2} \frac{\delta F}{\alpha_d} \left[(1 - e^{\alpha_d \Delta t}) \left(\frac{1 - e^{[(\alpha_a - \alpha_d)\Delta t - \alpha_a \Delta \tau]k}}{1 - e^{[(\alpha_a - \alpha_d)\Delta t - \alpha_a \Delta \tau]}} - 1 \right) \right. \\ \quad \left. + (1 - e^{\alpha_d(t-t_k)}) \right] e^{-\alpha_d(t-t_k)} & [t_k, t_k + \Delta t_k) \\ \frac{D^2}{2} \frac{\delta F}{\alpha_d} \left[(1 - e^{\alpha_d \Delta t}) \left(\frac{1 - e^{[(\alpha_a - \alpha_d)\Delta t - \alpha_a \Delta \tau]k}}{1 - e^{[(\alpha_a - \alpha_d)\Delta t - \alpha_a \Delta \tau]}} - 1 \right) \right. \\ \quad \left. + (1 - e^{\alpha_d \Delta t_k}) \right] e^{(\alpha_a - \alpha_d)\Delta t_k - \alpha_a(t-t_k)} & [t_k + \Delta t_k, t_k + \Delta \tau_k) \end{cases} \quad (3.4)$$

This final equation set allows us to describe the integrated effect of consecutive Mistrals and to easily pick apart the effects of the Mistral's different attributes, including the frequency of the events.

To determine the value of the restoring coefficients, a normalized function was derived for each section of a Mistral event (derivation shown in Sec. 2.5.2.3.1 for during an event and Sec. 2.5.2.3.2 for after an event). The resulting normalized functions were fitted against the NEMO δSI results in Fig. 3.6 for the denoted ideal events in Table 3.1 (denoted d for the dates with ideal destratification taking place during the event and a for the dates with ideal restratification taking place after the

event) and given the average event values of $\overline{\Delta t} = 5.69 \text{ days}$ and $\overline{\Delta \tau} = 10.88 \text{ days}$. The result of the fitting is shown in Fig. 3.9, with α_d having a fitted value of 0.235 day^{-1} and α_a having a fitted value of 0.021 day^{-1} . If we recall the meaning of α_d and α_a from the derivation of the simple model in Sec. 2.5, this means the advective term in Eq. 2.24 has a larger role in the destratification phase of the Mistral event than in the restratification phase, as it is an order of magnitude larger. This result suggests horizontal mixing occurs between events, as a smaller value for the restoration coefficient during the restratification phase means the existence of weaker horizontal gradients than during the preceding destratification phase.

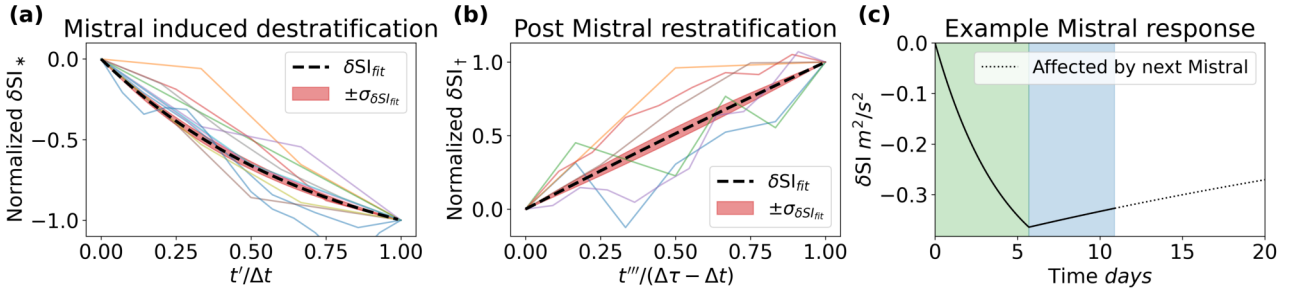


Figure 3.9: The normalized theoretical solutions (Eq. 2.68 and 2.74) for during, (a), and after, (b), a destratification event fitted to the ideal Mistral events from Table 3.1 and δSI values from the NEMO results in Fig. 3.6. A value of 0.235 day^{-1} for α_d and a value of 0.021 day^{-1} for α_a was found. Plot (c) shows the δSI response using the determined restoration coefficients, given an ideal Mistral event with the average values of 5.69 days for the duration and 10.88 days for the period. The average strength of a Mistral, $\delta F = 4.01 \times 10^{-8} \text{ s}^{-2} \text{ day}^{-1}$, was taken from values found in Table 3.5.

The strength of each Mistral event, δF_k , was found similarly by solving for δF_k after noting the initial value of $\delta SI_k(t_k)$ is equal to $\delta SI_{k-1}(t_k)$ (derivation found in Sec. 2.5.2.4). Then the values of δSI from the NEMO results in Fig. 3.6 were plugged in to determine the values of δF_k (see Table 3.5 for the resulting values).

Date	$\delta F_k \text{ s}^{-2} \text{ day}^{-1} \times 10^{-8}$	Date	$\delta F_k \text{ s}^{-2} \text{ day}^{-1} \times 10^{-8}$
2012-08-30	1.81	2012-11-27	5.46
2012-09-12	2.67	2012-12-08	6.37
2012-09-19	2.66	2012-12-17	5.30
2012-09-28	2.73	2012-12-21	5.03
2012-10-12	3.04	2012-12-26	4.39
2012-10-27	4.59	2013-01-02	3.80
2012-11-11	4.84	2013-01-23	3.53
2012-11-19	3.92		

Table 3.5: The Mistral strengths, δF_k , for each of the preconditioning phase events, using α_d and α_a from Sec. 2.5.2.3, and the rest of the preconditioning period Mistral characteristics from Table 3.1, plugged into Eq. 2.76. $\overline{\delta F_k} = 4.01 \times 10^{-8} \text{ s}^{-2} \text{ day}^{-1}$ and $\sigma_{\delta F_k} = 1.196 \times 10^{-8} \text{ s}^{-2} \text{ day}^{-1}$.

3.5.3 Mistral Strength and Destratification

Mistral events do not always lead to destratification. Some events in Fig. 3.6 fail to create further destratification and actually continue to restratify the water column. The simple model can describe these phenomena. To determine which events lead to destratification versus not, we take the derivative with respect to time of Eq. 3.3 for during an event (from Sec. 2.5.2.5). This results in the following equation:

$$\frac{\partial \delta SI_k(t)}{\partial t} = -\alpha_d \left[\delta SI_{k-1}(t_k) + \frac{D^2}{2} \frac{\delta F_k}{\alpha_d} \right] e^{-\alpha_d(t-t_k)} \quad (3.5)$$

The quantity $\frac{\partial \delta SI_k(t)}{\partial t}$ must be less than zero for destratification to occur, which means if α_d is a positive quantity (refer to Sec. 2.5.2.3 or Fig. 3.9), $\delta SI_{k-1}(t_k) + \frac{D^2}{2} \frac{\delta F_k}{\alpha_d}$ must be a positive quantity. If some destratification has already occurred relative to the seasonal stratification, such that $\delta SI_{k-1}(t_k) < 0$, then $\frac{D^2}{2} \frac{\delta F_k}{\alpha_d}$ must be larger than $-\delta SI_{k-1}(t_k)$ for destratification to occur. Recalling that δF_k is positive when heat is removed from the water column, this means that additional Mistral events must overcome the current amount of destratification to further destratify the water column. Otherwise, no destratification occurs or even restratification occurs. An example of this can be seen with the Mistral event starting on Jan. 2nd, 2013, that lasts for 17 days in Fig. 3.6 (b). The event starts off with an initial destratification of $-0.48 \text{ m}^2/\text{s}^2$ and ends at $-0.41 \text{ m}^2/\text{s}^2$, a net restratification of $0.07 \text{ m}^2/\text{s}^2$. This is despite the fact this event has a positive δF_k value of $3.80 \times 10^{-8} \text{ s}^{-2} \text{ day}^{-1}$ (from Table 3.5).

The combined overall effect of this result can be seen in Fig. 3.6 (b), as the consecutive Mistral events during the preconditioning phase cause destratification to a minimum of $-0.6 \text{ m}^2/\text{s}^2$ for δSI on Dec. 11th, 2012. Proceeding events after this minimum fail to continue to destratify the water column and, instead, restratification occurs on the anomaly timescale, even before deep convection occurs. The seasonal stratification, SI_S , and along with the anomaly destratification, δSI , brings the total SI to zero on Feb. 13, 2013, resulting in deep convection.

3.5.4 Dominating Mistral Attribute

A pertinent question to ask is which attribute of the Mistral, the frequency, strength, or duration, is the most important when it drives destratification. Figure 3.11 and 3.10 show the results of varying δF , Δt , and $\Delta \tau$ individually (in subplots (a), (b), and (c)), respectively) in Eq. 3.4. The other variables are kept at the mean value when not varied. The dashed lines in both figures show the limit of potential destratification per case. What we can see is stronger Mistral events, with an increased value for δF , result in more destratification, with the reverse happening with decreased values. Decreasing the event duration, Δt , results in less destratification, however, increasing event duration causes more destratification up to the limit where the individual events converge into one single long event and the destratification converges to the dashed line limit. After this, there

is no additional destratification. Increasing or decreasing the frequency of events (decreasing or increasing the period, $\Delta\tau$), only minimally changes the accrued destratification, due to the fact that the magnitude of $\frac{\partial\delta SI}{\partial t}$ is dependent on the strength of the current Mistral event and the already achieved destratification. Decreasing the frequency (increasing the period), allows for more restratification to occur after an event, but the proceeding event has a larger difference between current destratification and the event strength, leading to destratification that almost reaches the same level as the case with more frequent events. Increasing the frequency has a similar effect to increasing the duration; when the period is zero, the forcing becomes one large event, converging the resulting destratification to the dashed line.

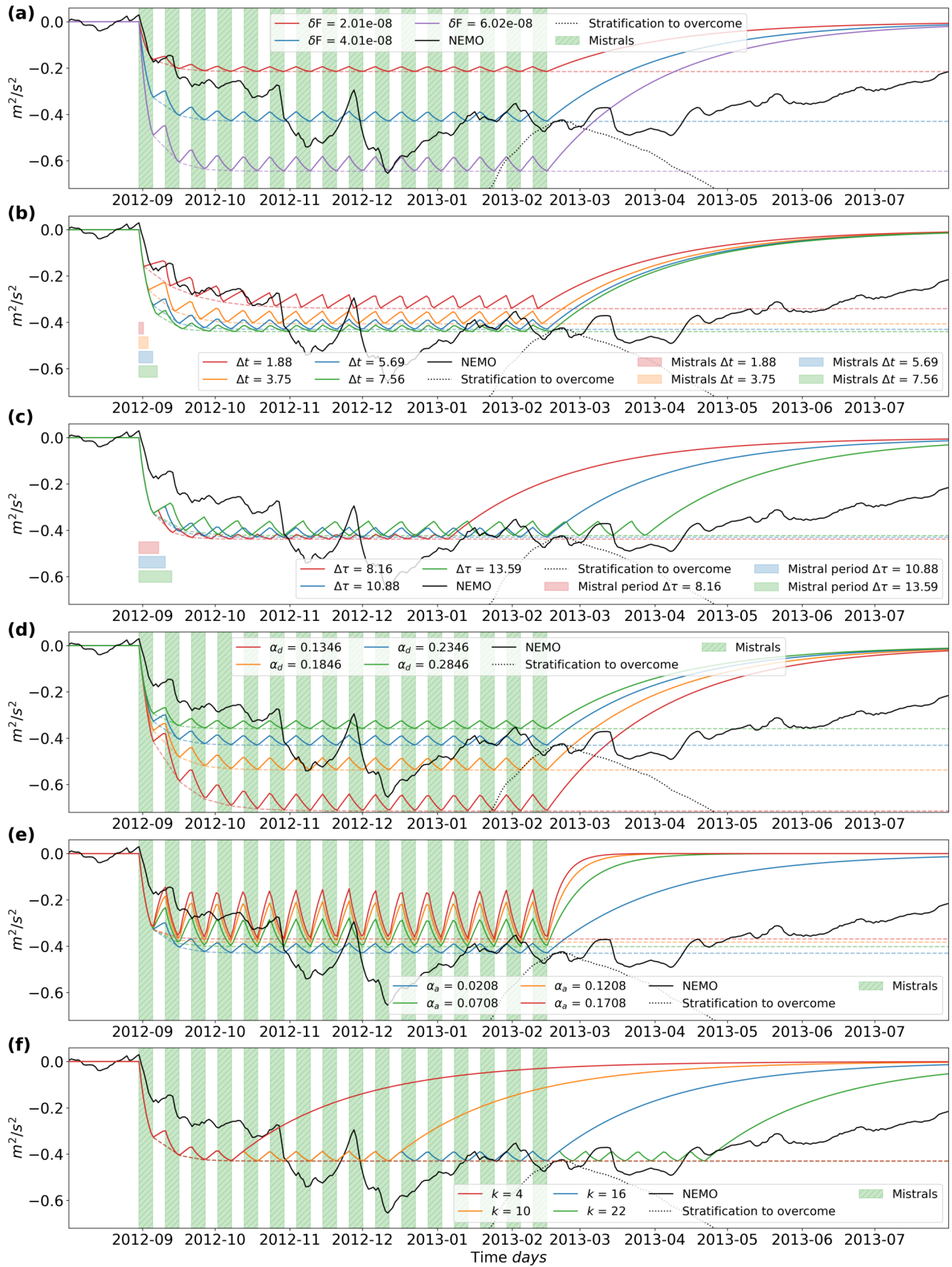


Figure 3.10: Equation (3.4) plotted with one variable varying in each plot with the other variables held constant at the mean value. (a) varies the strength of the Mistral, δF , (b) varies the duration, Δt , and (c) varies the period between events, $\Delta \tau$. (d) varies the restoration coefficient during the destratification phase, α_d and (e) varies the restoration coefficient for the restratification phase. (f) varies the number of events.

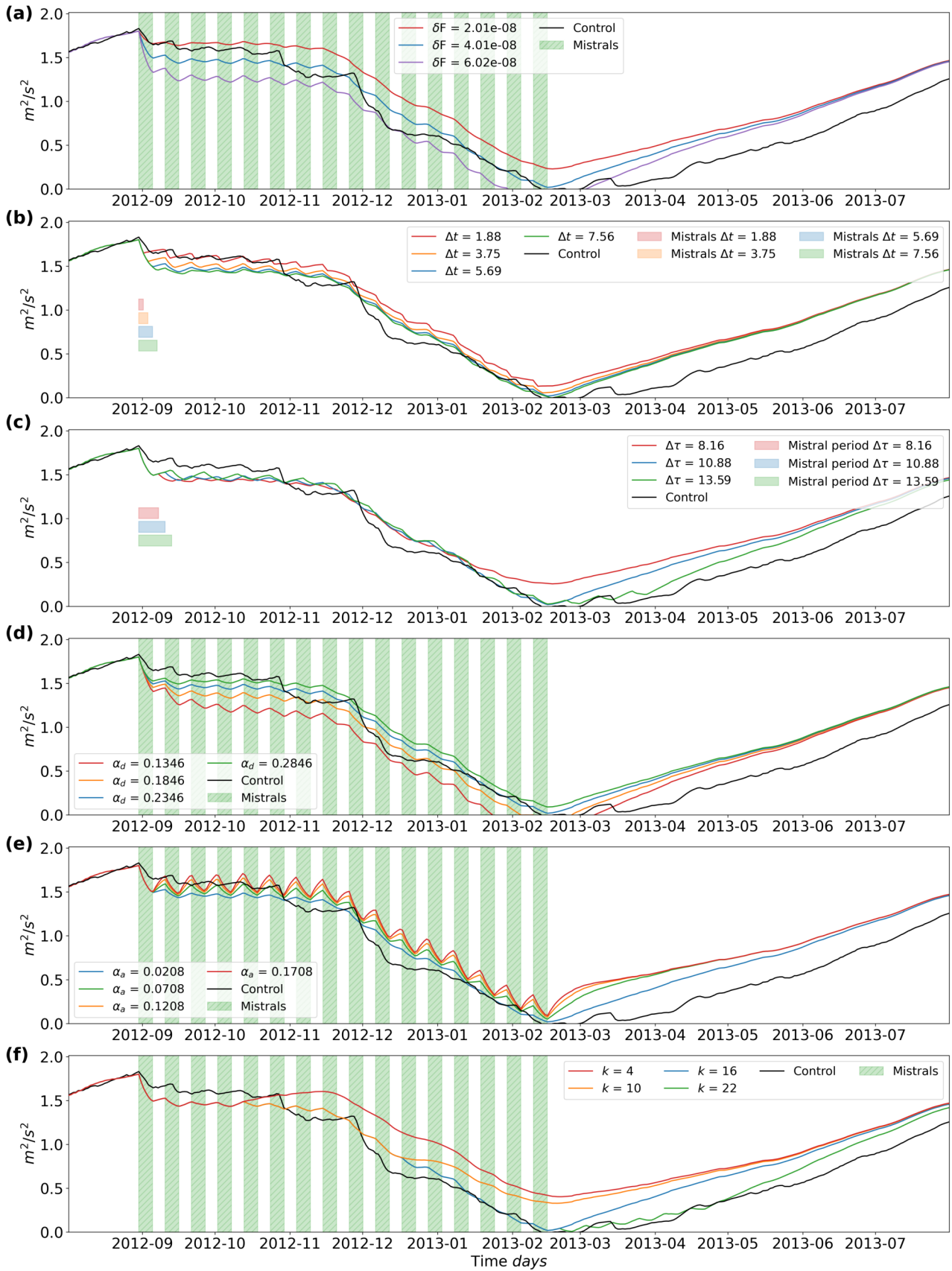


Figure 3.11: Same as Fig. 3.10, however, SI_S is added to the results from Eq. 3.4.

To more accurately quantify the effect of each attribute, we separate δSI into its total derivative in terms of the Mistral attributes:



$$d\delta SI = \underbrace{\frac{\partial \delta SI}{\partial \delta F} d\delta F}_{\text{Strength}} + \underbrace{\frac{\partial \delta SI}{\partial \Delta t} d\Delta t}_{\text{Duration}} + \underbrace{\frac{\partial \delta SI}{\partial \Delta \tau} d\Delta \tau}_{\text{Period}} \quad (3.6)$$

Due to the lack of available total derivatives for δF , Δt , and $\Delta \tau$, we approximate them with their respective standard deviation: $\sigma_x \approx dx$. Before we determine the partial derivatives for each attribute, note that in Fig. 3.10 and 3.11 subplot f that changing the number events, k , does not change the potential destratification limit (the dashed line). This means the potential destratification does not change with the number of events. Another notation to make is the character of the potential destratification limit: it approaches some asymptotic value as k approaches infinity. We can take advantage of this by differentiating the destratification phase of Eq. set 3.4 with respect to k , taking $t = \Delta \tau$, at the end of the phase, where the destratification equals the potential destratification (from Sec. 2.5.2.6):

$$\frac{\partial \delta SI_k(t = t_k + \Delta t)}{\partial k} = \frac{D^2 \delta F}{2 \alpha_d} \frac{(e^{-\alpha_d \Delta t} - 1)}{(1 - e^{(\alpha_a - \alpha_d) \Delta t - \alpha_a \Delta \tau})} (-e^{[(\alpha_a - \alpha_d) \Delta t - \alpha_a \Delta \tau]k}) ((\alpha_a - \alpha_d) \Delta t - \alpha_a \Delta \tau) \quad (3.7)$$

Plugging in the mean values of Δt , $\Delta \tau$, and ΔF , and taking $k = 16$, for the 16 events that occurred during the preconditioning phase, the above derivative equates a very small value of $-5.93 \times 10^{-11} \text{ m}^2/\text{s}^2$ per event. This confirms the small change in the potential destratification with increasing events. Taking k to infinity and noting that $\alpha_d > \alpha_a$ results in the following:

$$\delta SI_\infty = \delta SI_\infty(t = t_k + \Delta t) = \frac{D^2 \delta F}{2 \alpha_d} (e^{-\alpha_d \Delta t} - 1) \left(\frac{1}{1 - e^{(\alpha_a - \alpha_d) \Delta t - \alpha_a \Delta \tau}} \right) \quad (3.8)$$

We have an equation that describes the potential destratification, δSI_∞ , in terms of the Mistral attributes, independent of the number of events. Differentiating by the different attributes (see Sec. 2.5.2.6 for the resulting analytical derivations) and plugging in the mean values where appropriate, we arrive at the resulting values: The derivative w.r.t. the strength of the Mistrals, $\partial \delta SI_\infty / \partial \Delta F$, equals a value of $-1.07 \times 10^7 \text{ m}^2/\text{day}$, the derivative w.r.t. the duration, $\partial \delta SI_\infty / \partial \Delta t$, equals $-7.60 \times 10^{-3} \text{ m}^2/\text{s}^2/\text{day}$, and the derivative w.r.t. the period, $\partial \delta SI_\infty / \partial \Delta \tau$, equals $2.77 \times 10^{-3} \text{ m}^2/\text{s}^2/\text{day}$ (larger periods mean less frequent Mistral events, hence less destratification), respectively. Replacing δSI with δSI_∞ in Eq. 3.6, we can now multiply the partial derivatives with the standard deviations to determine which attribute leads to the most potential destratification. The strength term is equal to $-1.28 \times 10^{-1} \text{ m}^2/\text{s}^2$, the duration term has a value of $-3.21 \times 10^{-2} \text{ m}^2/\text{s}^2$, and the period term has a value of $1.27 \times 10^{-2} \text{ m}^2/\text{s}^2$. With the strength term an order of magnitude larger than the other two terms, according to this simple model, the strength of the Mistral event is the most sensitive attribute when it comes to the effect of the Mistral on destratification, followed by its duration.

3.5.5 Simple Model Results

A complete and average Mistral destratification and restratification event according to Eq. 3.4 is given in Fig. 3.9 (c), which took the average Mistral values from Table 3.1 and 3.5, and the restoring coefficients from Sec. 2.5.2.3. During the event, marked in green, the Mistral causes destratification. After the event, marked in blue, the ocean column restratifies until another event occurs (denoted by the dashed line). This is the same behavior we see in Fig. 3.6.

If we put together Eq. 3.3 with the duration and period information from Table 3.1, and Mistral strength information from Table 3.5, we can create a time series of δSI to compare the integrated response of the simple model to the NEMO model results. This comparison is presented in Fig. 3.12. The simple model results resemble the NEMO simulation results quite well, which is expected as the fitted values for the restoring coefficients and the values for the Mistral event strengths are extracted from the NEMO model results. However, this means that a series of variable pulse like Mistral events can recreate with decent accuracy the patterns that we see in the NEMO results for δSI . This essentially confirms that the Mistral events are the primary driving component of heat loss at the anomaly timescale leading to destratification.

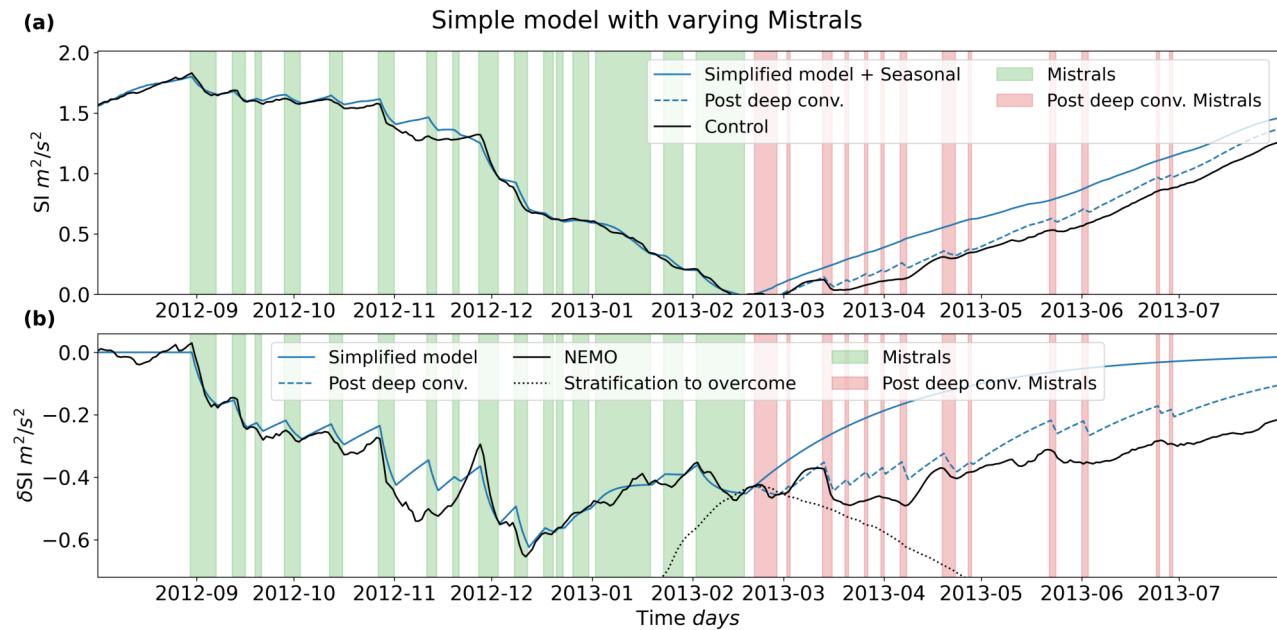


Figure 3.12: The combined effect of Eq. 3.3 for multiple Mistrals with the Mistral data from Table 3.1 and 3.5. (a) shows the calculated $\delta SI + SI_S$ response, while (b) is the calculated simple model δSI versus the NEMO δSI simulation results. Effects from Mistrals after deep convection are included with the dashed blue line and show that Mistrals after deep convection can retard the proceeding restratification during the restratification phase.

3.6 Comparison with Additional Years

To understand the results of the 2013 deep convection year in a more generalized context, two additional years were simulated and analyzed in a similar fashion: the 1994 and 2005 winters (the June 1st, 1993 to May 31st, 1994 year, and the June 1st, 2004 to May 31st, 2005 year, respectively). The 2005 featured a deep convection event [12, 58], whereas the 1994 winter did not [142]. These years were chosen for the sake of having an additional deep convection year and year without deep convection, to see if there are any significant differences for non-deep convection years and other deep convecting years. Simulations for the additional years were run in the same manner as the 2012 to 2013 year and with the same model and configuration. The seasonal run similarly had its atmospheric forcing filtered with the same method as in Sec. 2.2.1, with the control run left unmodified. The only differences between these additional years' simulations and the 2012-2013 year simulations are the initial conditions, restoration data, and start dates of the simulations. For the additional years, the NEMO simulations were initialized with and restored to the MEDRYS reanalysis [57]. This was done as the initial conditions and restoration data for the 2012-2013 simulations were only available for that year. The starting time beginning in June rather than July was an arbitrary decision and is not believed to significantly affect the results or comparisons. ²

3.6.1 Stratification Index

As we are comparing separate years together, the time series simulation results were spatially averaged over a larger area for the additional years: from 42 to 42.5 ° N and 4.25 to 5 ° E. Figure 3.13 and 3.14 show the SI time series for the 1994 and 2005 winters, respectively. The increased spatial averaging reduces the extent at which the SI destratifies, due to surrounding stratified water being averaged in, which makes the 2005 winter appear as though it's too stratified to deep convect ($0.22 \text{ m}^2/\text{s}^2$), even though it's more destratified than the 1994 winter ($0.36 \text{ m}^2/\text{s}^2$). The MLD, however, clarifies that the 2005 winter experiences deep convection in the simulation results and the 1994 winter does not (not shown), which is consistent with other findings [12, 58, 142].

Similar to the 2013 winter simulation set, the seasonal run for the 2005 winter does not experience deep convection, again demonstrating the necessity to include forcing on both timescales for deep convection to occur. The 1994 winter reveals something conversely interesting: the δSI is more negative for the 1994 winter, at $-0.55 \text{ m}^2/\text{s}^2$, than for the 2013 winter at the time of minimum control SI (with deep convection in the latter but not the former), at $-0.43 \text{ m}^2/\text{s}^2$. This means even a larger anomaly driven destratification is not able to overcome the residual stratification in a non convecting year, despite the fact that both the 1994 and 2005 winters each featured a lower maximum control SI than the 2013 winter: $1.83 \text{ m}^2/\text{s}^2$ for the 2013 winter and 1.73 and $1.79 \text{ m}^2/\text{s}^2$ for the 1994 and 2005 winters, respectively. This emphasizes the importance of the destratification caused by the seasonal forcing.

²The simulations for the additional years are from the simulations performed for Chap. 4.

A note of interest for the 2005 and 2013 winters is the occurrence of the δSI minimum. In the 2013 winter, the minimum occurs significantly before deep convection, in December. For the 2005 winter, the minimum occurs roughly about the time of deep convection (around the beginning of March; seen more clearly in the MLD; not shown), and also during a Mistral event, much like the 2013 winter. However, unlike the 2013 winter, the seasonal destratification is less active at the time of deep convection, whereas the anomaly destratification drops almost $-0.62 m^2/s^2$, most of it occurring during a larger Mistral event, to start deep convection. This suggests that the Mistral event occurring during this time triggers the deep convection event. While deep convection does not occur in the 1994 winter, the δSI minimum is also at about the same time as the minimum in the control SI , with a small Mistral event occurring at that date and with seasonal destratification remaining roughly constant. This suggests that if this year had further seasonal destratification or less initial destratification, the Mistral may have been the main trigger to deep convect as well, along with the larger Mistral event preceding it.

A note of interest for all three winters is the location of the seasonal SI minimum and the time of deep convection (or minimum of control SI for 1994). For the 2013 winter, the minimum is at roughly the time of deep convection, but is almost a month after in the 2005 winter. And for the 1994 winter, the minimum occurs before the control minimum. This brings to question if the location of the seasonal SI minimum relative to the control SI minimum is important, and if so, how important is it in terms of deep convection occurring versus not.

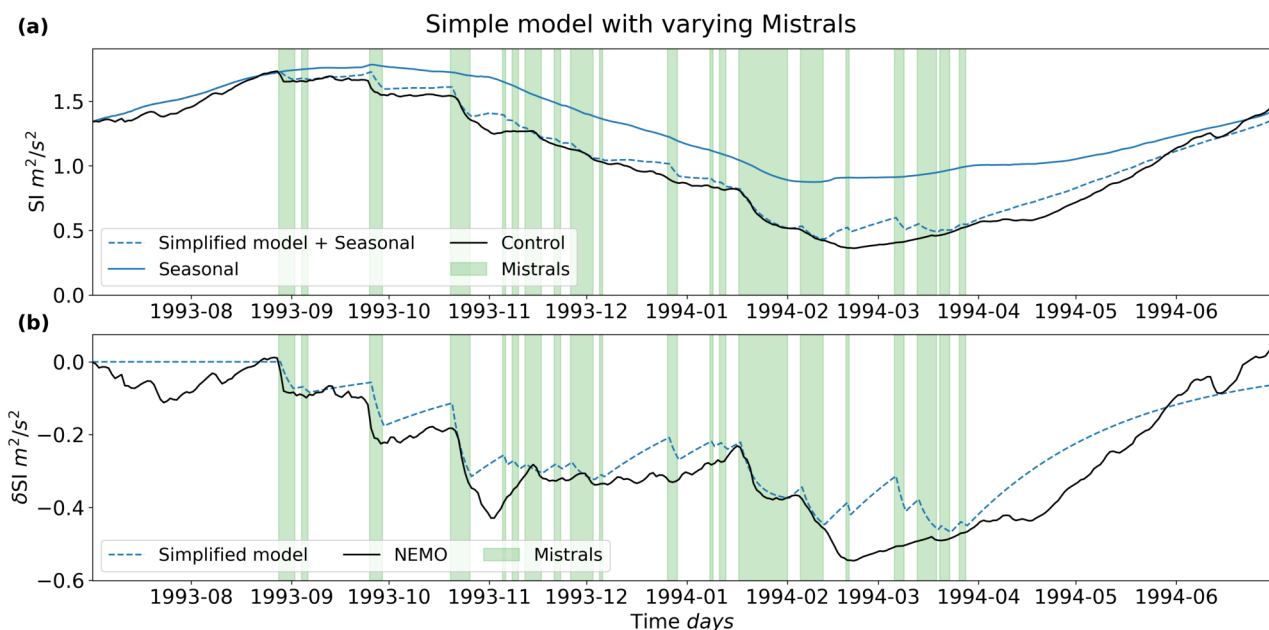


Figure 3.13: The stratification index for the 1994 winter for both the control and seasonal runs are in subplot (a), spatially averaged over the area of 42 to 42.5° N and 4.25 to 5° E. The simplified model anomaly solution added to the seasonal SI is denoted by the dashed line. Subplot (b) shows the NEMO determined δSI and the δSI calculated from the anomaly solution of the simple model.

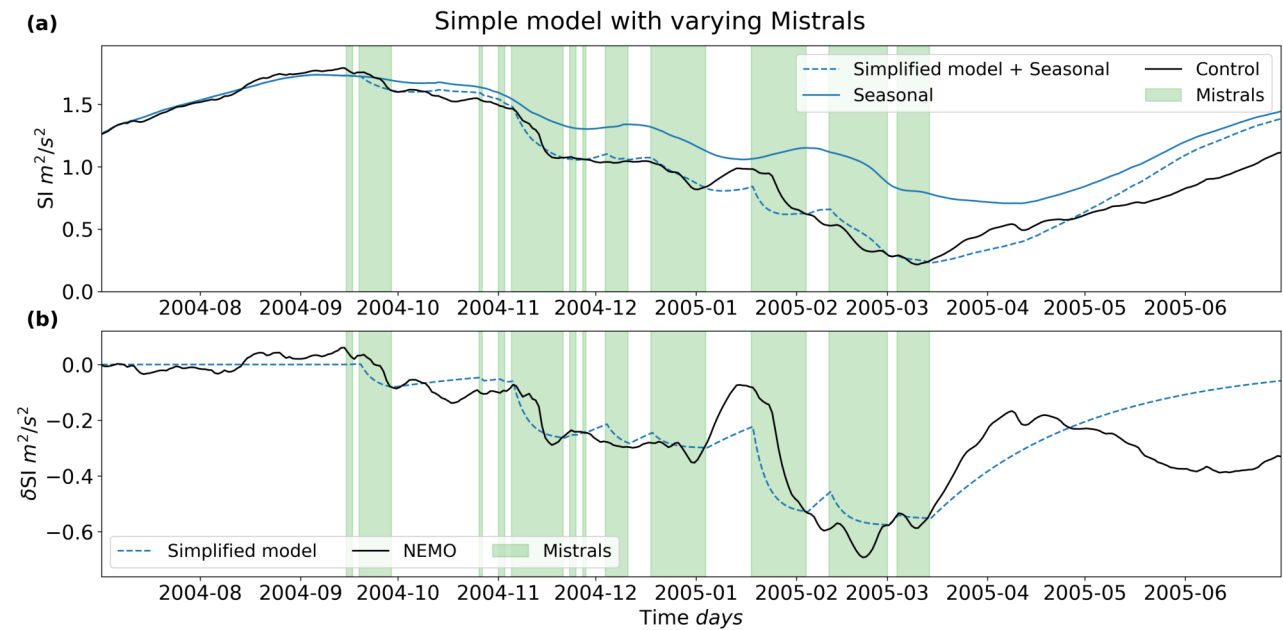


Figure 3.14: Same as Fig. 3.13 for the 2005 winter.

3.6.2 Seasonal Forcing

The seasonal sea surface fluxes for both years resemble the fluxes of the 2013 winter (see Fig. 3.15). The solar radiation component drives the main shape of the SI time series, with the major component contributing to the asymmetry being the latent heat flux, followed by the sensible heat flux. However, in the 2005 winter, the latent heat flux has a larger heat loss value than the 1994 year, reaching over 300 W/m^2 versus under 200 W/m^2 in the latter, driving the net heat flux more negative and causing more destratification according to the simple model, resulting in deep convection encompassing a few days on either side of the beginning of March.

The simple model for the seasonal SI is fairly accurate for the 1994 winter, similar to the 2013 winter, but is not quite as accurate for the 2005 winter (see Fig. 3.15). For the 2005 winter, the simple model deviates during the deepest part of the winter. This could be due to more advective behavior captured by the destratification with the larger spatial averaging, which is neglected in the seasonal component of the simple model.

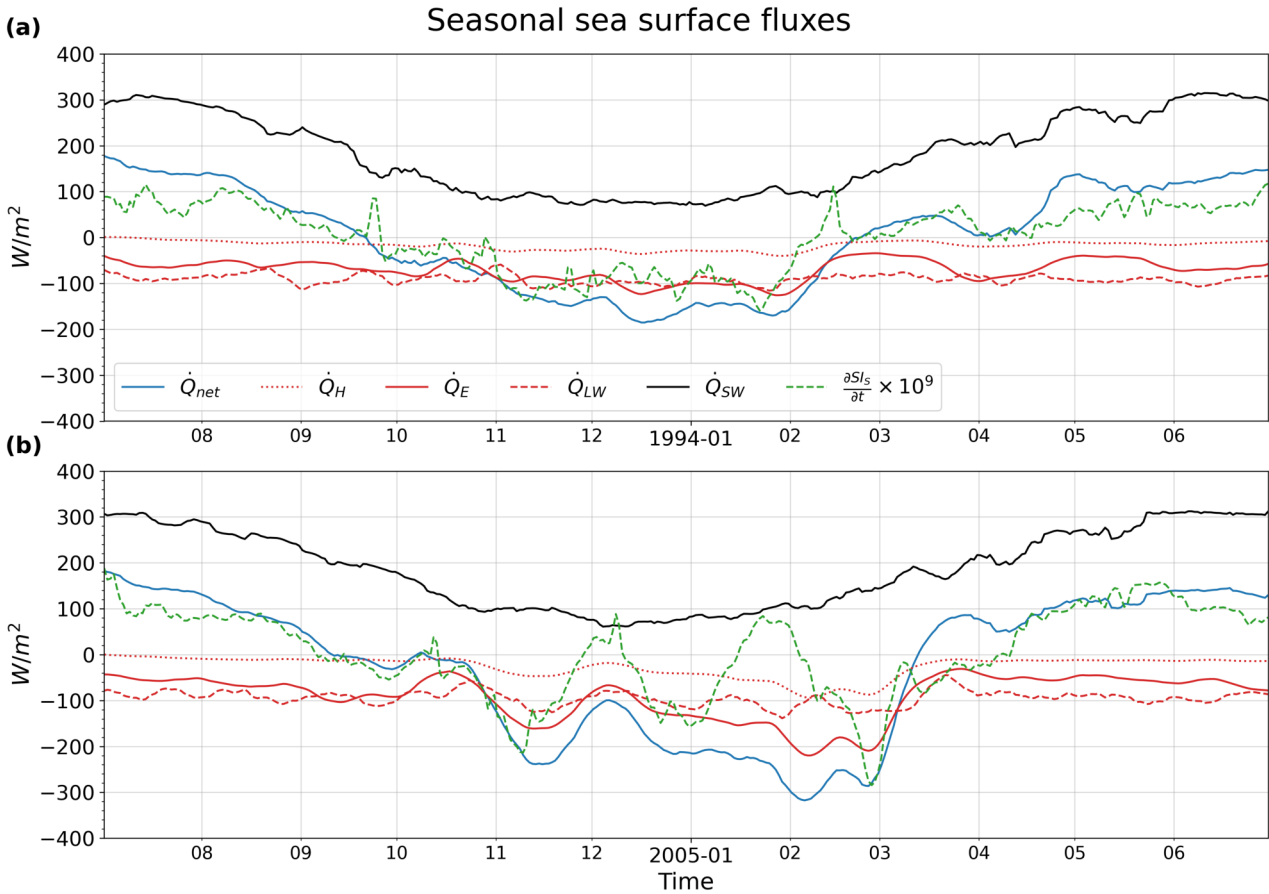


Figure 3.15: The smoothed seasonal sea surface fluxes spatially averaged over the 42 to 42.5 ° N and 4.25 to 5 ° E area, with the green dashed line denoting the estimated derivative w.r.t. time of the seasonal *SI* from the NEMO results, multiplied by $10^9 \text{ m}^4/\text{Js}^2$. A negative value means heat is leaving the ocean.

3.6.3 Anomaly Forcing

The simple model for the anomaly scale was calculated for both the 1994 and 2005 winters, following the same steps in Sec. 3.5.2. The value of the restoration coefficients, α_d and α_a , were carried over from the 2013 winter analysis, with the Mistral dates determined through the same process outlined in Sec. 3.2 and were manually adjusted to fit visual data (again with the same method described in Sec. 3.2). The Mistral strengths of the events during the preconditioning phase were determined through the same process as in Sec. 3.5.2. The Mistral dates and strengths are presented in Sec. 3.6. The results are shown in Fig. 3.13 and 3.14, and the simple model follows quite closely to the NEMO simulation results, only deviating majorly at extreme peaks and troughs, despite utilizing the restoration coefficients from the 2013 winter. This reinforces the importance of the Mistral as a dominating factor for destratification on the anomaly timescale.

The different components of Mistral (strength, δF , duration, Δt , and period, $\Delta \tau$) are separated in the same manner as for the 2013 winter, to determine the main factor of the Mistral leading to destratification, according to these additional years. For the 1994 winter, the contribution due to strength, duration, and period equal: -8.71×10^{-2} , -6.39×10^{-2} , and $5.83 \times 10^{-2} \text{ m}^2/\text{s}^2$ (recall

that a larger period means less frequent Mistral events). For the 2005 winter, the contribution due to strength, duration, and period equal: -1.51×10^{-1} , -5.23×10^{-2} , and $4.89 \times 10^{-2} \text{ m}^2/\text{s}^2$. The 2005 winter results have the same order of magnitude as the 2013 winter results, with all three winters having the same order of importance for the Mistral attributes: first strength, then duration, followed by the length of the period. Only for the 1994 winter was the strength term found not to be as dominant as in the other years, with the term having the same order of magnitude as the other terms. However, as the order of importance was still the same for all three years, this aids the conclusion that, in general, the strength term of the Mistral is its most important factor driving destratification.

3.7 Discussion

The 2012-2013 deep convection year (2013 winter) in the Gulf of Lion was investigated to determine the effect the Mistral winds have on deep convection. Two NEMO ocean simulations were run, one forced with unmodified WRF/ORCHIDEE atmospheric forcing (control) and one forced with atmospheric fields filtered to remove the Mistral signature (seasonal). Separating the atmospheric forcing into the long-term and anomaly timescales revealed that the Mistral winds do not act alone to destabilize the northwestern Mediterranean Sea. Both the seasonal atmospheric change, reflected in the long-term timescales, and the Mistral winds, reflected in the anomaly timescales, combine to destabilize and destratify the water columns in the GOL in roughly equal amounts (favoring the seasonal change).

When the NEMO simulation results were probed further by developing a simple model, the simple model conveyed the underlying drivers of the long-term, or seasonal timescale. The evolution of the seasonal stratification index is proportional to the net heat flux leaving the ocean. As the net heat flux follows the shape of the incoming solar radiation, the maximum and minimum values for the seasonal stratification index occur around Sept. 21st and March 21st, respectively, or the fall and spring equinoxes. Shifted negative by the latent, sensible, and longwave radiation heat fluxes, the net heat flux allows for a seasonal cycle of destratification during the winter and restratification during the summer. If any of the three negative shifting components are unable to cool the ocean surface enough, deep convection may fail to appear, unless the contribution of the Mistral winds is able to compensate.

The simple model results go on to confirm the hypothesis that the Mistral acts on the anomaly timescale to destratify the water column, and is the primary driver in this timescale. These results further conveyed that additional Mistral events need to be stronger in terms of heat transfer than previous events to create further destratification. Otherwise, no destratification, or even restratification, occurs. The simple model then goes on to reveal, after some additional derivation, that the most important part of a Mistral event is its strength, regarding potential destratification. Changing the duration or frequency has an effect, but this effect is on a order of magnitude smaller than changing the Mistral strength.

Two additional years were also studied with the same method of running a control simulation and a filtered atmospheric forcing seasonal simulation: the year of 1993-1994 (1994 winter) and the year of 2004-2005 (2005 winter). These years were then also studied with the simple model framework. The 2005 winter featured a deep convection event like the 2013 winter, but the 1994 winter did not, allowing for the comparison between deep convecting and non-deep convecting years. The conclusions determined in the 2013 winter are largely supported by the results of the two additional years. The seasonal change in SI accounts for a larger part of the destratification, while the 2005 winter still required destratification from the anomaly scale to deep convect. The solar radiation component of the seasonal forcing was also found to be the component giving the cyclical structure to the stratification index, with the latent and sensible heat fluxes creating the asymmetry. On the anomaly scale forcing, the Mistral strength was again found to be the dominating component leading to destratification, although its magnitude is slightly less pronounced in the 1994 winter.

However, some of the NEMO simulation results bring further questions. Sec. 3.4 noted that the seasonal change in stratification brought the preconditioned water column in the GOL to the point of deep convection simultaneously with a Mistral event, for the winter of 2012-2013, as the Mistral induced preconditioning had already passed its minimum destratification beforehand, with both the seasonal change and a Mistral event acting to destratify at the moment of deep convection. In the 2005 winter, the maximum seasonal destratification had not yet occurred during the time of deep convection, but the Mistral induced destratification brought the stratification down to point of deep convection, triggering it with a Mistral event. Despite deep convection not occurring, a similar structure appears in the SI and δSI for the winter of 1994. Additionally, the date of the seasonal SI minimum was different relative to the date of deep convection (control SI minimum for the 1994 winter), for all three winters.

This brings up two questions. The first is whether the Mistral truly triggers deep convection for all deep convection events, or if the change in the seasonal destratification at the time of deep convection is a more prominent factor. The second is, what is the importance of the location of the seasonal SI minimum and does it make a difference in regard to the possibility of deep convection. Is it possible for the Mistral induced destratification to cause deep convection after the minimum has passed, despite being hindered by the restratifying seasonal SI .

Another question brought around by the simulation results is what is the effect of the maximal stratification at the beginning of the preconditioning phase on the ocean's ability to experience deep convection for a given year? The maximal stratification must be overcome by the Mistral and seasonal forcing for deep convection to occur, with the ability of the forcing to do so varying per year. For our results, the 2013 winter had a larger maximum control SI than the other two winters investigated and still deep convected. Similarly, the 2005 winter had a larger maximum stratification than the winter of 1994: 1.79 vs. $1.73 \text{ m}^2/\text{s}^2$. However, all three winters had a maximal stratification within $0.1 \text{ m}^2/\text{s}^2$ of each other, which is only about 6% of the maximum.

For example, for the 2004-2005 winter the atmospheric forcing was more than enough to overcome the initial stratification and a milder winter would have lead to deep convection as well, according to other works [51]. [142] investigated initial stratification and over a longer time period

than [51] (1995-2005 vs. 1980-2013), however they calculated the stratification index at the beginning of December rather than at the beginning of September, where the maximum stratification of $1.83 \text{ m}^2/\text{s}^2$ occurs for the 2012-2013 winter. By December, the SI already dropped to $1 \text{ m}^2/\text{s}^2$, which means almost half of the destratification has already occurred, with their calculation missing about half of the preconditioning phase. The same is true when looking at the 1994 and 2005 winters. A maximum SI calculated near the beginning of September may be more representative of the water columns ability to deep convect and needs to be investigated. A related question is how does the accumulation (or reduction) of stratification transferred to the proceeding year affect deep convection in the following years? For the winter of 2005, where very few of the preceding 15 years deep convected due to milder winters, the result was warmer and saltier WDMW production [58].

These questions are outside the scope of the current article, as they rely on investigating multiple years to evaluate the inter-annual variability of the atmospheric forcing. The 2013 winter featured an above average year in terms of destratification, leading to deep convection, while multiple years in the 1990s saw minimal MLD growth (including the 1994 winter; [142] and references therein). This may have been due to an above average number of Mistral (stormy) days, as suggested by [142], which coincides with our results of 36%, 61%, and 54% of the preconditioning days having a Mistral event for the winters of 1994, 2005, and 2013, respectively. But it may have also been due to a larger than average contribution from the seasonal forcing, as the seasonal SI saw more destratification than the anomaly stratification index, δSI , which isn't clearly discernible with just three winters.

We believe the approach of separating the atmospheric forcing into the seasonal and anomaly components will reveal more answers to these questions over larger set of multiple years, and we are preparing additional works to address them. We hope these works will provide us with more information on how the Gulf of Lion deep convection system will evolve in the future.

Chapter 4

Variability of Seasonal Atmospheric Drivers affecting Deep Convection

Contents

4.1 Introduction	65
4.2 Model Validation	67
4.3 Results and Discussion	70
4.3.1 Seasonal Contribution	70
4.3.2 Prior Questions	77
4.4 Conclusions	80

This second study focuses on the climatic behavior of deep convection in the Gulf of Lion, particularly on the impact of the seasonal atmospheric change. The methodology behind the study is essentially the same as the first study (Chap. 3), where two sets of simulations were run to extract the effect of the Mistral: a control set and a seasonal set. However, for this study 20 years were simulated in this fashion, from July 1st, 1993 to June 30th, 2013. This allowed us to determine if there are any major trends or if the contribution of the Mistral to deep convection holds the same weight as it does in the first study. Seven years featured deep convection from 1993 to 2013 in our results: 1999, 2000, 2005, 2009, 2011, 2012, and 2013. The results for this study include:

1. model validation against observations (CTD and Argo; Sec. 4.2)
2. the relative contributions of the Mistral and seasonal atmospheric change to destratification (Sec. 4.3.1)
3. the main seasonal atmospheric drivers of destratification (Sec. 4.3.1.1)
4. answering questions left unanswered by the first study (Chap. 3; Sec. 4.3.2):

- Does the Mistral trigger deep convection, or does the seasonal change trigger it?
- Does the maximum SI_S play a role in deep convection?
- Does the timing of the SI_S minimum matter and can the Mistral contribution overcome a restratifying SI_S ?
- Does the previous year's level of stratification affect the proceeding year?

Finally, the closing remarks are presented in Sec. 4.4. ¹

4.1 Introduction

Deep convection, or open-ocean convection, occurs in the higher latitude regions of the world and is an important ocean circulation process [97]. It is formed when the stable density gradient along the ocean column is eroded by surface buoyancy loss, leading to an overturning that can span the entire depth of the column. In the western basin of the Mediterranean Sea (Med. Sea), this process can occur in the Gulf of Lion (GOL) and assists in the thermohaline circulation of the sea [118] by forming the Western Mediterranean Deep Water (WMDW). When it does occur, the WMDW produced spreads out along the bottom of the northwest basin [104]. Some is transported along the northern boundary current towards the Balearic Islands [130], and some of it completes the general circulation by flowing down towards the Algerian Basin and the Strait of Gibraltar [12, 150]. In the GOL, deep convection also plays an important role in the marine biology of the region, as the springs following deep convection events also experience increased phytoplankton blooming [132], due to the increased levels of nutrients and oxygenation from the mixing process [22, 132].

Significant deep convection events occur every few years in the GOL [13, 142, 62, 97, 105], driven by the Mistral and Tramontane winds. These sister, northerly flows bring cool, continental air through the Rhône Valley (Mistral) and the Aude Valley (Tramontane), leading to large heat transfer events with the warmer ocean surface [31, 43]. These large cooling, evaporative events destabilize the water column in the GOL, and are a primary source of buoyancy loss leading to deep convection [82, 62, 87, 81, 58, 79, 110, 97, 105, 92, 125, 91, 90, 47]. The other main source of buoyancy loss in the region is the seasonal atmospheric change and reduction of solar heating during the winter [70].

The annual stratification cycle of the GOL regulates the occurrence of deep convection events. It consists of a destratification phase and restratification phase that is roughly sinusoidal in appearance. These two phases form due to the net heat flux into the ocean surface changing sign roughly at the spring and fall equinoxes: positive between March and September and negative between September and March. When the net heat flux is positive, the ocean column is being heated, increasing its stability, hence an increase in stratification from March to September. When the heat net heat

¹This chapter is adapted from a paper in review in JGR: Oceans: Keller et al. "Untangling the Mistral and Seasonal Atmospheric Forcing Driving Deep Convection in the Gulf of Lion: 1993-2013". The preprint is available on ESSOAr (<https://doi.org/10.1002/essoar.10512293.1>)

flux is negative, the ocean column is being cooled, reducing its stability, thereby decreasing its stratification from September and March. The net heat flux gains its shape from its four main components: solar heating, infrared cooling, the sensible heat flux, and the latent heat flux. The solar heating gives the net heat flux its sinusoidal shape. The infrared cooling, sensible heat flux, and latent heat flux shift this sinusoidal shape negative, causing it to flip sign at the spring and fall equinoxes. The asymmetries in the net heat flux come from the sensible and latent heat fluxes, causing the sinusoidal shape to be distorted slightly in the winter [70].

If the cooling from the sensible and latent heat fluxes is large enough (the infrared cooling tends to remain constant as it depends on the sea surface temperature), then a third phase appears: the deep convection phase. This occurs when the sensible and latent heat fluxes reduce the stratification to point it can overturn. These three phases then form the canonical deep convection cycle [104, 53], where the destratification phase is typically referred to as the preconditioning phase. For this study, we are focusing on the destratification/preconditioning and deep convection phases, as they drive the variability of this cycle in the GOL.

In Chap. 3, we determined the importance of the seasonal atmospheric change regarding its impact on the destratification phase and discovered it was a more significant source of destratification than the Mistral/Tramontane winds (referred to as just the Mistral), providing roughly 2/3 of the destratification for the 2012 to 2013 winter. The current study continues this investigation and looks into the variability of the contribution to destratification for each component, the seasonal and the Mistral, over multiple years. 20 years of the Med. Sea, from July 1st, 1993 to June 30th, 2013, were simulated using the NEMO ocean model. NEMO was driven by two sets of WRF/ORCHIDEE atmospheric data: a control set and a filtered (seasonal) set. This resulted in two sets of the simulated ocean data: one set including the effects of the Mistral and the seasonal effects, and the other set just including the seasonal effects, allowing us to separate the effects due to the Mistral.

In particular, our findings determine:

- the variability of both the seasonal and Mistral based contributions to destratification,
- and the primary components, and their drivers, of the seasonal contribution leading to deep convection.

Our findings also address questions posed at the end of Chap. 3 that were outside the scope of that study. These questions can be summarized as the following:

1. Does the Mistral trigger deep convection, or does the seasonal change trigger it?
2. Does the maximum SI_S play a role in deep convection?
3. Does the timing of the SI_S minimum matter and can the Mistral contribution overcome a restratifying SI_S ?
4. Does the previous year's stratification affect the proceeding year?

	Start	End	Above 500 <i>m</i>	Below 500 <i>m</i>	Total
Argo	2005-01-01 08:10	2011-12-30 23:56	1948	1493	1949
CTD	1993-07-05 07:43	2013-06-29 13:02	978	236	980
Total	—	—	2926	1729	2929

Table 4.1: Number of and start and end dates for the Argo and CTD profiles from the Coriolis database for the July 1st, 1993, to June 30th, 2013. The number of profiles used for the spatial distribution of bias in the layers above and below 500 *m* in depth are shown in their respective columns.

4.2 Model Validation

To validate the control set of the ocean simulations, Argo and CTD vertical profile observations from the period of July 1st, 1993 to June 30th, 2013 were collected from the Coriolis database (<https://www.coriolis.eu.org/Data-Products/Data-selection>; last accessed: Aug. 23rd, 2022). These vertical profiles were compared to the model vertical profiles to determine and verify the accuracy of the model. The model outputs salinity in terms of practical salinity, in units of *PSU*, which is the same as the observational data. However, for temperature, the model outputs potential temperature, whereas the observed temperature is provided in terms of in situ temperature measurements. To make a direct comparison, the observational temperature data was converted to potential temperature with the **GSW-Python** python package [42], which uses the TEOS-10 ocean equation of state for the conversion (<https://www.teos-10.org/index.htm>; last accessed Aug. 23rd, 2022).

2929 temperature and salinity in situ profiles were taken from the Coriolis database to validate the control set of the ocean simulations. 1949 profiles were from Argo profiling and 980 were from CTD profiling (breakdown in Table 4.1). Each profile of calculated potential temperature and salinity was then compared to the model profile from the nearest grid point in the NEMOMED12 grid and nearest time stamp (daily temporal resolution for the ocean simulation data; the model data was interpolated vertically to match the levels of the observations). The bias (model minus observation) and root mean squared error (RMSE) were calculated from the comparisons.

To look at the vertical distribution of bias and RMSE, the observations and nearest model data were vertically binned (55 bins) according to depth. The bias was then calculated per observation/model result pair. The mean and standard deviation of the bias per each bin are plotted in Fig. 4.1 (a) and (b), for potential temperature and salinity, respectively. For each bin, the RMSE was computed, and is shown in Fig. 4.1 (c) and (d), for potential temperature and salinity, respectively.

As seen in Fig. 4.1, most of the differences between the model and observations lie within the first 500 *m* of the ocean column. The largest differences and variability in the bias are found at the surface, with a mean bias and RMSE of +0.40 °C and 1.18 °C, for potential temperature, and -0.04 *PSU* and 0.01 *PSU*, for salinity. Below 500 *m*, the bias and RMSE are much smaller, with the mean bias and RMSE averaging at -0.006 °C and 0.081 °C, for potential temperature, and +0.004 *PSU* and 0.021 *PSU*, for salinity. The larger differences in the upper 500 *m* can be explained by the diurnal cycle that isn't captured in the daily temporal resolution of the model data. The sea

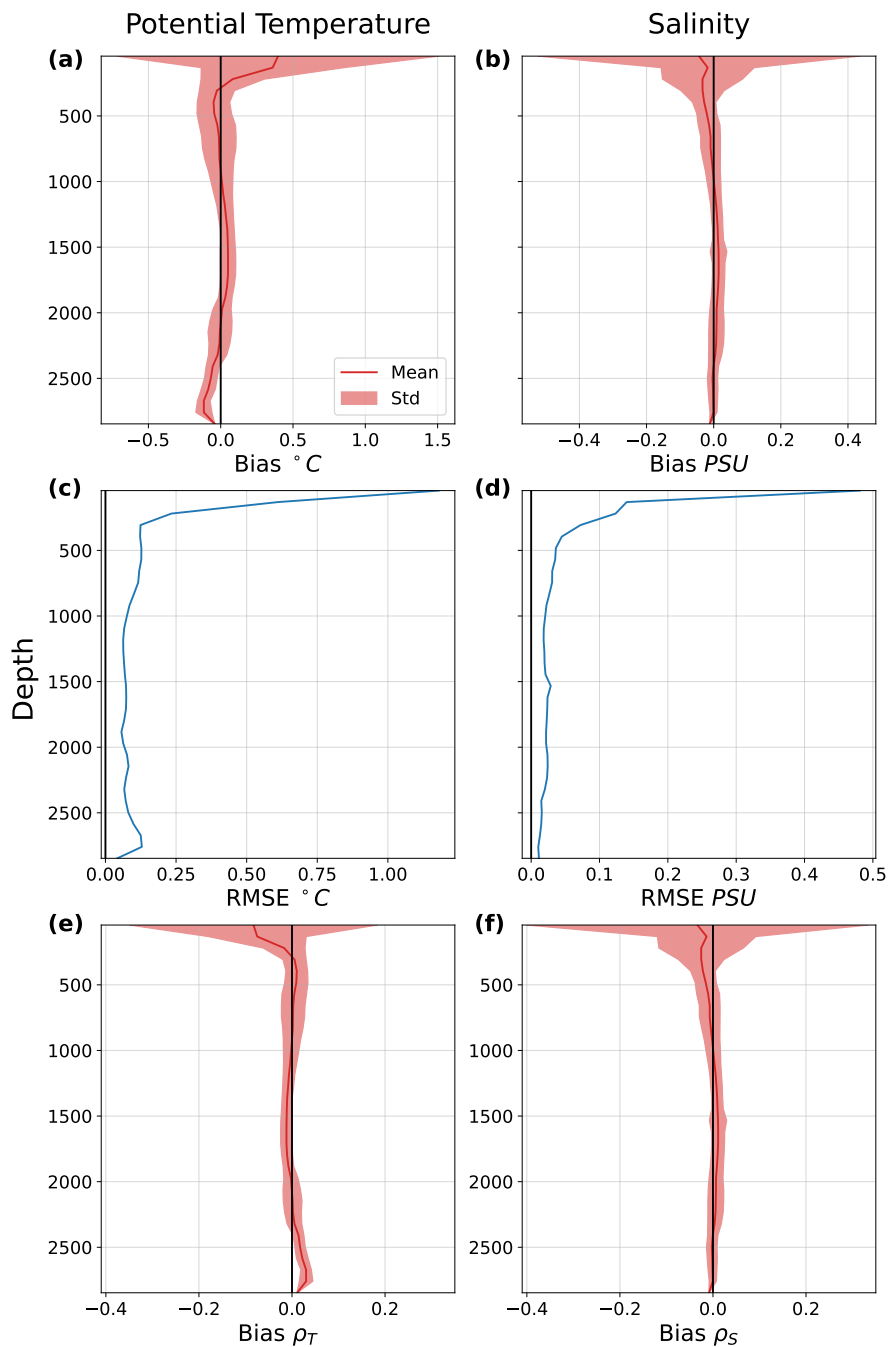


Figure 4.1: Vertical distribution of bias (model minus observation) and RMSE from the comparison of our control set model results and combined Argo/CTD observations. (a) and (b) show the mean and standard deviation of the bias for potential temperature and salinity, respectively. The mean is the solid red line, with the shading representing the area encompassed by ± 1 standard deviation. (c) and (d) show the RMSE for potential temperature and salinity, respectively.

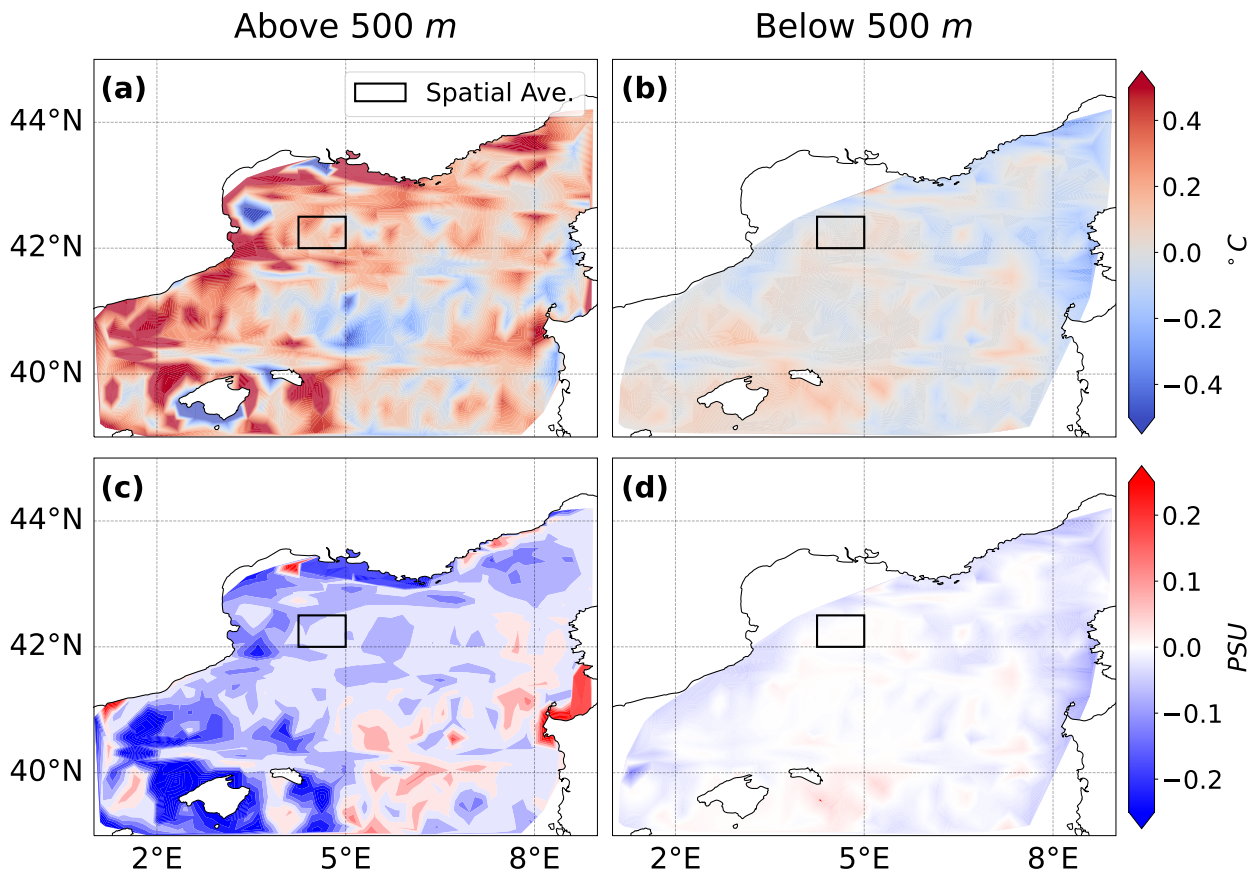


Figure 4.2: Spatial distribution of the bias from the comparison of our control set model results and combined Argo/CTD observations. (a) and (b) show the bias in the potential temperature for the layers above and below 500 *m*, respectively. (c) and (d) show the same for salinity. The black box from 42 to 42.5 °N and from 4.25 to 5 °E bounds the spatial averaging performed in Sec. 4.3.

surface layer destratifies and restratifies with the diurnal cycle [81, 80], whereas the lower layers are less effected, hence showing less error between the observations and model output. With that caveat noted, the model is fairly representative of the vertical column in the GOL, with slightly warmer and fresher surface waters relative to observations and fairly accurate temperature and salinity for the deeper waters.

To see if there is any notable features in the spatial distribution of bias, the averaged bias of the water above and below 500 *m* are plotted in Fig. 4.2, with subplots (a) and (c) for above 500 *m* and (b) and (d) for below, for potential temperature and salinity, respectively. The area bounded by the black box in Fig. 4.2 is from 42 to 42.5 °N and from 4.25 to 5 °E. The vertical column of water within this bounding box is spatially averaged to study the temporal trends in Sec. 4.3, and is therefore a relevant area to investigate for major biases. Within this box, the bias follows the trends found in Fig. 4.1: fresher and warmer water at the surface and fairly accurate at the lower layers. As we look at the whole vertical column for our study, we therefore believe the model results to be representative enough for our purpose of studying deep convection over multiple years.

4.3 Results and Discussion

4.3.1 Seasonal Contribution

The center of the minimum point of stratification in the GOL varies from year to year. To compare the destratification from different years to each other, an area encompassing the minimum point over the 20 years was averaged: a box with the limits of 42 to 42.5 ° N and 4.25 to 5 ° E (shown in Fig. 4.2). Seven years featured deep convection events in the model results of the control set: 1999, 2000, 2005, 2009, 2011, 2012, and 2013, shown by the significantly deep mixed layer depths (MLD) (in Fig. 4.3; the years are highlighted with green text). This is in agreement with Somot et al. 2016 but in disagreement with observations shown in Bosse et al. 2021 and Houpert et al. 2016. Observations showed deep convection also occurred in 2010, but, as seen in Fig. 4.4 and Fig. 4.6, our results show similar levels of stratification for 2010 as the adjacent years, therefore capturing some of the behavior despite deep convection not occurring in the model. Our years of deep convection had the lowest stratification levels during convection, according to the stratification index (Fig. 4.4), as expected (for the rest of the article, deep-convection years will refer to the deep-convection years found in the model results). Ideally, the stratification would be zero to denote a deep convection event. However, due to the area-averaging, some still stratified columns are captured, resulting in some remaining stratification at the SI minimum for years with deep convection. This is particularly apparent for the year of 2009, a deep-convection year, that has some remaining stratification larger than the following years, due to 2009 having a deep-convection zone with a relatively small horizontal extent (not shown).

The lack of deep convection in the seasonal set of simulations is immediately noticeable; the MLD for the seasonal runs never reached deeper than 173 m (Fig. 4.3), regardless of the year. This confirms that the Mistral component is necessary for deep convection, as found for the winter of 2013 in Chap. 3. However, there is a large variability of SI_S . For example, for the winter of 2000 (referring to the winter spanning 1999 to 2000), the seasonal stratification closely follows the total stratification, whereas the next winter, the winter of 2001, the seasonal stratification diverges quite strongly in Feb. 2001 and remains diverged until June 2001 (Fig. 4.4). To compare the variability between the different years, the seasonal and Mistral contributions, $SI_{S,Cont}$ and δSI_{Cont} , respectively, are determined according to Fig. 4.5. The contributions are determined at the time when the total stratification reaches a minimum, $t_{SI_{min}}$, as this is where deep convection occurs in the years that feature an event. This allows us to separate the contribution to destratification at each timescale:

$$SI_{S,Cont} = SI_{S,max} - SI_S(t = t_{SI_{min}}) \quad (4.1)$$

$$\delta SI_{Cont} = SI_S(t = t_{SI_{min}}) - SI_{min} \quad (4.2)$$

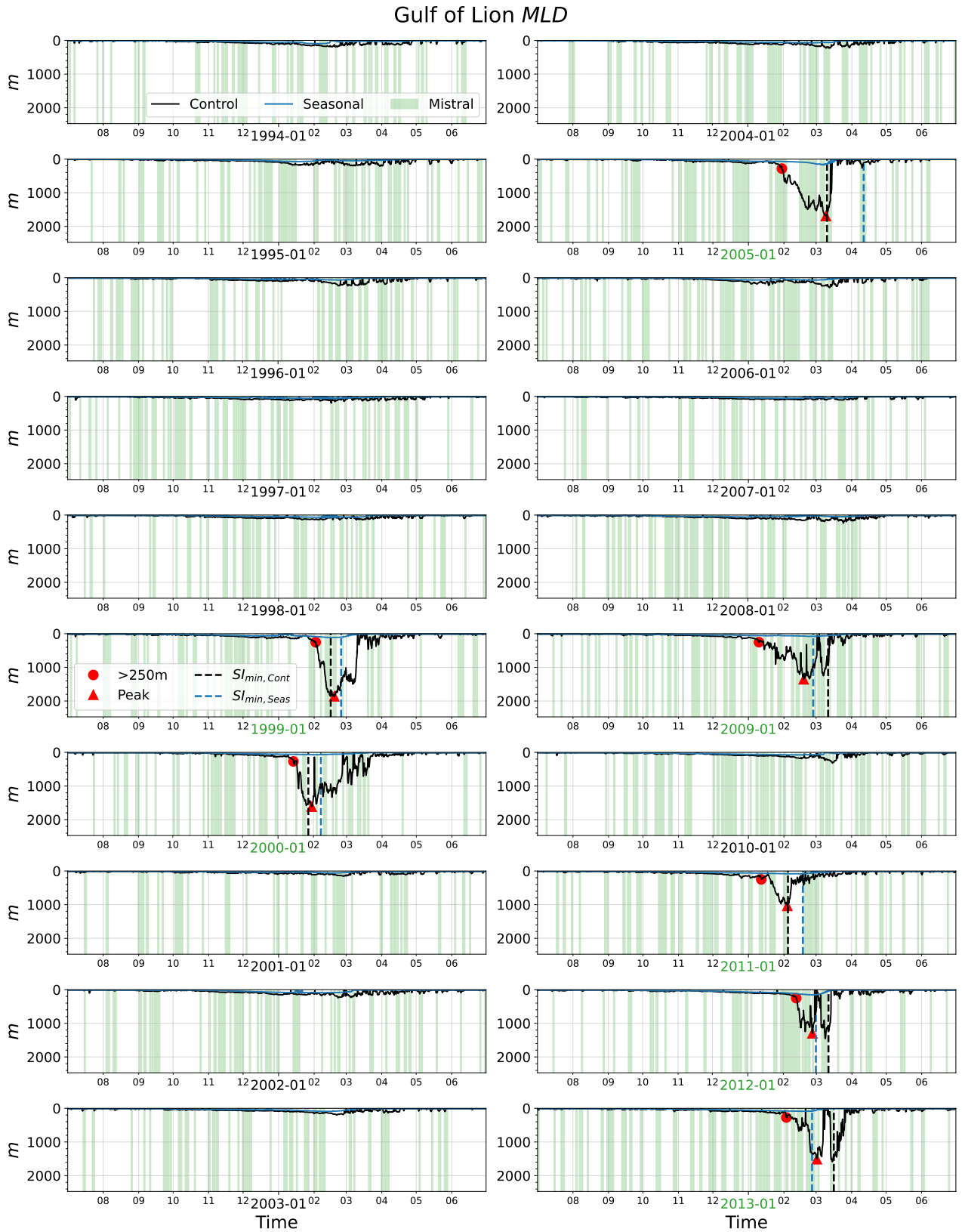


Figure 4.3: Mixed layer depth of the averaged area in Fig. 4.2 for the 20 years, calculated by the point in the column with a vertical diffusivity less than $5 \times 10^{-4} \text{ m}^2/\text{s}$. The red circle labels the first point at which the MLD is deeper than 250m and the red triangle marks the first main maximum depth for the deep-convection years. Mistral events are shown with the colored green shading.

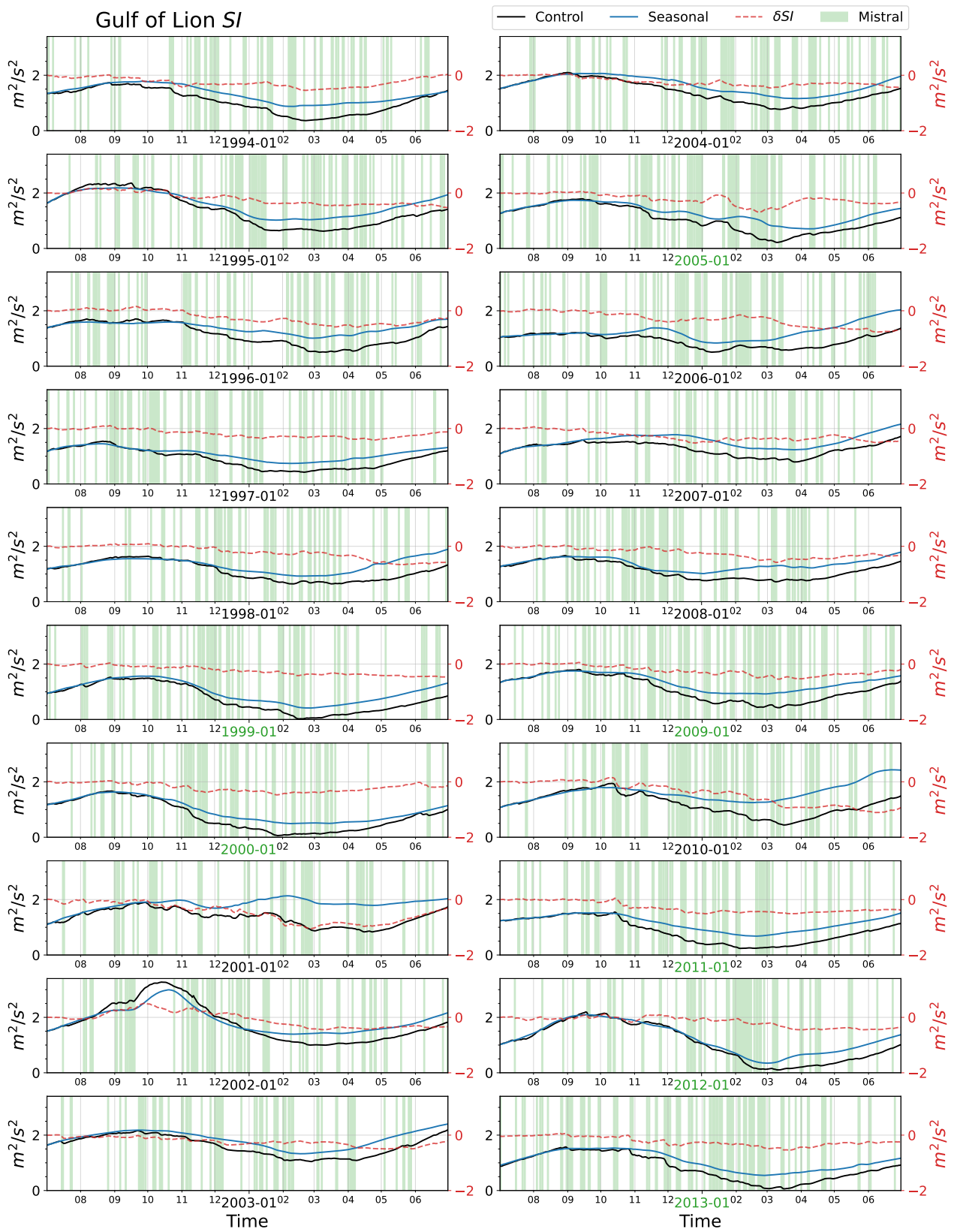


Figure 4.4: The stratification index of the area averaged in Fig. 4.2 for the 20 years, with the control run, $SI_S + \delta SI$, in black and the seasonal run, SI_S , in blue. The difference between the control and seasonal stratification index, δSI , is shown with a dashed red line with a separate scale. Mistral events are shown with the colored green shading.

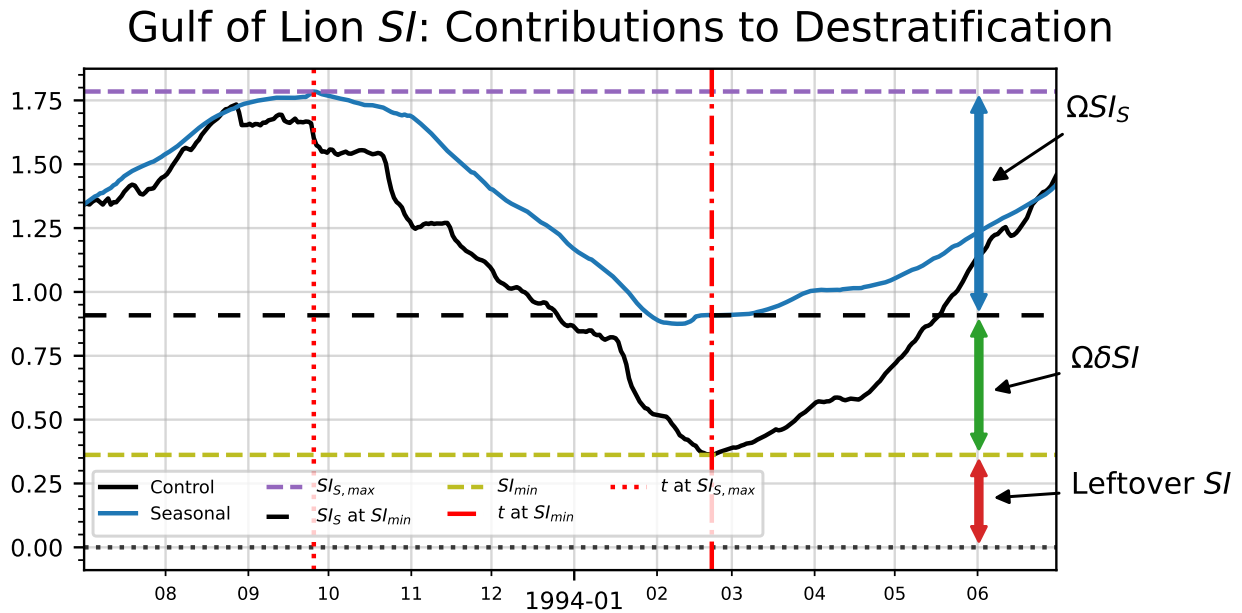


Figure 4.5: The stratification index for the winter of 1994 to demonstrate how the contributions from the different timescales are calculated.

The maximum SI_S is used as the reference point for the maximum stratification, at $t_{SI_{S,max}}$, as the seasonal stratification maximum is the overall stratification that both the Mistral and seasonal atmospheric change must overcome to cause deep convection. Consequently, the time $t_{SI_{S,max}}$ is taken to be the time the preconditioning phase begins, and the time $t_{SI_{min}}$ where it ends.

The varying levels of contributions and maximum levels of seasonal stratification, $SI_{S,max}$, are displayed in Fig. 4.6. We can see in Fig. 4.6 (a) that the years with deep convection have maximum seasonal stratification levels that are below average for the 20-year period (deep-convection (DC) years are denoted by the hatching). If we look at the separated contributions in subplots (b) and (c) of the same figure, the years with deep convection typically feature higher than average levels of destratification coming from the seasonal contribution, with most of the destratification in 2012 coming from the seasonal timescale. For the Mistral timescale contributions, years with deep convection also saw above average levels, except for the year of 2012. A keynote of interest is the average levels of contribution from the two timescales. On average, the seasonal timescale provides 45.7% of the annual destratification, with the Mistral timescale providing only 28.0% of the annual destratification. This agrees with the results of Chap. 3. Taken a step further, the mean values for the different normalized timescale contributions separated by DC and non-deep-convection (NDC) years are provided in Table 4.2. Corroborating the observations made above in Fig. 4.6, DC seasonal contributions exceeded the overall average: 0.618 versus 0.457. The distinction between DC Mistral contributions and the overall average is less clear however: 0.287 versus 0.280, as the contribution for the year of 2012 reduces the mean significantly for DC years.

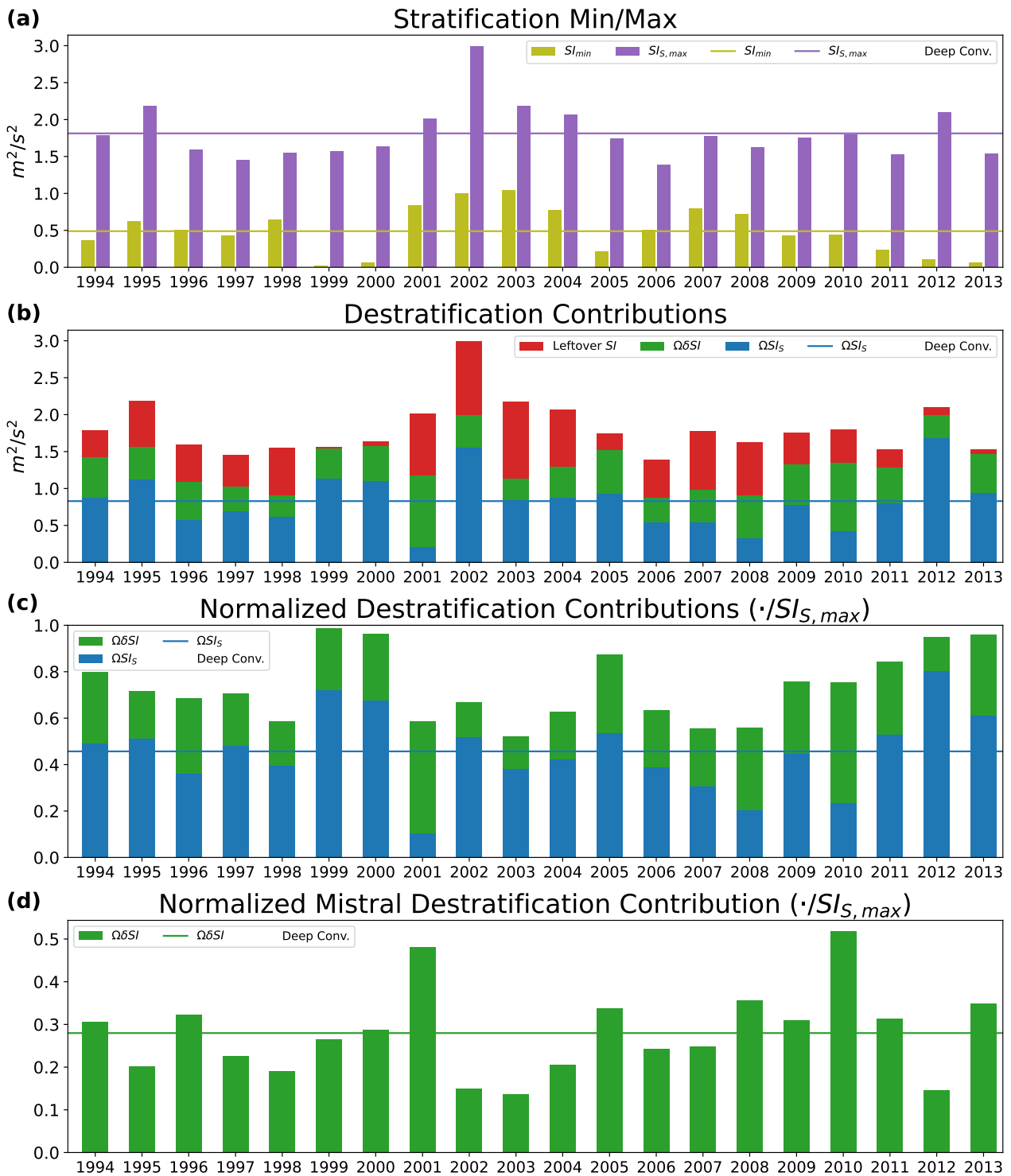


Figure 4.6: The seasonal maximum stratification and minimum control stratification is shown in subplot (a). The seasonal and Mistral contributions are shown in (b) and (c) (normalized in (c)). (d) shows just the normalized Mistral contribution to de-stratification.

	MEAN		STD		MIN		MAX	
	$SI_{S,Cont}$	δSI_{Cont}						
DC	0.618	0.287	0.115	0.063	0.446	0.146	0.805	0.349
NDC	0.370	0.276	0.122	0.114	0.104	0.137	0.519	0.518
All	0.457	0.280	0.169	0.099	0.104	0.137	0.805	0.518

Table 4.2: Statistics for the normalized $SI_{S,Cont}$ and δSI_{Cont} contributions from Fig. 4.6 (c) and (d).

4.3.1.1 Components of the Seasonal Contribution

As the variability of the seasonal contribution, $SI_{S,Cont}$, plays a key role in the occurrence of deep convection, it was separated into the different surface heat flux components, as described by Eq. 2.39, with $t_0 = t_{SI_{S,max}}$ and $t_1 = t_{SI_{S,min}}$. The distributions of the different flux components over the years are shown in Fig. 4.7 (a), with DC years colored in blue and NDC years colored in red. What Fig. 4.7 (a) conveys, is that the years with increased latent, Q_E , and sensible, Q_H , heat fluxes during the preconditioning period are the years with deep convection. This is seen by the differences in the mean values for each subgroup ($\overline{DC} - \overline{NDC}$): 0.04, -0.11, -0.17, and -0.43 for Q_{SW} , Q_{LW} , Q_H , and Q_E , respectively. Initially, it appears that the longwave upward radiation also acts as an indicator for years with deep convection. However, if we normalize these differences by the average value of all the years for each component ($(\overline{DC} - \overline{NDC})/All$), then we can easily identify the sensible and latent heat fluxes as the main indicators: 0.03, 0.08, **0.43**, and **0.33** (in the same order as the previous list).

To determine which atmospheric component drove the differences evident in the latent and sensible heat fluxes, Δq , $\Delta\theta$, and the wind speed ($|\Delta\vec{u}| \approx |\vec{u}_z|$, as the sea surface current is typically very small relative to the wind speed; typically $\mathcal{O}(mm/s)$ vs $\mathcal{O}(m/s)$, respectively) was ensemble averaged for DC and NDC years (blue and red, respectively). These values were selected as they are the atmospheric components found in Eq. 2.1 used to calculate the latent and sensible heat fluxes. The ensemble averaging is shown in Fig. 4.7 subplots (b), (c), and (d), respectively. While there are differences in both Δq and $\Delta\theta$ between DC and NDC years, the wind speed, $|\vec{u}_z|$ is the main differentiator between the two groups of years.

To better demonstrate $|\vec{u}_z|$ as the main differentiator, a sensitivity analysis was performed by estimating the change in destratification due to the latent and sensible heat fluxes, with either the DC or NDC ensemble averaged values for Δq , $\Delta\theta$, and $|\vec{u}_z|$. Using Eq. 2.39, the change in the estimated destratification due to changes in Q_E and Q_H can be calculated as (simplifying the fraction to 10^{-9} , as mentioned in Sec. 2.5.1):

$$\Delta SI_{Est,i,j} = 10^{-9} \times \int_{t_0}^{t_1} \Delta Q_{i,j} dt \quad (4.3)$$

Where $\Delta Q_{i,j} = Q_{i,j} - Q_{i,Ref}$. i is either E or H for the latent and sensible heat flux, respectively, and j is either Δq , $\Delta\theta$, or $|\vec{u}_z|$. Here, j stands for the variable changed to the DC ensemble averaged value (denoted by the subscript DC), setting the remaining variables to the NDC ensemble averaged values (denoted by the subscript NDC). $Q_{i,Ref}$ has all variables set to the NDC ensemble averaged

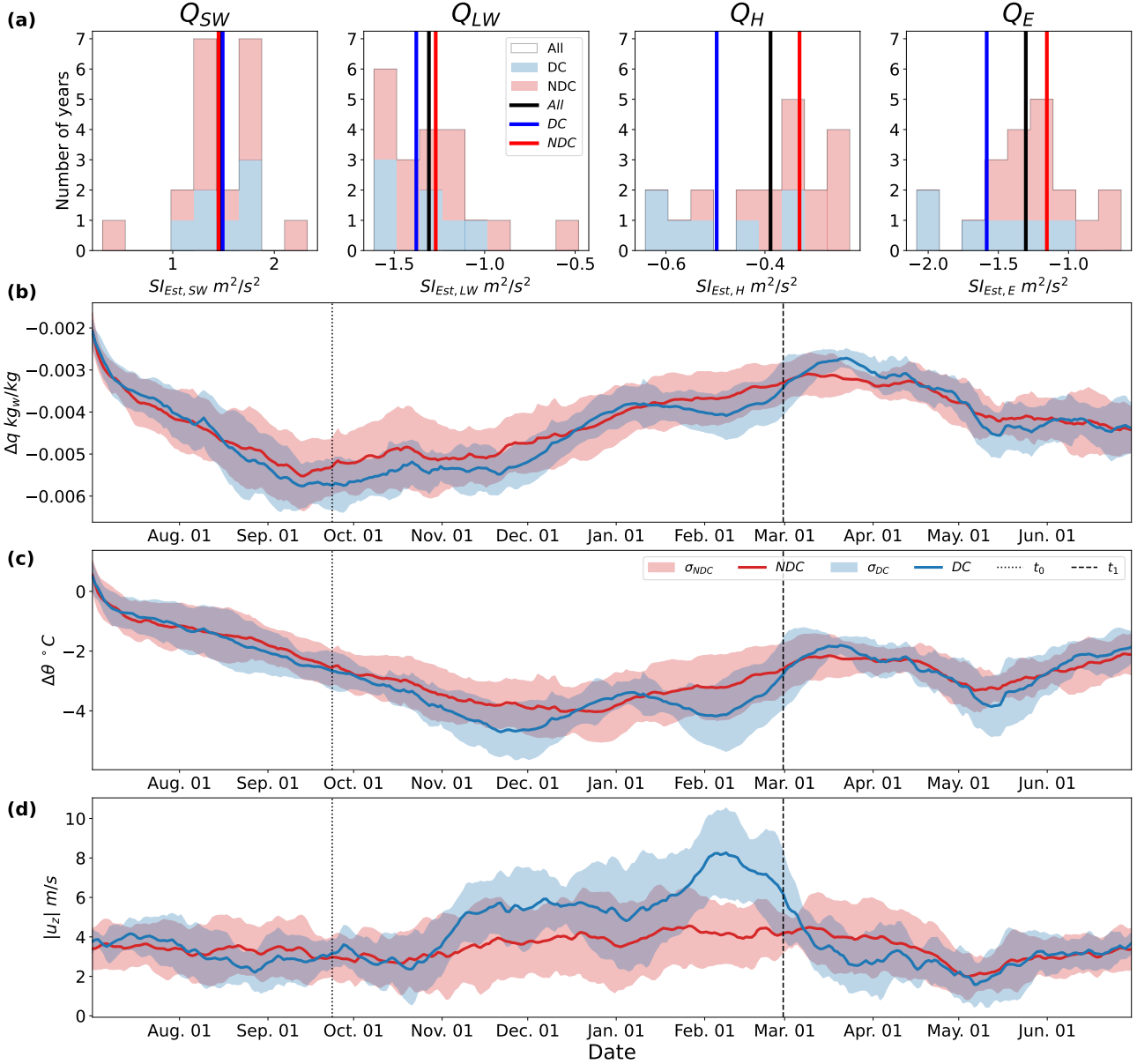


Figure 4.7: Distributions of the different flux components making the stratification change in SI_S , determined using Eq. 2.39 per component, i , are shown in subplot (a). DC and NDC stand for deep-convection and non-deep-convection, respectively. Subplots (b), (c), and (d) show the ensemble averaged (discarding Feb. 29th from leap years) driving components of the flux bulk formulae in Eq. 2.1, Δq , $\Delta\theta$, and $|\vec{u}_z|$. **Note:** in this plot $SI_{Est,i} = SI_{S,Q,i}$.

j	$\Delta SI_{Est,E,j} \text{ m}^2/\text{s}^2$	$\Delta SI_{Est,H,j} \text{ m}^2/\text{s}^2$	Total m^2/s^2
Δq	-0.066	-0	-0.066
$\Delta \theta$	-0	-0.042	-0.042
$ \vec{u}_z $	-0.322	-0.102	-0.424

Table 4.3: Estimated changes in destratification due to changing one variable at a time (between Δq , $\Delta \theta$, and $|\vec{u}_z|$) to DC versus NDC ensemble averaged values, utilizing Eq. 4.3. Note, the saturation humidity is based on sea surface temperature, which means keeping the temperature at NDC ensemble averaged values is technically non-physical, as the saturation humidity would change with a different air temperature.

values. For example, $\Delta Q_{E,\Delta q}$ would be:

$$\Delta Q_{E,\Delta q} = Q_{E,\Delta q} - Q_{Ref} = \rho_{a,0} \Lambda C_E (\Delta q_{DC}) |\vec{u}_z|_{NDC} - \rho_{a,0} \Lambda C_E (\Delta q_{NDC}) |\vec{u}_z|_{NDC}$$

We can then determine the direct influence DC ensemble averaged values for Δq , $\Delta \theta$, and $|\vec{u}_z|$ have on destratification. The results of this analysis are found in Table 4.3. As $|\vec{u}_z|$ influences both Q_E and Q_H , it easily makes a larger difference in terms of destratification than either Δq or $\Delta \theta$: $-0.424 \text{ m}^2\text{s}^{-2}$ versus $-0.066 \text{ m}^2\text{s}^{-2}$ and $-0.042 \text{ m}^2\text{s}^{-2}$, respectively.

The source of this difference in wind speed between DC and NDC years obfuscates the distinction between seasonal and Mistral contributions, however. The filtering, as discussed in Sec. 2.2.1, primarily removes the high frequency component of the Mistral. However, as also pointed out, the Mistral has a low frequency seasonal component as well, with more frequent and stronger Mistrals occurring in winter versus summer (see Givon et al. 2021 for a more complete analysis). With the moving average window, this low frequency component is partially filtered out, removing some of the Mistral's low frequency component (when viewed in the spectral domain), however part of it still remains. This remaining part is the overall increase in the mean wind speed during the winter months due to more frequent Mistral events, and hence appears in the seasonal forcing. The percentage of the preconditioning days ($t_{SI_{max}}$ to $t_{SI_{min}}$) that feature a Mistral event is consistent with this observation, with DC years at 34.3% and NDC years at 28.6%.

4.3.2 Prior Questions

As mentioned in the introduction, at the end of Chap. 3 a few questions were posed that couldn't be answered by the scope of that study. We will readdress them here.

4.3.2.1 Does the Mistral trigger deep convection, or does the seasonal change trigger it?

To determine if the Mistral or seasonal change triggered deep convection in our study, we first located the main growth phase of the MLD during deep convection. The main growth phase was chosen to be the first point in time at which the MLD became deeper than 250 m (labeled by a red circle in

Fig. 4.3 for DC years) to the point at which the MLD reaches its first maximum (first if two major peaks were present, such as for the years of 2009, 2012, and 2013, otherwise the overall maximum was used; labeled by a red triangle in Fig. 4.3 for the same years). Then the ratio of the averaged gradient, with respect to time, of δSI and SI_S ($\overline{\partial_t \delta SI} / \overline{\partial_t SI_S}$) was computed for this growth phase for each DC year. The years of 2000, 2009, and 2013 saw a larger destratifying contribution from the Mistral component than the seasonal component, with ratios greater than unity: 1.45, 4.71, and 2.15, respectively. This demonstrates that the Mistral was the main triggering component for these years. However, for the years of 1999, 2005, 2011, and 2012, the seasonal component was the main triggering agent, with ratios less than unity: 0.43, 0.40, 0.18, and 0.05, respectively. This means both the Mistral and seasonal component trigger deep convection in roughly equal amounts of our studied DC years.

4.3.2.2 Does the maximum SI_S play a role in deep convection?

According to our results, the maximum SI_S does play a role. As previously pointed out, DC years are almost entirely years with a lower than average SI_S maximum (except for 2012). Which is intuitive, as a larger maximum of SI_S means that both the seasonal component and Mistral component must overcome a larger amount of stratification to form deep convection. However, more importantly, years with above average $SI_{S,Cont}$ are more often than not, DC years. We saw the origin of this difference in Fig. 4.7 and Table 4.2, in the difference of wind speed. This means that the seasonal contribution to destratification, through the wind speed, has a particularly important role in the overall destratification of the GOL, as well as the seasonal maximum stratification it must overcome.

4.3.2.3 Does the timing of the SI_S minimum matter and can the Mistral contribution overcome a restratifying SI_S ?

The third question, broken down into a few separate yet related questions, poses: does the timing of the SI_S minimum matter? Can the Mistral, δSI , overcome the restratifying SI_S ? Or, in other words, do any of the deep convection events occur after the SI_S minimum?

For our results, three of the seven DC years (2009, 2012, and 2013) experienced a control SI minimum that occurred after the SI_S minimum (vertical dashed lines in Fig. 4.3). In each of these three years, according to the MLD (Fig. 4.3), deep convection ceased temporarily between the control and seasonal stratification minimum. Then deep convection resumed with an additional peak in the MLD before the control SI reached its minimum. This means that the Mistral can overcome a restratifying SI_S to continue deep convection. However, it is unclear whether it can trigger deep convection after the seasonal minimum or not, as our model results don't feature such an example.

While a larger dataset of deep convection events will be required to more definitively answer this question, we can infer that the case of triggering deep convection after or continuing it beyond the SI_S minimum will be rarer than the case of the control SI minimum occurring before the SI_S minimum. This is due to a weakening contribution from Mistral events as the preconditioning period

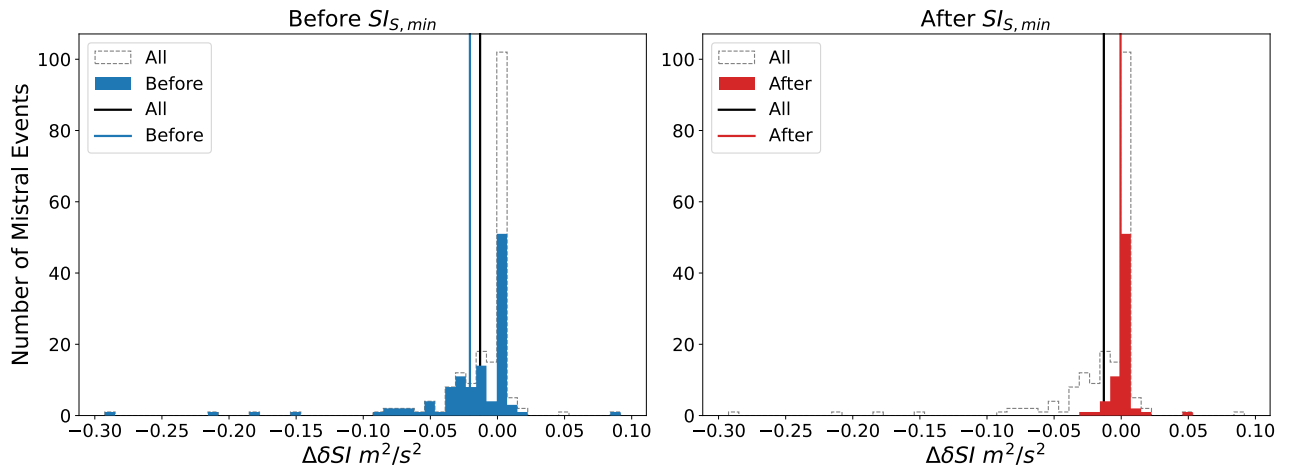


Figure 4.8: Distributions of the destratification incurred by Mistral events during DC years. $\Delta\delta SI$ is calculated using Eq. 2.64 per event k .

occurs. Eq. 2.78 shows that succeeding Mistral events need to be stronger than the current level of destratification to cause more destratification. When the year transitions out of the preconditioning period into the summer (essentially after the SI_S minimum), Mistral events destratify less because the water column has already incurred a significant amount of destratification. We can see this change by looking at the destratification caused by individual Mistral events depending on their timing with Eq. 2.64. The results are shown in Fig. 4.8. Events before the SI_S minimum exhibit a wider spread in terms of destratification, but also have a mean destratification ($-0.021 \text{ m}^2\text{s}^{-2}$) that is less than the events that occur after the minimum ($-0.001 \text{ m}^2\text{s}^{-2}$). This limits the likelihood that Mistral events can overcome a restratifying SI_S .

4.3.2.4 Does the previous year's level of stratification affect the proceeding year?

For our results, five of the seven DC years occurred adjacently: the years of 1999 and 2000 occurred together and the years 2011 to 2013 occurred together as well. Otherwise, the two remaining years were in between two NDC years. This seems to suggest DC years occur consecutively, which intuitively makes sense, as the water column following a deep convection event will have had a significant amount of heat removed from it (resulting in buoyancy loss, driving destratification). This heat must be re-injected into the water column to restratify it, whereas years with persisting stratification don't need this initial addition of heat. However, the newly formed dense water post deep convection must also vacate before the following winter. If the newly formed dense water is unable to vacate due to mesoscale flow patterns, this dense water will increase the density gradient in the GOL after restratification due to advection occurs, increasing the stratification of the water column. Then the following winter must provide enough buoyancy loss to reduce the density of the surface waters to match the dense water before convection can occur. Therefore, there is a balance between the mobility of the newly formed dense water and the surface buoyancy loss forming the dense water to promote a setting for future deep convection events to occur.

Returning to our results, however, in terms of stratification (through the stratification index and

contributions derived from the SI), there doesn't appear to be any discernible pattern or trend for the 20-year period. A larger scoped study that investigates additional features, such as the composition of the formed dense water masses (e.g. the saltier dense water formed during the 2005 deep convection event [58]), the long term trends of said composition [62], or changes in the Med. Sea circulation [4], may be able to provide more answers. For example, the study of Parras-Berrocal et al. 2022 found that increasingly saline Levantine Intermediate Water and freshening Inflow Atlantic Water at the Strait of Gibraltar leads to increasing stratification in the GOL for climatic scenario runs up to the year 2100.

4.4 Conclusions

Our study investigated deep convection in the GOL over a 20-year period, using the NEMO ocean model forced by filtered and unfiltered RegIPSL WRF/ORCHIDEE atmospheric data. By looking at the difference between the two sets of ocean simulation results forced by the two different forcings, we could extract the effect the Mistral and seasonal atmospheric change had on the annual stratification cycle of the GOL. The control model results represented reality fairly well with respect to Argo and CTD profiling. While deep convection occurs in only seven of the 20 years in the model results, whereas it occurs in eight of the 20 years in observations [62, 13], we were able to extract information regarding the impact of the seasonal atmospheric change on destratification. We found the seasonal contribution to be the main driver in terms of destratification during the preconditioning period, with it being larger during DC years. When breaking down what causes destratification in the seasonal contribution, we found the latent and sensible heat fluxes to be the most important components, shifting more negative during DC years. It was then found that the differences in the latent and sensible heat fluxes between DC and NDC years were caused by increased wind speeds during DC years. These increased wind speeds themselves were caused by the seasonal aspect of the occurrence of Mistral events, with more events occurring during the winters with deep convection.

When addressing the questions asked in Chap. 3, we found that the Mistral and seasonal atmospheric change roughly trigger deep convection an equal number of times. It was also determined that the maximum SI_S an important quantity as it is the amount of stratification the seasonal and Mistral contributions must overcome to cause deep convection. Additionally, the Mistral contribution can overcome a restratifying SI_S to extend deep convection, however it is unlikely it can trigger deep convection after the SI_S minimum. Finally, there is a balance between the mobility of newly formed dense water and overall reduced heat content in the vertical column from a deep convection event. The reduced heat content allows for less cooling needed to destratify the water in the proceeding year, improving the likelihood of deep convection occurring. But any remaining dense water in the lower layers after the restratification phase can increase the density gradient, if it is unable to readily flow to other regions, inhibiting deep convection.

Our study shows the importance of the seasonal atmospheric change and its drivers on the deep convection cycle of the GOL. Future studies investigating the change in variability of the seasonal

atmospheric forcing and vertical composition of the GOL waters with a warming atmosphere will be necessary to understand the evolution of deep convection in the GOL with a changing climate.

Chapter 5

Impact of Climate Change on Water Masses in the Gulf of Lion

Contents

5.1 Evolution of Seasonal Stratification and Forcing	83
5.1.1 Changes in Atmospheric Forcing	83
5.1.2 Advected Stratification	89
5.2 Conclusions	96

This third study looks at the NEMO model results driven by the CMIP6 results of Météo France's RCSM6 regional model. The years of 2015 to 2100 are studied, under the SSP5 8.5 scenario (the worst case SSP scenario); comparing the control and seasonal ocean response, just like the first two studies. The preliminary results are presented.

We investigate here the effect of climate change on stratification in the Gulf of Lion. The methodology is the same as that in Chap. 3 and 4, where two sets of simulations are run to distinguish the effect of the Mistral, yet also highlight the effects of the seasonal forcing. To quantify the effect of climate change, the forcing and restoring data used in this experiment come from the CNRM-RCSM6 [131] coupled regional model forced by the CNRM-ESM2-1 [128] earth system model, configured to simulate the CMIP6 SSP5-8.5 scenario (Sec. 2.2). Two main results come about from this investigation:

1. the change in atmospheric forcing due to a warming atmosphere and sea (Sec. 5.1.1)
2. the changes in the water column composition advected into the region (Sec. 5.1.2)

Some closing points are provided in Sec. 5.2. ¹

¹This chapter is in preparation to be submitted to the Journal of Geophysical Research: Oceans.

5.1 Evolution of Seasonal Stratification and Forcing

5.1.1 Changes in Atmospheric Forcing

As the point of minimum stratification changes from year to year in the Gulf of Lion, all the results to be displayed and discussed have been produced by spatially averaging the atmospheric and oceanic model outputs contained in the bounding box from 42 to 42.5 °N and from 4.25 to 5 °E. Additionally, unless otherwise specified, results and variables refer to the seasonal ocean simulation set. From 2015 to 2060, the maximum SI_S and minimum control SI per winter in the GOL remain relatively constant. However, after 2060 both values begin to increase at roughly the same constant rate until 2100, as seen in Fig. 5.1 (a). This means the amplitude of the annual cycle of the stratification remains fairly constant, with only its intercept shifting positive. As expected, the seasonal and Mistral contributions remain relatively constant as shown in subplot (b), with only a slight increase in variability near the end of the period. However, the leftover stratification constantly increases after 2060 at the same rate as seen in SI_{min} and $SI_{S,max}$ in (a).

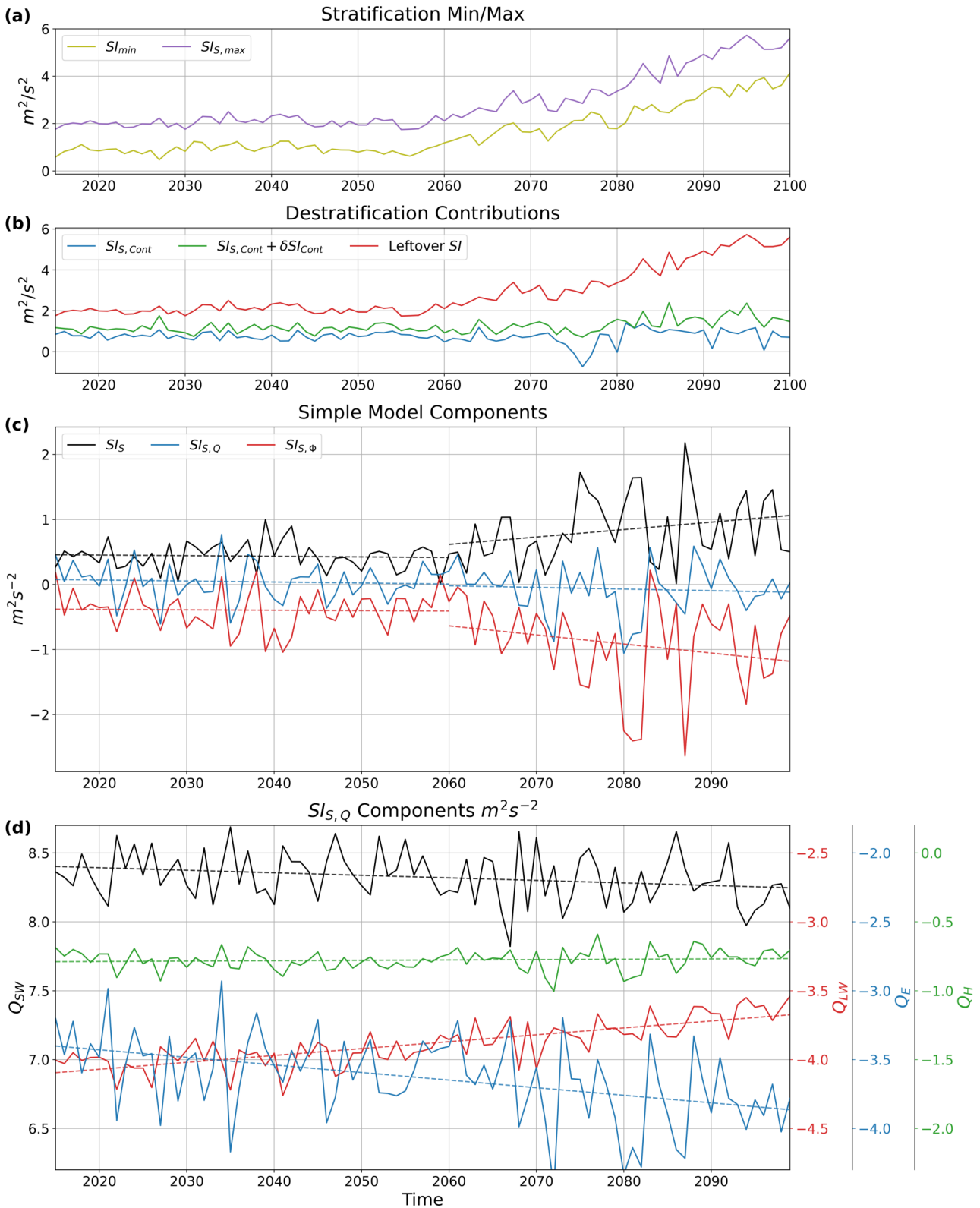


Figure 5.1: The change in stratification in the Gulf of Lion over the 2015 to 2100 period. The minimum of the control stratification index, SI_{min} , and maximum seasonal stratification index, $SI_{S,max}$ are shown in subplot (a). (b) shows the stratification contributions due to the seasonal change, $SI_{S,Cont}$, and seasonal change plus the Mistral, δSI_{Cont} . See Fig. 4.5 and Sec. 4.3.1 in Chap. 4 for the definition of stratification contributions and Fig. 4.6 for the results of the 1993 to 2013 period. (c) shows the trends (in dashed lines; one set for 2015 to 2060 and one set for 2060 to 2100) of the different components in Eq. 2.38: SI_S , the total, $SI_{\Phi,S}$, the advective component, and $SI_{Q,S}$, the component due to the net heat flux. $t_0 = t_{SI_{S,max}}$ and $t_1 = t_{SI_{min}}$. (d) shows the trends of the different components of $SI_{Q,S}$, after separating $Q_{net,S}$ into its individual parts (Eq. 2.1). Trends found in (d) are quantified in Tab. 5.1.

To determine the main cause leading to the increased stratification after 2060 seen in the leftover SI , Eq. 2.38 is used to compare the contributions to stratification of both the advective and atmospheric components of the seasonal timescale. Note, similar to Sec. 3.5 and 4.3.1.1, we will assume $\frac{g}{2\rho c_p T_0} \approx 10^{-9} m^4 J s^{-2}$. However, as this approximation is not perfect, we have included a coefficient, ω , to equate the variance of SI_S and $SI_{S,Q}$:

$$\omega^2 \sigma_{SI_{S,Q}}^2 = \sigma_{SI_S}^2 \quad (5.1)$$

Therefore, $SI_{S,Q} = 10^{-9} \times \omega \int_{t_0}^{t_1} Q_{net,S} dt$. In our case, $\omega = 0.36$.

The results are shown in Fig. 5.1 (c). The atmospheric contribution remains fairly constant throughout the entire study, as expected from subplot (b), with a slight negative trend leading to slightly more destratification at the end of the period. On the other hand, the advective contribution significantly stratifies the GOL after 2060 (more negative means more stratification, as it is on the left-hand side of Eq. 2.38). This demonstrates that the atmospheric forcing is not driving the increase in stratification, but is being advected into the GOL through the transport of water masses with changing properties. This will be further investigated in Sec. 5.1.2.

However, the question remains as to why the atmospheric contribution remains relatively unchanged, despite a changing climate. Separating the net heat flux, $Q_{net,S}$, into its components reveals which fluxes are changing and which are not over the 85-year period. Figure 5.1 (d) shows the results. The relatively constant atmospheric contribution to stratification is caused by a combination of changing fluxes that roughly cancel each other out. The shortwave radiation, Q_{SW} , and sensible heat, Q_H , components do not change much over the study period (linear regression trend line change, Δ , of $-0.15 m^2 s^{-2}$ and $0.02 m^2 s^{-2}$, respectively), with Q_H failing to reject the null hypothesis that no trend exists (95% confidence interval; see Tab. 5.1). However, most of the change occurs in the longwave radiation, Q_{LW} , and latent heat, Q_E , components: Q_{LW} increasing with a $\Delta = 0.42 m^2 s^{-2}$ and Q_E decreasing with a $\Delta = -0.46 m^2 s^{-2}$ (Tab. 5.1). These two components effectively cancel each other out. This leads to the atmospheric stratification contribution changing very little over time.

	SI_Q Components m^2/s^2				Humidity kg/kg		
	Q_E	Q_H	Q_{LW}	Q_{SW}	Δq	q_z	q_0
Δ	-0.46	0.02	0.42	-0.15	-0.0007	0.0028	0.0035
% Δ	-13.59	2.83	10.26	-1.84	-14.11	30.87	25.11
p-value	~ 0.0	0.41	~ 0.0	0.02	~ 0.0	~ 0.0	~ 0.0
	Wind m/s	Radiation W/m^2			Temperature $^\circ C$		
	$ \vec{u}_z $	$Q_{LW,A}$	$Q_{LW,O}$	Q_{SW}	$\Delta\theta$	θ_z	SST
Δ	-0.02	30.45	-21.06	-3.95	0.17	3.77	3.60
% Δ	-0.70	9.30	-5.07	-2.04	5.84	1.30	1.23
p-value	0.09	~ 0.0	~ 0.0	0.03	~ 0.0	~ 0.0	~ 0.0

Table 5.1: Trends of the atmospheric variables and surface heat fluxes. Δ is the change from the beginning value, x_{beg} , to the final value, x_{end} , of the linear regression trend line from 2015 to 2100. % Δ is the relative change of the is difference, equal to $(x_{end} - x_{beg})/|x_{beg}|$. The p-value is the 95% confidence null hypothesis that no trend exists (value over 0.05 fail to reject the null hypothesis and have been emboldened). Δ for e is 4.43 mb.

To understand why the latent heat and longwave radiation fluxes change and the sensible heat flux does not in a changing climate, the surface atmospheric variables have been plotted in Fig. 5.2 to discern any notable trends. Like in Fig. 5.1 (d), the trends are quantified in Tab. 5.1. The shortwave radiation flux is ignored as its main components, solar radiation and the Med. Sea's surface albedo, are effectively constant.

$\Delta\theta$ and $|\vec{u}_z|$ ($|\Delta\vec{u}| \approx |\vec{u}_z|$, as the wind speed is typically much larger than the ocean current) are the primary evolving variables determining the sensible heat flux. $\Delta\theta$ in Fig. 5.2 (a) shows very little change over time, trending positively by only 0.17 $^\circ C$ over the 2015 to 2100 period (Tab. 5.1). The temperature difference remains roughly constant as the surface atmospheric temperature, θ_z , and sea surface temperature, SST , increase by roughly the same amount: 3.77 and 3.60 $^\circ C$, respectively. Paired with a constant wind forcing, failing to reject the null hypothesis of zero trend at a 95% confidence interval (p-value = 0.09), the sensible heat flux remains roughly constant over the time period. The primary variable determining the latent heat flux, as the wind forcing is constant, is Δq . The difference between the atmospheric humidity and saturation humidity at the sea surface deepens as seen in Fig. 5.2 (b), despite both increasing individually. This is due to the saturation humidity, q_0 , growing faster (+0.0007; Tab. 5.1) due to the increasing sea surface temperature, as $q_0 \propto e^{-SST}$. Thus, the latent heat flux grows over time due the warming sea surface.

The simulation providing the atmospheric variables was forced according to the SSP5-8.5 socio-economic pathway, effectively resulting in an 8.5 W/m^2 increased forcing averaged globally by 2100, driven by anthropogenic emissions [111]. In the case of the GOL, the resulting increased radiative forcing is found in the longwave radiation flux, Q_{LW} . Q_{LW} is equal to the sum of the atmospheric downwelling component, $Q_{LW,A}$, and oceanic downwelling component, $Q_{LW,O} = -\epsilon\sigma SST^4$ (Eq. 2.1). Understandably, with the warming sea surface, the oceanic component becomes more negative, as seen in Fig. 5.2 (d). However, the increasing atmospheric component shown in the same subplot cannot be so easily attributed, as the temperature, water vapor pressure, e , and cloud cover all play a role in determining its magnitude. Cloud cover over the Mediterranean region is expected

to decrease rather than increase, [122, 37] and is therefore likely not the reason for the increased $Q_{LW,A}$.

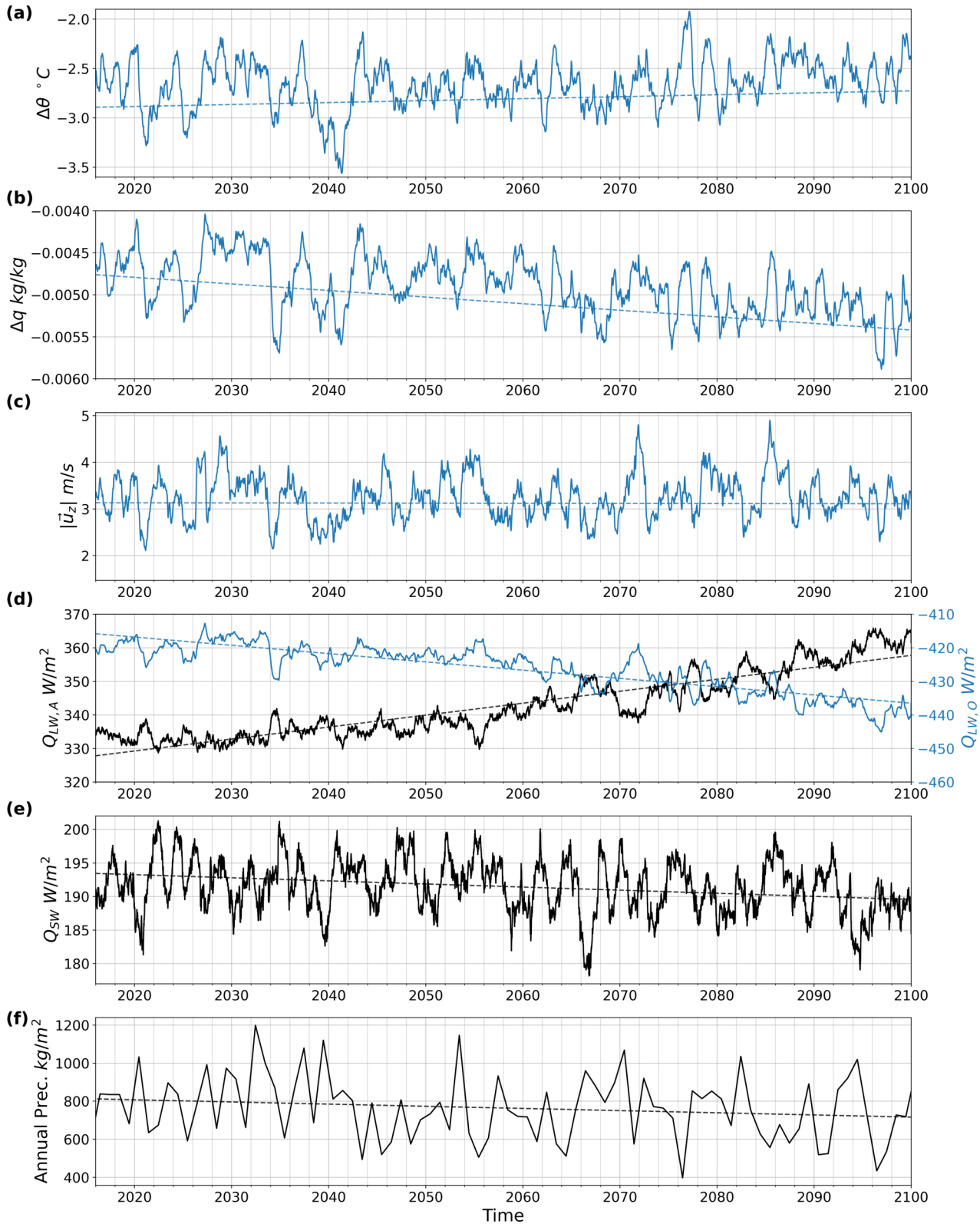


Figure 5.2: Evolution of the driving variables in the bulk formulae for NEMO (Eq. 2.1). (a) shows the difference in atmospheric and sea surface temperature, $\Delta\theta = \theta_z - SST$. (b) shows the difference in atmospheric and sea surface humidity (assumed to be saturated), $\Delta q = q_z - q_0$. (c) shows the wind speed, $|\bar{u}_z| \approx |\Delta\bar{u}|$. (d) shows the atmospheric longwave downwelling, $Q_{LW,A}$, and the oceanic downwelling component, $Q_{LW,O}$. (e) shows the atmospheric shortwave downwelling, Q_{SW} . The oceanic component is not shown as it is just the reflected atmospheric shortwave downwelling and has a effectively constant albedo. (f) shows the annual precipitation (rain and snowfall). The dashed lines are the linear regression trend lines.

To determine a likely cause, we use a semi-empirical clear sky longwave radiation model [66, 124]:

$$Q_{LW,A} = \frac{\epsilon\sigma SST^4(0.61 - 0.05\sqrt{e}) - 4\epsilon\sigma SST^3(SST - \theta_z)}{1 - \eta} \quad (5.2)$$

Where η is the longwave reflectance, equal to 0.045. e is calculated from q_z with the following:

$$e = \frac{q_z P}{(1 - q_z)(0.622 + q_z/(1 - q_z))} \quad (5.3)$$

Where P is the total atmospheric pressure, taken to be 1000 *mb*. Taking $\epsilon = 0.98$ [124] and plugging in the values for our time period into Eq. 5.2 returns a positive linear trend for $Q_{LW,A}$ of 29.78 Wm^{-2} . This is 98% of the 30.45 Wm^{-2} increase found in Tab. 5.1, meaning the increase in $Q_{LW,A}$ can be effectively explained by the evolving atmospheric temperature and humidity and sea surface temperature. To determine which of these three variables causes the largest change, the total derivative of Eq. 5.2 was determined:

$$dQ_{LW,A} = \frac{\partial Q_{LW,A}}{\partial SST} dSST + \frac{\partial Q_{LW,A}}{\partial \theta_z} d\theta_z + \frac{\partial Q_{LW,A}}{\partial e} de \quad (5.4)$$

With the respective partial derivatives:

$$\frac{\partial Q_{LW,A}}{\partial SST} = \frac{(4(0.61) + 4(0.05\sqrt{e}) - 16)\epsilon\sigma SST^3 + 12\epsilon\sigma SST^2\theta_z}{1 - \eta} \quad (5.5)$$

$$\frac{\partial Q_{LW,A}}{\partial \theta_z} = \frac{4\epsilon\sigma SST^3}{1 - \eta} \quad (5.6)$$

$$\frac{\partial Q_{LW,A}}{\partial e} = \frac{(0.05)\epsilon\sigma SST^4}{(1 - \eta)2\sqrt{e}} \quad (5.7)$$

Using the average values of 294.29 *K*, 291.48 *K*, and 16.72 *mb* for SST , θ_z , and e , respectively, for the 2015 to 2100 period in Eq. 5.5 and taking dx to approximately equal their respective Δ values in Tab. 5.1, Eq. 5.4 reveals which variable contributed the most to the increasing $Q_{LW,A}$. The sea surface temperature corrected the increase by -4.57 Wm^{-2} , whereas the atmospheric temperature provides the most increase in downward flux at 22.34 Wm^{-2} , versus the atmospheric humidity's contribution of 11.82 Wm^{-2} (all three totalling to 29.59 ; $\approx 29.78 \approx 30.45 \text{ Wm}^{-2}$). Thus, the longwave downwelling radiation increases primarily due to the changes in atmospheric temperature and humidity.

5.1.2 Advected Stratification

Returning our focus to the advected stratification brought into the GOL, the evolution of the water column properties are displayed in Fig. 5.3. To more definitely determine where in the vertical column the stratification accumulates, the integrand for the stratification index equation, Eq. 2.5, $N^2 z$, has been plotted in Fig. 5.3 (a). It's change over time has been plotted in subplot (b).

Immediately, we can see that initially the stratification accumulates in the upper 200 meters of the vertical column, but after 2060 it intensifies and expands deeper, reaching nearly 800 meters of the 2344 meter deep column. Figure 5.4 (a) shows this increase more concretely, as the integrated value from 150 to 600 meters shows a stark increase after 2060, with a smaller increase in the deepest layer (600 meters to the bottom). As the main variable in the integrand is the Brunt-Väisälä frequency, which depends on the vertical density gradient (Eq. 2.11), we will investigate the changes in potential density. Looking at the potential density (Fig. 5.3 (c)) reveals a decreasing density trend in the upper 600 meters (also visible in Fig. 5.4 (b)), which increases the density gradient with the underlying water. Peering into the changes in potential temperature (Fig. 5.3 (d) and Fig. 5.4 (c)) and salinity (Fig. 5.3 (d) and Fig. 5.4 (d)) that lead to the density changes, we can see a warming trend in the in upper 600 meters, reducing the density, but two trends for salinity. In the upper 150 to 200 meters, the water becomes fresher, in agreement with CMIP5 ensemble modelling of the Med. Sea, but becomes more saline from roughly 200 to 800 meters, also in agreement with ensemble modelling [144]. The freshening at the surface and the rising salinity in the intermediate levels increases the overall density gradient as well.

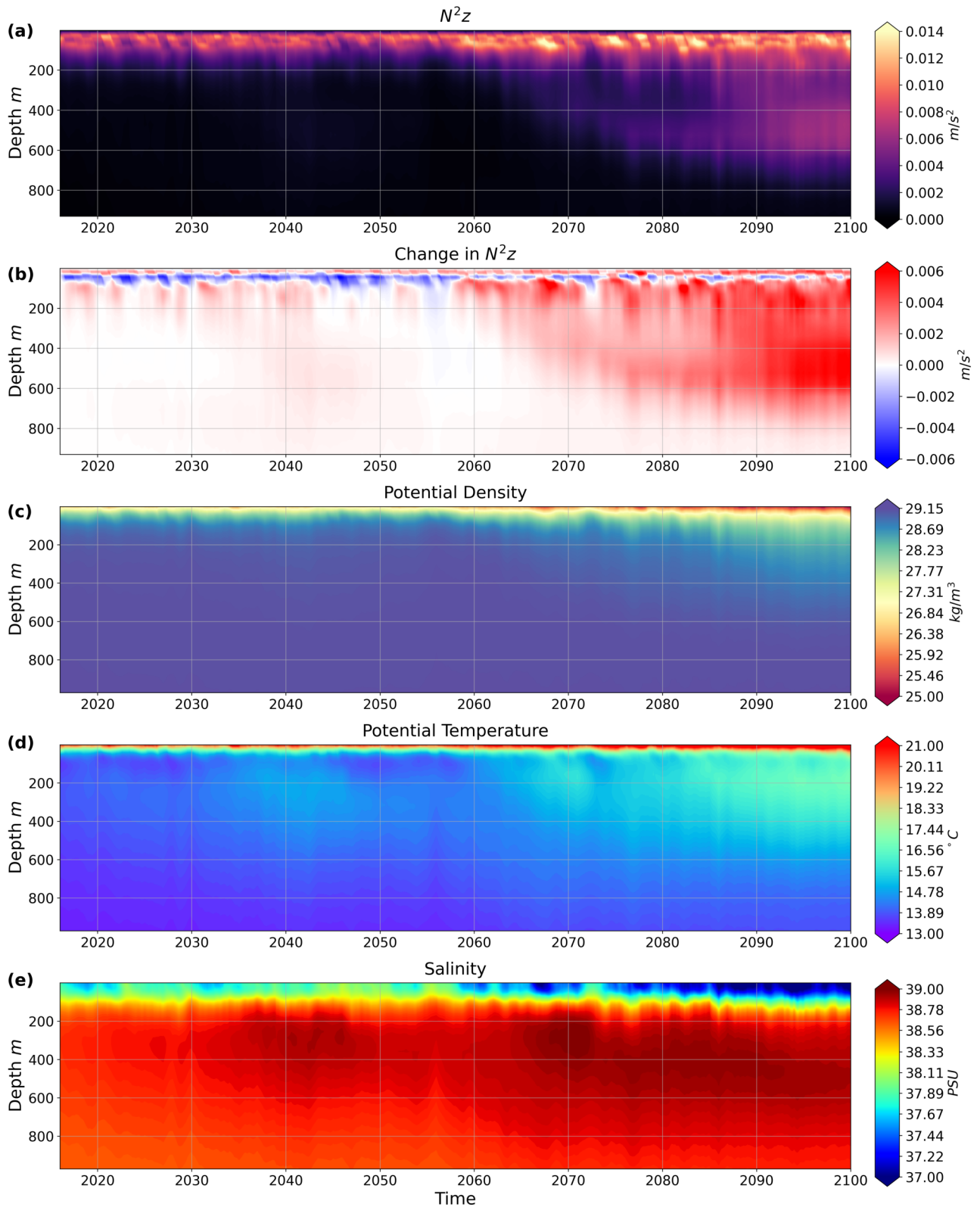


Figure 5.3: Evolution of the vertical column properties in the simulation results. Only the upper 800 meters of the 2344 meter deep column is shown, as these are the most active water masses. The results have been averaged with a moving average with a window size of a year to more easily display the decadal trends, particularly in the upper 150 meters, as is evident by the cycling in Fig. 5.4. (a) shows the plot of the integrand of Eq. 2.5 and (b) shows its change from 2015. (c), (d), and (e) show the potential density, potential temperature, and salinity respectively.

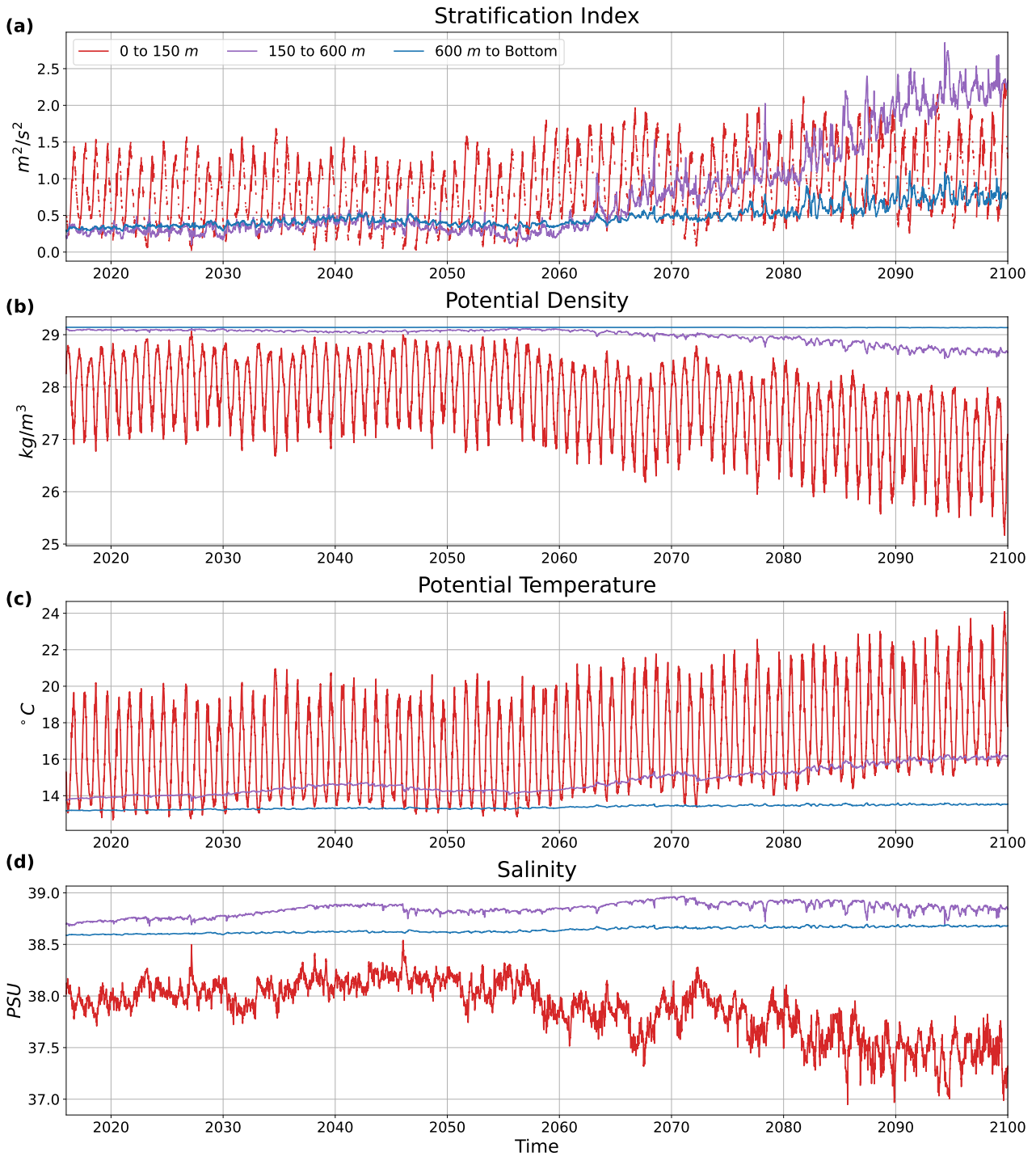


Figure 5.4: Evolution of the vertical column properties averaged (with exception for (a)) over the ranges of 0 to 150 meters, 150 to 600 meters, and 600 meters to the bottom. (a) was instead integrated over these ranges. (a) shows the stratification index, (b) shows the potential density, (c) shows the potential temperature, and (d) shows the salinity.

To determine if either the potential temperature or salinity is the main driver of the increasing stratification, we can utilize a simple equation of state for the potential density available in the NEMO ocean model [55]:

$$\rho = -a_0(1 + 0.5\lambda_1 T_a + \mu_1 z)T_a + b_0(1 - 0.5\lambda_2 S_a - \mu_2 z)S_a - \nu T_a S_a + \rho_0 \quad (5.8)$$

Where $T_a = T - 10$, $S_a = S - 35$ and therefore $\frac{\partial T_a}{\partial z} = \frac{\partial T}{\partial z}$ and $\frac{\partial S_a}{\partial z} = \frac{\partial S}{\partial z}$. The coefficients a_0 , b_0 , λ_1 , λ_2 , ν , μ_1 , and μ_2 are described in Tab. 5.2. Taking the partial derivative with respect to z of Eq. 5.8 gives us the following:

$$\begin{aligned} \frac{\partial \rho}{\partial z} = & -a_0 \underbrace{\left[\left(0.5\lambda_1 \frac{\partial T_a}{\partial z} + \mu_1 \right) T_a + (1 + 0.5\lambda_1 T_a + \mu_1 z) \frac{\partial T_a}{\partial z} \right]}_{\text{Temperature}} \\ & + b_0 \underbrace{\left[\left(-0.5\lambda_2 \frac{\partial S_a}{\partial z} - \mu_2 \right) S_a + (1 - 0.5\lambda_2 S_a - \mu_2 z) \frac{\partial S_a}{\partial z} \right]}_{\text{Salinity}} \\ & + \underbrace{-\nu \left[\frac{\partial T_a}{\partial z} S_a + \frac{\partial S_a}{\partial z} T_a \right]}_{\text{Combined}} \end{aligned} \quad (5.9)$$

We can now plug Eq. 5.9 into Eq. 2.11 and directly see which term, the temperature, salinity, or combined term, has the largest impact on the stratification.

Coeff.	Value	Units	Desc.
a_0	1.6550×10^{-1}	$kgm^{-3} \circ C^{-1}$	Linear thermal exp. coeff.
b_0	7.6554×10^{-1}	$kgm^{-3} PSU^{-1}$	Linear haline exp. coeff.
λ_1	5.9520×10^{-2}	$\circ C^{-1}$	Cabbeling coeff. for T^2
λ_2	5.4914×10^{-4}	PSU^{-1}	Cabbeling coeff. for S^2
ν	2.4341×10^{-3}	$\circ C^{-1} PSU^{-1}$	Cabbeling coeff. for TS
μ_1	1.4970×10^{-4}	m^{-1}	Thermobaric coeff. for T
μ_2	1.1090×10^{-5}	m^{-1}	Thermobaric coeff. for S

Table 5.2: Coefficients for Eq. 5.8, available in the NEMO ocean model [55].

The results are shown in Fig. 5.5. The contribution from the combined effect was found to be negligible, and is not included. What we see in Fig. 5.5 subplots (a) and (b) is that the temperature contribution reduces stratification slightly at the surface, yet increases it with depth, with a local maximum around the 600 meter mark. Conversely, the salinity change increases the stratification in the upper 600 meters, yet reduces it below. This is more clearly seen in subplot (c), as the integrated surface layer (down to 150 meters) shows a minimal contribution from temperature (Δ of $0.04 m^2 s^{-s}$), yet shows strongly positive contributions from the remaining layers (Δ s of 1.18 and $2.37 m^2 s^{-2}$ for the intermediate and bottom layer, respectively). As noted before, salinity increases stratification in the upper two layers (Δ s of 0.43 and $0.54 m^2 s^{-2}$ for the upper and intermediate layer, respectively), but reduces stratification in the lowest layer (Δ of $-1.37 m^2 s^{-2}$). The overall effect is the majority of the stratification comes from the intermediate layer (150 to 600 meters; combined Δ of $1.72 m^2 s^{-2}$, versus 0.47 and $1.00 m^2 s^{-2}$ for the upper and bottom layer, respectively), driven primarily by increasing temperature. The results are summarized in Tab. 5.3. As a confirmation of our results, we can see in Fig. 5.5 (d) the rapid increase in the stratification index (integrated from the surface to each depth) between 150 and 600 meters deep before leveling off for much of the

remaining column.

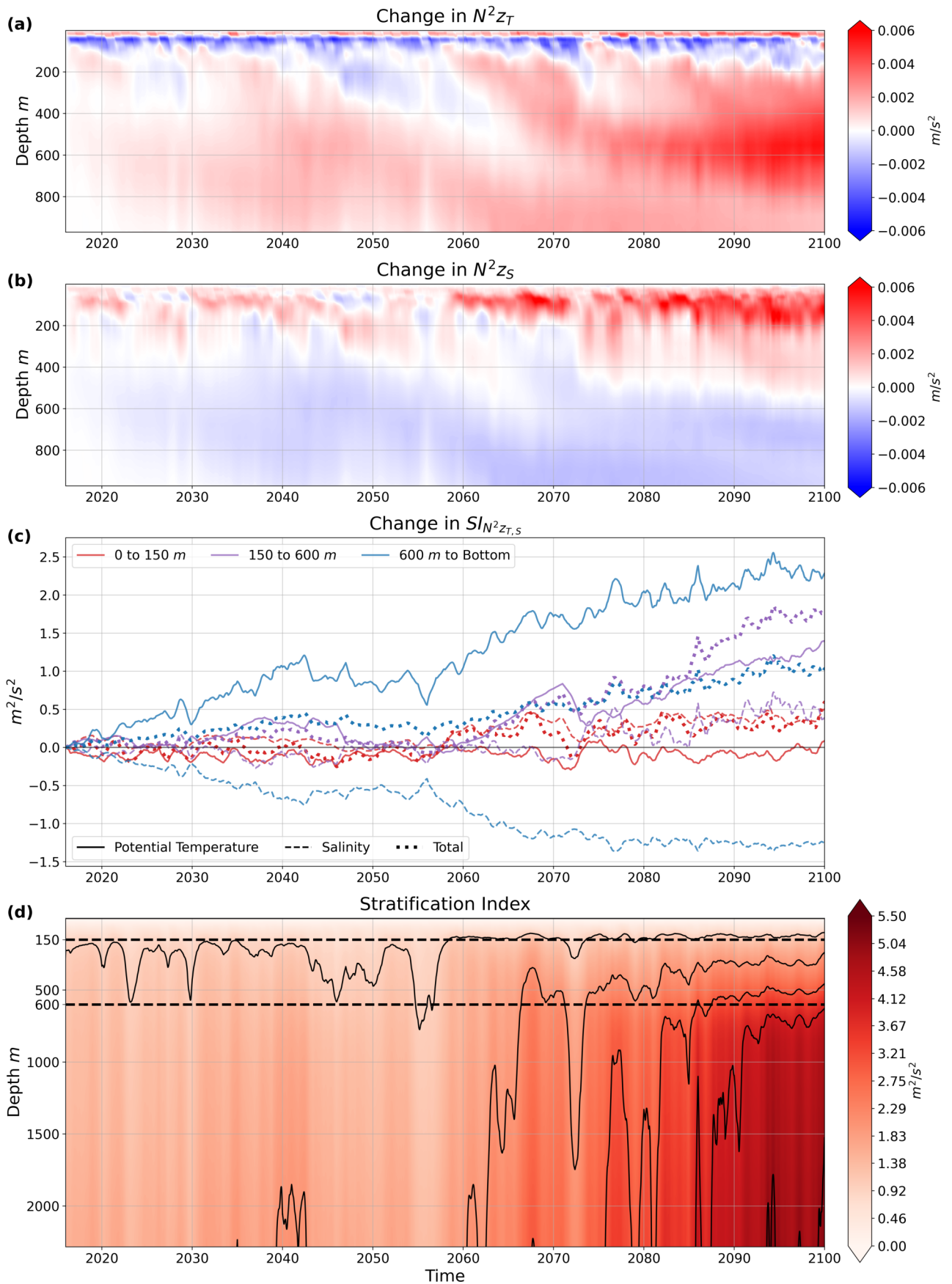


Figure 5.5: Contributions to stratification from potential temperature, $N^2 z_T$, (a), and salinity, $N^2 z_S$, (b), with the overall stratification shown in (d). (c) shows the contributions separated and integrated over the ranges given in Fig. 5.4. **Note:** (a), (b), and (c) show the difference in the contributions from their initial value during the year of 2015. Like Fig. 5.3, the values have been averaged with a moving window of a year in length to more easily see the decadal trends.



	Pot. Temp. m^2s^{-2}	Salinity m^2s^{-2}	Total m^2s^{-2}
	Δ		
0 to 150 <i>m</i>	0.04	0.43	0.47
150 to 600 <i>m</i>	1.18	0.54	1.72
>600 <i>m</i>	2.37	-1.37	1.00
	$\% \Delta$		
0 to 150 <i>m</i>	11.63	139.96	70.17
150 to 600 <i>m</i>	811.50	396.65	611.50
>600 <i>m</i>	686.46	-82.12	49.49

Table 5.3: Trends of the components of the stratification index integrand, $N^2 z_{S,T}$ (see Eq. 2.11 and 5.9). Δ is the change from the beginning value, x_{beg} , to the final value, x_{end} , of the linear regression trend line from 2015 to 2100. $\% \Delta$ is the relative change of the is difference, equal to $(x_{end} - x_{beg})/|x_{beg}|$. All linear regressions rejected the null hypothesis of zero trend (p-value equal to 0.0).

5.2 Conclusions

For this study we have run 85 years of future scenario simulations to determine the effect of climate change on the stratification of the Gulf of Lion. Other studies have already determined that deep convection in the gulf will cease at sometime in the near future [144, 113], primarily due to increased stratification. This trend is already apparent in the current climate [96]. Parras-Berrocal et al. 2022 has already shown that the atmospheric forcing is projected to remain constant in a CMIP5 regional simulation, and that freshening and warming surface waters atop increasingly saline intermediate waters will increase the stratification. Where this study stands apart is the quantification of which component, temperature or salinity, leads to the most increase in stratification, as well as why the atmospheric contribution remains constant despite the evolving climate. Our results show that the increase in temperature in the intermediate layer contributes the most to the rising stratification, and that the sea surface and atmospheric temperature cancel each other out in terms of their contribution to the sea surface heat fluxes.

Chapter 6

Climate Change Attenuation and Mitigation in the Mediterranean

Contents

6.1	Introduction	98
6.2	Methodology	99
6.2.1	Power generation	101
6.2.2	Environmental risk	103
6.2.3	Methanol production - pyseafuel	103
6.3	Power Generation	109
6.3.1	Solar	109
6.3.2	Wind	110
6.4	Environmental Hazards	111
6.5	Methanol Production	112
6.6	Integrated Production	115
6.7	Optimal Locations	118
6.8	Remote and Island Communities	121
6.9	Discussion	121

This chapter is slightly different from the prior chapters. As we could see in Chap. 5, climate change will have some concerning effects, especially on the ocean. This chapter turns to investigating a potential technology that could help mitigate some of these effects: carbon sequestration and utilization (CSU). We use the atmospheric forcing data and ocean model data from Chap. 4 to support the study, however most of this chapter will look at the availability of renewable energy to support CSU in the Mediterranean. ¹

¹This chapter has been adapted from a paper published in the journal *Energies*: Keller et al. "Offshore CO₂

6.1 Introduction

Carbon dioxide (CO_2) levels in the atmosphere continue to rise, despite efforts to limit sources of anthropogenic emissions, such as through the Paris Agreement to limit global warming to under 2°C [154]. In March 2022, the monthly global average atmospheric CO_2 was at a concentration of 418.28 ppm, almost 3 ppm more than the value in March 2021 (Fig. 6.1).

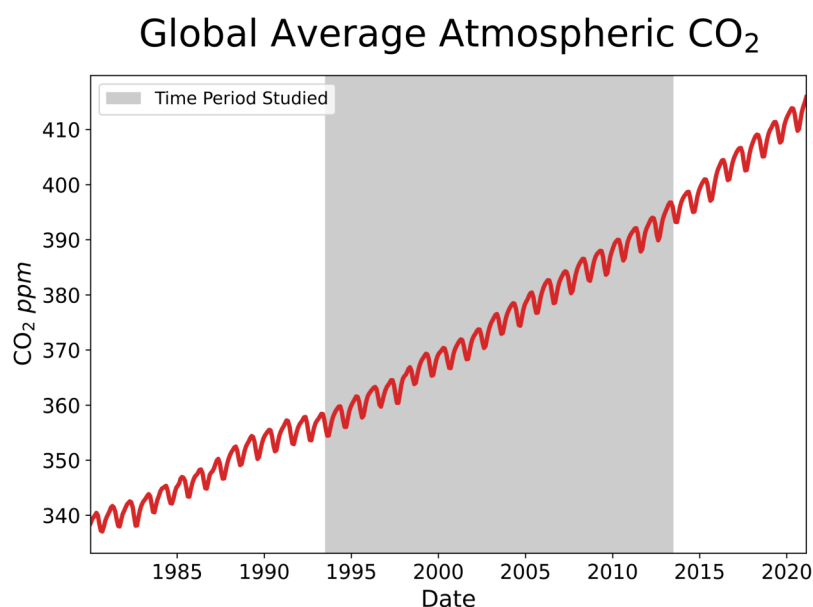


Figure 6.1: Global atmospheric CO_2 (Ed Dlugokencky and Pieter Tans, NOAA/GML; <https://gml.noaa.gov/ccgg/trends/>; last accessed June 13th, 2022).

To combat this continuing increase, carbon dioxide removal (CDR) is being extensively studied as it could potentially reverse emissions enough to return warming trends to only a 1.5°C global temperature increase [26]. Examples include bioenergy with carbon capture and storage (BECCS) where crops are used to produce biofuels from captured atmospheric CO_2 , direct air carbon dioxide capture and storage (DACCS) which extracts CO_2 from flue or exhaust gas in industrial applications, and indirect capture through the extraction of CO_2 from the ocean [26]. In the latter example, the decrease in dissolved CO_2 reduces its partial pressure in the ocean, leading to the atmospheric CO_2 to equilibrate with the ocean and reinsert atmospheric CO_2 into the waters.

One such device that utilizes indirect capture through the ocean is the renewable energy powered methanol-producing island [115]. This device completes the anthropogenic carbon cycle, reducing the need for fossil fuels, potentially helping to alleviate the global carbon emission crisis. Said device operates by extracting the atmospheric CO_2 dissolved in the seawater and combines it with hydrogen gas. The two gasses react, producing methanol, which can be refined into longer chain hydrocarbons, used as is, or stored. When the methanol is burned, it releases CO_2 back into the atmosphere, thereby completing the cycle.

capture and utilization using floating wind/PV systems: site assessment and efficiency analysis in the Mediterranean” [69]

In our study, we are interested in determining the optimal locations to put such a device in the Mediterranean Sea. It was marked as a potential location in Patterson et al. 2019 for solar methanol islands, due to its high insolation. Other studies have found the Mediterranean to be a hotspot for solar and wind power [33, 145], with strong persistent winds that can also become a hazard to floating structures [32]. Close to 7.6% of the world's population lives in the region [33], with a steadily increasing oil and gas consumption. Additionally, these devices could be used to improve the independence and self sustainability of remote and island communities by providing a means of local fuel production. There are over 191 islands in the Mediterranean, with 7 that have a significant population size (Corsica, Crete, Cyprus, Majorca, Malta, Sardinia, Sicily). This makes the overall region a prime location to study the placement of an alternative, renewable fuel source that can be locally produced.

To determine the optimal locations, we numerically simulate a methanol island and its production over 20 years, from 1993 to 2013. Atmospheric and oceanic model data from the RegIPSL model are used to drive the methanol island simulation. Our criteria for optimal locations consists of three main constraints:

- available power,
- environmental risk,
- available methanol production.

The power constraint will be analyzed in terms of available wind and solar energy in the region. Other energy extraction methods exist, but are not as mature as wind or solar [145]. Environmental risk is assessed through the maximum wave heights found in different parts of the region. The available methanol production is analyzed in terms of volumetric flow rate per Watt and per required area of power generation. Then the methanol production will be compared to the energy consumption of two island communities to determine its potential use for these communities.

The organization of the paper is as follows: Sec. 6.2 outlines the modelling of the methanol-producing island through python package called **pyseafuel** and covers the atmospheric and ocean model data used to drive said modelling. Section 6.3 presents the power availability of the region for the two power resources. Section 6.4 presents the maximum wave heights calculated for the region. Section 6.5 covers the simulated methanol production and its results. Section 6.7 presents the optimal locations. Section 6.8 discusses the potential use of the device in an island community setting. Concluding comments are presented in Sec. 6.9.

6.2 Methodology

To numerically simulate the methanol island in the Mediterranean, data from Earth system modelling from the years of 1993 to 2013 are utilized. The variables utilized and their flow paths to determine available power and available methanol production are provided in Fig. 6.2. To determine

the solar and wind power available to the methanol island, 10 meter wind speeds and shortwave downward radiation from an atmospheric model are used in conjunction with two python packages, **windpowerlib** and **pplib**. The environmental risk is considered through the modelled maximum wave heights, which are calculated from the 10 meter wind speed. The sea surface temperature and salinity from an oceanic model are provided to a purpose built python package for this study, **pyseafuel**, to model methanol production. Figure 6.2 shows the data flow and structure of the analysis in the study.

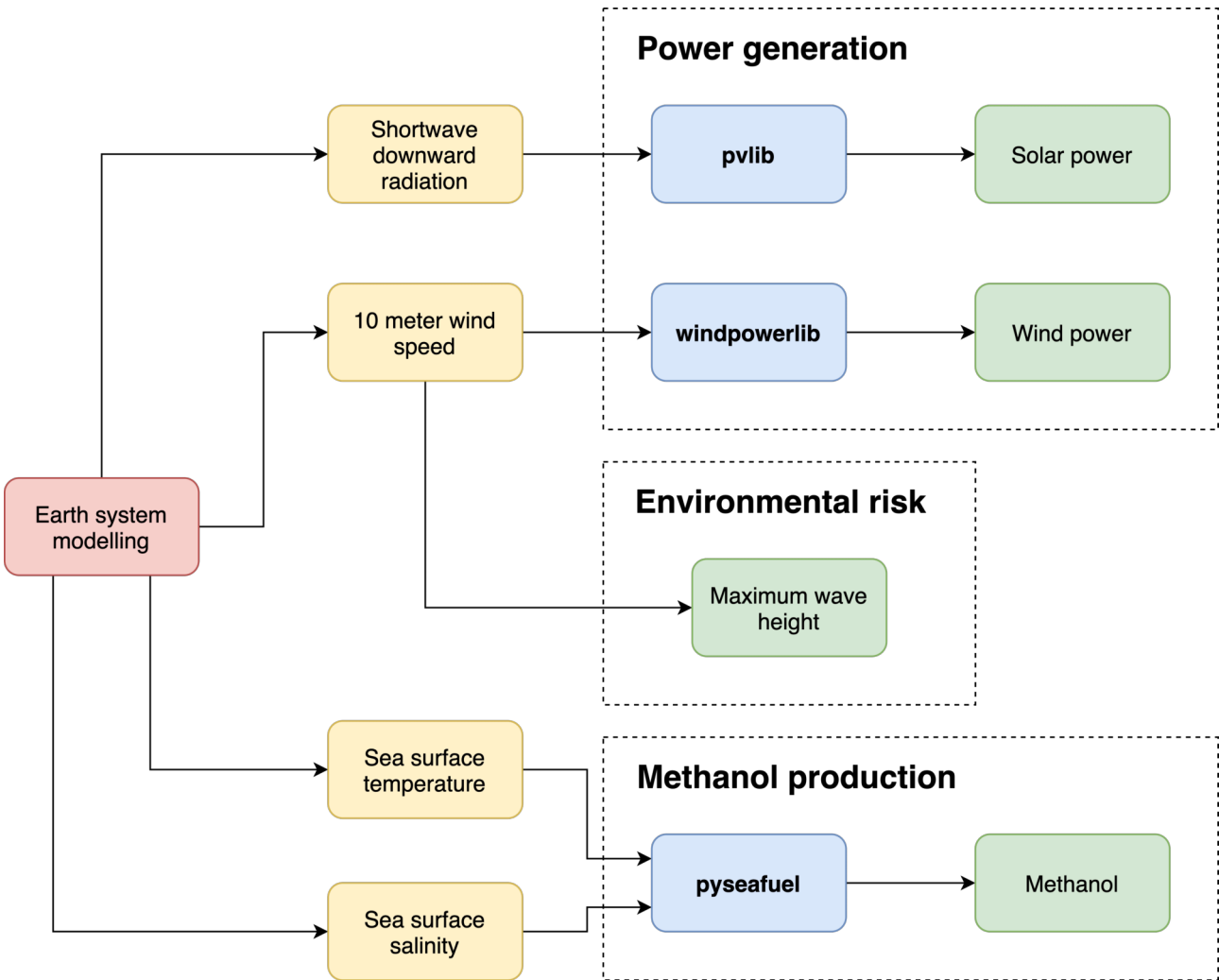


Figure 6.2: Earth system modelling provides shortwave downward radiation, 10 meter wind speed and direction, sea surface temperature, and sea surface salinity. The shortwave downward radiation and 10 meter wind speed are used to determine the power availability in the region. The 10 meter wind speed is used to determine maximum wave height. The sea surface temperature and salinity are used to determine the methanol production.

The atmospheric model data used in this study are the outputs of a RegIPSL simulation, the regional climate model of IPSL [54]. This run used the coupling of the Weather Research and Forecasting Model (WRF) [135] and the ORCHIDEE Land Surface Model [75]. The run was a hind-cast simulation (ERA Interim downscaling), performed at 20 km resolution, spanning the period of 1979 to 2016, within the Med-CORDEX framework [121]. The domain is shown in Fig. 6.3 (a). In addition to being used to calculate the available solar and wind power and maximum wave

heights, the 10 meter horizontal wind components and shortwave radiation are used to force the ocean modelling described below. The 2 meter temperature, 2 meter specific humidity, longwave radiation, precipitation, and snowfall from the atmospheric model data were also used to force the ocean modelling.

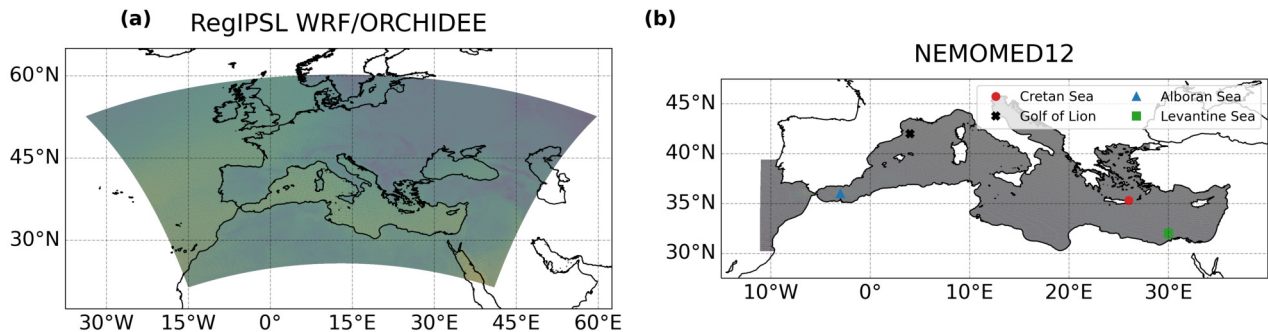


Figure 6.3: Domains of the WRF/ORCHIDEE simulation, (a), and NEMO simulations (b). Both were run within the RegIPSL regional model.

The **N**ucleus for **E**uropean **M**odelling of the **O**cean (NEMO) ocean model (<https://www.nemo-ocean.eu/>; last accessed: June 13th, 2022) is used to simulate the Mediterranean Sea in one year runs for 20 years, from July 1st, 1993 to June 30th, 2013. The model is run in bulk configuration to calculate the surface fluxes, utilizing the aforementioned atmospheric variables. In addition to using the bulk configuration, the NEMO model (v3.6) is also run in the NEMOMED12 configuration. NEMOMED12 is described, with boundary conditions, in [157, 57, 12, 80]; a brief description follows: the domain covers the Mediterranean Sea and a portion of the Atlantic Ocean (see Fig. 6.3 (b)). The latter buffer zone is used to represent the exchanges between the two bodies of water at the Strait of Gibraltar, and its sea surface height (SSH) fields are restored towards the ORAS4 global ocean reanalysis [8]. The 3-D temperature and salinity fields of the buffer zone are restored towards the MEDRYS reanalysis [57]. The Black Sea, runoff of 33 major rivers, and coastal runoff are represented by climatological data from [88]. The initial conditions for each one year run were pulled from the MEDRYS reanalysis [57]. The sea surface temperature and salinity from this model data are used to simulate the power required for the methanol production process.

6.2.1 Power generation

6.2.1.1 Solar

The effective irradiance and solar panel power are calculated using the **pvlib** python library [61]. The global horizontal irradiance (GHI) is provided with the shortwave downwelling radiation from the WRF/ORCHIDEE model data. The direct normal irradiance (DNI) is determined using the DISC model [101] with the NREL implementation. The diffuse horizontal irradiance (DHI) is then calculated from GHI and DNI (<https://pvpmc.sandia.gov/modeling-steps/1-weather-design-inputs/irradiance-and-insolation-2/global-horizontal-irradiance/>, last accessed June 13th,

2022):

$$DHI = GHI - DNI \cos \theta_z, \quad (6.1)$$

Where θ_z is the zenith angle of the sun. The effective irradiance is then determined with the SAPM model from Sandia National Laboratory [74] and assuming an isotropic atmosphere. The SAPM model is also used to calculate the power generation of an arbitrary commercial solar panel, a 2009 SunPower 128-Cell Module, the data of which is provided in **pvlib** [61].

6.2.1.2 Wind

As stated above, the 10 meter horizontal wind components are provided by the WRF/ORCHIDEE model run. However, to simulate the output of an offshore wind turbine, the London Array wind farm will be used as a template, which operates 175 Siemens Gamesa SWT-3.6-120 turbines. These turbines have a hub height of 87 meters. Therefore, the wind speed at 87 meters is estimated with the empirical power law [94]:

$$U_e = U_r \left(\frac{z}{z_r} \right)^\alpha, \quad (6.2)$$

Where U_e is the estimated wind speed at height z . U_r is the reference wind speed at reference height z_r , in this case at 10 meters. α is the empirical coefficient unique to different locations and surface types. For this study, we use $\alpha = 0.11$ [5] for the open sea. From the estimated 87 meter wind speed, the estimated power production of a SWT-3.6-120 turbine can be calculated.

The estimated power production from a Siemens Gamesa SWT-3.6-120 turbine is calculated with the **windpowerlib** python package [56], which provides the power curve for the turbine (see Fig. 6.4). A noteworthy feature of the turbine power curve is the power cutoff if too high of wind speeds are encountered. This cutoff is common to many commercially available turbines to prevent damage from stronger winds. This also limits the productivity of the areas with the highest wind speeds. This turbine has a rotor diameter of 120 meters, which is used to calculate the power generation in terms of power per swept area of the turbine, allowing it to be compared to the solar panel power generation.

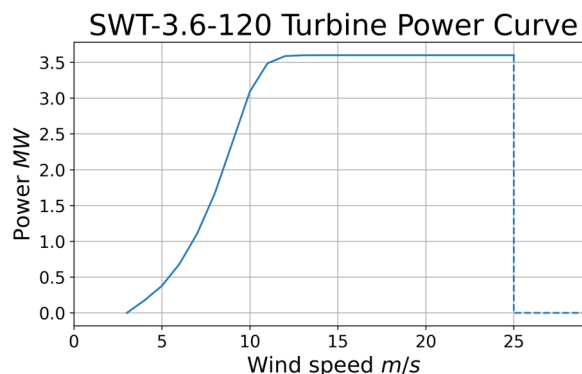


Figure 6.4: Power curve for the SWT-3.6-120 turbine. Provided by the **windpowerlib** python library [56].

6.2.2 Environmental risk

6.2.2.1 Max wave height

The maximum wave height is calculated with the following empirical relationship [112], which assumes a fully developed sea:

$$H_{max} = 2 \left(\frac{U}{12.5} \right)^2, \quad (6.3)$$

Where H_{max} is the maximum wave height, and U is the 10 meter wind speed in knots. Accurately modelling wave heights is a much more complex topic than Eq. 6.3 alludes to, requiring information such as fetch, sea depth, wind direction, and basin geometry and is not calculated in the NEMO ocean model utilized in this study. Therefore, we use Eq. 6.3 to determine potential areas of concern for this study.

6.2.3 Methanol production - pyseafuel

A python package, **pyseafuel** (<https://gitlab.in2p3.fr/energy4climate/public/pyseafuel>; last accessed August 6th, 2022), was specifically made by the authors to numerically simulate the methanol island for this study. This section (6.2.3) describes the structure and theory used in the package. Four subprocesses make up methanol island, as seen in Fig. 6.5, and are simulated by **pyseafuel**: degassing, desalinating, electrolyzing, and reacting. Seawater is fed into both a degasser and desalinator in separate flows. The degasser extracts the CO_2 from the seawater and passes it along to the reactor. The degassed seawater is expelled at this point. Meanwhile, the seawater fed into the desalinator is purified (expelling the brine back to the ocean) and passed along to an electrolyzer. The electrolyzer then separates the purified water into hydrogen gas (H_2) and oxygen gas (O_2). The oxygen is expelled to the atmosphere. The hydrogen is passed to the reactor alongside the carbon dioxide, where they react to form methanol (CH_3OH). Of the four subprocesses, only the reactor subprocess is exothermic and doesn't require additional power except that required to keep it at its operating temperature and pressure. The other three subprocesses all require a supply of power to operate. The subprocesses are described separately below.

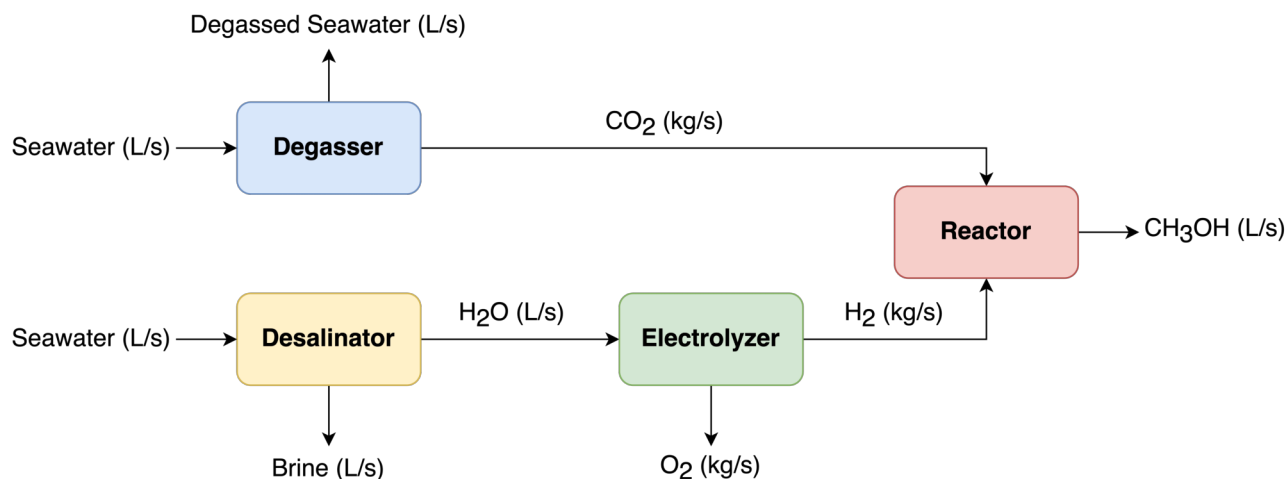


Figure 6.5: Layout of a methanol island simulated by **pyseafuel**. Two arms are fed seawater, one through the degasser to extract CO_2 and one through the desalinator and electrolyzer to produce H_2 . The CO_2 and H_2 is then combined in the reactor to produce CH_3OH , methanol. Waste brine and O_2 are produced as part of the process.

6.2.3.1 Degassing

pyseafuel calculates the degassing subprocess using experimental results from Eisaman et al. 2012. CO_2 dissolved into the ocean immediately reacts with ocean carbon buffer system, represented by the following equilibrium equations [89]:



As the two species are difficult to distinguish from one another, aqueous carbon dioxide ($\text{CO}_2(aq)$) and carbonic acid (H_2CO_3), are typically grouped together as CO_2^* . These equilibrium equations rely on the available hydrogen ions (H^+), as seen in Eq. 6.6 and 6.7, the equations for carbonic acid and carbonate (CO_3^{2-}). The carbon dioxide extraction process implemented currently in **pyseafuel** is based upon the method employed by Eisaman et al. 2012. This method makes use of the dependence of the buffer system on the freely available hydrogen ions. If the buffer system is shifted to a very acidic solution ($\text{pH} < 4.5$), almost all the carbon shifts to exist in the form of CO_2^* , as seen in Fig. 6.6, and readily off-gasses $\text{CO}_2(g)$. The off-gas $\text{CO}_2(g)$ can then be captured and utilized.

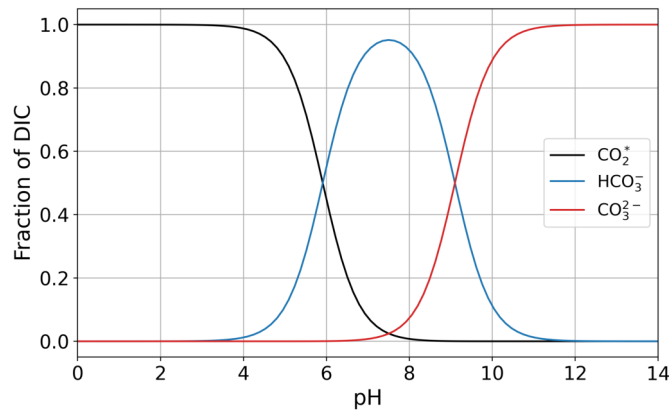


Figure 6.6: The ocean carbon buffer system. The equilibriums and dominant species were calculated using Eq. 6.4 through 6.7. Dissolved inorganic carbon (DIC) is the sum of the three species.

Eisaman et al. 2012 performs this pH shift by splitting the flow into two separate streams, acidifying one stream and basifying the other by using a series of bipolar membranes with an applied potential difference. The off-gassed $\text{CO}_2(\text{g})$ is then collected with a membrane contactor from the acidified stream. The two streams are then recombined, returning the overall flow to a neutral pH, which is then discarded. This process is simulated in **pyseafuel** by fitting quadratic curves to the experimental data provided in the Supplementary Information of Eisaman et al. 2012. The fitted curves for both the energy consumption per mole of extracted $\text{CO}_2(\text{g})$ versus pH and pH versus the ratio of the out-flowing $\text{CO}_2(\text{g})$ (at STP L min^{-1}) and in-flowing seawater (L min^{-1}) data are shown Fig. 6.7. The power requirement and $\text{CO}_2(\text{g})$ extraction of this subprocess are then estimated from these curves.

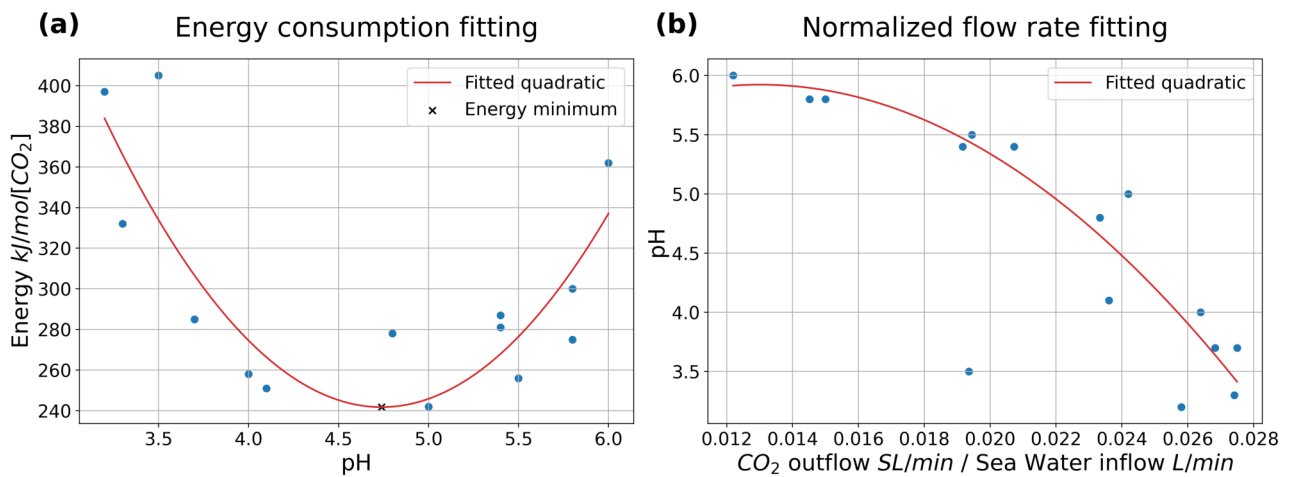


Figure 6.7: The fitted quadratic curves for the energy consumption per mole of extracted CO_2 depending on pH, (a), and for pH versus the ratio of outflow CO_2 over inflow seawater, (b). The fitted equation for (a) is $58.29x^2 - 524.44x + 1423.21 = 0$ where $x = pH$, and for (b) is $-1195.47x^2 + 311.11x + 3.90 - pH = 0$ where $x = \text{the } \text{CO}_2 \text{ outflow} / \text{seawater inflow ratio}$.

6.2.3.2 Desalination

The desalination subprocess is calculated with **pyseafuel** by assuming the process is performed with electrodialysis. Electrodialysis desalinates seawater by applying a potential difference over a

series of cation and anion exchange membranes (CEMs and AEMs; inclusively called ion exchange membranes, IEMs) [161]. These series of IEMs separate the incoming saline flow (feed flow) into a more saline brine flow and a nearly purified fresh water flow, depending on the desired separation. Keeping the power constraint in mind to determine optimal locations for the device, the equation for energy consumption, EC (J L^{-1}), for this subprocess for a single stage setup is (assuming perfect exclusion of the correct ions at the IEMs) [161]:

$$EC = 2RT_f(c_f - c_p) \ln \frac{c_b}{c_p}, \quad (6.8)$$

Where R is the ideal gas constant (taken as $8.3145 \text{ J mol}^{-1} \text{ K}^{-1}$), T_f is the temperature of the feed flow in Kelvin, and c_f , c_p , and c_b are the salinity concentrations of the feed, product, and brine flows (mol L^{-1}). For a multistage process with n stages, the following equation can be derived (using the relevant information from Wang et al. 2020):

$$EC = 2RT_f \zeta_n \ln \left(\frac{1}{(1 - \zeta_n)(1 - R_w^{1/n})} - \frac{R_w^{1/n}}{1 - R_w^{1/n}} \right) c_f \sum_{i=1}^n (1 - \zeta_n)^{i-1}, \quad (6.9)$$

Where $\zeta_n = 1 - (1 - \zeta)^{1/n}$ is the salt removal percentage per stage n , with ζ as the overall salt removal percentage of the subprocess. R_w is the ratio of the fresh water outflow over the saline feed flow.

6.2.3.3 Electrolysis

The electrolysis subprocess is calculated in **pyseafuel** using the simplified model for proton (or polymer) exchange membrane (PEM) electrolysis, derived by Shen et al. 2011:

$$P_e = IV = K(V - IZ - E_0)^2 + I^2Z, \quad (6.10)$$

Where P_e is the subprocess power consumption per stack area (W cm^{-2}), I is the operating current per stack area (A cm^{-2}), V is the operating voltage (V), K is the power coefficient ($\Omega^{-1} \text{ cm}^{-2}$), Z is the internal resistance of the electrolyzing cell per stack area ($\Omega \text{ cm}^{-2}$), and E_0 is the cell reversible potential of electrolysis for the separation of water into hydrogen and oxygen gas (V). PEM electrolysis works by applying a voltage across a membrane in contact with a pure water flow. The pure water dissociates into H^+ ions and O_2 from the applied potential and the PEM then only permits the H^+ ions to cross, whereby the ions then combine with electrons to form H_2 . The value for Z is measured for a given experimental cell, then K can be determined from fitting Eq. 6.10 to the experimentally measured I and V . In implementation, I is determined by the desired outflow of H_2 (and therefore required inflow of pure water) and then Eq. 6.10 is solved for in terms of V , given K , Z , and E_0 are known. P_e can then be computed.

6.2.3.4 Reactor

The reactor subprocess is simulated in **pyseafuel** using the plug flow reactor model described by Terreni et al. 2020 (Fig. 6.8). The following equations describe the model:

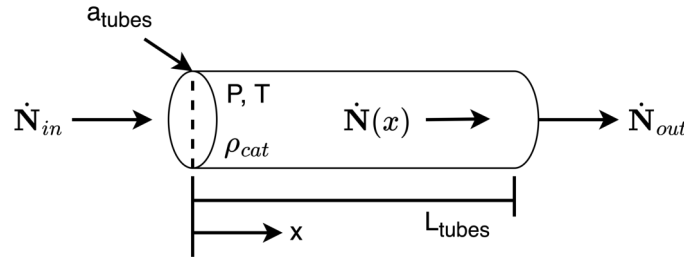


Figure 6.8: A single tube for a plug flow reactor. a_{tubes} is the single tube area. P and T are the reactor operating pressure and temperature. x is the coordinate along the length of the tube, which has a length of L_{tubes} . ρ_{cat} is the density of the catalyst packed into the reactor tube. $\dot{N}(x)$ is the molar flow rate along the length of the tube, with subscripts in for the inflow and out for outflow.

$$\frac{d\dot{N}_i(x)}{dx} = \rho_{cat} A_{tubes} R_i(\mathbf{p}(x)), \quad (6.11)$$

$$\mathbf{p} = \frac{P}{P_0} \frac{\dot{N}}{\sum_j \dot{N}_j}, \quad (6.12)$$

Where ρ_{cat} is the density of the catalyst in the plug flow tubes, A_{tubes} is the cross-sectional area of all the tubes (number of tubes multiplied by a_{tubes} ; see Fig. 6.8), and \mathbf{p} is the array of reduced partial pressures, with P as the reactor operating pressure (bars) and P_0 as the reference pressure (taken as 1.01325 bars). The i and j are the indexes for the following arrays:

$$\dot{N} = (\dot{N}_{CO}, \dot{N}_{CO_2}, \dot{N}_{H_2}, \dot{N}_{H_2O}, \dot{N}_{CH_3OH}), \quad (6.13)$$

$$\mathbf{R} = (R_{CO}, R_{CO_2}, R_{H_2}, R_{H_2O}, R_{CH_3OH}) = (-r_1 + r_2, -r_2 - r_3, -2r_1 - r_2 - 3r_3, r_2 + r_3, r_1 + r_3). \quad (6.14)$$

Where \dot{N} is the array of molar flows of the labeled species and \mathbf{R} is the array of composite reaction rates for the labeled species, with the individual subcomponents described in the following:

$$r_1 = k_1 K_{CO} \left[P_{CO} P_{H_2}^{3/2} - \frac{P_{CH_3OH}}{P_{H_2}^{1/2} K_1^{eq}} \right] / D, \quad (6.15)$$

$$r_2 = k_2 K_{CO_2} \left[P_{CO_2} P_{H_2} - \frac{P_{H_2O} P_{CO}}{K_2^{eq}} \right] / D, \quad (6.16)$$

$$r_3 = k_3 K_{CO_2} \left[P_{CO_2} P_{H_2}^{3/2} - \frac{P_{CH_3OH} P_{H_2O}}{P_{H_2}^{3/2} K_3^{eq}} \right] / D, \quad (6.17)$$

$$D = (1 + K_{CO}P_{CO} + K_{CO_2}P_{CO_2}) \left[P_{H_2}^{1/2} + \frac{K_{H_2O}}{K_{H_2}^{1/2}} P_{H_2O} \right], \tag{6.18}$$

Where r_m are the reaction rates ($m = 1 \rightarrow 3$), P_j are the partial pressures of the j components, and k_m and K_* are the equilibrium coefficients, available in Terreni et al. 2020. In the reactor, the H_2 and the CO_2 interact with the catalyst to combine to form CH_3OH , however they can also combine to form carbon monoxide (CO) and water (H_2O) as part of the reverse water gas shift (RWGS) reaction [149]. The effectiveness of the conversion from the CO_2 to CH_3OH depends strongly on the operating pressure, P , and temperature T of the reactor, as well as on the ratio of the initial molar flows of CO_2 and H_2 ($r = \dot{N}_{H_2}^0 / \dot{N}_{CO_2}^0$). The dependence on P and T can be seen in Fig. 6.9 (a), where the fractional conversion of initial CO_2 to CH_3OH , ξ ($= \dot{N}_{CH_3OH} / \dot{N}_{CO_2}^0$), is larger with larger pressures and lower temperatures. ξ is calculated using the equilibrium model provided in Terreni et al. 2020 (see the article for details).

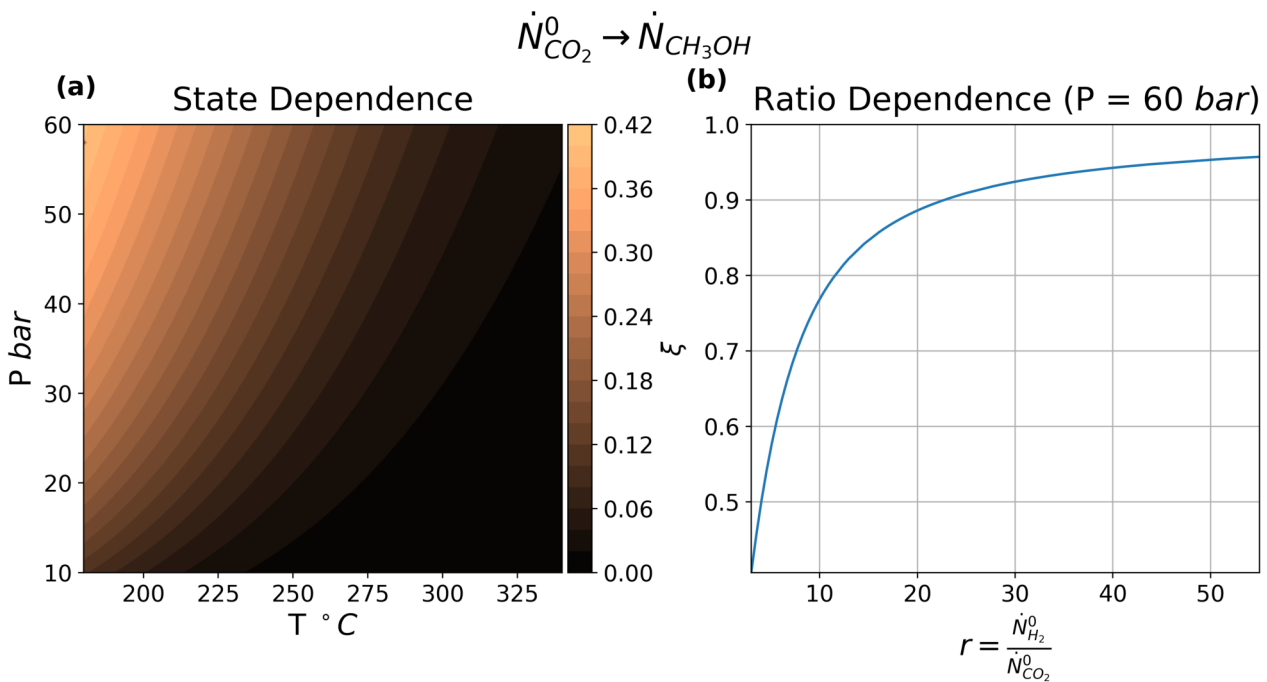


Figure 6.9: The conversion factor, ξ , or the percentage of moles of CO_2 transformed into CH_3OH . It was calculated using the equilibrium equations presented in Terreni et al. 2020, with varying state conditions (P and T) and molar ratios of H_2 and CO_2 . The state dependence curve was calculated with a H_2/CO_2 molar ratio of 3, which is the stoichiometric ratio.

When looking at the initial ratio of molar flows in Fig. 6.9 (b), "over-saturating" the reaction with H_2 improves ξ (calculated with the same equilibrium model as before) significantly to a point, after of which there are diminishing returns with an increasing ratio. However, as will be shown later in this study, the process of producing H_2 requires a significant amount of power, so a favorable r must be balanced with a reasonable power requirement.

6.3 Power Generation

6.3.1 Solar

The results for the 20 years are primarily presented in seasonal averages, arranged by the months of December, January, and February (DJF) for winter, March, April, and May (MAM) for spring, June, July, and August (JJA) for summer, and September, October, and November (SON) for fall. The results for the calculated and averaged effective irradiance are shown in Fig. 6.10. The mean values over the sea range from 276.16 W m^{-2} in the summer, to a low of 179.63 W m^{-2} in the winter. As expected, the lowest values are found in winter, with the largest in summer. There's also a north/south variation, which is much more apparent during the winter and fall, due to the increased length of night during these seasons. The effective irradiance is essentially the available solar power that the solar panel can capture. As such, the solar panel power generation follows the same spatial variance as the effective irradiance, see Fig. 6.11, just at reduced values. Mean values over the sea range from 118.56 W m^{-2} in summer to 82.93 W m^{-2} in winter, with intermediate values in the shoulder seasons. The resulting prime locations for solar power are along the north coast of Africa and the Levantine Sea, as these areas benefit from larger amounts of insolation during the fall and winter months.

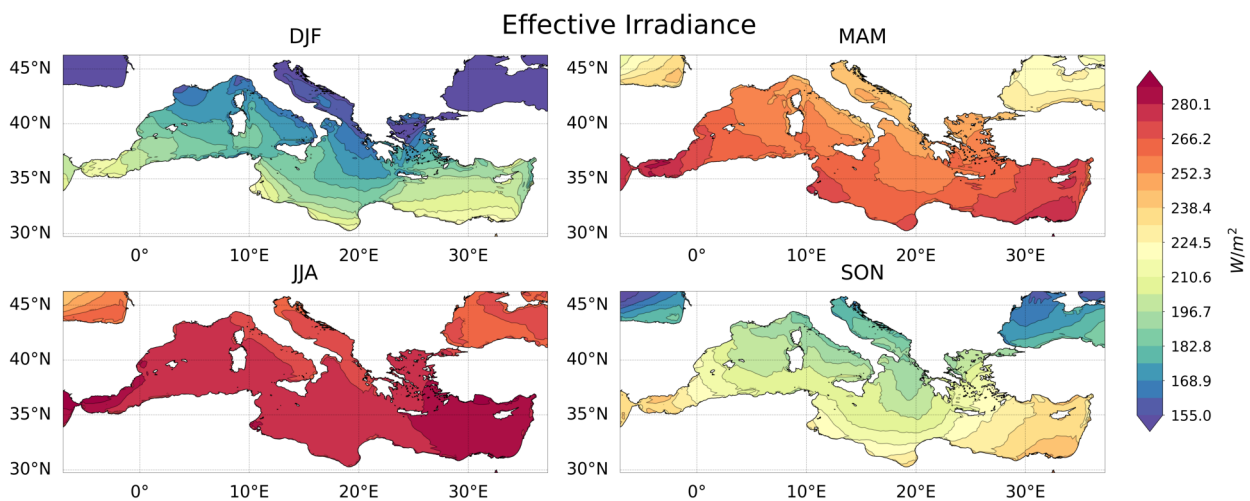


Figure 6.10: Seasonally averaged effective irradiance calculated from with the **pvlb** python package and WRF/ORCHIDEE shortwave radiation data.

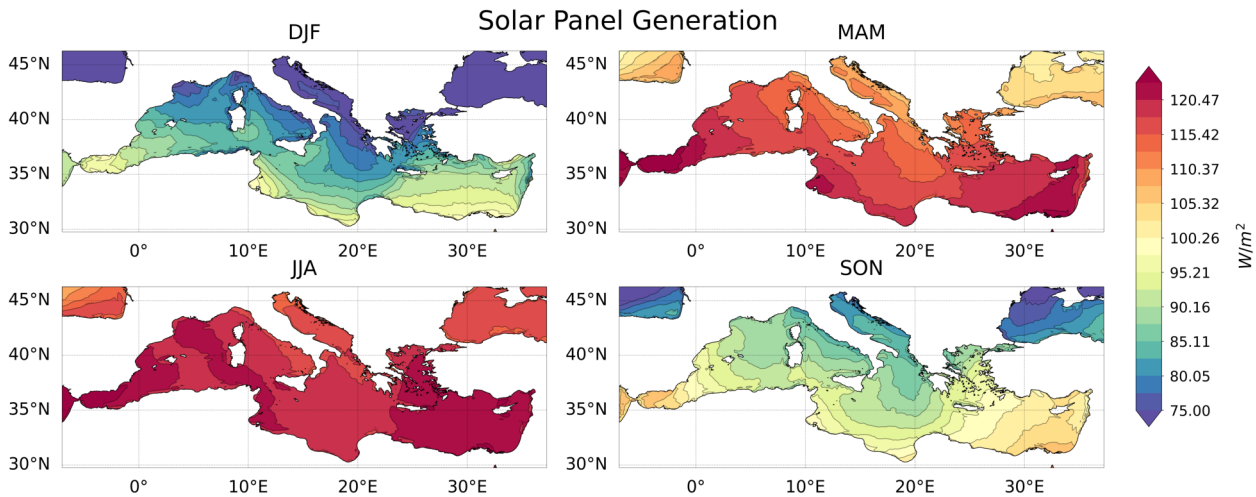


Figure 6.11: Same as Fig. 6.10 but for the calculated solar panel power generation.

6.3.2 Wind

The seasonally averaged winds are shown in Fig. 6.12. Two main regions are affected by strong winds in the Mediterranean: the Aegean Sea during the entire year but with the strongest winds in summer, the Etesians, where seasonal average speeds over 6 m/s can be found, and the Gulf of Lion during the winter, where it experiences the Mistral winds that are more frequent and stronger during the winter months [50]. The calculated power generation per swept area for the SWT-3.6-120 turbine is shown in Fig. 6.13. It follows the same trends as the winds, however, only the two areas mentioned above with stronger, more persistent winds show any meaningful production, despite that wind speed seasonal averages over 3 m/s can be found over most of the Mediterranean basin over most of the year.

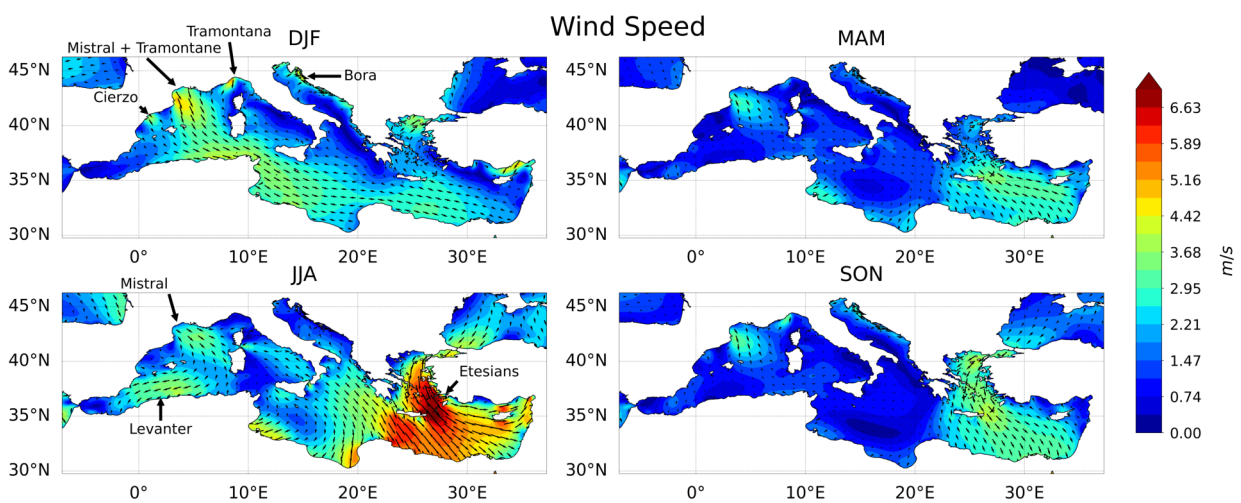


Figure 6.12: Seasonally averaged wind speeds and directions of the WRF/ORCHIDEE 10 meter wind data. During the winter months, the Bora [67], Mistral and Tramontane [36, 31], Tramontana [164], and Cierzo [100] winds can be seen. During the summer months, the summer Mistral [34], Levanter [164], and Etesian [165] winds can be seen.

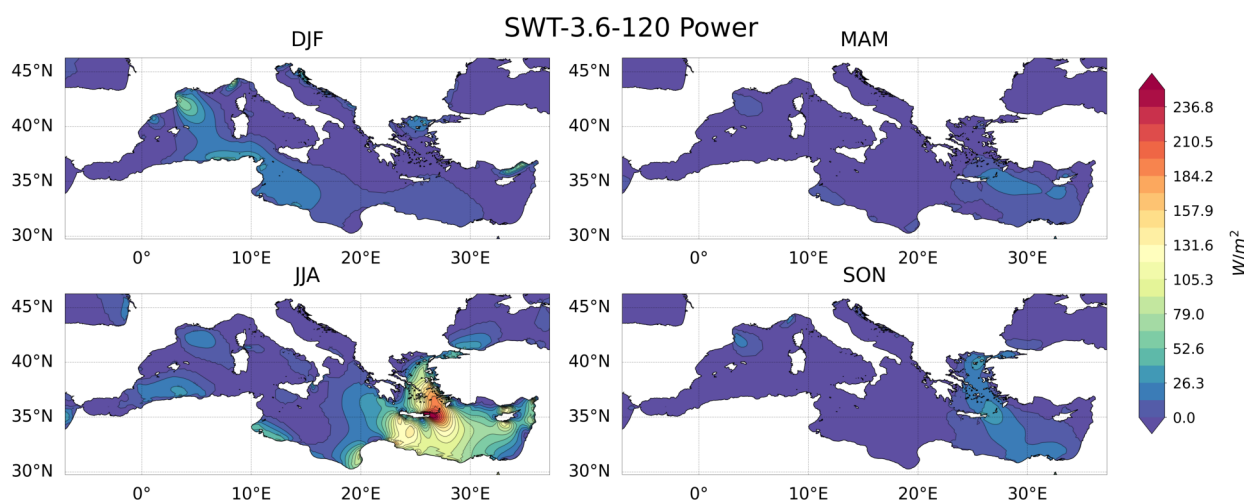


Figure 6.13: Seasonally averaged calculated power generation using a SWT-3.6-120 industrial turbine with height corrected wind speed data (with Eq. 6.2) from the WRF/ORCHIDEE 10 meter wind speed data.

6.4 Environmental Hazards

With regard to the potential hazard the methanol island structure can experience, the maximum wave height is just one ingredient needed to evaluate the risk to the structure. Much like accurately modelling ocean surface waves requires more variables than what is within the scope of this study, as discussed in Sec. 6.2.2.1, accurately measuring the risk to ocean installations that surface waves impose requires more information from the wave properties than just the maximum wave height. Variables such as the wave directions, periods, and height spectra are needed to estimate structure loading [115], as well as details about the structure itself, for both floating solar panels [68] and offshore wind turbines [98]. However, the maximum wave height gives us preliminary guidance for areas to avoid when placing a methanol island.

The maximum wave heights over the 20-year period are shown in Fig. 6.14. The largest wave heights are co-located with the strongest winds, as expected, given the wind dependency in Eq. 6.3. Overall, there are larger values in the western Mediterranean basin than in the eastern basin. In particular, areas affected the most include (moving from west to east) the Gulf of Lion, the Balearic Sea and parts of the Algerian basin, the Gulf of Gabes off the coast of Tunisia, the Ionian Sea, and the Aegean Sea, with most of the peak values in these areas at around 2.5 meters. Otherwise, the rest of the Mediterranean shows values under 1.75 meters. These results appear to agree with the general spatial variability of the significant wave height, which is related to the maximum wave height ($H_{max} \approx 2H_S$, where H_S is the significant wave height; [112]), presented in Galanis et al. 2011, with the exception that the Aegean Sea is less of a hotspot in their study than in our results. With this information, the aforementioned sites should be avoided for methanol island placement.

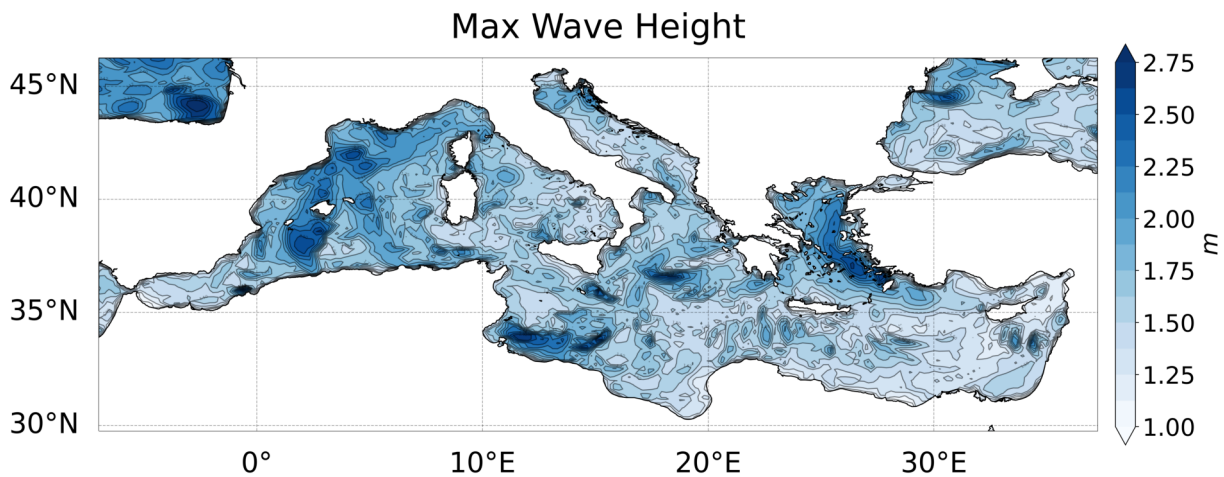


Figure 6.14: Calculated maximum wave heights using the 10 meter wind speeds from the WRF/ORCHIDEE model outputs and Eq. 6.3.

6.5 Methanol Production

The values used for the **pyseafuel** simulation are summarized in Table 6.1. The simulated methanol island is given a flow rate of 10 L s^{-1} for the carbon production arm (the degasser), which is around $2/3$ the flow rate of a French fire hydrant (1000 L min^{-1}). The hydrogen production arm (the desalinators and electrolyzer) is given a flow rate of 0.01 L s^{-1} , which is about a tenth of the flow rate from a European kitchen faucet (6 L min^{-1}). These are small flow rates and would be much larger in full scale application, however, our analysis will be confined to the "production efficiency" the methanol island or the methanol production flow rate divided by the required power. This normalizes the analysis, making it applicable to studying the spatial variability of the production.

Parameter	Value	Parameter	Value
Degasser			
Seawater inflow	10 L/s		
Desalinator			
Seawater inflow	0.01 L/s	n stages	1
R_w	0.5	ζ	0.99
Electrolyzer			
E_0	1.4 V	K	$27.8 \Omega^{-1} \text{ cm}^{-2}$
R	$0.15 \Omega \text{ cm}^{-2}$	A_{stack}	250 cm^2
Reactor			
T	180 °C	P	60 bars
A_{tubes}	3.14 m^2	L_{tubes}	3 m
ρ_{cat}	1000 kg m^3		

Table 6.1: These are parameters and their values that are used to numerically simulate a methanol island with **pyseafuel**, separated by subprocess (Fig. 6.5). The electrolyzer parameters are common values in industry [134, 106]. T and P for the reactor are within the range of previously tested temperatures and pressures for the methanol production from carbon dioxide hydrogenation [136]. Note: around 2 V minimum is typically required to generate the necessary current densities for electrolysis to occur [52].

The flow rates for the two arms, 10 L s^{-1} and 0.01 L s^{-1} , result in a H_2 to CO_2 mole ratio of 25.83. This results in a conversion factor for the plug flow reactor of 0.91, which is very similar to the equilibrium obtained conversion factor shown in Fig. 6.9 (b).

The simulated island has three main power draws: from the degasser, the desalinator, and the electrolyzer. With the current configuration, only one depends on the spatial variability of the Mediterranean surface waters: the desalination subprocess, which depends on the sea surface temperature (Fig. 6.15) and the sea surface salinity (Fig. 6.16). However, for the flow rate simulated here, it is the lowest of the three power draws, ranging from $106.57 \pm 78.6 \text{ W}$ in the spring (mean \pm standard deviation) to $109.17 \pm 80.52 \text{ W}$ in the summer, when compared to 2617.66 W consumed by the degassing subprocess and 2887.65 kW consumed by the electrolysis subprocess. Here, the electrolysis subprocess is by far the largest power draw, consuming multiple orders of magnitude larger than either the degassing or desalination subprocesses. Since this process produces the hydrogen for the reactor, it is necessary to balance the benefit of an improved conversion factor, ξ , from a higher hydrogen to carbon dioxide ratio (see Fig. 6.9 (b)) with the higher power cost of producing more hydrogen to optimize the efficiency of the overall methanol production.

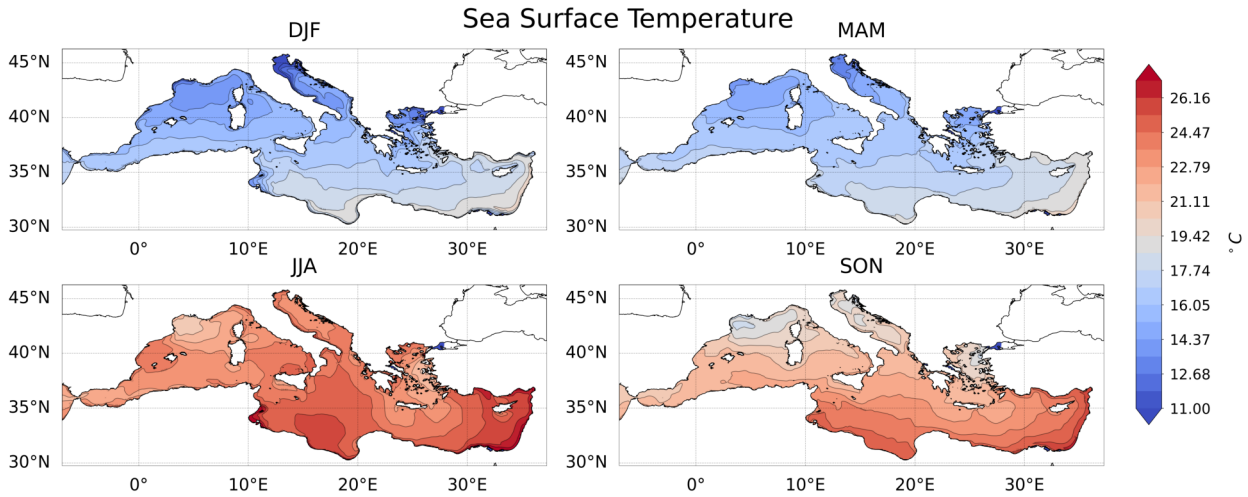


Figure 6.15: Seasonally averaged sea surface temperature from the NEMO simulation set.

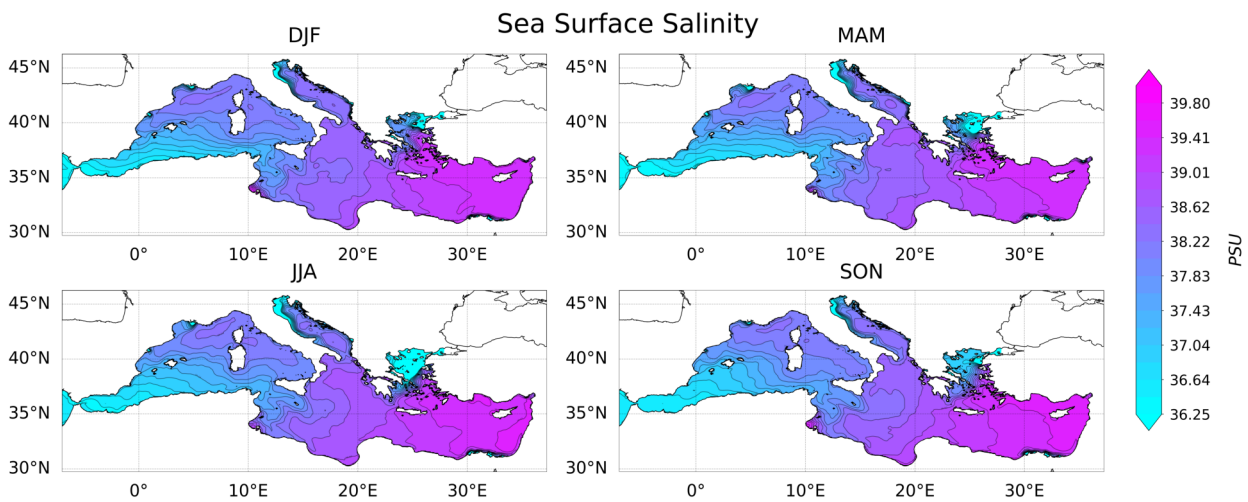


Figure 6.16: Seasonally averaged sea surface salinity from the NEMO simulation set.

Keeping in mind that only the desalination subprocess depends on spatial variability and is the smallest of the three subprocesses in terms of power consumption, the methanol production per power, in units of $\mu\text{L day}^{-1} \text{W}^{-1}$, varies very little over the Mediterranean basin. A mean value of $11.94 \mu\text{L day}^{-1} \text{W}^{-1}$ is found over all the seasons, with the standard deviation changing from $\pm 0.00032 \mu\text{L day}^{-1} \text{W}^{-1}$ in winter and spring to $\pm 0.00033 \mu\text{L day}^{-1} \text{W}^{-1}$ in summer and fall.

To compare the methanol production powered by either solar power or wind power, the methanol production efficiency is multiplied by power generation in terms of W m^{-2} , resulting in a flow rate over area of power generation. For solar panels, this area is the area of panels needed for power generation, whereas for wind power, this area is the swept area of the turbine. Organizing the results in this manner allows us to compare areas that would need larger power generation installations versus areas that would need less for a given methanol flow rate. Figure 6.17 shows this flow rate per power generation area for a simulated island powered off of solar panels. Figure 6.18 shows the same but for an island powered off of wind energy.

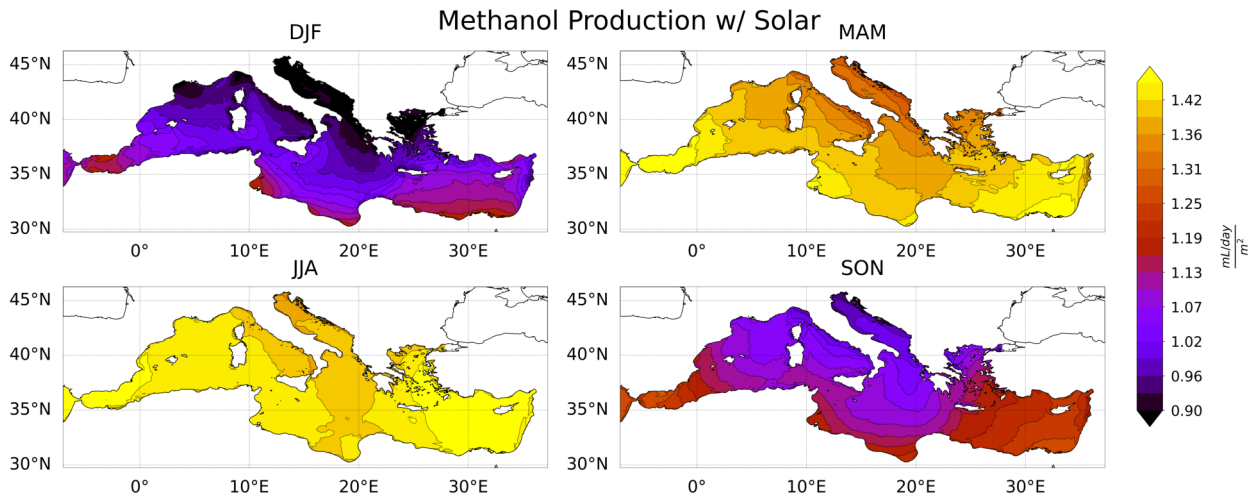


Figure 6.17: Methanol production powered by the solar panel power shown in Fig. 6.11. Note the values are in milliliters per day per area.

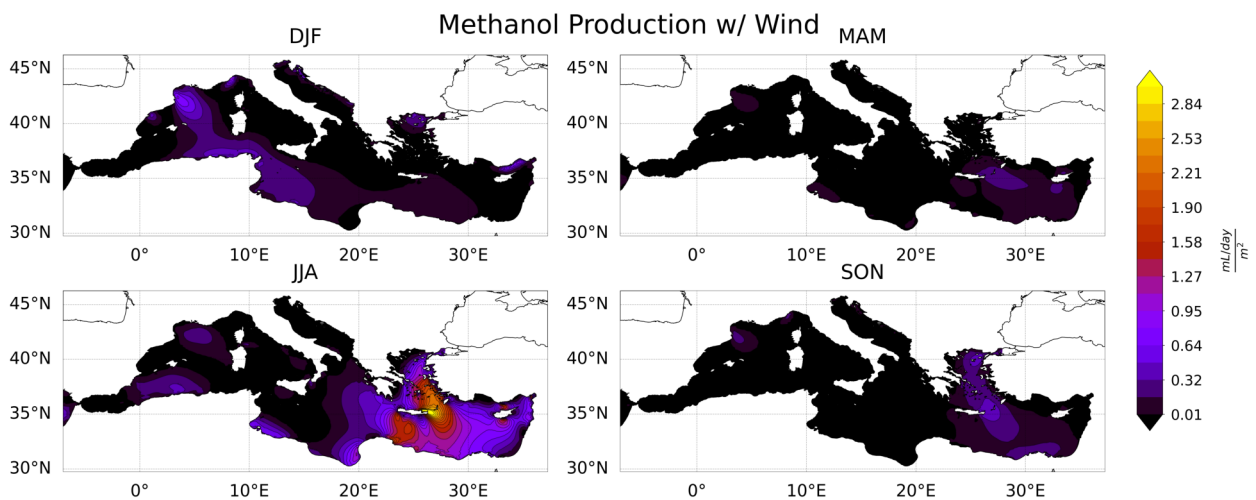


Figure 6.18: Same as Fig. 6.17 but the production is powered with the turbine power from Fig. 6.12.

As the methanol production per Watt is essentially constant over the entire Mediterranean basin, the results in Fig. 6.17 and 6.18 essentially show the same results as Fig. 6.11 and 6.12, respectively, as the power generation is just multiplied with an effectively constant coefficient. Larger production rates per power generation area are found in the southern part of the basin during the winter, spring, and fall for a solar panel powered methanol island, with high production rates over most of the basin during the summer. For the wind powered methanol island, higher production rates are found in the Gulf of Lion and Aegean Sea (as well as part of the Levantine), just as the wind power generation was higher in these regions as well, during their respective productive seasons.

6.6 Integrated Production

To look at how the methanol production changes over the course of the year with a finer temporal resolution, example locations have been selected to be examined in more detail. These locations

are in the Alboran Sea, the Gulf of Lion, the Cretan Sea, and the Levantine Sea. Exact coordinates are given in Table 6.2 and the locations are shown in Fig. 6.3 (b). These locations were selected as they were located in the solar power and wind energy supply hotspots pointed out in Sec. 6.3. The atmospheric and oceanic derived data were ensemble averaged over the 20 years into a single year. The results for solar panel and turbine power generation, and methanol production with solar power and wind energy are shown in Fig. 6.19.

Location	Alboran Sea	Gulf of Lion	Cretan Sea	Levantine Sea
Coordinates	36° N -3 ° E	42° N 4 ° E	35.30° N 26 ° E	32° N 30 ° E
Max Wave Height (m)	1.54	2.54	1.55	1.36
Integrated Methanol Production (mL/m²)				
Solar	494.21	445.52	465.10	484.70
Wind	20.80	219.60	457.29	152.85

Table 6.2: Point locations examined in more detail due to their favorable solar and wind power generation.

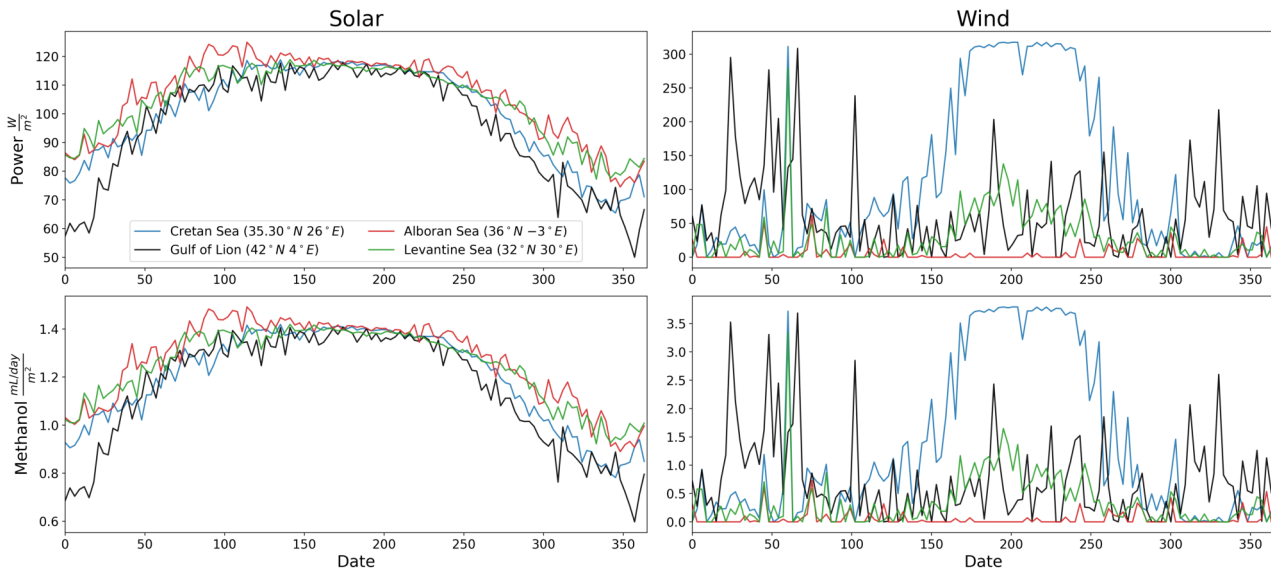


Figure 6.19: Ensemble time series for the point locations in Table 6.2. Solar panel and SWT-3.6-120 wind power generation are presented, as well as the corresponding methanol production from the two power resources. The solar panel power generation and methanol production time series are window averaged to make the temporal trends more visible, as production drops to zero every night.

What we see from the figures is that the solar power generation is fairly consistent among the different locations, with maximum values approaching 140 W m^{-2} level in summer time and falling to around 60 W m^{-2} in winter time (again in Fig. 6.19, the values are window averaged to better show the trend and therefore hide some of the peak variability). The Gulf of Lion sees less power available from solar over the course of the year, as it is further north than the other locations. However, both it and the Cretan Sea see more available power from wind energy, with values reaching 300 W m^{-2} in both locations. In fact, the Cretan Sea location experiences a limit in generated power due to the SWT-3.6-120 power cutoff (Fig. 6.4), and is limited to values under about 315 W m^{-2} . The main negative of the wind resource is its temporal variability with respect to solar power. While peak wind power values are around 300 W m^{-2} compared to solar power's 140 W m^{-2} , values are

often closer to zero during less productive times of the year. For example, the Cretan Sea location sees a peak during the summer and fall months, but has lower levels of power generation during the rest of the year, or off season. The Gulf of Lion shows a similar, yet less pointed trend with the on and off season timing reversed. The methanol production values follow the power curves closely for both the solar and wind energy, and thus reflect the same consistency/variability, just as they had in Fig. 6.17 and 6.18. An important note however, is that the methanol production process operates as a quasi steady state process. It would be unable to handle extreme short timescale variations, potentially requiring the wind power to be smoothed before using it to power the island, whereas solar power may not.

To more accurately compare methanol production between the two power resources, the production was integrated over the year span, resulting in a single value per location. These values are presented in Table. 6.2. Production amounts with solar power are similar across the different locations, with the Alboran and Levantine Sea locations producing the most. On the other hand, production amounts with wind energy are much more varied, following suit with the prior discussion. Only one location produced more methanol with wind than with solar power, the Cretan Sea location, which produced 7% more with wind. The runner-up, the Gulf of Lion, produced 42% less with wind, even though it was the other wind energy hotspot in the Mediterranean.

This same procedure was done for all the spatial points in the Mediterranean and is presented in Fig. 6.20, including the integrated production for solar, wind, and the difference between the two. The production based on solar power features the highest levels along the north coast of Africa, specifically in the Alboran and Levantine Sea. The production based on wind power features the largest levels in the Gulf of Lion, Aegean Sea, and parts of the Levantine Sea. Unsurprisingly, the simulated island produces more powered by solar power everywhere except for around the eastern side of the island of Crete, where wind produces slightly more.

Integrated Methanol Production

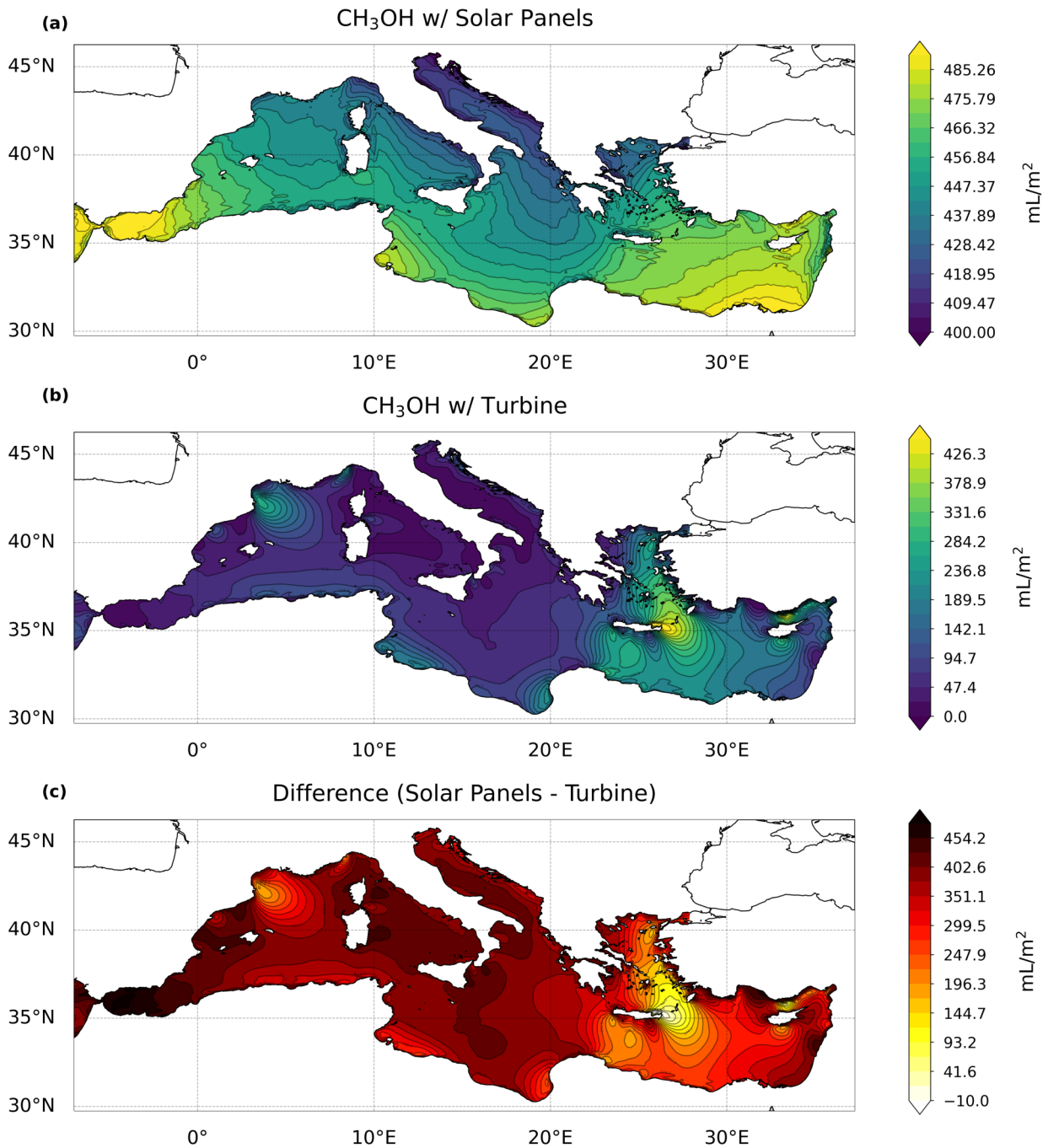


Figure 6.20: The integrated methanol production over the course of the ensemble averaged year for a simulated island running on solar power, wind power, and the difference between the two production simulations.

6.7 Optimal Locations

Pooling together the results from Sec. 6.4 and 6.5 allows us to label optimal locations for both solar and wind powered methanol producing islands.

As previously stated in Sec. 6.4, more information is needed to determine the limiting factors more accurately when it comes to the effect of environmental hazards. However, information on the limiting significant wave height for certain installations procedures for offshore wind farms are used to estimate sensitive areas to wave height [117]. Areas with maximum significant wave heights greater than 1.5 meters are considered poor locations as this height is the maximum height that the most sensitive vessels are unable to mitigate (tug boats and crew transfer vessels; see Ramachandran et al. 2022 Table 3). Marginal locations are areas with maximum significant wave heights between 1 and 1.5 meters, as these locations are manageable for some of the sensitive vessels in Table 3 of Ramachandran et al. 2022. The remaining areas are considered good locations for placement. Poor, marginal, and good locations for wave heights are shown in Fig. 6.21 subplot (a).

For the results from Sec. 6.5, the thresholds to separate the production rates into the different categories are more arbitrary. However, optimal locations follow the trends that were highlighted in that section. Fig. 6.21 (b) shows the optimal locations for solar-powered islands, in conjunction with the wave height information, with the poor locations featuring rates of less than 400 mL m^{-2} integrated over the year. Marginal locations are marked by rates between 400 and 475 mL m^{-2} , with good locations marked by rates higher than 475 mL m^{-2} . Therefore, when considering both the limitations due to maximum significant wave heights and methanol production, the most optimal locations for solar-powered islands are in the Alboran and Levantine Sea, with some locations along the northern coast of Africa.

For wind powered islands, poor locations are marked by areas producing less than 140 mL m^{-2} over the course of a year. Marginal locations are marked by rates between 140 and 350 mL m^{-2} , with any location over 350 mL m^{-2} marked as a good location. Fig. 6.21 (c) shows the optimal locations for wind powered islands, again in conjunction with the wave height limitations found in subplot (a). Wind powered islands have less optimal locations than solar-powered islands, with the best locations around the eastern side of the Greek island of Crete, and just north of the island nation of Cyprus.

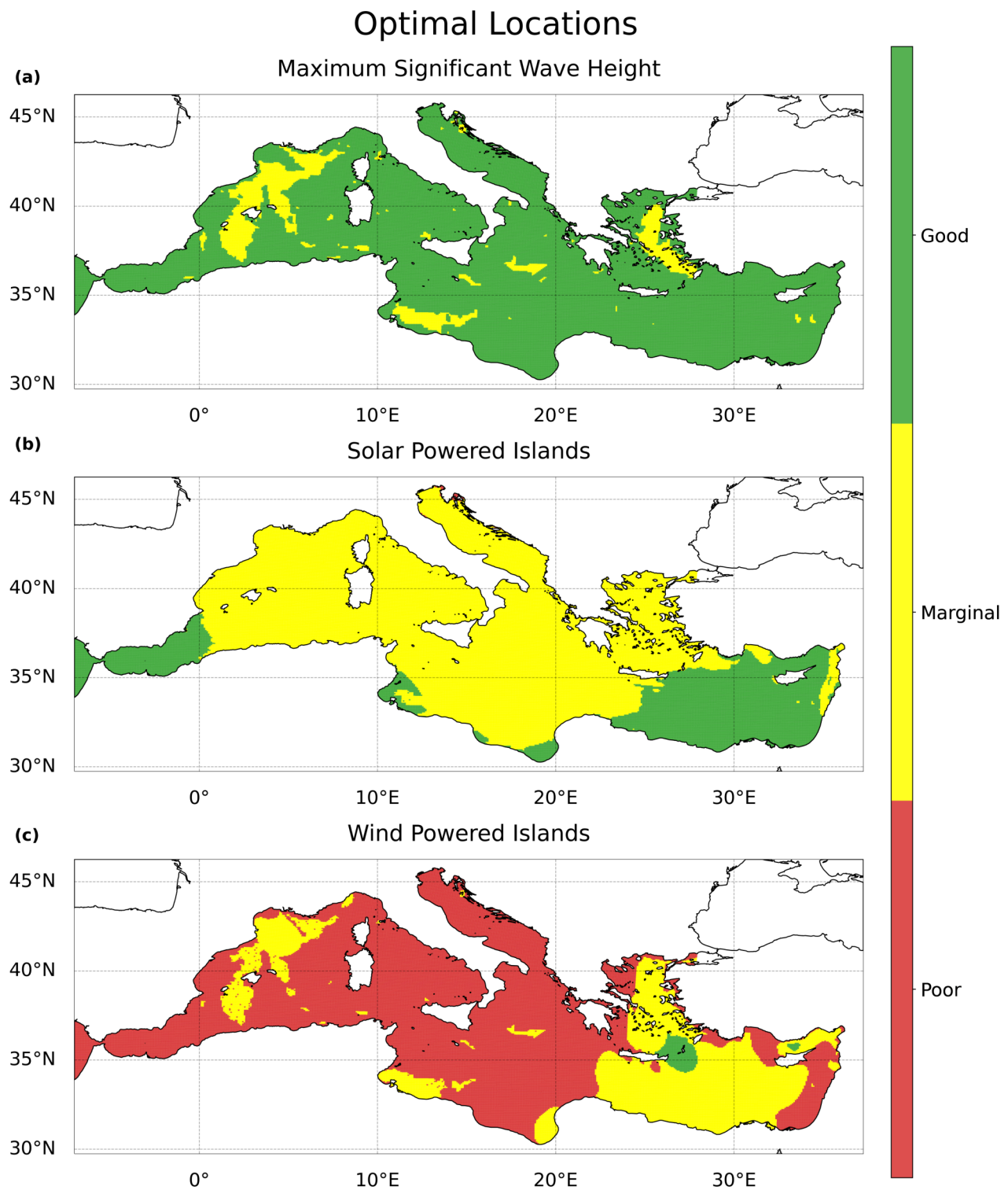


Figure 6.21: Optimal locations for solar or wind powered methanol producing islands. Subplot (a) shows the poor (none shown), marginal, and good locations according to the maximum significant wave heights (poor: above 1.5 m, marginal: between 1 and 1.5 m, good: below 1 m). (b) shows the combined above maximum significant wave height and solar-powered methanol production optimal locations (poor: below 400 mL m^{-2} integrated methanol production over a year, marginal: between 400 and 470 mL m^{-2} , good: above 470 mL m^{-2}). (c) is the same as (b) but for wind powered islands (poor: below 140 mL m^{-2} , marginal: between 140 and 350 mL m^{-2} , good: above 350 mL m^{-2}).

6.8 Remote and Island Communities

Remote and island communities typically depend on oil for their energy needs [19]. The oil has to be shipped in, increasing the cost relative to the prices available to mainland communities, especially for islands (Smart Islands Initiative, <https://www.smartislandsinitiative.eu/en/index.php>; last accessed June 13th, 2022). This makes island communities prime candidates for the device described in this study, as they can produce methanol or methanol derived products on site. The Mediterranean Sea contains a number of island communities, from the islands of Greece, Italy, and Spain just to name a few. We will take two examples into consideration, the Greek island of Crete and the Spanish Balearic Islands.

For the first example, Crete consumed 3.95 TWh of gasoline and diesel during the year of 2016 [156]. Taking the energy density of methanol as $1.56 \times 10^7 \text{ J L}^{-1}$, 0.91 GL of methanol would be needed to replace the consumed energy from oil. To produce this amount of methanol per year with a solar-powered methanol producing island, about 1962 km^2 of solar panels, or about a quarter of the surface area of Crete (8336 km^2), would be needed to supply the necessary power. If a wind powered device was used, 176447 SWT-3.6-120 turbines would be needed. The London Array construction cost was £1.8 billion for 175 turbines. If the cost is proportionally scaled, to supply Crete with the necessary methanol through wind power, the turbines would cost £1.8 trillion. Without considering the sea surface usage of either power method, this would not be a plausible solution for Crete. However, as part of a diversified energy mixture [19], storing energy as methanol and burning it when needed could be an effective alternative to hydrogen, as it is a much more stable substance to store.

For the second example, the entire economy of the Balearic Islands consumed 30.84 TWh of energy for the year of 2012 [48]. To supply these islands with the same amount of energy in methanol, 7.12 GL of methanol would be needed. For a solar-powered device, 15863 km^2 of solar panels would be needed. For a wind powered device, 605096054 turbines would be needed. The energy consumption is an order of magnitude larger than Crete's oil consumption, with the required amount of power sources following suit. The same conclusions for Crete apply here as well.

6.9 Discussion

The simulated methanol island presented here requires information from the ocean and atmosphere. When calculating the power requirement to run the device, the desalination process relies on the sea surface salinity and temperature, however, it is the only process to rely on the ocean surface variables. This is because the other potentially effected process, the degassing subprocess, is decoupled from the concentration of CO_2 in the surface waters. Eisaman et al. 2012 used artificial seawater, as do other groups studying CO_2 extraction from seawater (3 of the 4 groups in Table 1 of Sharifian et al. 2021 use artificial seawater), which has a constant concentration of CO_2 , and

therefore a varied concentration can't be tested. This means it is difficult to accurately estimate the CO_2 given a certain concentration of dissolved inorganic carbon (DIC) in the feed flow. However, in the Mediterranean surface waters, the values of DIC don't vary too much from one side of the sea to the other, and are all around $2300 \mu\text{mol kg}^{-1}$ [3]. Because of this, the spatial variability of DIC shouldn't affect our results much, even if the extraction process was dependent on DIC concentration. The remaining two subprocesses, the electrolysis and reactor subprocesses, don't depend on the ocean variables nor atmospheric variables, at least not directly. Depending on the environment the methanol island is placed in, heating/cooling from the atmosphere or ocean on either subprocess could affect its performance, however this can be addressed in the physical design of the island to minimize such influences. The result is, from the process side, the system is relatively agnostic of the ocean surface variables, as the desalination process, the only process affected by the ocean, has a minimal contribution to the overall power requirement of the device, hence why the simulated methanol production efficiency is more or less constant over the entire basin.

Here we only consider the surface waters of the Mediterranean, as these are the easily accessible waters to a methanol island. Deeper waters can be accessed, if the reservoir of DIC in the surface layer is depleted, through siphons pulling inflow from the deeper layers. However, a parcel of surface layer water with a cross-sectional area of 1 m^2 and a depth of 25 m (average thickness of the mixed layer for the Med. Sea), contains roughly 2.6 kg of carbon (if it is all extracted as CO_2 and assuming a DIC concentration of $2300 \mu\text{mol kg}^{-1}$). At the flow rate of 10 L s^{-1} used to simulate the island in this study, the 2.6 kg would be extracted in about 1.5 hours . However, a surface current of 1 mm s^{-1} would advect the water parcel a meter away in 0.5 hours , preventing the device from extracting all the DIC. If higher flow rates are used, a more in depth study of the DIC extraction, and ocean buffer system interaction with the atmosphere, will be needed to conclude the limitations of the resource replenishment. State of the art suggests the replenishing rate of the DIC in the surface layers from the atmosphere may be the limiting factor for effective carbon capture methods utilizing the ocean [10].

The factor dominating the optimal locations for placing the methanol island is the power availability, due to the aforementioned spatially constant methanol production efficiency. As previously stated, the production efficiency behaves as a constant coefficient, such that the production per area of power generation varies the same as the power availability. This essentially merges our power availability constraint and methanol production constraint into a single production per area of power generation constraint that strongly depends on the power availability. Therefore, the atmospheric variables, the wind speed and solar forcing, provide the determining factor for methanol island placement, as they drive the power availability. The resulting optimal locations become apparent after integrating the production over the course of a year, with the Alboran, Levantine, and Cretan Sea being the best locations. These areas also escape the worst locations in terms of maximum wave height (and by proxy significant wave height; even though the Cretan Sea is part of the Aegean Sea, the portion of the sea with increased levels of wind power generation avoid the larger maximum wave heights just north of it), and are therefore recommended for methanol island placement (refer to Fig. 6.21).

Aside from the optimal locations for a methanol island, communities that could greatly benefit from this type of device include island communities. These communities require oil and gas but are required to ship these resources to the island, increasing the cost and carbon footprint of the imported resource. With a methanol island, island communities could produce their own fuel on location, avoiding the need to import oil and gas, gaining independence and safety (e.g. marine oil spillage) from outside resources. According to our results, the island of Crete could benefit from this type of system as part of a diversified energy economy, as well as being optimally located.

Chapter 7

Conclusions

In this thesis, we have investigated the answer to the three research questions relating to the deep convection process in the Gulf of Lion, and it's forcing that we presented in the introduction (Chap. 1):

1. How does the cooling of the Mistral compare to the seasonal change in the atmosphere in terms of forcing deep convection?
2. How does the seasonal and Mistral forcing and its effects on deep convection evolve over multiple years?
3. How does climate change impact the air-sea interaction in the Gulf of Lion?

Three separate studies were performed:

1. a case study on the 2012 to 2013 winter, which featured a well observed deep convection event in the GOL (Chap. 3)
2. a climatology study from 1993 to 2013, which featured seven deep convection years (Chap. 4)
3. a scenario study from 2015 to 2100, investigating the changes in stratification and atmospheric forcing in the gulf with climate change (Chap. 5)

A fourth study was performed in response to the projections of climate change we expect today (Chap. 6). Its purpose was to investigate the potential of a climate change mitigating technology if it were to be operated in the Mediterranean region.

In this thesis, we used an ocean model forced by the outputs of two different atmospheric models: one used for the first two studies and the fourth study and the other used for the third study. These atmospheric forcings were filtered such that we could compare the results of the control simulation with the simulation forced by the filtered forcing to determine the effect of the Mistral on deep convection. We then validated the results for the control simulations with observations collected for

the HyMeX observational framework for the 2012 to 2013 case study and with observations from the Coriolis database for the 1993 to 2013 study.

A simple model was developed that related the change in the stratification index to the change in the atmospheric fluxes on both the low and high frequencies. From this model, we could determine the main parts of the Mistral and seasonal atmospheric forcing that lead to destratification of the gulf. It was used extensively in all three studies relating to deep convection.

In the first study, our case study of the 2012-2013 winter deep convection event, we determined that the Mistral was not the primary driver of preconditioning in the gulf. In fact, the seasonal atmospheric change played a bigger role in destratifying the water column over the course of the fall and winter leading up to deep convection. 2/3 of the destratification came from the low frequency forcing rather than the high frequency, pulse like forcing of the Mistral. This answers our research question.

We also dissected the Mistral and the seasonal forcing with the simple model to discern how each part contributed to destratification. The frequency, duration, and strength of the Mistral were compared to determine which contributed most. We found that the strength was the most important aspect, followed by the duration and frequency. We additionally found that consecutive Mistral events must increasingly become stronger to continue destratifying, otherwise restratification occurs. Conceptually, this is the balance between maintaining a certain level of baroclinic instability and increasing it. Stronger events can create greater instability, whereas events of the same strength or weaker cannot.

The seasonal forcing was found to be comprised of four main surface fluxes: the longwave and shortwave radiation fluxes and the sensible and latent heat fluxes. The shortwave, or solar, radiation flux controls the annual cycle of stratification in the gulf, where the remaining fluxes act as destabilizers, removing buoyancy from the water column. If these three fluxes are strong enough, deep convection can occur, otherwise it cannot.

While the first study provided some interesting results, we couldn't answer the following questions:

- Does the Mistral trigger deep convection, or does the seasonal change trigger it?
- Does the maximum level of stratification play a role in deep convection?
- Does the timing of the seasonal stratification minimum matter and can the Mistral contribution overcome a restratifying seasonal forcing?
- Does the previous year's level of stratification affect the proceeding year?

We attempted to answer them in the second study, our climatological study focusing on the years from 1993 to 2013, along with determining the inter-annual variability of the Mistral and seasonal forcing. We found that Mistral and seasonal atmospheric forcing roughly trigger deep convection equally during deep convection years, which answers our first question. We also found that the maximum seasonal stratification places a requirement on the necessary destratifying fluxes to cause

deep convection: more destratification is required with a larger seasonal stratification maximum. This answers our second question. For the third question, our results weren't conclusively, as we would need a larger dataset to definitely say whether the timing of the seasonal stratification cycle minimum played a role or not. However, we can suggest that it would be more difficult for Mistral to overcome a restratifying ocean column versus an ocean column being destratified simultaneously with the seasonal forcing. The final question also cannot be conclusively determined. A different experimental simulation setup would be required to confirm whether there is an effect of precedence regarding the levels of stratification in the gulf or not. That being said, it can be inferred that years of deep convection would follow one another, as the proceeding year should have less stratification carried over than a year without deep convection.

In regard to answering the second research question of the thesis, we actually found an interesting detail about the Mistral that makes it challenging to fully separate the effects of the Mistral from the effects of the seasonal forcing: the Mistral has a seasonal component. The seasonal component comes from the fact that Mistral winds are more common in the winter time than in the summer time, which is due to the higher rates of cyclogenesis in the winter over the Mediterranean region. Coupled with the fact that the main separating factor between deep convection and non-deep convection years was the wind speed in determining the destratifying fluxes, means that we cannot truly differentiate the seasonal behavior of the Mistral from the rest of the seasonal forcing. What we can definitely say, however, is that the high frequency behavior of the Mistral doesn't destratify as much as the seasonal forcing (low frequency behavior of the Mistral included), with similar split as in our first study (2/3 from seasonal forcing).

The third study shifts the focus to the change of the GOL with climate change. Here we used a scenario (SSP5 8.5) atmospheric forcing and ocean initial states provided by Météo France to drive our own set of ocean model scenario simulations. As discussed in the introduction of this thesis (Chap. 1), deep convection is expected to disappear in the gulf. The disappearance will mainly be due to the increase in stratification in the gulf with an increasingly fresh modified Atlantic waters (MAW) and increasingly salty and warm Levantine intermediate waters (LIW). The main contributor of this increase in stratification is increasing temperatures in the LIW.

However, a perplexing result is that the net atmospheric forcing at the surface of the gulf isn't expected to change, despite the warming atmosphere. From our results, we were able to determine that while the net effect doesn't change, the fluxes do change individually. The latent heat flux becomes stronger, due to an increasing humidity gradient at the sea's surface. But, this strengthening is counterbalanced by the strengthening of the atmospheric longwave downward radiation, itself caused mainly by the increase in atmospheric temperature (with some effect from humidity). These two results from the third study answer our third research question.

In response to this and other undesirable effects projected to occur due to climate change, we performed a fourth study. This fourth study took the ocean model results and atmospheric forcing from our second study and used to determine potential locations to place a methanol producing island powered by renewable energy. Power availability limits the locations acceptable for such a device in the Mediterranean, as the production of hydrogen consumes a lot of energy. Consequently, solar

power availability marks the Alboran and Levantine Seas as the best locations for device placement, while the Cretan Sea has the wind power available to operate the device at similar levels. That being said, this device could play a large role in remote and island communities, such as the island of Crete, as part of an energy mixture, as these communities would greatly benefit from being able to produce hydrocarbons locally.

There are still areas to explore after these four studies. With regard to the Mistral, and its forcing of the gulf, determining how its behavior changes with climate change still needs to be assessed. An extension of this point would be to also investigate the change in cyclogenesis over the Ligurian Sea with climate change, as it is the main driver of the Mistral. Another question to answer is what caused the change in the LIW in the SSP5 8.5 model simulation? The answer to this question is especially pertinent as the change in LIW is dramatic and causes the collapse of deep convection in the gulf. An additional area to study is the modification of the thermohaline circulation of the Mediterranean Sea due to the shutdown of deep convection. It's possible that this could stagnate the bottom layers of the sea, as waters would no longer be regularly oxygenated. As for future work for the climate mitigation study, work is underway to understand the effects of capture removal on the marine biology of the Mediterranean and its efficiency at indirectly removing atmospheric carbon dioxide.

Thus concludes this thesis. Four studies were performed: three on effect of the Mistral and seasonal atmospheric forcing on the deep convection cycle in the Gulf of Lion and fourth on carbon capture in the Mediterranean. Two of the studies/chapters have been published (Chap. 3 and Chap. 6) and one is in review (Chap. 4). The final one is in preparation (Chap. 5).

Bibliography

- [1] Fanny Adloff, Samuel Somot, Florence Sevault, Gabriel Jordà, Roland Aznar, Michel Déqué, Marine Herrmann, Marta Marcos, Clotilde Dubois, Elena Padorno, Enrique Alvarez-Fanjul, and Damià Gomis. Mediterranean sea response to climate change in an ensemble of twenty first century scenarios. *Climate Dynamics*, 45(9-10):2775–2802, feb 2015.
- [2] Urs Aebischer and Christoph Schär. Low-Level Potential Vorticity and Cyclogenesis to the Lee of the Alps. *Journal of the Atmospheric Sciences*, 55:186–2070094–8276/08/2008GL033257, 1998.
- [3] M. Álvarez, H. Sanleón-Bartolomé, T. Tanhua, L. Mintrop, A. Luchetta, C. Cantoni, K. Schroeder, and G. Civitarese. The CO₂ system in the mediterranean sea: a basin wide perspective. *Ocean Science*, 10(1):69–92, feb 2014.
- [4] Yael Amitai, Yosef Ashkenazy, and Hezi Gildor. The Effect of the Source of Deep Water in the Eastern Mediterranean on Western Mediterranean Intermediate and Deep Water. *Frontiers in Marine Science*, 7(615975), January 2021.
- [5] Muhammad Arshad and Brendan C. O’Kelly. Offshore wind-turbine structures: a review. *Proceedings of the Institution of Civil Engineers - Energy*, 166(4):139–152, nov 2013.
- [6] Vincenzo Artale. Role of surface fluxes in ocean general circulation models using satellite sea surface temperature: Validation of and sensitivity to the forcing frequency of the mediterranean thermohaline circulation. *Journal of Geophysical Research*, 107(C8), 2002.
- [7] P.A. Auger, C. Ulses, C. Estournel, L. Stemann, S. Somot, and F. Diaz. Interannual control of plankton communities by deep winter mixing and prey/predator interactions in the NW mediterranean: Results from a 30-year 3d modeling study. *Progress in Oceanography*, 124:12–27, may 2014.
- [8] Magdalena A. Balmaseda, Kevin E. Trenberth, and Erland Källén. Distinctive climate signals in reanalysis of global ocean heat content. *Geophysical Research Letters*, 40(9):1754–1759, may 2013.
- [9] Karine Béranger, Yann Drillet, Marie-Noëlle Houssais, Pierre Testor, Romain Bourdallé-Badie, Bahjat Alhammoud, Alexandra Bozec, Laurent Mortier, Pascale Bouruet-Aubertot, and Michel

- Crépon. Impact of the spatial distribution of the atmospheric forcing on water mass formation in the mediterranean sea. *Journal of Geophysical Research: Oceans*, 115(C12), dec 2010.
- [10] Manon Berger, Laurent Bopp, David T. Ho, and Lester Kwiatkowski. Assessing global macroalgal carbon dioxide removal potential using a high-resolution ocean biogeochemistry model. mar 2022.
- [11] J. P. Bethoux, B. Gentili, J. Raunet, and D. Tailliez. Warming trend in the western mediterranean deep water. *Nature*, 347(6294):660–662, oct 1990.
- [12] J. Beuvier, K. Béranger, C. Lebeaupin Brossier, S. Somot, F. Sevault, Y. Drillet, R. Bourdallé-Badie, N. Ferry, and F. Lyard. Spreading of the western mediterranean deep water after winter 2005: Time scales and deep cyclone transport. *Journal of Geophysical Research: Oceans*, 117(C7):n/a–n/a, jul 2012.
- [13] Anthony Bosse, Pierre Testor, Pierre Damien, Claude Estournel, Patrick Marsaleix, Laurent Mortier, Louis Prieur, and Vincent Taillandier. Wind-forced submesoscale symmetric instability around deep convection in the northwestern mediterranean sea. *Fluids*, 6(3):123, mar 2021.
- [14] Anthony Bosse, Pierre Testor, Loïc Houpert, Pierre Damien, Louis Prieur, Daniel Hayes, Vincent Taillandier, Xavier Durrieu de Madron, Fabrizio d'Ortenzio, Laurent Coppola, Johannes Karstensen, and Laurent Mortier. Scales and dynamics of submesoscale coherent vortices formed by deep convection in the northwestern mediterranean sea. *Journal of Geophysical Research: Oceans*, 121(10):7716–7742, oct 2016.
- [15] Cindy Lebeaupin Brossier, Thomas Arsouze, Karine Béranger, Marie-Noëlle Bouin, Emilie Bresson, Véronique Ducrocq, Hervé Giordani, Mathieu Nuret, Romain Rainaud, and Isabelle Taupier-Letage. Ocean mixed layer responses to intense meteorological events during HyMeX-SOP1 from a high-resolution ocean simulation. *Ocean Modelling*, 84:84–103, dec 2014.
- [16] Andrea Buzzi, Silvio Davolio, and Maurizio Fantini. Cyclogenesis in the lee of the alps: a review of theories. *Bulletin of Atmospheric Science and Technology*, 1(3-4):433–457, oct 2020.
- [17] Karine Béranger, Pierre Testor, and Michel Crépon. Modelling water mass formation in the gulf of lions (mediterranean sea). *CIESM Workshop Monographs*, 2009.
- [18] S. Castellari, N. Pinardi, and K. Leaman. Simulation of water mass formation processes in the mediterranean sea: Influence of the time frequency of the atmospheric forcing. *Journal of Geophysical Research: Oceans*, 105(C10):24157–24181, oct 2000.
- [19] Marine Cauz, Lionel Bloch, Christian Rod, Lionel Perret, Christophe Ballif, and Nicolas Wyrsh. Benefits of a diversified energy mix for islanded systems. *Frontiers in Energy Research*, 8, jul 2020.

- [20] R. A. Clarke and J. Gascard. The Formation of Labrador Sea Water: Part I: Large-Scale Processes. *Journal of Physical Oceanography*, 13(10):1764–1778, 1983.
- [21] M. J. Coates, G. N. Ivey, and J. R. Taylor. Unsteady, Turbulent Convection into a Rotating, Linear Stratified Fluid: Modeling Deep Ocean Convection. *Journal of Physical Oceanography*, 25:3032–3050, 1995.
- [22] L. Coppola, L. Prieur, I. Taupier-Letage, C. Estournel, P. Testor, D. Lefevre, S. Belamari, S. LeReste, and V. Taillandier. Observation of oxygen ventilation into deep waters through targeted deployment of multiple argo-o2floats in the north-western mediterranean sea in 2013. *Journal of Geophysical Research: Oceans*, 122(8):6325–6341, aug 2017.
- [23] Josep Cos, Francisco Doblas-Reyes, Martin Jury, Raúl Marcos, Pierre-Antoine Bretonnière, and Margarida Samsó. The mediterranean climate change hotspot in the CMIP5 and CMIP6 projections. *Earth System Dynamics*, 13(1):321–340, feb 2022.
- [24] Anqing Cui and Robert L. Street. Large-eddy simulation of turbulent rotating convective flow development. *Journal of Fluid Mechanics*, 447:53–84, oct 2001.
- [25] P. Damien, A. Bosse, P. Testor, P. Marsaleix, and C. Estournel. Modeling Postconvective Submesoscale Coherent Vortices in the Northwestern Mediterranean Sea. *Journal of Geophysical Research: Oceans*, 122(12):9937–9961, dec 2017.
- [26] H. de Coninck, A. Revi, M. Babiker, P. Bertoldi, M. Buckeridge, A. Cartwright, W. Dong, J. Ford, S. Fuss, J.-C. Hourcade, D. Ley, R. Mechler, P. Newman, A. Revokatova, S. Schultz, L. Steg, and T. Sugiyama. *Strengthening and Implementing the Global Response. In: Global Warming of 1.5 C. An IPCC Special Report on the impacts of global warming of 1.5 C above pre-industrial levels and related global greenhouse gas emission pathways, in the context of strengthening the global response to the threat of climate change, sustainable development, and efforts to eradicate poverty*, chapter 4, pages 313–444. Cambridge University Press, New York, NY, USA, jun 2018. <https://doi.org/10.1017/9781009157940.006>.
- [27] X. Durrieu de Madron, L. Houpert, P. Puig, A. Sanchez-Vidal, P. Testor, A. Bosse, C. Estournel, S. Somot, F. Bourrin, M. N. Bouin, M. Beauverger, L. Beguery, A. Calafat, M. Canals, C. Cassou, L. Coppola, D. Dausse, F. D'Ortenzio, J. Font, S. Heussner, S. Kunesch, D. Lefevre, H. Le Goff, J. Martín, L. Mortier, A. Palanques, and P. Raimbault. Interaction of dense shelf water cascading and open-sea convection in the northwestern mediterranean during winter 2012. *Geophysical Research Letters*, 40(7):1379–1385, apr 2013.
- [28] X. Durrieu de Madron, S. Ramondenc, L. Berline, L. Houpert, A. Bosse, S. Martini, L. Guidi, P. Conan, C. Curttil, N. Delsaut, S. Kunesch, J. F. Ghiglione, P. Marsaleix, M. Pujo-Pay, T. Séverin, P. Testor, and C. Tamburini and. Deep sediment resuspension and thick nepheloid layer generation by open-ocean convection. *Journal of Geophysical Research: Oceans*, 122(3):2291–2318, mar 2017.

- [29] D. P. Dee, S. M. Uppala, A. J. Simmons, P. Berrisford, P. Poli, S. Kobayashi, U. Andrae, M. A. Balmaseda, G. Balsamo, P. Bauer, P. Bechtold, A. C. M. Beljaars, L. van de Berg, J. Bidlot, N. Bormann, C. Delsol, R. Dragani, M. Fuentes, A. J. Geer, L. Haimberger, S. B. Healy, H. Hersbach, E. V. Hólm, L. Isaksen, P. Kållberg, M. Köhler, M. Matricardi, A. P. McNally, B. M. Monge-Sanz, J.-J. Morcrette, B.-K. Park, C. Peubey, P. de Rosnay, C. Tavolato, J.-N. Thépaut, and F. Vitart. The ERA-interim reanalysis: configuration and performance of the data assimilation system. *Quarterly Journal of the Royal Meteorological Society*, 137(656):553–597, apr 2011.
- [30] Katty Donoso, François Carlotti, Marc Pagano, Brian P. V. Hunt, Rubén Escribano, and Léo Berline. Zooplankton community response to the winter 2013 deep convection process in the NW Mediterranean sea. *Journal of Geophysical Research: Oceans*, 122(3):2319–2338, mar 2017.
- [31] P. Drobinski, B. Alonzo, C. Basdevant, P. Cocquerez, A. Doerenbecher, N. Fourrié, and M. Nuret. Lagrangian dynamics of the mistral during the HyMeX SOP2. *Journal of Geophysical Research: Atmospheres*, 122(3):1387–1402, feb 2017.
- [32] P. Drobinski, P. Alpert, L. Cavicchia, E. Flaounas, A. Hochman, and V. Kotroni. *Strong Winds: Observed Trends, Future Projections, in The Mediterranean Region under Climate Change - A Scientific Update*, chapter 1, pages 115–122. IRD Editions, 2016.
- [33] P. Drobinski, B. Azzopardi, H. Ben Janet Allal, V. Bouchet, E. Civel, A. Creti, N. Duic, N. Fylaktos, J. Mutale, S. Pariente-David, J. Ravetz, C. Taliotis, and R. Vautard. *Energy transition in the Mediterranean. In: Climate and Environmental Change in the Mediterranean Basin – Current Situation and Risks for the Future*, chapter 3, pages 265–322. Union for the Mediterranean, Plan Bleu, UNEP/MAP, Marseille, France, 2020.
- [34] P. Drobinski, S. Bastin, V. Guenard, J.-L. Caccia, A.M. Dabas, P. Delville, A. Protat, O. Reitebuch, and C. Werner. Summer mistral at the exit of the rhône valley. *Quarterly Journal of the Royal Meteorological Society*, 131(605):353–375, jan 2005.
- [35] P. Drobinski, V. Ducrocq, P. Alpert, E. Anagnostou, K. Béranger, M. Borga, I. Braud, A. Chanzy, S. Davolio, G. Delrieu, C. Estournel, N. Filali Boubrahmi, J. Font, V. Grubišić, S. Gualdi, V. Homar, B. Ivančan-Picek, C. Kottmeier, V. Kotroni, K. Lagouvardos, P. Lionello, M. C. Llasat, W. Ludwig, C. Lutoff, A. Mariotti, E. Richard, R. Romero, R. Rotunno, O. Roussot, I. Ruin, S. Somot, I. Taupier-Letage, J. Tintore, R. Uijlenhoet, and H. Wernli. HyMeX: A 10-year multidisciplinary program on the mediterranean water cycle. *Bulletin of the American Meteorological Society*, 95(7):1063–1082, jul 2014.
- [36] Philippe Drobinski, Cyrille Flamant, Jan Dusek, Pierre H. Flamant, and Jacques Pelon. Observational evidence and modelling of an internal hydraulic jump at the atmospheric boundary-layer top during a tramontane event. *Boundary-Layer Meteorology*, 98(3):497–515, mar 2001.

- [37] Aaron Enriquez-Alonso, Arturo Sanchez-Lorenzo, Josep Calbó, Josep-Abel González, and Joel R. Norris. Cloud cover climatologies in the mediterranean obtained from satellites, surface observations, reanalyses, and CMIP5 simulations: validation and future scenarios. *Climate Dynamics*, 47(1-2):249–269, sep 2015.
- [38] C. Estournel. Observation and modeling of the winter coastal oceanic circulation in the gulf of lion under wind conditions influenced by the continental orography (FETCH experiment). *Journal of Geophysical Research*, 108(C3), 2003.
- [39] Claude Estournel, , Pierre Testor, Isabelle Taupier-Letage, Marie-Noelle Bouin, Laurent Coppola, Pierre Durand, Pascal Conan, Anthony Bosse, Pierre-Etienne Brilouet, Laurent Beguery, Sophie Belamari, Karine Béranger, Jonathan Beuvier, Denis Bourras, Guylaine Canut, Alexis Doerenbecher, Xavier Durrieu de Madron, Fabrizio D'Ortenzio, Philippe Drobinski, Véronique Ducrocq, Nadia Fourrié, Hervé Giordani, Loïc Houpert, Laurent Labatut, Cindy Lebeau-pin Brossier, Mathieu Nuret, Louis Prieur, Odile Roussot, Leo Seyfried, and Samuel Somot. HyMeX-SOP2: The field campaign dedicated to dense water formation in the northwestern mediterranean. *Oceanography*, 29(4):196–206, dec 2016.
- [40] Claude Estournel, Pierre Testor, Pierre Damien, Fabrizio D'Ortenzio, Patrick Marsaleix, Pascal Conan, Faycal Kessouri, Xavier Durrieu de Madron, Laurent Coppola, Jean-Michel Lellouche, Sophie Belamari, Laurent Mortier, Caroline Ulses, Marie-Noelle Bouin, and Louis Prieur. High resolution modeling of dense water formation in the north-western mediterranean during winter 2012–2013: Processes and budget. *Journal of Geophysical Research: Oceans*, 121(7):5367–5392, jul 2016.
- [41] Giusy Fedele, Elena Mauri, Giulio Notarstefano, and Pierre Marie Poulain. Characterization of the atlantic water and levantine intermediate water in the mediterranean sea using 20 years of argo data. *Ocean Science*, 18(1):129–142, jan 2022.
- [42] Eric Firing, , Filipe, Andrew Barna, and Ryan Abernathey. Teos-10/gsw-python: v3.4.1.post0, 2021.
- [43] Cyrille Flamant. Alpine lee cyclogenesis influence on air-sea heat exchanges and marine atmospheric boundary layer thermodynamics over the western mediterranean during a tramontane/mistral event. *Journal of Geophysical Research: Oceans*, 108(C2):n/a–n/a, feb 2003.
- [44] Emmanouil Flaounas, Silvio Davolio, Shira Raveh-Rubin, Florian Pantillon, Mario Marcello Miglietta, Miguel Angel Gaertner, Maria Hatzaki, Victor Homar, Samira Khodayar, Gerasimos Korres, Vassiliki Kotroni, Jonilda Kushta, Marco Reale, and Didier Ricard. Mediterranean cyclones: current knowledge and open questions on dynamics, prediction, climatology and impacts. *Weather and Climate Dynamics*, 3(1):173–208, feb 2022.

- [45] Jordi Font, Pere Puig, Jordi Salat, Albert Palanques, and Mikhail Emelianov. Sequence of hydrographic changes in nw mediterranean deep water due to the exceptional winter of 2015. *Scientia Marina*, 71(2):339–346, 2007.
- [46] J. Gascard and R. A. Clarke. The Formation of Labrador Sea Water: Part II: Mesoscale and Smaller-Scale Processes. *Journal of Physical Oceanography*, 13(10):1779–1797, 1983.
- [47] J. C. Gascard. Mediterranean deep water formation baroclinic instability and oceanic eddies. *Oceanologica Acta*, 1978.
- [48] Francisco Javier Ginard-Bosch and Jesús Ramos-Martín. Energy metabolism of the balearic islands (1986–2012). *Ecological Economics*, 124:25–35, apr 2016.
- [49] Hervé Giordani, Cindy Lebeau-pin-Brossier, Fabien Léger, and Guy Caniaux. A PV-approach for dense water formation along fronts: Application to the northwestern mediterranean. *Journal of Geophysical Research: Oceans*, 122(2):995–1015, feb 2017.
- [50] Yonatan Givon, Douglas Keller Jr., Vered Silverman, Romain Pennel, Philippe Drobinski, and Shira Raveh-Rubin. Large-scale drivers of the mistral wind: link to rossby wave life cycles and seasonal variability. *Weather and Climate Dynamics*, 2(3):609–630, jul 2021.
- [51] L. Grignon, D. A. Smeed, H. L. Bryden, and K. Schroeder. Importance of the variability of hydrographic preconditioning for deep convection in the gulf of lion, NW mediterranean. 6(2):573–586, jun 2010.
- [52] S.A. Grigoriev, V.N. Fateev, D.G. Bessarabov, and P. Millet. Current status, research trends, and challenges in water electrolysis science and technology. *International Journal of Hydrogen Energy*, 45(49):26036–26058, oct 2020.
- [53] The Lab Sea Group. The labrador sea deep convection experiment. *Bulletin of the American Meteorological Society*, 79(10):2033–2058, oct 1998.
- [54] Antoine Guion, Solène Turquet, Jan Polcher, Romain Pennel, S. Bastin, and Thomas Arsouze. Droughts and heatwaves in the western mediterranean: impact on vegetation and wildfires using the coupled wrf-orchidee regional model (regips). *Climate Dynamics*, 58(9-10):2881–2903, sep 2021. in review.
- [55] Madec Gurvan, Romain Bourdallé-Badie, Jérôme Chanut, Emanuela Clementi, Andrew Coward, Christian Ethé, Doroteaciro Iovino, Dan Lea, Claire Lévy, Tomas Lovato, Nicolas Martin, Sébastien Masson, Silvia Mocavero, Clément Rousset, Dave Storkey, Simon Müeller, George Nurser, Mike Bell, Guillaume Samson, Pierre Mathiot, Francesca Mele, and Aimie Moulin. Nemo ocean engine. 2022.
- [56] Sabine Haas, Uwe Krien, Birgit Schachler, Stickler Bot, Kyri-Petrou, Velibor Zeli, Kumar Shivam, and Stephen Bosch. wind-python/windpowerlib: Silent improvements, 2021.

- [57] Mathieu Hamon, Jonathan Beuvier, Samuel Somot, Jean-Michel Lellouche, Eric Greiner, Gabriel Jordà, Marie-Noëlle Bouin, Thomas Arsouze, Karine Béranger, Florence Sevault, Clotilde Dubois, Marie Drevillon, and Yann Drillet. Design and validation of MEDRYS, a mediterranean sea reanalysis over the period 1992–2013. *Ocean Science*, 12(2):577–599, apr 2016.
- [58] Marine Herrmann, Florence Sevault, Jonathan Beuvier, and Samuel Somot. What induced the exceptional 2005 convection event in the northwestern mediterranean basin? answers from a modeling study. *Journal of Geophysical Research*, 115(C12), dec 2010.
- [59] Marine Herrmann, Samuel Somot, Florence Sevault, Claude Estournel, and Michel Déqué. Modeling the deep convection in the northwestern mediterranean sea using an eddy-permitting and an eddy-resolving model: Case study of winter 1986–1987. *Journal of Geophysical Research*, 113(C4), apr 2008.
- [60] Marine J. Herrmann and Samuel Somot. Relevance of ERA40 dynamical downscaling for modeling deep convection in the mediterranean sea. *Geophysical Research Letters*, 35(4), feb 2008.
- [61] William F. Holmgren, Clifford W. Hansen, and Mark A. Mikofski. pvlib python: a python package for modeling solar energy systems. *Journal of Open Source Software*, 3(29):884, sep 2018.
- [62] L. Houpert, X. Durrieu de Madron, P. Testor, A. Bosse, F. D'Ortenzio, M. N. Bouin, D. Dause, H. Le Goff, S. Kunesch, M. Labaste, L. Coppola, L. Mortier, and P. Raimbault. Observations of open-ocean deep convection in the northwestern mediterranean sea: Seasonal and interannual variability of mixing and deep water masses for the 2007–2013 period. *Journal of Geophysical Research: Oceans*, 121(11):8139–8171, nov 2016.
- [63] Brian P. V. Hunt, François Carlotti, Katty Donoso, Marc Pagano, Fabrizio D'Ortenzio, Vincent Taillandier, and Pascal Conan. Trophic pathways of phytoplankton size classes through the zooplankton food web over the spring transition period in the north-west mediterranean sea. *Journal of Geophysical Research: Oceans*, 122(8):6309–6324, aug 2017.
- [64] Helen Jones and John Marshall. Convection with Rotation in a Neutral Ocean: A Study of Open-Ocean Deep Convection. *Journal of Physical Oceanography*, 23:1009–1039, 1993.
- [65] Helen Jones and John Marshall. Restratification after Deep Convection. *Journal of Physical Oceanography*, 27:2276–2287, 1997.
- [66] Simon A. Josey, Daniel Oakley, and Robin W. Pascal. On estimating the atmospheric longwave flux at the ocean surface from ship meteorological reports. *Journal of Geophysical Research: Oceans*, 102(C13):27961–27972, dec 1997.

- [67] Vesna Jurčec. On mesoscale characteristics of bora conditions in yugoslavia. *Pure and Applied Geophysics PAGEOPH*, 119(3):640–657, may 1980.
- [68] Mustafa Kemal Kaymak and Ahmet Duran Şahin. Problems encountered with floating photovoltaic systems under real conditions: A new FPV concept and novel solutions. *Sustainable Energy Technologies and Assessments*, 47:101504, oct 2021.
- [69] Douglas Keller, Yonatan Givon, Romain Pennel, Shira Raveh-Rubin, and Philippe J Drobinski. Untangling the mistral and seasonal atmospheric forcing driving deep convection in the gulf of lion: 1993-2013. sep 2022.
- [70] Douglas Keller Jr., Yonatan Givon, Romain Pennel, Shira Raveh-Rubin, and Philippe Drobinski. Untangling the mistral and seasonal atmospheric forcing driving deep convection in the Gulf of Lion: 2012–2013. *Ocean Science*, 18(2):483–510, apr 2022.
- [71] Faycal Kessouri, Caroline Ulses, Claude Estournel, Patrick Marsaleix, Fabrizio D'Ortenzio, Tatiana Severin, Vincent Taillandier, and Pascal Conan. Vertical mixing effects on phytoplankton dynamics and organic carbon export in the western mediterranean sea. *Journal of Geophysical Research: Oceans*, 123(3):1647–1669, mar 2018.
- [72] Faycal Kessouri, Caroline Ulses, Claude Estournel, Patrick Marsaleix, Tatiana Severin, Mireille Pujó-Pay, Jocelyne Caparros, Patrick Raimbault, Orens Pasqueron de Fommervault, Fabrizio D'Ortenzio, Vincent Taillandier, Pierre Testor, and Pascal Conan. Nitrogen and phosphorus budgets in the northwestern mediterranean deep convection region. *Journal of Geophysical Research: Oceans*, 122(12):9429–9454, dec 2017.
- [73] Peter D. Killworth. Deep convection in the world ocean. *Reviews of Geophysics*, 21(1):1, 1983.
- [74] Jay Kratochvil, William Boyson, and David King. Photovoltaic array performance model. Technical report, aug 2004.
- [75] G. Krinner, Nicolas Viovy, Nathalie de Noblet-Ducoudré, Jérôme Ogée, Jan Polcher, Pierre Friedlingstein, Philippe Ciais, Stephen Sitch, and I. Colin Prentice. A dynamic global vegetation model for studies of the coupled atmosphere-biosphere system. *Global Biogeochemical Cycles*, 19(1), feb 2005.
- [76] W. G. Large and S. G. Yeager. The global climatology of an interannually varying air–sea flux data set. *Climate Dynamics*, 33(2-3):341–364, aug 2008.
- [77] William Large and Stephen Yeager. Diurnal to decadal global forcing for ocean and sea-ice models: The data sets and flux climatologies. Technical report, 2004.
- [78] A. Lascaratos. Estimation of deep and intermediate water mass formation rates in the mediterranean sea. *Deep Sea Research Part II: Topical Studies in Oceanography*, 40(6):1327–1332, jan 1993.

- [79] C. Lebeaupin-Brossier and P. Drobinski. Numerical high-resolution air-sea coupling over the gulf of lions during two tramontane/mistral events. *Journal of Geophysical Research*, 114(D10), may 2009.
- [80] Cindy Lebeaupin-Brossier, Karine Béranger, Charles Deltel, and Philippe Drobinski. The mediterranean response to different space–time resolution atmospheric forcings using perpetual mode sensitivity simulations. *Ocean Modelling*, 36(1-2):1–25, jan 2011.
- [81] Cindy Lebeaupin-Brossier, Karine Béranger, and Philippe Drobinski. Sensitivity of the north-western mediterranean sea coastal and thermohaline circulations simulated by the 1/12°-resolution ocean model NEMO-MED12 to the spatial and temporal resolution of atmospheric forcing. *Ocean Modelling*, 43-44:94–107, jan 2012.
- [82] Cindy Lebeaupin-Brossier, Fabien Léger, Hervé Giordani, Jonathan Beuvier, Marie-Noëlle Bouin, Véronique Ducrocq, and Nadia Fourrié. Dense water formation in the north-western mediterranean area during HyMeX-SOP2 in 1/36° ocean simulations: Ocean-atmosphere coupling impact. *Journal of Geophysical Research: Oceans*, 122(7):5749–5773, jul 2017.
- [83] Fabien Léger, Cindy Lebeaupin Brossier, Hervé Giordani, Thomas Arsouze, Jonathan Beuvier, Marie-Noëlle Bouin, Émilie Bresson, Véronique Ducrocq, Nadia Fourrié, and Mathieu Nuret. Dense water formation in the north-western mediterranean area during HyMeX-SOP2 in 1/36° ocean simulations: Sensitivity to initial conditions. *Journal of Geophysical Research: Oceans*, 121(8):5549–5569, aug 2016.
- [84] Sonya Legg, Helen Jones, and Martin Visbeck. A Heton Perspective of Baroclinic Eddy Transfer in Localized Open Ocean Convection. *Journal of Physical Oceanography*, 26:2251–2266, 1996.
- [85] Marina Lévy, Laurent Mémer, and Gurvan Madec. The onset of a bloom after deep winter convection in the northwestern mediterranean sea: mesoscale process study with a primitive equation model. *Journal of Marine Systems*, 16(1-2):7–21, sep 1998.
- [86] Marina Lévy, Laurent Mémer, and Gurvan Madec. Combined effects of mesoscale processes and atmospheric high-frequency variability on the spring bloom in the MEDOC area. *Deep Sea Research Part I: Oceanographic Research Papers*, 47(1):27–53, jan 2000.
- [87] Blandine L'Hévéder, Laurent Li, Florence Sevault, and Samuel Somot. Interannual variability of deep convection in the northwestern mediterranean simulated with a coupled AORCM. *Climate Dynamics*, 41(3-4):937–960, sep 2012.
- [88] Wolfgang Ludwig, Egon Dumont, Michel Meybeck, and Serge Heussner. River discharges of water and nutrients to the mediterranean and black sea: Major drivers for ecosystem changes during past and future decades? *Progress in Oceanography*, 80(3-4):199–217, mar 2009.

- [89] Timothy J Lueker, Andrew G Dickson, and Charles D Keeling. Ocean pCO₂ calculated from dissolved inorganic carbon, alkalinity, and equations for k₁ and k₂: validation based on laboratory measurements of CO₂ in gas and seawater at equilibrium. *Marine Chemistry*, 70(1-3):105–119, may 2000.
- [90] Gurvan Madec, Michel Chartier, and Michel Crépon. The effect of thermohaline forcing variability on deep water formation in the western mediterranean sea: a high-resolution three-dimensional numerical study. *Dynamics of Atmospheres and Oceans*, 15(3-5):301–332, apr 1991.
- [91] Gurvan Madec, Pascale Delecluse, Michel Crepon, and Michel Chartier. A three-dimensional numerical study of deep-water formation in the northwestern mediterranean sea. *Journal of Physical Oceanography*, 21(9):1349–1371, sep 1991.
- [92] Gurvan Madec, François Lott, Pascale Delecluse, and Michel Crépon. Large-scale preconditioning of deep-water formation in the northwestern mediterranean sea. *Journal of Physical Oceanography*, 26, August 1996.
- [93] Katia Mallil, Pierre Testor, Anthony Bosse, Félix Margirier, Loïc Houpert, Hervé Le Goff, Laurent Mortier, and Ferial Louanchi. The levantine intermediate water in the western mediterranean and its interactions with the algerian gyres: insights from 60 years of observation. *Ocean Science*, 18(4):937–952, jul 2022.
- [94] J. F. Manwell. *Wind energy explained*. Wiley, 2009.
- [95] Félix Margirier, Anthony Bosse, Pierre Testor, Blandine L'Hévéder, Laurent Mortier, and David Smeed. Characterization of convective plumes associated with oceanic deep convection in the northwestern mediterranean from high-resolution in situ data collected by gliders. *Journal of Geophysical Research: Oceans*, 122(12):9814–9826, dec 2017.
- [96] Félix Margirier, Pierre Testor, Emma Heslop, Katia Mallil, Anthony Bosse, Loïc Houpert, Laurent Mortier, Marie-Noëlle Bouin, Laurent Coppola, Fabrizio D'Ortenzio, Xavier Durrieu de Madron, Baptiste Mourre, Louis Prieur, Patrick Raimbault, and Vincent Taillandier. Abrupt warming and salinification of intermediate waters interplays with decline of deep convection in the northwestern mediterranean sea. *Scientific Reports*, 10(1), dec 2020.
- [97] John Marshall and Friedrich Schott. Open-ocean convection: Observations, theory, and models. *Reviews of Geophysics*, 37(1):1–64, feb 1999.
- [98] Michele Martini, Raúl Guanache, José A. Armesto, Iñigo J. Losada, and César Vidal. Met-ocean conditions influence on floating offshore wind farms power production. *Wind Energy*, 19(3):399–420, apr 2015.
- [99] D. G. Martinson, P. D. Killworth, and A. L. Gordon. A Convective Model for the Weddell Polynya. *Journal of Physical Oceanography*, 11(4):466–488, 1981.

- [100] Valéry Masson and Philippe Bougeault. Numerical simulation of a low-level wind created by complex orography: A cieszko case study. *Monthly Weather Review*, 124(4):701–715, apr 1996.
- [101] Eugene L. Maxwell. A Quasi-Physical Model for Converting Hourly Global Horizontal to Direct Normal Insolation. Technical report, 1987.
- [102] Nicolas Mayot, Fabrizio D'Ortenzio, Vincent Taillandier, Louis Prieur, Orens Pasqueron de Fommervault, Hervé Claustre, Anthony Bosse, Pierre Testor, and Pascal Conan. Physical and biogeochemical controls of the phytoplankton blooms in north western mediterranean sea: A multiplatform approach over a complete annual cycle (2012–2013 DEWEX experiment). *Journal of Geophysical Research: Oceans*, 122(12):9999–10019, dec 2017.
- [103] Nicolas Mayot, Fabrizio D'Ortenzio, Julia Uitz, Bernard Gentili, Joséphine Ras, Vincenzo Vellucci, Melek Golbol, David Antoine, and Hervé Claustre. Influence of the phytoplankton community structure on the spring and annual primary production in the northwestern mediterranean sea. *Journal of Geophysical Research: Oceans*, 122(12):9918–9936, dec 2017.
- [104] MEDOC. Observation of formation of deep water in the mediterranean sea, 1969. *Nature*, 227, September 1970.
- [105] C. Mertens and F. Schott. Interannual variability of deep-water formation in the northwestern mediterranean. *Journal of Physical Oceanography*, 28(7):1410–1424, jul 1998.
- [106] P. Millet, R. Ngameni, S.A. Grigoriev, N. Mbemba, F. Brisset, A. Ranjbari, and C. Etiévant. PEM water electrolyzers: From electrocatalysis to stack development. *International Journal of Hydrogen Energy*, 35(10):5043–5052, may 2010.
- [107] Claude Millot and Isabelle Taupier-Letage. Circulation in the mediterranean sea. In *The Mediterranean Sea*, pages 29–66. Springer Berlin Heidelberg, 2005.
- [108] MODIS Science Team. Mod02qkm modis/terra calibrated radiances 5-min l1b swath 250m, 2017.
- [109] MODIS Science Team. Myd02hkm modis/aqua calibrated radiances 5-min l1b swath 500m, 2017.
- [110] Yign Noh, Woo Geun Cheon, and Siegfried Raasch. The role of preconditioning in the evolution of open-ocean deep convection. *Journal of Physical Oceanography*, 33(6):1145–1166, jun 2003.
- [111] Brian C. O'Neill, Claudia Tebaldi, Detlef P. van Vuuren, Veronika Eyring, Pierre Friedlingstein, George Hurtt, Reto Knutti, Elmar Kriegler, Jean-Francois Lamarque, Jason Lowe, Gerald A. Meehl, Richard Moss, Keywan Riahi, and Benjamin M. Sanderson. The scenario model inter-comparison project (ScenarioMIP) for CMIP6. *Geoscientific Model Development*, 9(9):3461–3482, sep 2016.

- [112] World Meteorological Organization. *Guide to wave analysis and forecasting*. Secretariat of the World Meteorological Organization, 2018.
- [113] Iván M. Parras-Berrocal, Rubén Vázquez, William Cabos, Dmitry V. Sein, Oscar Álvarez, Miguel Bruno, and Alfredo Izquierdo. Surface and intermediate water changes triggering the future collapse of deep water formation in the north western mediterranean. *Geophysical Research Letters*, 49(4), feb 2022.
- [114] Ivan M. Parras-Berrocal, Ruben Vazquez, William Cabos, Dmitry Sein, Rafael Mañanes, Juan Perez-Sanz, and Alfredo Izquierdo. The climate change signal in the mediterranean sea in a regionally coupled atmosphere–ocean model. *Ocean Science*, 16(3):743–765, jun 2020.
- [115] Bruce D. Patterson, Frode Mo, Andreas Borgschulte, Magne Hillestad, Fortunat Joos, Trygve Kristiansen, Svein Sunde, and Jeroen A. van Bokhoven. Renewable CO₂ recycling and synthetic fuel production in a marine environment. *Proceedings of the National Academy of Sciences*, 116(25):12212–12219, jun 2019.
- [116] Antonio Pusceddu, Marianna Mea, Cristina Gambi, Silvia Bianchelli, Miquel Canals, Anna Sanchez-Vidal, Antoni Calafat, Serge Heussner, Xavier Durrieu De Madron, Jérôme Avril, Laurenz Thomsen, Rosa García, and Roberto Danovaro. Ecosystem effects of dense water formation on deep mediterranean sea ecosystems: an overview. *Advances in Oceanography and Limnology*, 1(1):67–83, jun 2010.
- [117] Rahul Chitteth Ramachandran, Cian Desmond, Frances Judge, Jorrit-Jan Serraris, and Jimmy Murphy. Floating wind turbines: marine operations challenges and opportunities. *Wind Energy Science*, 7(2):903–924, apr 2022.
- [118] A.R. Robinson, W.G. Leslie, A. Theocharis, and A. Lascaratos. Mediterranean sea circulation. In *Encyclopedia of Ocean Sciences*, pages 1689–1705. Elsevier, 2001.
- [119] Wolfgang Roether, Beniamino B. Manca, Birgit Klein, Davide Bregant, Dimitrios Georgopoulos, Volker Beitzel, Vedrana Kovacevic, and Anna Luchetta. Recent Changes in Eastern Mediterranean Deep Waters. *Science*, 271(5247):333–335, 1996.
- [120] Joy Romanski, Anastasia Romanou, Michael Bauer, and George Tselioudis. Atmospheric forcing of the eastern mediterranean transient by midlatitude cyclones. *Geophysical Research Letters*, 39(3):n/a–n/a, feb 2012.
- [121] P. M. Ruti, S. Somot, F. Giorgi, C. Dubois, E. Flaounas, A. Obermann, A. Dell’Aquila, G. Pisacane, A. Harzallah, E. Lombardi, B. Ahrens, N. Akhtar, A. Alias, T. Arsouze, R. Aznar, S. Bastin, J. Bartholy, K. Béranger, J. Beuvier, S. Bouffies-Cloch e, J. Brauch, W. Cabos, S. Calmanti, J.-C. Calvet, A. Carillo, D. Conte, E. Coppola, V. Djurdjevic, P. Drobinski, A. Elizalde-Arellano, M. Gaertner, P. Gal an, C. Gallardo, S. Gualdi, M. Goncalves, O. Jorba, G. Jord a, B. L’Heveder, C. Lebeau-pin-Brossier, L. Li, G. Liguori, P. Lionello, D. Maci as,

- P. Nabat, B. Önoel, B. Raikovic, K. Ramage, F. Sevault, G. Sannino, M. V. Struglia, A. Sanna, C. Torma, and V. Vervatis. Med-CORDEX initiative for mediterranean climate studies. *Bulletin of the American Meteorological Society*, 97(7):1187–1208, jul 2016.
- [122] Arturo Sanchez-Lorenzo, Aaron Enriquez-Alonso, Josep Calbó, Josep-Abel González, Martin Wild, Doris Folini, Joel R. Norris, and Sergio M. Vicente-Serrano. Fewer clouds in the mediterranean: consistency of observations and climate simulations. *Scientific Reports*, 7(1), feb 2017.
- [123] Johannes Sander, Dieter Wolf-Gladrow, and Dirk Olbers. Numerical studies of open ocean deep convection. *Journal of Geophysical Research*, 100(C10):20579, 1995.
- [124] M. E. Schiano, M. Borghini, S. Castellari, and C. Luttazzi. Climatic features of the mediterranean sea detected by the analysis of the longwave radiative bulk formulae. *Annales Geophysicae*, 18(11):1482–1487, nov 2000.
- [125] Friedrich Schott, Martin Visbeck, Uwe Send, Jürgen Fischer, Lothar Stramma, and Yves Desaubies. Observations of deep convection in the gulf of lions, northern mediterranean, during the winter of 1991/92. *Journal of Physical Oceanography*, 26(4):505–524, apr 1996.
- [126] K. Schroeder, A. Ribotti, M. Borghini, R. Sorgente, A. Perilli, and G. P. Gasparini. An extensive western mediterranean deep water renewal between 2004 and 2006. *Geophysical Research Letters*, 35(18), sep 2008.
- [127] K. Schröder, G. P. Gasparini, M. Tangherlini, and M. Astraldi. Deep and intermediate water in the western mediterranean under the influence of the eastern mediterranean transient. *Geophysical Research Letters*, 33(21), nov 2006.
- [128] Roland Séférian, Pierre Nabat, Martine Michou, David Saint-Martin, Aurore Voltaire, Jeanne Colin, Bertrand Decharme, Christine Delire, Sarah Berthet, Matthieu Chevallier, Stéphane Sénési, Laurent Franchisteguy, Jessica Vial, Marc Mallet, Emilie Joetzjer, Olivier Geoffroy, Jean-François Guérémy, Marie-Pierre Moine, Rym Msadek, Aurélien Ribes, Matthias Rocher, Romain Roehrig, David Salas y Méliá, Emilia Sanchez, Laurent Terray, Sophie Valcke, Robin Waldman, Olivier Aumont, Laurent Bopp, Julie Deshayes, Christian Éthé, and Gurvan Madec. Evaluation of CNRM earth system model, CNRM-ESM2-1: Role of earth system processes in present-day and future climate. *Journal of Advances in Modeling Earth Systems*, 11(12):4182–4227, dec 2019.
- [129] Uwe Send and John Marshall. Integral Effects of Deep Convection. *Journal of Physical Oceanography*, 25:855–872, 1995.
- [130] Uwe Send and Pierre Testor. Direct observations reveal the deep circulation of the western mediterranean sea. *Journal of Geophysical Research: Oceans*, 122(12):10091–10098, dec 2017.

- [131] Florence Sevault, Samuel Somot, Antoinette Alias, Clotilde Dubois, Cindy Lebeau-pin-Brossier, Pierre Nabat, Fanny Adloff, Michel Déqué, and Bertrand Decharme. A fully coupled mediterranean regional climate system model: design and evaluation of the ocean component for the 1980–2012 period. *Tellus A: Dynamic Meteorology and Oceanography*, 66(1):23967, dec 2014.
- [132] Tatiana Severin, Faycal Kessouri, Mathieu Rembauville, Elvia Denisse Sánchez-Pérez, Louise Oriol, Jocelyne Caparros, Mireille Pujo-Pay, Jean-François Ghiglione, Fabrizio D'Ortenzio, Vincent Taillandier, Nicolas Mayot, Xavier Durrieu De Madron, Caroline Ulses, Claude Estournel, and Pascal Conan. Open-ocean convection process: A driver of the winter nutrient supply and the spring phytoplankton distribution in the northwestern mediterranean sea. *Journal of Geophysical Research: Oceans*, 122(6):4587–4601, jun 2017.
- [133] Léo Seyfried, Claude Estournel, Patrick Marsaleix, and Evelyne Richard. Dynamics of the north balearic front during an autumn tramontane and mistral storm: air–sea coupling processes and stratification budget diagnostic. *Ocean Science*, 15(1):179–198, mar 2019.
- [134] Muzhong Shen, Nick Bennett, Yulong Ding, and Keith Scott. A concise model for evaluating water electrolysis. *International Journal of Hydrogen Energy*, 36(22):14335–14341, nov 2011.
- [135] William Skamarock, Joseph Klemp, Jimy Dudhia, David Gill, Dale Barker, Wei Wang, Xiang-Yu Huang, and Michael Duda. A description of the advanced research wrf version 3. Technical report, 2008.
- [136] J. Skrzypek, M. Lachowska, and D. Serafin. Methanol synthesis from CO₂ and h₂: dependence of equilibrium conversions and exit equilibrium concentrations of components on the main process variables. *Chemical Engineering Science*, 45(1):89–96, 1990.
- [137] R.J. Small, S. Carniel, T. Campbell, J. Teixeira, and R. Allard. The response of the ligurian and tyrrhenian seas to a summer mistral event: A coupled atmosphere–ocean approach. *Ocean Modelling*, 48:30–44, may 2012.
- [138] R. O. Smith, H. L. Bryden, and K. Stansfield. Observations of new western mediterranean deep water formation using argo floats 2004–2006. *Ocean Science*, 4(2):133–149, may 2008.
- [139] Taimoor Sohail, Bishakhdatta Gayen, and Andrew McC. Hogg. The dynamics of mixed layer deepening during open-ocean convection. *Journal of Physical Oceanography*, 50(6):1625–1641, jun 2020.
- [140] S. Somot, F. Sevault, and M. Déqué. Transient climate change scenario simulation of the mediterranean sea for the twenty-first century using a high-resolution ocean circulation model. *Climate Dynamics*, 27(7-8):851–879, jul 2006.
- [141] Samuel Somot. *Modélisation Climatique du Bassin Méditerranéen : Variabilité et Scénarios de Changement Climatique*. phdthesis, Université Toulouse III, December 2005.

- [142] Samuel Somot, Loic Houpert, Florence Sevault, Pierre Testor, Anthony Bosse, Isabelle Taupier-Letage, Marie-Noelle Bouin, Robin Waldman, Christophe Cassou, Emilia Sanchez-Gomez, Xavier Durrieu de Madron, Fanny Adloff, Pierre Nabat, and Marine Herrmann. Characterizing, modelling and understanding the climate variability of the deep water formation in the north-western mediterranean sea. *Climate Dynamics*, 51(3):1179–1210, aug 2016.
- [143] Xiangzhou Song and Lisan Yu. Air-sea heat flux climatologies in the mediterranean sea: Surface energy balance and its consistency with ocean heat storage. *Journal of Geophysical Research: Oceans*, 122(5):4068–4087, may 2017.
- [144] Javier Soto-Navarro, G. Jordá, A. Amores, W. Cabos, S. Somot, F. Sevault, D. Macías, V. Djurdjevic, G. Sannino, L. Li, and D. Sein. Evolution of mediterranean sea water properties under climate change scenarios in the med-CORDEX ensemble. *Climate Dynamics*, 54(3-4):2135–2165, jan 2020.
- [145] Takvor Soukissian, Dimitra Denaxa, Flora Karathanasi, Aristides Prospathopoulos, Konstantinos Sarantakos, Athanasia Iona, Konstantinos Georgantas, and Spyridon Mavrakos. Marine renewable energy in the mediterranean sea: Status and perspectives. *Energies*, 10(10):1512, sep 2017.
- [146] M. Stabholz, X. Durrieu de Madron, M. Canals, A. Khripounoff, I. Taupier-Letage, P. Testor, S. Heussner, P. Kerhervé, N. Delsaut, L. Houpert, G. Lastras, and B. Dennielou. Impact of open-ocean convection on particle fluxes and sediment dynamics in the deep margin of the gulf of lions. *Biogeosciences*, 10(2):1097–1116, feb 2013.
- [147] Fiammetta Straneo and Mitsuhiro Kawase. Comparisons of Localized Convection due to Localized Forcing and to Preconditioning. *Journal of Physical Oceanography*, 29:55–68, 1999.
- [148] Taupier-Letage Isabelle. CTD SOP2, Provence - Tethys 2, 2013.
- [149] Jasmin Terreni, Andreas Borgschulte, Magne Hillestad, and Bruce D. Patterson. Understanding catalysis—a simplified simulation of catalytic reactors for CO₂ reduction. *ChemEngineering*, 4(4):62, nov 2020.
- [150] P. Testor and J-C. Gascard. Large-scale spreading of deep waters in the western mediterranean sea by submesoscale coherent eddies. *Journal of Physical Oceanography*, 33(1):75–87, jan 2003.
- [151] Pierre Testor, Anthony Bosse, Loïc Houpert, Félix Margirier, Laurent Mortier, Hervé Legoff, Denis Dausse, Matthieu Labaste, Johannes Karstensen, Daniel Hayes, Antonio Olita, Alberto Ribotti, Katrin Schroeder, Jacopo Chiggiato, Reiner Onken, Emma Heslop, Baptiste Mourre, Fabrizio D'ortenzio, Nicolas Mayot, Héloïse Lavigne, Orens de Fommervault, Laurent Coppola, Louis Prieur, Vincent Taillandier, Xavier Durrieu de Madron, Francois Bourrin, Gael Many,

- Pierre Damien, Claude Estournel, Patrick Marsaleix, Isabelle Taupier-Letage, Patrick Raimbault, Robin Waldman, Marie-Noelle Bouin, Hervé Giordani, Guy Caniaux, Samuel Somot, Véronique Ducrocq, and Pascal Conan. Multiscale observations of deep convection in the northwestern mediterranean sea during winter 2012-2013 using multiple platforms. *Journal of Geophysical Research: Oceans*, 123(3):1745–1776, mar 2018.
- [152] J. S. Turner. *Buoyancy Effects in Fluids*. Cambridge University Press, 1973.
- [153] C. Ulses, P.-A. Auger, K. Soetaert, P. Marsaleix, F. Diaz, L. Coppola, M.J. Herrmann, F. Kessouri, and C. Estournel. Budget of organic carbon in the north-western mediterranean open sea over the period 2004-2008 using 3-d coupled physical-biogeochemical modeling. *Journal of Geophysical Research: Oceans*, 121(9):7026–7055, sep 2016.
- [154] United Nations Climate Change. The Paris Agreement. <https://unfccc.int/process-and-meetings/the-paris-agreement/the-paris-agreement>, 2015. Accessed June 13th, 2022.
- [155] Martin Visbeck, John Marshall, and Helen Jones. Dynamics of Isolated Convective Regions in the Ocean. *Journal of Physical Oceanography*, 26:1721–1734, 1996.
- [156] John Vourdoubas. Studies on the electrification of the transport sector in the island of crete, greece. *Open Journal of Energy Efficiency*, 07(01):19–32, 2018.
- [157] Robin Waldman, Nils Brüggemann, Anthony Bosse, Michael Spall, Samuel Somot, and Florence Sevault. Overturning the mediterranean thermohaline circulation. *Geophysical Research Letters*, 45(16):8407–8415, aug 2018.
- [158] Robin Waldman, Marine Herrmann, Samuel Somot, Thomas Arsouze, Rachid Benshila, Anthony Bosse, Jerome Chanut, Herve Giordani, Florence Sevault, and Pierre Testor. Impact of the mesoscale dynamics on ocean deep convection: The 2012-2013 case study in the north-western mediterranean sea. *Journal of Geophysical Research: Oceans*, 122(11):8813–8840, nov 2017.
- [159] Robin Waldman, Samuel Somot, Marine Herrmann, Florence Sevault, and Pål Erik Isachsen. On the chaotic variability of deep convection in the mediterranean sea. *Geophysical Research Letters*, 45(5):2433–2443, mar 2018.
- [160] Robin Waldman, Samuel Somot, Marine Herrmann, Pierre Testor, Claude Estournel, Florence Sevault, Louis Prieur, Laurent Mortier, Laurent Coppola, Vincent Taillandier, Pascal Conan, and Denis Dausse. Estimating dense water volume and its evolution for the year 2012-2013 in the northwestern mediterranean sea: An observing system simulation experiment approach. *Journal of Geophysical Research: Oceans*, 121(9):6696–6716, sep 2016.
- [161] Li Wang, Camille Violet, Ryan M. DuChanois, and Menachem Elimelech. Derivation of the theoretical minimum energy of separation of desalination processes. *Journal of Chemical Education*, 97(12):4361–4369, nov 2020.

- [162] Frank White. *Viscous fluid flow*. McGraw-Hill Higher Education, New York, NY, 2011.
- [163] Peili Wu and Keith Haines. Modeling the dispersal of levantine intermediate water and its role in mediterranean deep water formation. *Journal of Geophysical Research: Oceans*, 101(C3):6591–6607, mar 1996.
- [164] S. Zecchetto and F. De Biasio. Sea surface winds over the mediterranean basin from satellite data (2000–04): Meso- and local-scale features on annual and seasonal time scales. *Journal of Applied Meteorology and Climatology*, 46(6):814–827, jun 2007.
- [165] Baruch Ziv, Hadas Saaroni, and Pinhas Alpert. The factors governing the summer regime of the eastern mediterranean. *International Journal of Climatology*, 24(14):1859–1871, 2004.

Titre : Impact de la variabilité spatio-temporelle du Mistral sur la formation d'eaux denses en Méditerranée

Mots clés : Méditerranée, formation d'eaux denses, Mistral, convection profonde

Résumé : La convection profonde dans le golfe du Lion conduit à la formation d'une eau dense qui entraîne une partie de la circulation thermohaline en mer Méditerranée. Le mélange vertical résultant de ce processus distribue l'oxygène et les nutriments dans toute la colonne d'eau, entraînant de grandes proliférations de phytoplancton. Par conséquent, la convection profonde et la formation d'eau dense qui en résulte dans le golfe du Lion est un processus important pour la circulation générale et les processus biologiques de la mer Méditerranée. L'objectif de la thèse est d'identifier les principaux attributs du Mistral et les forçages atmosphériques saisonniers qui contrôlent le préconditionnement de la convection profonde et la formation d'eau dense dans le Golfe du Lion.

Pour cela, nous avons utilisé des données de modèles atmosphériques (WRF/ORCHIDEE et RCM6) et un modèle océanique (NEMO) qui nous ont permis de simuler en détail la circulation océanique dans le Golfe du Lion. Deux séries de simulations NEMO ont été utilisées, une série témoin et une série saisonnière. La série saisonnière a été forcée avec un forçage atmosphérique filtré, qui a supprimé l'effet du Mistral. Les deux séries ont ensuite été comparées pour déterminer l'effet du Mistral et des changements atmosphériques saisonniers sur la réponse de l'océan. Trois études dans cette thèse ont utilisé cette technique : une étude de cas de l'année 2012 à 2013, une étude de climatologie des années 1993 à 2013, et une étude de scénario des années 2015 à 2100.

La première étude a révélé l'importance de la composante saisonnière du forçage atmosphérique sur le préconditionnement de la stabilité verticale de l'océan, démontrant qu'elle représentait plus de la moitié de la déstratification conduisant à la convection profonde. L'étude a également déterminé que l'attribut le plus important du Mistral pour la déstratification est sa force, plutôt que sa durée ou sa fréquence.

La deuxième étude a déterminé que l'existence de la composante basse fréquence du Mistral, qui apparaît en hiver, contrôle quelles années présentent une convection profonde et quelles années ne le font pas. Les années avec des vitesses de vent plus élevées dans le forçage saisonnier, causées par la composante basse fréquence du Mistral, comportaient une convection profonde, contrairement aux autres.

La troisième étude a déterminé que le forçage atmosphérique dans la région reste à peu près constant jusqu'à la fin du scénario, l'advection apportant des eaux plus stratifiées dans la région à partir de 2060. Le résultat est une colonne verticale fortement stratifiée en raison de l'advection, conduisant à l'extinction de la convection profonde dans la région après l'année 2060.

Une quatrième étude, légèrement distincte des autres études, utilise les données du modèle de la deuxième étude et examine une méthode potentielle pour atténuer l'utilisation des combustibles fossiles en Méditerranée et capturer le carbone de l'océan : une île productrice de méthanol. Les résultats de cette étude suggèrent que le meilleur endroit pour placer une telle île se trouve dans les mers d'Alboran, Levantine et Crétoise, en raison de la disponibilité de l'énergie solaire (Alboran et Levantine) et éolienne (Crétoise). Un tel dispositif pourrait permettre aux communautés insulaires et éloignées de devenir plus indépendantes énergétiquement.

La conclusion générale de cette thèse est que le mistral et le forçage atmosphérique saisonnier entraînent une convection profonde et une déstratification océanique dans le golfe du Lion. La composante saisonnière contribue davantage, mais ni le Mistral ni la composante saisonnière ne sont en mesure de surmonter la stratification par advection prédite dans le futur. Cela conduit à l'effondrement de la convection profonde dans la région, soulignant l'importance de l'atténuation du changement climatique et la nécessité d'appareils comme l'îlot de production de méthanol.

Title : Impact of the spatial and temporal variability of the Mistral on dense water formation in the Mediterranean Sea

Keywords : Mediterranean Sea, dense water formation, Mistral, deep convection

Abstract : Deep convection in the Gulf of Lion leads to the formation of dense water that drives part of the thermohaline circulation in the Mediterranean Sea. The vertical mixing from this process distributes oxygen and nutrients throughout the water column, leading to large phytoplankton blooms. Therefore, deep convection and the resulting formation of dense water in the Gulf of Lion is an important process for the general circulation and biological processes of the Mediterranean Sea. The aim of the thesis is to identify key attributes of the Mistral and seasonal atmospheric forcing that control the preconditioning of deep convection and formation of dense water in the Gulf of Lion.

For this purpose, we used atmospheric model data (WRF/ORCHIDEE and RCM6) and an ocean model (NEMO) that allowed us to simulate in detail the ocean circulation in the Gulf of Lion. Two series of NEMO simulations were used, one control series and one seasonal series. The seasonal series was forced with filtered atmospheric forcing, that removed the effect of the Mistral. The two series were then compared to determine the effect of the Mistral and seasonal atmospheric change on the ocean response. Three studies in this thesis used this technique: a case study of the year 2012 to 2013, a climatology study of the years 1993 to 2013, and a scenario study of the years 2015 to 2100.

The first study revealed the importance of the seasonal component of the atmospheric forcing on preconditioning the ocean vertical stability, demonstrating it accounted for more than half of the de-stratification leading to deep convection. The study also determined that the most important attribute of the Mistral for de-stratification is its strength, rather than its duration or frequency.

The second study determined that the existence of the low fre-

quency component of the Mistral, which appears in the winter, controls which years feature deep convection and which years do not. Years with higher wind speeds in the seasonal forcing, caused by the low frequency component of the Mistral, featured deep convection, while the others did not.

The third study determined that the atmospheric forcing in the region remains roughly constant until the end of the scenario, with advection bringing in more stratified waters to the region starting after 2060. The result is a strongly stratified vertical column due to the advection, leading to the extinction of deep convection in the region after the year of 2060.

A fourth study, slightly separate from the other studies, utilizes the model data from the second study and looks at a potential method to mitigate fossil fuel use in the Mediterranean and capture carbon from the ocean: a methanol producing island. Results from this study suggest the best place to place such an island are in the Alboran, Levantine, and Cretan Seas, due to solar (Alboran and Levantine) and wind power (Cretan) availability. Such a device could allow island and remote communities to become more energy independent.

The overall conclusion for this thesis is both the Mistral and seasonal atmospheric forcing drive deep convection and ocean de-stratification in the Gulf of Lion. The seasonal component contributes more, but neither the Mistral nor seasonal component are able to overcome the advected stratification predicted in the future. This leads to the collapse of deep convection in region, highlighting the importance of climate change mitigation and the need for devices like the methanol producing island.